



**BERGISCHE
UNIVERSITÄT
WUPPERTAL**

Investigation of Ion-Solvent Interactions in Electrospray Ionization Mass Spectrometry

Dissertation

zur Erlangung des akademischen Grades
Doktor der Naturwissenschaften (Dr. rer. nat.)

vorgelegt von
Christine Polaczek

Bergische Universität Wuppertal
Fakultät 4 - Mathematik und Naturwissenschaften
Physikalische und Theoretische Chemie
unter der Anleitung von Prof. Dr. Thorsten Benter

Wuppertal, August 2021

The PhD thesis can be quoted as follows:

urn:nbn:de:hbz:468-urn:nbn:de:hbz:468-20211221-093827-9

[<http://nbn-resolving.de/urn/resolver.pl?urn=urn%3Anbn%3Ade%3Ahbz%3A468-20211221-093827-9>]

DOI: 10.25926/xntq-c882

[<https://doi.org/10.25926/xntq-c882>]

*„Der Sinn des Lebens kann doch nicht sein, eine aufgeräumte
Wohnung zu hinterlassen.“*

Elke Heidenreich
Schriftstellerin und Literaturkritikerin

Für meinen Vater

Danksagung

Viele Menschen haben dazu beigetragen, dass ich diese Arbeit anfertigen konnte. Ich bin sehr dankbar dafür, diese Menschen kennen gelernt zu haben, mit ihnen zusammen studiert, gearbeitet und geforscht zu haben. Ich bin dankbar dafür, mich bei diesen Menschen für ihre Anwesenheit und Begleitung, für ihre Zeit und Gedankenarbeit und für ihre hilfreichen Kompetenzen und Fertigkeiten bedanken zu können. Ich möchte an dieser Stelle den Menschen danken, denen ich heute meinen Dank nicht mehr persönlich aussprechen kann.

Ich danke Ian Barnes dafür, dass er im Physikalische Chemie I Praktikum eine Lern- und Arbeitsatmosphäre geschaffen hat, in der ich als Studentin die Praktikumsversuche mit viel Freude und Neugierde durchführen und später als Assistentin mein Wissen und meine Erfahrung emanzipiert und gleichzeitig reflektiert an Studierende weitergeben konnte. Ian hat auf diese Weise dazu beigetragen, dass ich die Schönheit der Physikalischen Chemie entdeckt und mich in der dazugehörigen Arbeitsgruppe wohl und wertgeschätzt gefühlt habe.

Ich danke Klaus Brockmann dafür, dass er in seinem Büro einen Raum der Begegnung geschaffen hat. Wenn es etwas zu diskutieren oder zu besprechen, etwas zu feiern oder zu verkünden, etwas zu essen oder zu trinken gab, dann wurde das Café Brockmann aufgesucht. Auch wenn man etwas oder jemanden oder auch die Antwort auf eine administrative oder fachliche Frage suchte, wurde man im Café Brockmann fündig. Wenn es nicht Klaus war, der einem weiter half, dann begegnete man dort einer anderen Person, die eine gute Idee oder Information hatte. Und manchmal genügte es auch, sich kurz auf das Sofa zu setzen und eine Tasse Kaffee zu trinken.

Ich danke meinem Vater dafür, dass er meine Wissbegierde genährt und mich zu einem kritisch denkenden und selbstständigen Menschen erzogen hat. Von meinem Vater habe ich gelernt, dass man die Prozesse, die in einer Maschine ablaufen, erst verstanden haben muss, bevor man die Maschine richtig benutzen kann.

Abstract

Techniques causing the increase of the average charge state of multiply charged ions in electrospray ionization mass spectrometry (ESI-MS) are of particular relevance, especially in the field of life sciences. Chemical modification of the gas as well as the solution phase can significantly alter the observed charge state distribution.

In this work, the impact of protic and aprotic polar modifiers on the ion distribution, recorded with a nanoESI setup, is studied. In experiments with Substance P, depletion of the higher charge state (3+) in favor of the lower charge state (2+) is observed with polar protic gas phase modifiers. Retention of the 3+ charge state is induced by the addition of polar aprotic compounds to the ESI solution (solution phase modification) or as vapors to the gas phase (gas phase modification). Charge retention is in both cases accompanied by observation of ion-modifier clusters. The crucial role of the formation of proton-bound ion-modifier clusters is elucidated in a charge retention/charge depletion model: Addition of a chemical modifier results in preferential solvation of the analyte ion by the modifier. Formation of these ion-modifier clusters facilitates intramolecular proton transfer to modifier clusters, when the gas-phase basicity (GB) of the modifier cluster solvating the charge site exceeds the GB of the charge site. It is hypothesized that due to their ability to form hydrogen-bond networks, the GB of an associated protic modifier cluster can increase until proton transfer becomes thermodynamically favorable. In contrast, the number of aprotic modifiers solvating a charge site is limited because aprotic ligands can only form one hydrogen bond. Furthermore, proton transfer to modifier clusters is driven by collisional activation of the ions during their passage through the transfer stages of the mass spectrometer.

This model is validated by a systematic experimental study on the impact of gas phase modifiers on the ion signal distribution of terminal alkyldiamines, which represent a model system for adjacent charge sites in multiply protonated macromolecules. This study addresses the influence of the chemical structure, particularly the alkyl chain length, of the diamines, the location of the gas phase modifier addition, and ion activation processes on external solvation of the ions and charge retention/depletion processes, respectively. By chemical modification of the collision gas in a quadrupole ion trap instrument, cluster reactions between doubly protonated diamines and neutral acetonitrile occurring in the gas phase are investigated and the implications of chemical modification for mass analysis are characterized.

In addition to the experimental studies, theoretical methods are applied to further elucidate ion-solvent interactions on a molecular level. Ab initio calculations of singly and doubly protonated ethylenediamine ions clustered with water (H₂O) and

acetonitrile (ACN) provide comparative analysis of the cluster structures and their stability as well as determination of thermodynamically favored reaction pathways. Calculations of collision cross sections and equilibrated cluster distributions enable comparison between modeled and measured ion mobilities of the dynamic cluster reaction systems. The theoretical results support the notion that intracuster proton transfer to aprotic solvent clusters is unlikely to occur, whereas proton transfer to protic solvent clusters is feasible.

In this work, a connection between liquid and gas phase based charge retention and depletion mechanisms is established. A distinction is drawn between protic and aprotic polar compounds and their impact on the observed charge state distribution of multiply protonated ions. The proposed model is based on multi-phase cluster chemistry and represents an extension to common charge partition mechanisms.

Contents

1	Scope of this Work	1
2	Introduction	4
2.1	Transferring Ions from the Solution to the Gas Phase	4
2.1.1	Solvation of Ions in Solution	4
	Solvation of Ions in Solvent Mixtures	6
2.1.2	Production of Charged Droplets by Electrospray	7
	Electrospray as an Electrolytic Cell	10
2.1.3	Formation of Gas-Phase Ions from Charged Droplets	10
	Solvation and Location of Ions in Nanodroplets	10
	Ion Evaporation Model (IEM)	12
	Charged Residue Model (CRM)	14
	Chain Ejection Model (CEM)	15
2.1.4	Charge State Distribution of Gas-Phase Ions	17
	Supercharging	17
2.2	Transferring Ions to the Mass Analyzer and Detector	19
2.2.1	Solvation of Gas-Phase Ions	20
	External Solvation by Polar Solvents	21
2.2.2	Proton Transfer to Solvents	25
2.2.3	Collisional Activation and Collision Induced Dissociation	29
3	Methods	32
3.1	Experimental Methods	32
3.1.1	Chemicals	32
3.1.2	Mass Spectrometry	32
	Nanoelectrospray Ionization Source	32
	Ion Trap Mass Spectrometer	34
	Time-of-Flight Mass Spectrometer	37
3.1.3	Ion Mobility Spectrometry	37
	Atmospheric Pressure Drift Tube Ion Mobility Spectrometer	37
3.2	Computational Methods	39
3.2.1	Ab Initio Calculations	39
3.2.2	Collision Cross Section Calculations	39
3.2.3	Determination of Cluster Distributions and Ion Mobilities	40

4	Results and Discussion: Substance P	42
4.1	Gas Phase Modification	43
4.1.1	Comparison Investigations with the Bruker CaptiveSpray nano-Booster	51
4.2	Combined Solution Phase and Gas Phase Modification	52
4.3	Collision Induced Dissociation	57
4.4	Charge Retention/Charge Depletion Model	59
4.5	Summary and Conclusions	61
5	Results and Discussion: Terminal Alkyldiamines	63
5.1	Gas Phase Modification: Charge Depletion vs. Charge Retention	64
5.1.1	Observed Ion Population	64
	Influence of the Solution Composition	64
	Impact of Gas Phase Modification by ACN and MeOH	66
	Influence of the Chemical Structure of the Diamines	68
	Average Cluster Number of $[M(\text{ACN})_n\text{H}_2]^{2+}$	72
5.1.2	Average Charge State	77
	Impact of the Alkyl Chain Length in Terminal Alkyldiamines	78
	Impact of the Location of Modifier Addition: Source vs. Capillary	83
5.1.3	Impact of Gas Phase Modification on CID	87
5.2	Chemical Modification of the Collision Gas	94
5.2.1	Measurement Procedure	94
5.2.2	Variation of the Cooling Time: Gas Phase Modification	95
5.2.3	Variation of the Cooling Time: Collision Gas Modification	98
5.2.4	Investigation of the Reaction Kinetics	101
	Decay of $[\text{MH}_2]^{2+}$	102
	Formation of $[\text{MH}]^+$	103
5.2.5	Implications of Chemical Modification of the Collision Gas for Mass Analysis	106
	Effects of Fragile Ions on Mass Resolution and Isolation	106
	Influence of the Collision Gas Pressure on the Peak Shape	108
	Influence of the Scan Rate on the Peak Shape	109
	Isolation and Excitation Processes	111
	Degree of Ion Fragility	112
5.3	Theoretical Investigations of Ion-Solvent Clusters	113
5.3.1	Cluster Structures and Thermochemistry	113
	Sequential Solvation by H_2O and ACN	114
	Ligand Switch Reactions	122
5.3.2	Cluster Distributions	124
5.3.3	Collision Cross Sections and Ion Mobilities	127
	Comparison with Ion Mobility Measurements	132
5.4	Proton Transfer Processes to Solvent Clusters	135
5.5	Summary and Conclusions	139

Contents

6 Conclusions and Outlook	142
List of Tables	146
List of Figures	147
List of Abbreviations	150
Bibliography	152

1 Scope of this Work

Motivation Mass spectrometry (MS) is a research field which is strongly impacted by and oriented towards applications; this is due to the wide variety of application possibilities and the resulting importance for instrumental chemical analysis. The analysis of complex mixtures (e.g., crude oil [1], pharmaceuticals [2] or food products [3]), elucidation of molecular structures (e.g., protein and gene sequencing [4,5]), and environmental analysis (e.g. persistent organic pollutants [6]) are examples from the large number of applications. Since ion sources operating at atmospheric pressure offer various advantages compared to conventional low-pressure systems, atmospheric pressure ionization (API) is widely used in modern mass spectrometry. API conditions are beneficial for routine operation, but inevitably lead to ionization mechanisms, which are characterized by complex *ion-molecule chemistry* [7, 8]. Due to the elevated background pressure inside the ionization source, the number of particles, which represent potential collision and thus reaction partners, is several orders of magnitude higher as in a vacuum ion source. As a consequence, there is a need for fundamental research on ion-molecule chemistry occurring in API-MS.

The research group, in which this work was carried out, developed a generalized mechanism for ionization methods at atmospheric pressure (e.g. APCI, APLI, APPI) [9]. This mechanism describes reactions between ions and neutral reactants (e.g. nitrogen, water, or other solvents) in the *homogeneous* gas phase. Most of the reactions proposed in the mechanism can be categorized as *ion-bound cluster chemistry*. Particularly in the field of life sciences, electrospray ionization (ESI) is an indispensable API-method [10, 11]. In ESI, the analytes are ionized in the solution phase and are, subsequently, transferred into the gas phase [12]. Thus, the analytes are present in both the solution and the gas phase, resembling a *heterogeneous* reaction system. Thus, processes occurring during the phase transfer have to be considered. In contrast to API methods operating in the gas phase, multiply charged ions can be produced by ESI. Therefore, besides the mass of the ion, another parameter has to be considered: the charge state. Although ESI is a widely used and characterized ionization method, no comprehensive model exists for the ESI mechanism. As a consequence, ESI mass spectra cannot be predicted satisfactorily and many experimentally observed effects are not fully understood.

The phenomenon *supercharging*, which is amply debated in the relevant scientific community [13–16], describes techniques causing the increase of the average charge state of multiply charged ions in ESI-MS. Highly charged (supercharged) ions are of particular relevance, especially in the field of proteomics and genomics, since they can be manipulated and, thus, investigated in a more targeted way. There are two

1 Scope of this Work

different approaches to achieve supercharging: Selected compounds (modifiers) are added to the solution phase, i.e., *prior* to the spray process (solution phase modification), or vaporized compounds are added to the gas phase *during* the spray process (gas phase modification). In both cases, a chemical matrix modification occurs. Solution and gas phase modifiers are initially added to different phases and, thus, to different stages of the ESI process. In general, gas phase modifiers are characterized by other chemical and physical properties than solution phase modifiers (also called supercharging agents (SCAs)).

The exposure of electrosprayed droplets to modifier vapors has been reported as a means to increase as well as to decrease the observed charge state of multiply charged ions [17–20]. Preliminary experiments on gas and solution phase modification revealed that an increase of the charge state (supercharging) is accompanied by the observation of ion-modifier clusters. This finding suggests that ion-bound cluster chemistry plays a crucial role also in the case of heterogeneous reaction systems. The integration of the ESI process into the general model of gas phase API methods, which is based on complex cluster chemistry, constitutes a long-term goal of current and future research efforts; this work is intended to contribute to this goal.

Aims A connection shall be established between the physicochemical properties of compounds applied as modifiers and the observed effects on the charge state distribution and ion population in the corresponding ESI mass spectra. As a result, desired charge states may be purposefully controlled due to the use of suitable modifiers. It is hypothesized that certain modifier molecules are able to protect charges, i.e., protons, that are already bound to the analyte in the solution phase. In other words, proton loss to reaction partners competing for the protons is prevented by these modifiers during both the transfer from the solution to the gas phase and the transfer to the mass analyzer. An inherent part of the envisioned model is that the modifiers form proton-bound clusters at the charge sites of the analyte.

The following hypotheses shall be examined by experimental as well as theoretical investigations:

- I Polar *aprotic* modifiers attach to multiply protonated ions and protect the charge(s) by formation of ion-modifier clusters.
- II Polar *protic* modifiers attach to multiply protonated ions and strip off protons to form proton-bound modifier clusters resulting in reduction of the ion charge state.
- III The occurrence of proton-bound clusters in the mass spectrum depends on the collision energies which the ions experience during the passage through the transfer stages of the mass spectrometer.
- IV The observed effects of both gas and solution phase modification are explainable by enrichment of the modifiers/SCAs in the droplets/clusters leading to preferential ion solvation by the modifiers/SCAs.

It is aimed to understand the ESI process more comprehensively by means of studying the ion-modifier interactions leading either to charge retention or charge depletion.

Structure Chapter 2 provides an introduction to ion transformation processes in electrospray ionization mass spectrometry (ESI-MS). The experimental and theoretical methods, which are applied in this work, are described in chapter 3. The experimental investigations presented in chapter 4 build upon preliminary work regarding the impact of chemical modifiers on the ion population of Substance P observed with nanoESI-MS. Supported by systematic studies with various protic and aprotic compounds, the combination of solution and gas phase modification, and a first estimation of the cluster stability, a charge retention/charge depletion model is proposed. To further verify this model, an in-depth study on ion-modifier interactions is conducted using terminal alkyldiamines with various chain length as model system; the results are presented and discussed in chapter 5. The focus is on gas phase modification by examining the modification of the gas phase in the ionization source as well as in the ion trap mass analyzer. In addition, the structure and stability of ion-solvent clusters is investigated theoretically to validate the experimental results and the drawn conclusions.

2 Introduction

2.1 Transferring Ions from the Solution to the Gas Phase

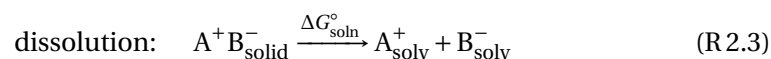
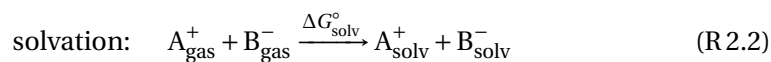
The transfer of ions from solution to the gas phase is an endothermic and endergonic process. The ion in solution interacts strongly with a number of solvent molecules (solvation): the ion is always surrounded by a solvation sphere. Therefore, energy is required to transfer an ion from solution to the gas phase [21]. In the electrospray process, this energy is not supplied at once, but the desolvation is achieved gradually at relatively low temperatures avoiding fragmentation of the ions. Hence, electrospray ionization is called a soft ionization technique [21]. Nevertheless, the structure of the gas-phase ions is not necessarily the same as in the solution. For instance, the charge state and the state of protonation, respectively, may vary from solution to the gas phase [21]. In the following sections, the physicochemical dynamics taking place between the initial stage, ions in solution, and the intended stage, ions in gas phase, are addressed with particular consideration of the charge state of ions. Then, ion transformation processes occurring during the transfer to the vacuum stage of the mass spectrometer are discussed in section 2.2.

2.1.1 Solvation of Ions in Solution

In the modern literature, the term *solvation* is used ambiguously. Solvation is considered as the sum of energetic and structural changes occurring in a *process* of transferring gaseous ions (or gaseous neutrals) into the liquid solvent resulting in the formation of a homogeneous solution [22].



The Gibbs energy of solvation, $\Delta G_{\text{solv}}^\circ$, cannot be directly measured but calculated. Dissolution, solvolysis, association, and protonation differ from solvation because these processes are accompanied by disruption of chemical bonds in the dissolved molecule and/or solvent molecules [22].



2.1 Transferring Ions from the Solution to the Gas Phase

By means of a Born-Haber cycle, e.g. for the dissolution of a salt A^+B^- (R 2.3), the standard molar Gibbs energy of solvation, $\Delta G_{\text{solv}}^\circ$, can be formulated as the difference between the standard molar Gibbs energy of solution, $\Delta G_{\text{soln}}^\circ$, and the standard molar crystal lattice energy, $\Delta G_{\text{latt}}^\circ$ viz. $\Delta G_{\text{solv}}^\circ = \Delta G_{\text{soln}}^\circ - \Delta G_{\text{latt}}^\circ$ [23].

Solvation is also used to describe the solvated *state* of ions (resulting from the solvation process), which is, in addition to solvent-solvent and ion-ion interactions, mainly characterized by ion-solvent interactions. Ion-solvent interactions include both the non-specific intermolecular forces (i.e., polarization, electrostatic and dispersion forces) and the specific formation of hydrogen bonds or electron pair donor/acceptor bonds at well localized points in the ionic compound. In the following, the structure and characteristics of solvated ions are elucidated, irrespective of the complex processes forming solvated ions. For a detailed description of the thermodynamics of solvation see refs. [22, 24, 25].

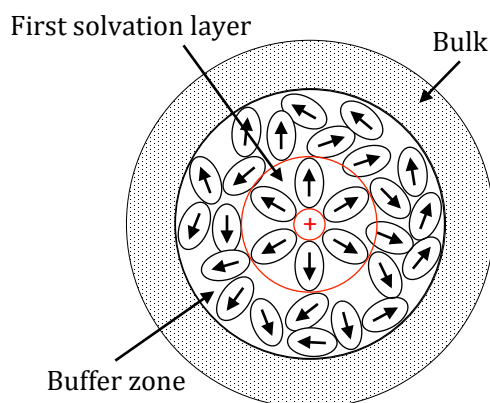


Figure 2.1: Model of a solvated ion in a polar solvent. Based on ref. [24].

Solvated ions result from coordination of a number of solvent molecules around the ions. Here, differentiation is made between the presence and the absence of contact between ions and solvent molecules [22]. In Figure 2.1 a model for ion solvation in polar solvents is depicted. According to this model, the first solvation layer (also known as primary, near, or chemical solvation, respectively) is composed of solvent molecules in contact with the ion. This solvation shell is highly ordered, the solvent molecules are localized. The number of solvent molecules in the first solvation layer defines the coordination number. The buffer zone (also known as secondary, far, or physical solvation, respectively) consists of more distant solvent molecules, which are only in direct contact to other solvent molecules. The solvent molecules exhibit a certain degree of order in this intermediate region, they are only loosely bound and therefore mobile. The solvation number includes the solvent molecules of the second solvation shell, i.e., the buffer zone. The solvent molecules in the bulk do not interact with the central ion. Here, the unperturbed structure of the pure solvent is present.

2 Introduction

The model depicted in Figure 2.1 applies to polar solvents, which exhibit a highly ordered structure in the bulk liquid, such as found in water. In contrast, solvents with less geometric structure in the bulk phase, such as hydrocarbons, form only one solvation shell and a disordered bulk solvent [23]. Since polar solvents are mainly used in ESI-MS experiments, the three-layer model in Figure 2.1 illustrates the solvated state of ions in ESI solutions.

In addition to the coordination and solvation number it is possible to measure the residence time of the solvent molecules in the different layers formed around the ion. Even in the case of strong interactions between solvent and ion, there is a continuous rotation and/or exchange of the solvent shell molecules. The exchange of solvent molecules in the first layer with molecules outside of that layer is slower than the exchange of molecules in the buffer zone, because the latter are much more mobile [23, 24]. Obviously, exchange rates as well as coordination and solvation numbers vary with each ion-solvent pair.¹ As a rule it can be stated that the smaller the ion and the larger its charge as well as the more dilute the solution, the stronger is the extent of ion solvation [23]. Since each ion-solvent interaction is specific, the solvated state of an ion in a solvent mixture is even more complex. Mixtures of solvents are often used for ESI solutions; the solvation of ions in binary solvent mixtures is described in the following.

Solvation of Ions in Solvent Mixtures

Considering a binary 1:1-mixture of the solvents S_1 and S_2 and ions A^+ (and B^-) solvated in a mixture, the ions are surrounded preferentially by the solvent, which leads to the higher negative Gibbs energy of solvation, $\Delta G_{\text{solv}}^\circ$ (reaction (R 2.1)). Therefore, the ratio of the solvent components in the solvent shell generally differs from that in the bulk solution (1:1). This circumstance - the local ion-induced inhomogeneity in a multicomponent solvent mixture on the molecular scale - is termed *selective* or *preferential solvation*. Furthermore, a distinction is made between homoselective solvation (both ions A^+ and B^- are solvated preferentially by the same solvent) and heteroselective solvation (the cation is solvated preferentially by one and the anion by the other solvent) [23]. Figure 2.2 shows models for both cases of selective solvation.

Preferential solvation can be investigated, e.g. by means of nuclear magnetic resonance (NMR) spectroscopy [26]. The competitive preferential solvation theory of weak molecular interactions (COPS theory) provides suitable quantitative descriptions of the preferential solvation of ions and neutrals and has been successfully applied to many physicochemical properties measured in mixed solvents. A detailed description of the theory and their applications can be found in [27, 28]. In this work, the presented models (cf. Figures 2.1 and 2.2) suffice to elucidate the initial state of ions in the electrospray ionization process.

¹Considering for instance single metal ions in water, coordination numbers range from approximately 4 for Be^{2+} to approximately 9 for Th^{4+} , although the majority of values are close to 6 [23].

2.1 Transferring Ions from the Solution to the Gas Phase

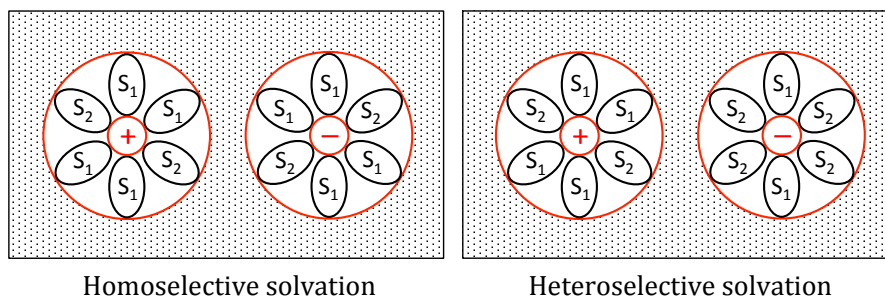


Figure 2.2: Model for the selective solvation of ions in a binary 1:1-mixture of the solvents S_1 and S_2 . Based on ref. [23].

2.1.2 Production of Charged Droplets by Electrospray

Electrospray (ES) is a method for transferring ions present in a solution² into the gas phase via generation of charged droplets followed by repeated solvent evaporation and droplet fission. The cone-jet mode is described in the following, which is only one of the possible electrospray operation modes and the most commonly used and best-characterized [12]. Initially, the production of charged droplets occurs at the capillary tip as shown for the positive ion mode in the schematic in Figure 2.3. A positive voltage (2 kV to 6 kV) is applied to the conductive capillary or the surrounding electrode in the positive ion mode. The capillary tip is located at a distance of a few mm to cm from the counter electrode. Because the capillary tip is very thin³ the local electric field gradient is high. The electric field penetrates the solution near the capillary tip. This causes polarization of the solvent molecules near the meniscus. Due to the presence of ions, the solution is sufficiently conductive and the positive and negative ions move under the influence of the field, resulting in an enrichment of the positive ions near the surface of the meniscus. The Coulomb repulsion between the positive ions overcomes the surface tension of the liquid and the surface begins to expand into a cone - called *Taylor cone* [29, 30] - pointing downfield. If the applied field is sufficiently high, a jet emerges from the cone tip, emitting droplets with excess of positive ions [12, 21, 31].

The initial charged droplets drift toward the counter electrode. Solvent evaporation⁴ leads to droplet shrinkage; the charge remains constant. At a given radius, the increasing repulsive Coulomb forces overcome the droplet's cohesive forces, i.e., the

²Compounds that are neutral in the solution can also be sprayed. In that case, the analyte is charged by, e.g. association with one or more ions present in the solution. The mechanisms of analyte charging operation in electrospray are discussed in detail in chapter 2 of [12].

³Typical values for inner capillary diameter are listed in Table 2.1 for conventional ESI and nanoESI.

⁴As mentioned before, the continuous evaporation is possible because the thermal energy required for the evaporation is provided by the ambient gas, e.g., air or nitrogen at atmospheric pressure [12]. Additionally, solvent evaporation is often assisted by thermal heating [33].

2 Introduction

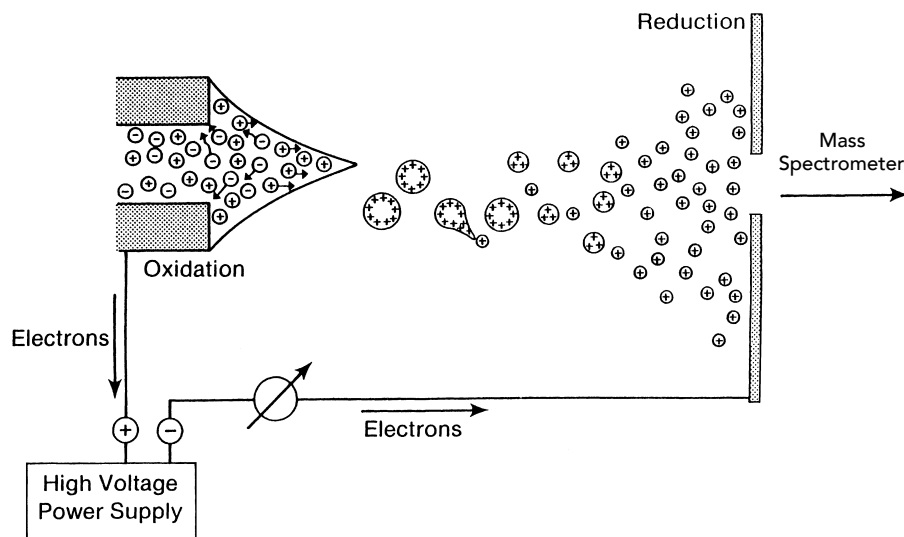


Figure 2.3: Schematic of the production of charged droplets by electrospray. Adapted from [32] with permission from Elsevier.

surface tension at the droplet surface. This causes a Coulomb fission of the droplet - called *Coulomb explosion* [12]. The condition for the Coulomb instability can be calculated by the Rayleigh equation [34]:

$$Q_{Ry} = z_{Ry}e = 8\pi\sqrt{\epsilon_0\gamma R^3} \quad (2.1)$$

where Q_{Ry} is the charge on the droplet, z_{Ry} is the number of elementary charges e , γ is the surface tension of the solvent (mixture), R is the radius of the droplet and ϵ_0 is the electrical permittivity [12]. Fission that leads to a smaller parent droplet due to release of a jet of smaller, nearly monodisperse, charged progeny droplets, occurring at or near the Rayleigh limit, has been confirmed in a number of experiments [12] and is called the Rayleigh limit Coulombic mechanism [31]. The progeny droplets have radii which are roughly one-tenth of the parent droplet radius [32]. They carry away approximately 2 % to 5 % of the parent mass but between 15 % and 25 % of the parent charge [12].⁵ Repeated solvent evaporation and fission lead to charged droplets with radii of a few nanometers. These highly charged nanodroplets are the *precursors of gas-phase ions* [32], which are subsequently detected by e.g. MS.

However, the initial size and charge of droplets as well as the evaporation rate vary considerably from one ESI source to another depending on the electrospray conditions (including inner diameter of the capillary, liquid flow rate, solvent vapor pres-

⁵An overview of different experimentally determined values is given in [12] (Table 1.2 in chapter 1).

2.1 Transferring Ions from the Solution to the Gas Phase

sure and surface tension, ionic concentration, assisting heating and/or encountered gas flow, see Table 2.1). Additionally, the residence time of charged droplets in the atmospheric pressure region of the instrument ranges from hundreds of microseconds to a few milliseconds [21]. Therefore, it is emphasized that the formation of these very small “final” droplets, on which the gas-phase ion release mechanisms are based, does not necessarily occur solely in the ESI source, i.e., in the atmospheric pressure region. In particular, there may be a considerable difference between two established operation modes, nanoESI and conventional ESI, regarding the amount of charged droplets entering the first differential pumping stage of the mass spectrometer, *prior* to releasing gas-phase ions.

The basic differences between conventional ESI and nanoESI are summarized in Table 2.1. In *nanoESI* the initial droplet diameter is much smaller as compared to conventional ESI. As a result, a lower number of evaporation/fission cycles is required to reach the final droplet diameter of a few nanometers. The evolution of nanospray droplets can be calculated: Considering an initial water droplet having a diameter of 0.3 μm and carrying 5000 charges, less than 50 microseconds are needed to distribute about half of the initial charges into nanodroplets [12]. This timescale is at least one order of magnitude smaller than the residence time of the charged droplets in the atmospheric pressure region, which ranges from hundreds of microseconds to a few milliseconds [21]. In contrast, droplets generated by conventional ESI, the formation of “final” nanodroplets occurs at several orders of magnitude longer time scales. Therefore, it is assumed that in conventional ESI highly charged droplets *pass* the mass spectrometer inlet. These highly charged droplets or clusters entering the ion transfer and analyzer systems - sometimes called *Asteroid ions* [35] - are currently experimentally and theoretically under examination [36–38]. Asteroid ions have m/z ratios outside of the mass range of typical multipole instruments and are normally not detected [35]. Since contaminations in MS instruments causing performance deterioration are attributed to these Asteroid ions, methods to prevent unwanted charged droplets from entering the vacuum system are examined [39].

Table 2.1: Differences between nanoESI and conventional ESI, data taken from [12] and [40]

Parameter	NanoESI	ESI
Inner capillary diameter	0.5-20 μm	50-100 μm
Liquid flow rate	1-1000 nL/min	0.5-1000 $\mu\text{L}/\text{min}$
Initial droplet diameter	$\approx 0.1 \mu\text{m}$	5-50 μm
Source voltage	1.5-2.5 kV	2-6 kV
Spray process	Forced by electric potential	Forced by sheath gas and electric potential

Electrospray as an Electrolytic Cell

The emission of charged droplets in the positive electrospray mode continuously carries off positive charge. Due to charge balance, an electrochemical conversion must be included in the electrospray process. Thus, an electrospray ionization source is representing an *electrolytic cell*. The oxidation occurs at the positive electrode (anode) at the liquid-metal (or other conductive material) interface of the capillary. Here, either positive ions are supplied to the solution or negative ions in the solution are removed by oxidation reactions. Depending on the composition of the solution and the material of the electrode and the capillary, respectively, the reaction with the lowest oxidation potential dominates. Reduction of the positive charge carriers takes place at the counter electrode (cf. Figure 2.3) or at the ion detector of the mass spectrometer. Since the influence of the electrochemical processes on the nature and distribution of ions recorded as mass spectrum is not taken into account in this work, references [41,42] and chapter 3 in [12] give an in-depth description of the electrochemical processes in electrospray ionization.

2.1.3 Formation of Gas-Phase Ions from Charged Droplets

There is a common agreement that highly charged nanodroplets are the precursors of gaseous analyte ions - in both, conventional ESI and nanoESI; while considerable doubts remain concerning the detailed mechanism whether ions are desorbing, evaporating or ejecting from the surface of charged and rapidly evaporating droplets [12, 31]. Three different, well-established gas-phase ion release mechanisms - i) the ion evaporation model (IEM) [43], ii) the charged residue model (CRM) [44, 45], and iii) the chain ejection model (CEM) [46, 47] will be described and discussed below. The models predominantly address the formation of positively charged gas-phase ions, in accord with the focus of this thesis. Unless otherwise stated, experimental as well as theoretical results, which relate to the positive ion mode in ESI, are described within this introduction. However, first the solvation and location of charges in nanodroplets is discussed.

Solvation and Location of Ions in Nanodroplets

In section 2.1.1 the solvation of ions in solution is discussed. In ES generated nanodroplets - mainly consisting of polar solvent molecules - the ion-solvent interactions also lead to solvated ions. Typically, the analyte is only one of many other ionic species present in the droplet: Hydronium and hydroxide ions from autoprotolysis of the solvent, e.g. water, ions as low-level contaminants, ionic species intentionally added to the ES solution (e.g., weak acids or weak bases), and ions generated by electrolytic reactions. The droplets carry an excess of cations or anions depending on the polarity of the applied voltage. This excess charge determines the net charge of the droplets. Coulomb repulsion forces the excess charges to separate as far as possible, i.e., towards the surface of the droplet [12]. Ions residing at the surface, however, is

2.1 Transferring Ions from the Solution to the Gas Phase

unfavorable due to partial loss of solvation. It can be assumed that *surface-active ions* (e.g., due to non-polar moieties)⁶ adopt positions near the surface and ions which tend to be highly solvated (e.g. metal ions) reside in the interior of the droplet [33].

The equilibrium partitioning model [48] separates the droplet in two phases: the interior and the surface. Unpaired ions carrying the excess charge are located at the surface and ions in the interior are paired with counterions. Since the environment of surface and interior ions is different, they are considered to be in different phases. The exchange of ions is treated as partition between two phases. The model postulates that there is competition among all cations (in case of positive ion mode) to carry the excess charge and that the surface ions carrying the excess charge are most likely to become gas-phase ions, which are analyzable by the mass spectrometer. In contrast, the ions in the interior will not be detected. Consequently, the model predicts that response in ESI correlates with the analytes' non-polar character and surface activity, respectively. This has been verified in several studies [12]. The considerations of this model and the experimental results are easily reconciled with the ion evaporation model, which is described below. Interestingly, the suppression of analytes with low surface activity is not observed in nanoESI. This result can be rationalized by the diverging evolution to the final droplets - called *droplet history* - between nanoESI and conventional ESI, which is mentioned in section 2.1.2. Since surface-active analytes located at the droplet surface preferentially enter the progeny droplets, these are enriched with surface active analytes after every droplet fission. Due to the small number of fission events in nanoESI, the discrimination against non-surface-active analytes is minimized [12]. Again, this represents a relevant consequence of the different *fission pathways* [49] in nanoESI and conventional ESI (cf. section 2.1.2).

Konermann et al. performed molecular dynamics (MD) simulations exploring Na⁺-containing water nanodroplets close to the Rayleigh limit [33]. The simulation results expand the postulates of the equilibrium partitioning model: The excess charge can be projected to the droplet surface by solvent molecules so that the excess ions are not necessarily located at the surface but can reside solvated in the interior. The excess ions induce large-scale orientational polarization of the surrounding polar solvent molecules, e.g. water, projecting the excess charge to the surface. Therefore, the net charge is located on the droplet surface and at the same time the solvation requirements of all ions are satisfied. Both these conflicting trends are thus reconciled [33].

In summary, it can be stated that the excess charge is always located on the droplet surface. The location of and chemical environment around an ion of interest highly depends on the analyte surface activity, the initial solution composition and the evolution to the nanodroplet (droplet history) [12]. One can therefore imagine that different processes generate gas-phase ions and consequently, various models exist, which

⁶ESI is typically performed with polar solvents. Thus, analytes with significant non-polar regions favor the air-solvent interface at the surface of the droplet, where the non-polar moieties can be desolvated. Such analytes are referred to as surface-active [12].

2 Introduction

describe the formation of gas-phase ions from charged nanodroplets.

Ion Evaporation Model (IEM)

Iribarne and Thomson proposed the ion evaporation model (IEM) [43] for the production of gas-phase ions from charged droplets. The IEM mechanism is schematically depicted in Figure 2.4 (left panel). The model predicts that direct ion emission from droplets becomes possible when the radii of the droplets decrease to a critical size ($R < 10\text{ nm}$), i.e., where the ion evaporation process becomes dominant over Coulomb fission. At this point, the ion evaporation limit is reached prior to the Rayleigh limit (cf. equation (2.1) in section 2.1.2). The model is based on *transition state theory*, which is used in chemical reaction kinetics, deriving an equation for the ejection rate coefficient. The activation barrier arises from the opposing electrostatic forces experienced by a solvated ion that has left the droplet: (i) attraction between the escaping ion and the droplet due to polarizability of the droplet, and (ii) Coulomb repulsion of the escaping ion by the excess droplet charge. The transition state occurs at a distance, where the attractive and repulsive energies are equal [12]. The primary IEM product is a small *gas-phase cluster*, consisting of the ejected ion and a few solvent molecules [33, 50].⁷ The model predicts that ions with more than one elementary charge do not evaporate due to a prohibitive energy barrier [50]. Unfortunately, quantitative predictions based on the model, i.e., the relative ejection rates of different ions, could not be validated by ESI-MS experiments [32]. However, qualitatively, the ion evaporation mechanism is experimentally well-supported for small inorganic and organic ions [12, 50]. Furthermore, Konermann and co-workers simulated successful IEM events culminating in the ejection of solvated ammonium ions (NH_4^+) from a Rayleigh-charged water/methanol nanodroplet [33, 47]. The MD simulations somewhat modified the picture of the transition state. The departing solvated ammonium ion initially remains connected to the droplet via an extended solvent bridge, which ruptures as the solvated ion is released [33]. This bridging phenomenon is illustrated in the schematic of the IEM mechanism in Figure 2.4, cf. the droplet in the center of the left panel representing the transition state.

Since the IEM describes the ejection of ions from the droplet surface, surface-active ions will generally be favored (cf. section 2.1.3). In addition, surface-active ions will undergo lower activation barriers because they are not well-solvated, facilitating IEM ejection [12, 33]. However, to recapitulate, the IEM is experimentally and computationally supported for small compounds, which are typically singly charged or protonated, respectively, e.g. alkali metal ions, NH_4^+ or H_3O^+ [12]. It is likely that be-

⁷The theory predicts that the clusters which evaporate incorporate 6 or 7 solvent molecules. Experimental results indicate that the number of solvent molecules may be higher [50]. Actually, the distinction between evaporation of a single, solvated ion and a fission event that produces a droplet constituted of a few solvent molecules, becomes blurred [33, 51]. The question arises as to how many solvent molecules represent a “droplet” in comparison to a “cluster”. As an alternative, the term microsolvation is used [52–54].

2.1 Transferring Ions from the Solution to the Gas Phase

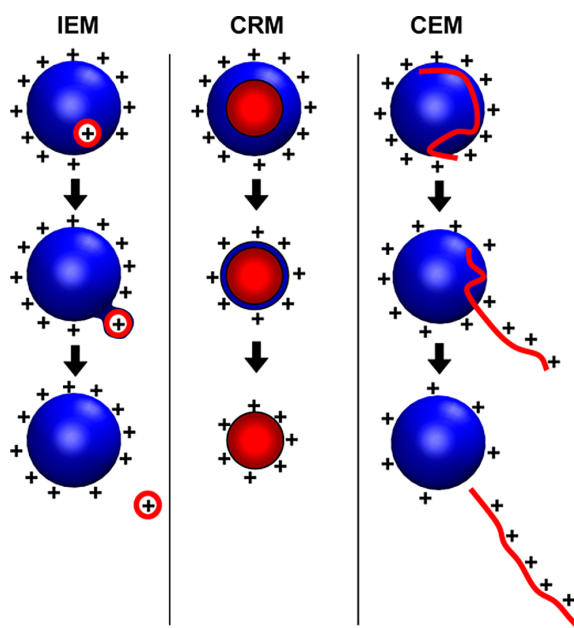


Figure 2.4: Comparison of well-established mechanisms for the formation of gas-phase ions from charged droplets. *Left:* Ion evaporation model: Small ion ejection from a charged droplet ($R < 10$ nm). *Center:* Charged residue model: Charge transfer from an evaporating droplet to a spherical analyte (ion). *Right:* Chain ejection model: Ejection of an unfolded analyte ion in a charge equilibration process. Reprinted with permission from [33]. ©2013 American Chemical Society.

yond a critical mass or a critical charge, ions are not transferred to the gas phase by IEM [55].⁸ Obviously, large proteins, in particular with linear dimensions near or even larger than the charged droplets ($R < 10$ nm), have to be released via another model. The production of large, multiply charged analyte ions is described by the charged residue model (CRM) and the chain ejection model (CEM), whereby a distinction is made between spherical analytes (CRM) and unfolded, linear analytes (CEM).

⁸Recently published MD simulations show that IEM events can take place for proteins. The computationally examined IEM events release proteins with a large solvent shell, therefore these IEM products can be interpreted as protein-containing offspring droplets, that subsequently develop as described by the CRM [56].

Charged Residue Model (CRM)

Gas-phase ion release of large⁹ spherical analytes such as natively folded proteins is commonly described by the charged residue model (CRM) that was proposed by Dole and co-workers [44, 45]. Native proteins are folded due to the *hydrophobic effect* [51]: the hydrophobic side chains of the protein build an hydrophobic core and the charged and polar side chains are situated on the solvent-exposed surface where they can interact with surrounding water molecules [33]. Additionally, intramolecular hydrogen bonds stabilize the folded protein structure. Computational studies have confirmed that extensive hydration of the protein exterior traps the spherical analyte within the droplet interior; a direct IEM ejection of the protein is therefore kinetically inhibited [33].¹⁰ In the CRM the Rayleigh-charged nanodroplet, which contains only one analyte molecule,¹¹ evaporates quantitatively; the mechanism is illustrated in Figure 2.4 (center panel). Throughout the entire evaporation process the droplet remains close to the Rayleigh limit (cf. equation (2.1)). The radius decreases due to solvent evaporation while some extra charge carriers evaporate by the IEM. As the last solvent shell evaporates, the charges at the surface of the vanished droplet are transferred to the analyte [12, 33, 51]. The CRM of a spherical analyte is a relatively slow process that occurs on a microsecond time scale. Direct MD simulations of a complete CRM process are therefore rendered difficult [33].

With the CRM the experimentally observed *charge state* of globular proteins can be predicted. The mechanism describes the charge transfer from a Rayleigh-charged droplet to the surface of an analyte. The maximum number of transferable charges, z_{Ry} in eq. (2.1), is therefore fixed by the Rayleigh-limit of the droplet having the radius of the dry analyte ion [55]. Experimentally, a good correlation between the average charge state of the gas-phase ion and the protein surface area¹² is observed [51]; furthermore, the charge state of the gas-phase ion - as predicted by the CRM - does not depend on the analyte charge in solution [33]. The Rayleigh-limit depends on the surface tension of the solvent (cf. equation (2.1)); thus, droplets with a higher surface tension can hold more charges before reaching the Rayleigh-limit. Therefore, following the CRM, the average charge state will also depend on the surface tension of the solvent. Indeed, higher charge states are obtained in experiments by using solvents or additives with high surface tension. For example, charging of cytochrome c increases with increasing surface tension of the least volatile solvent [14, 19]. However, charging significantly above the Rayleigh-limit is also observed. Some additives de-

⁹Here, “large” refers to species which have a molecular weight greater than 6 kDa. Most of the studied analytes are proteins [55].

¹⁰Since the analyte is located in the droplet interior, it has to compete with other ions for the charge left in the droplet but it will not follow the equilibrium partition model (described above) [12].

¹¹More than one protein molecule could reside in the droplets. Therefore, in the mass spectra not only monomers, but also dimers, trimers, and higher multimers are observed [12].

¹²While the spherical shape provides a best fit for the spherical charged droplets, erroneous results for the predicted charge state are expected when the protein shape deviates from a sphere. Therefore a better approach is to use the protein surface area [12].

2.1 Transferring Ions from the Solution to the Gas Phase

nature the protein, leading to unfolding of the globular shape; the unfolding favors higher charge states [51,57].

In summary, the CRM has allowed quantitative predictions of protein charge states in the gas phase and is well-supported for large, globular proteins of widely varying mass. The rather drastic limitation to globular macromolecules indicates a need for a mechanism dealing with unfolded species. Many different mechanisms [46,55,58–63] for the formation of unfolded gas-phase ions were proposed, including various hybrid scenarios. In the following, the chain ejection model is described.

Chain Ejection Model (CEM)

In accordance with the CRM, the chain ejection model (CEM) [46,47] is based on a spherical nanodroplet carrying a net charge that can be estimated from the Rayleigh equation (cf. equation (2.1)). The droplets are assumed to contain a single analyte molecule. In contrast to the CRM, an unfolded, extended macromolecule, such as a denatured protein, is considered (see Figure 2.4, right panel). As already mentioned, the driving force for the folded, globular structure of proteins is to bury the non-polar moieties forming a hydrophobic core and to maximize the favorable interactions between the charged/polar residues and the solvent [33,51]. Thus, unfolding changes the properties - besides from compact to extended - also from hydrophilic to hydrophobic. Due to the hydrophobic character, the protein does not reside within the droplet interior but is located at the droplet surface [33], as in the case for a surface-active ion (cf. section 2.1.3). To represent the unfolded macromolecule a bead-spring model¹³ is used: A linear chain with identical beads, that are held together by springs, constitutes the backbone. Side beads are bound to the backbone, some of which carry negative or positive charges [46,64]. This method minimizes the complexity of the overall system, while still allowing qualitative comparisons with experimental data.

In ESI-MS experiments unfolded proteins lead to very broad charge state distributions significantly above the charge state of the native protein. The CEM rationalizes the high charge states in terms of a *charge equilibration* process occurring during ejection of the unfolded proteins. Prior to the ejection, the chain of the protein adopts a random coil conformation and the excess charge of the droplet is evenly distributed on the droplet surface, cf. Figure 2.4. The ejection process commences with the first side chain that emerges from the surface, enabling proton migration to the exposed portion of the chain, while the remaining part of the linear chain is still solvated in the droplet close to the droplet surface. The chain is further expelled from the droplet in a stepwise sequential way, one charged residue at a time, until complete separation of the chain from the droplet has occurred, leading to the formation of a free gas-phase macromolecular ion.¹⁴ The process is driven by Coulomb repulsion

¹³The bead-spring model employed here is not meant to represent a specific chemical species, but it shares several basic features with protein chains [64].

¹⁴This sequence of events bears analogies to the IEM, where ions are ejected from the surface of an intact droplet by field emission. A central element of the IEM is the assumption of one energy barrier

2 Introduction

between cationic side chains and the excess charge at the droplet surface and by unfavorable interactions between water and the hydrophobic backbone. The stepwise ejection is accompanied by charge equilibration between the droplet and the macromolecule: Mobile charge carriers rapidly distribute into a pattern that minimizes the overall electrostatic energy; this charge transfer occurs until the entire chain is separated from the droplet. Therefore, the charge state of the ejected macromolecular ion depends on the excess charge and the radius, respectively, of the initial droplet. The model predicts that small droplets produce ions with lower charge states, whereas large droplets¹⁵ generate higher charge states. Thus, protein ejection from differently sized droplets appears to cause the broad charge state distributions observed for denaturing conditions [46].¹⁶ In addition to the shift and the broadening of the charge state distribution, an enhanced ESI signal intensity and efficiency, respectively, is observed for unfolded proteins, as compared to their folded structures. This signal enhancement can be attributed to the different ionization mechanisms - CRM for the native, folded protein and CEM for the denatured, unfolded protein. The CRM is a relatively slow process (time scale of μs). In contrast, the CEM leads to rapid ejection (time scale of ns). This high CEM rate may enhance the ion yield and therefore the signal intensity [46, 64].

In summary, the CEM provides an adequate explanation for the observed differences (charge state distributions and ion sensitivities) between native and denatured ESI-MS. The formation of highly charged unfolded macromolecules from nanodroplets is described by a rapid charge equilibration process, which is supported by MD simulations and experimental results [33, 46, 58, 64].

Three different models addressing the formation of gaseous ions from charged nanodroplets are described in the previous sections: the IEM for small ions, the CRM for Rayleigh-charged globular (folded) macromolecules, and the CEM for highly charged disordered (unfolded) macromolecules. Each of these models is able to predict and explain phenomena, which are experimentally observed and well-documented in ESI-MS as well as computationally studied in MD simulations of charged nanodroplets. Since the IEM is well-supported exclusively for very small and singly charged ions, e.g. alkali metal ions, and the CRM as well as the CEM are successfully applied to macromolecules ($> 6 \text{ kDa}$) and proteins in particular, there is a wide gap of analytes and ionic species, respectively, which are not covered by these models. Consequently, the models provide mechanisms and predictions for limiting cases. Thus, many issues in ESI-MS are not explainable by these models; mechanistic studies are

that separates the droplet-bound ion from the free gas phase state. In CEM the expulsion of unfolded chains occurs, however, in a sequential, multistep process including charge equilibration [64].

¹⁵The maximum droplet radius leading to CEM is around 10 nm. The minimum possible radius is determined by the chain dimensions [46].

¹⁶An additional source of charge state heterogeneity may be encountered when protein samples encompass different degrees of unfolding, e.g., due to partially structured regions, or when samples contain a mixture of native and denatured proteins [46].

2.1 Transferring Ions from the Solution to the Gas Phase

an ongoing topic of research [15, 59, 61, 65, 66].

One focus of current research in ESI-MS are the determinants for the observed charge state distributions of multiply charged ions. The term supercharging is often used in such works. The phenomenon supercharging yields new insights in the formation processes of multiply charged ions.

2.1.4 Charge State Distribution of Gas-Phase Ions

In general, the analyte charge state observed in the gas phase is not the same as in the bulk solution. Several factors influence the extent of analyte charging in ESI, including, as already mentioned, molecular conformation, competition for charge between the analyte and other solutes, and surface tension of the solvent, as well as instrumental factors. A comprehensive discussion of all factors influencing the observed charge state (distribution) is not provided in the present work, interested readers are referred to the works of Richard Cole [12, 21]. In ESI-MS, ion-release processes from droplets are of central importance in determining the charge state distributions of macromolecules. How far the elucidated models (IEM, CRM and CEM) are correctly predicting the average or maximum charge state and explaining experimental influences on the observed charge states, is discussed in the previous section 2.1.3. In this section, an intended shift of the observed charge state distribution to higher charge states - called *supercharging* - is discussed. The formation of supercharged gas-phase ions due to the modification of solution-phase properties is described in the following.

In addition to processes occurring in the solution phase, the gas phase matrix into which the ions are released influences the observed charge state distribution. It is stressed that, once highly charged ions enter the gas phase, they can only maintain, reduce, or redistribute their charge, irrespective of the applied release model. The repulsive potential between gas-phase ions with the same polarity prohibits any gas-phase reactions leading to an increase in charge [15, 67, 68]. However, modification of the gas phase can alter the observed charge state distribution. The gas-phase processes affecting the charge of gas-phase ions are discussed in chapter 2.2.

Supercharging

The term supercharging, established by Williams and co-workers [69], refers to the observed increase of the average as well as the maximum charge state of macromolecular ions by adding *m*-nitrobenzyl alcohol (*m*-NBA) or glycerol, respectively, into the electrospray solution. In addition to *m*-NBA and glycerol also dimethyl sulfoxide (DMSO), sulfolane, *m*-chlorophenol, and formamide are used as so-called *supercharging agents* (SCA) [14]. Usage of the term supercharging has expanded to encompass different techniques causing increased charging, e.g., due to addition of trivalent lanthanum cations [70] or by electrothermally-induced denaturation [71]. However, conventional (chemical) supercharging is restrained to increased charging

2 Introduction

associated with the addition of SCAs to native or denaturing solutions.

The mechanism of supercharging is highly debated, particularly with regard to the distinction between native and denaturing electrospray solutions and resulting charge state distributions (cf. section 2.1.3). The high surface tension and low vapor pressure of SCAs play a crucial role in this debate. The low vapor pressure leads to an enrichment of the SCA in the droplet during solvent evaporation and droplet fission. If the solution without SCA has a lower surface tension than the SCA, the surface tension of the droplet increases in the later stages of the desolvation process. In accord with the CRM and equation (2.1), an increase of the surface tension leads to higher charge states in native ESI-MS [14]. Nevertheless, the elevated charge states formed in the presence of SCAs are inconsistent with the predicted Rayleigh-values, implying that supercharging is not a simple surface tension effect [72, 73]. Results from Williams and co-workers clearly demonstrate a direct relationship between protein destabilization/unfolding and SCA addition. Protein unfolding will occur in the electrospray droplet as a result of chemical and/or thermal denaturation¹⁷ caused by elevated SCA concentration. The effect of protein unfolding on charging is stated to be stronger than those of increased droplet surface tension as long as analytes undergo conformational changes [57, 74, 75]. MD simulations, conducted by Konermann and co-workers, reconcile these conflicting experimental results in native ESI-MS: Supercharging is rationalized in terms of a charge-trapping mechanism [66]. A water nanodroplet enriched with SCA molecules undergoes solvent segregation, resulting in an aqueous core containing the protein and an outer shell of SCA molecules. Charge carriers are solvated in the aqueous core; as a consequence, the IEM ejection of charge carriers during evaporation proceeds at a lower rate. Once the water has evaporated, all remaining charge carriers bind to the protein due to poor solvation afforded by the SCA; the charge carriers are trapped. After SCA evaporation the protein is released into the gas phase via CRM. As a result of their elevated charging, supercharged protein ions undergo electrostatically driven unfolding in the gas phase [66].

Determining the precise physicochemical properties of SCAs that enhance the extent of protein charging remains challenging. Suitable solvents to operate as SCA tend to have much lower vapor pressure and higher surface tension than typical electrospray solvents,¹⁸ are moderately miscible with water, and exhibit high dipole moments and low gas- and solution-phase basicities [76, 77]. Dipolar properties of SCAs appear to play an important role in denaturing ESI-MS. Here, direct interactions between the SCA molecules and the charged sites of the analyte are proposed. Supporting this hypothesis, an increase of the extent of supercharging with increasing dipole moment of the SCA is observed; furthermore, with increasing charge state an concomitantly increase of adducts (analyte + SCA) is discovered in denaturing ESI mass spectra. Higher charge states are thus stabilized through charge delocaliza-

¹⁷As the concentration of the low vapor pressure SCA increases, evaporative cooling will be reduced compared to droplets that do not contain SCAs. Therefore, the temperature of the droplet will be higher in the late droplet lifetime [74].

¹⁸SCAs usually have lower surface tension than water [14].

2.2 Transferring Ions to the Mass Analyzer and Detector

tion due to the high dipole moment of the SCA [78, 79].¹⁹ These considerations are also supported by theoretical examinations with a CEM supercharging model. The proposed model is based on residual SCA molecules that stabilize protonated basic sites on the protruding protein via charge-dipole interactions so that proton migration from the unfolded chain to the droplet (charge equilibration, cf. section 2.1.3) is prevented [80].

In summary, the phenomenon supercharging is rationalized for both non-denaturing and denaturing solutions by mechanisms according to CRM and CEM, respectively. The requirements for additives acting as potential SCAs are still under research. Apparently, different physicochemical parameters and effects are operative in the several mechanisms leading to supercharging. The crucial properties may depend on the conformation and chemical structure of the analyte as well as on the solution composition.

In conclusion, the challenge of studying the formation of gas-phase ions from droplets lies mostly in the transfer from a macrosystem (droplet) to a microsystem (gas-phase ion). Macroscopic parameters (e.g., droplet size, Rayleigh limit/charge, surface tension, pH value) as well as microsystemic properties (molecular diameter, structure and weight, inter- and intramolecular interactions) are considered to be crucial for the proposed mechanisms. Some mechanisms are derived mainly from a macroscopic approach (e.g. IEM, CRM) whereby others (e.g. CEM and supercharging mechanisms) draw upon microsystemic properties and effects. Microsystemic properties, e.g. inter- and/or intramolecular ion-dipole interactions, appear to be crucial for analyte charging. Transfer from the macrosystem to the microsystem is accompanied by transfer from the solution to the gas phase. Loo and co-workers established the concept of the intermediate regime [15]: “Ions from solution may enter the intermediate regime, and ions released from the intermediate regime enter the gas phase [...]. Intermediate regime species are assumed to have properties lying between those of solution and gas phase [...]” This quote highlights that microsystemic properties (e.g., the basicity of a charge site) can change during the transfer; the intermediate properties remain uncertain though [15].

In the following chapter, processes that ions can undergo after entering the gas phase are described.

2.2 Transferring Ions to the Mass Analyzer and Detector

In the previous section the formation of gas-phase ions from droplets in ESI is described. After formation the ions are transported into the vacuum system of the mass spectrometer to be analyzed and detected. During this transfer the ions pass through a region, where the neutral gas density and pressure, respectively, is low-

¹⁹Lars Konermann frequently uses the term “juicy dipoles” describing the dipolar properties of SCAs and their tendency to form adducts.

2 Introduction

ered rapidly. While the collision rate between ions and neutrals decreases, the reduced field strength and the collision energy increase. Therefore, the interactions of gas-phase ions with neutrals initially are dominated by chemical transformation processes, i.e., ion-molecule chemistry; in the high pressure region thermodynamic equilibrium prevails. On the contrary, in the vacuum region interactions may lead to ion activation, e.g., collision induced dissociation (CID). The vacuum region is dominated by non-equilibrium reaction dynamics. Neutrals may be solvent molecules or other vapor-phase species resulting from evaporation of the spray solution as well as background gas molecules, typically nitrogen, purified air, helium and/or argon.

The chemical transformations can be divided in two major processes: (a) charge stabilization and (b) charge reduction. Charge stabilization is accomplished by solvation in ESI as well as in API in general. In 1997 Richard B. Cole stated in the book *Electrospray Ionization Mass Spectrometry* [21]: “Protonated basic groups which are not stabilized by intramolecular hydrogen bonding will be solvated by one or more solvent molecules. The solvent molecules may have been retained in the transition from droplet to gas phase or acquired later from the solvent vapor present in the atmospheric pressure region of the ES ion source.” Charge reduction occurs via charge/proton transfer reactions (cf. section 2.2.2) or via collision induced dissociation (cf. section 2.2.3).

2.2.1 Solvation of Gas-Phase Ions

Cole's quote is based on and supported by numerous experimental and computational studies on solvation of aminic gas-phase ions [81–89]. Protonated sites, in particular in multiply charged ions, are solvated in the gas phase whenever possible. This proceeds via intramolecular interactions (*internal*), i.e., by polar (or polarizable) groups leading to reorientation or cyclization, or via intermolecular interactions (*external*) with solvent molecules. Solvation is a process that is generally energetically favorable. In all cases the driving force for solvation is - besides the formation of intramolecular or intermolecular interactions (e.g. hydrogen bonds) - the resulting decrease in Coulomb repulsion due to charge dispersion and shielding. Therefore, the extent of external solvation, in other words the free energy of solvation by solvent molecules, is dependent on the charge separation and the possibility of internal solvation [83, 86]. Solvation of gas-phase ions by polar solvents is also well-known for gas phase API techniques [9, 81, 90, 91], where, however, only singly charged ions are observed.

External solvation of protonated ions by solvent molecules produces gas-phase charge-bound clusters. These clusters are formed during the formation of gas-phase ions from droplets. Prior to the formation of the naked (unsolvated) gas-phase ion, a gas-phase cluster, consisting of the ion and solvent molecules, is generated. Regarding the IEM, this cluster formation is described in the model as an integral part of the ejection mechanism: ions formed by ion evaporation enter the gas phase with a solvation shell (cf. section 2.1.3). In the CRM and CEM mechanisms, cluster formation

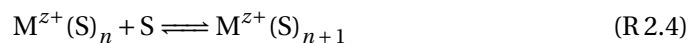
2.2 Transferring Ions to the Mass Analyzer and Detector

is not explicitly stated but the solvent evaporation process in the CRM leads always to a gas-phase cluster before the presumed “dry” analyte ion is obtained. MD simulations of the CEM process show the ejection of unfolded macromolecules carrying solvent molecules at their charged residues [33, 47]. Therefore, ion-solvent clusters are formed either from an ion evaporation or a charge residue or a chain ejection process. Furthermore, comparative investigations on the hydration of heptylamine formed by ESI and APCI, respectively, provide evidence that clusters in ESI-MS are formed by two processes: (a) solvent evaporation from extensively hydrated ions or from droplets and (b) solvent condensation on unsolvated or partially solvated ions [89]. Clusters are built up by solvent condensation; this occurs in the ion source due to elevated solvent vapor concentrations and/or during the expansion into the low pressure region due to cooling [85].²⁰ In the early 1980s, homo- and heteromolecular clusters produced by jet expansions into vacuum have been characterized as a “new form of matter” in a state of transition between gaseous and condensed phases [88]. However, the transfer of clusters is nearly prevented and/or efficient declustering is realized in ESI-MS systems depending on the instrumental parameters (e.g., the use of heating and/or dry/sheath gas, ion transfer layout and settings leading to energetic collisions with neutral carrier gas molecules). Therefore, cluster species are hardly observed in ESI mass spectra [12, 88].

Internal and external solvation play an important role in studies regarding the conformation, charge site(s), and reactivity of gas-phase ions. Since internal solvation can lessen external solvation, the presence of e.g. intramolecular hydrogen bonds has to be considered when studying external solvation [81]. In 2005 Michael Meot-Ner published a comprehensive review on the ionic hydrogen bond, in which hydrogen-bonded clusters and their characteristics are covered in detail [94]. In the following, external solvation by polar solvents in ESI-MS²¹ is discussed.

External Solvation by Polar Solvents

External solvation of a positive²² gas-phase ion M^{z+} by a solvent S is described by the general reaction



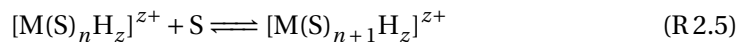
²⁰In several publications dealing with solvation of gas-phase ions in ESI-MS the authors noted that they are unable to unambiguously determine which process (solvent evaporation, solvent condensation prior to expansion, solvent condensation during expansion) occurs (predominantly) in their experiments [83, 88, 92, 93].

²¹External solvation has been intensively studied also with differential mobility spectrometry (DMS) [52, 95], mostly with a focus on singly protonated species and their enhanced separation due to small differences in ion-solvent interactions [96–101].

²²Since the formation and solvation of negative ions in ESI-MS is not addressed in this work, interested readers are referred to [12, 102] for information about solvent effects in negative ESI-MS.

2 Introduction

representing an equilibrium reaction with individual clustering steps ($n, n + 1$). Considering a protonated gas-phase ion MH_z^{z+} the reaction can be written as follows:



The free energy of solvation, $\Delta G_{(n,n+1)}^\circ$, is defined and can be calculated and/or measured for each step. In general, with increasing cluster size, $-\Delta G_{(n,n+1)}^\circ$ decreases, i.e., the exergonicity of the solvation reaction declines, due to charge dispersion and delocalization as well as to repulsion between the solvent molecules. It should also be noted that solvation reactions are always entropically unfavorable. The total charge transferred to the solvent (S) $_n$ increases with n , but the local charge on each solvent molecule decreases. In parallel, in case of protonated gas-phase ions, ionic hydrogen bonds become longer and weaker with increasing cluster size [94]. $\Delta G_{(n,n+1)}^\circ$ will reach the limiting value $\Delta G_{\text{condens}}^\circ$ because the cluster increasingly resembles a neutral liquid droplet and approaches liquid-like behavior [103].

Kebarle and co-workers [82–84] as well as Meot-Ner and co-workers [81] measured $\Delta G_{(n,n+1)}^\circ$ for the sequential hydration of singly protonated ($\text{NH}_2(\text{CH}_2)_k\text{NH}_3^+$, $k = 2\text{--}10, 12$) and doubly protonated ($\text{NH}_3^+(\text{CH}_2)_k\text{NH}_3^+$, $k = 2, 4, 5\text{--}10, 12$) alkyldiamines, among other protonated peptides, produced by ESI. Clusters with up to three H_2O molecules are observed for the singly protonated diamines, while clusters with a maximum of seven H_2O molecules are observed for the doubly protonated diamines in equilibrium experiments. The singly protonated diamines are barely detected as hydrated ions in the spectrum: the major species are the naked ions, whereas the doubly protonated species are preferentially hydrated by four H_2O molecules. Williams and co-workers observed hydrated clusters of $\text{NH}_3^+(\text{CH}_2)_7\text{NH}_3^+$ with n up to 24 in non-equilibrium experiments, but only the singly protonated cluster ions with $n = 1\text{--}3$ have significant abundance in the mass spectra [89]. Comparing the determined $-\Delta G_{(n,n+1)}^\circ$ values between the singly and doubly protonated diamines, higher values for the doubly protonated species are obtained [81–84], as shown in Figure 2.5. The two charges in the doubly protonated species mutually increase the strength of the H-bonding interactions with H_2O molecules due to higher partial positive charge [83, 84]. This substituent effect decreases with the chain length k so that $-\Delta G_{(n,n+1)}^\circ$ for a given n decreases significantly as the length of the carbon chain in the doubly protonated diamines is increased [82]. This trend is also observed for the solvation of $\text{NH}_3^+(\text{CH}_2)_k\text{NH}_3^+$ ($k = 8, 10, 12$) by NH_3 [104]. However, the weak hydration of the singly protonated diamine is not only caused by the missing substituent effect but rather by the formation of an intramolecular H-bond between the protonated and the neutral amino group. This internal solvation results in cyclization which reduces the exergonicity of the hydration reactions.²³ In the smallest diamine, $\text{NH}_2(\text{CH}_2)_2\text{NH}_3^+$, the cyclization leads to a large ring strain, which decreases with increasing chain

²³The proton-induced cyclization (and the related charge delocalization) of terminal alkyldiamines is supported by ion mobility measurements [105, 106] and by computational methods [107–109].

length k . Cyclization is thus thermodynamically more favored for longer chains [110]. Therefore, $-\Delta G_{(n,n+1)}^\circ$ for a given n decreases with increasing chain length k of the singly protonated diamines [81], which is in analogy to the case of the doubly protonated diamines, cf. Figure 2.5.

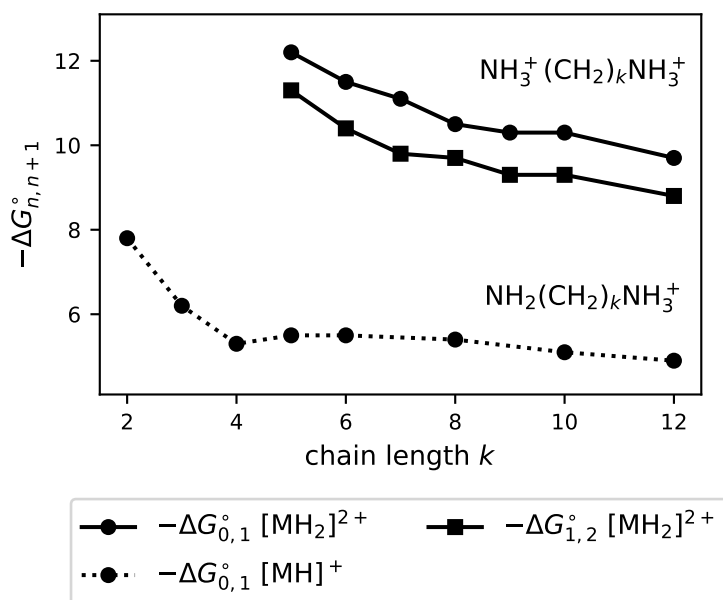


Figure 2.5: Measured solvation energy $-\Delta G_{(n,n+1)}^\circ$ for the hydration of singly ($\text{NH}_2(\text{CH}_2)_k\text{NH}_3^+$, $[\text{MH}]^+$) and doubly protonated ($\text{NH}_3^+(\text{CH}_2)_k\text{NH}_3^+$, $[\text{MH}_2]^{2+}$) alkyldiamines in dependence of their chain length k . $-\Delta G_{(n,n+1)}^\circ$ $[\text{MH}_2]^{2+}$ with $n = 0, 1$ was taken from [84] and $-\Delta G_{(0,1)}^\circ$ $[\text{MH}]^+$ was taken from [83].

In addition to the hydration reactions, Fenn and co-workers studied the solvation of a singly protonated peptide by various alcohols [88]. They observed variations in the patterns of the cluster ion abundances and cluster numbers depending on the applied alcohol: “As the number of carbon atoms in the alcohols goes from zero in water to four in the butanols, the fraction of primary ions that becomes solvated increases, as does the fraction of ions in higher solvation states.” [88] This dependency is explained by an increasing polarizability and an increasing dispersion binding force as the size of the alcohol is increased; even small changes in binding force have a large effect on the extent of solvation [88].

The substituent effect, which was already mentioned for the doubly protonated diamines, is even more pronounced for multiply protonated molecules. Since solvation energies increase with Coulomb repulsion, the observed cluster size should increase with the charge state of the ion. In experiments, solvation is indicated by *adduct tail-*

2 Introduction

ing of multiply protonated mass peaks in ESI mass spectra, whereby higher charge-state species are observed to engage in a higher degree of solvation [21, 84, 111, 112]. For example, extensive hydration of cytochrome c leading to adduct tailing is observed when water vapor is added to the capillary interface of the mass spectrometer [85]. Ethyl acetate and acetonitrile lead to cluster formation for the high charge states of cytochrome c, myoglobin, and ubiquitin [93]. Furthermore, external solvation by sulfolane is observed and increases strongly with increasing charge state of cytochrome c [78]. Comparable results are obtained with *m*-NBA and multiply protonated myoglobin [15]. Charge stabilization in highly protonated macromolecules through charge delocalization by polar solvents is also discussed in the context of supercharging, see section 2.1.4.

Solvent Shell Filling and Magic Numbers in Cluster Distributions Measurements of $-\Delta G_{(n,n+1)}^\circ$ for the stepwise growth of gas-phase clusters show in some clustering series a drop in the energies at a particular step $n_S \rightarrow n_S + 1$. This observation is attributed to filling of solvent shells, i.e., the cluster with $n = n_S$ is a closed solvent shell cluster and the next solvent molecule starts an outer shell at $n = n_S + 1$. Without shell filling the binding energy decreases monotonically and the difference between each step becomes smaller. Shell-filling effects may not be observed when the energies approach the limiting condensation energies before shell filling occurs [94]. The formation of solvent shells around protons and several other singly charged, small ions has been intensively studied [90, 91, 103, 113]. Since the thermodynamic shell-filling effects are often within the error limits of the measurements [94], experimental results are validated by computational methods, as published in recent articles [91, 114, 115].

Thermodynamic data for the sequential solvation of multiply protonated ions are thus rarely published. As mentioned above, the hydration of doubly protonated diamines is well investigated including the first solvent shell at $n_S = 4$ [82, 83]. However, investigations on the hydration of larger multiply protonated gas-phase ions do not involve determinations of $-\Delta G_{(n,n+1)}^\circ$ and distinct solvent shells, but determinations of so called magic numbers in observed cluster distributions [89, 92, 116]. Such magic numbers have anomalously high abundance, thus they indicate the presence of ions with higher stability and lower dissociation rate constants, respectively [89, 92]. Distributions of clusters generated by supersonic beams are sensitive probes of even small energy effects of shell filling because the observed clusters are formed by the dissociation of larger clusters [94]. Furthermore, cluster distributions can reflect competition between internal and external solvation. For instance, ESI mass spectra of the peptide gramicidin S show low abundances of ions clustered with less than six water molecules as compared to the unsolvated ion. Consequently, solvation of the two charges (protons) by fewer than six water molecules is less favorable than self-solvation by the naked ion [92].

Preferential Solvation Similar to the solvation of ions in solution (cf. Section 2.1.1), preferential solvation also occurs in the gas phase; but it is noted that the latter may not necessarily correspond to the behavior in the solution. For example, in a mixture of water and methanol, alkali metal ions are preferentially solvated by water. In contrast, gas-phase experiments regarding the competitive solvation by water and methanol have shown a preferential solvation by methanol [117, 118].²⁴ Hopkins and co-workers studied the preferential solvation of different derivatives of protonated quinoline generated by ESI with DMS [53]. Exposure of the protonated ions to mixtures of water, acetonitrile, and isopropyl alcohol vapor, respectively, were experimentally and computationally examined. The results show that the solvation characteristics in the gas phase are predominantly governed by the strength of the ion-solvent binding interaction ($-\Delta G_{(0,1)}^\circ$) and not by the mixing ratio of the solvents [53].

2.2.2 Proton Transfer to Solvents

Besides charge stabilization by internal and/or external solvation, charge transfer can occur in the gas-phase. This charge transfer is called proton transfer if a protonated ion results from the transfer. When gas-phase proton transfer reactions occur in ESI-MS, they typically involve a solvent, facilitated by the high mixing ratio or concentration of solvents [12]. Gas-phase proton transfer to a solvent is described by the reaction



in which the charge of the ion MH_z^{z+} will decrease by one. The parameters gas-phase proton affinity (PA) and gas-phase basicity (GB) are typically used to describe the thermodynamics of gas-phase proton transfer reactions. Considering the theoretical protonation reaction



the protonation leads to a change in enthalpy ($\Delta_R H^\circ$) and change in Gibbs free energy ($\Delta_R G^\circ$) at 298 K.

$$\text{PA}(\text{MH}_{z-1}^{(z-1)+}) = -\Delta_R H^\circ \quad (2.2)$$

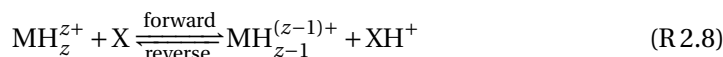
$$\text{GB}(\text{MH}_{z-1}^{(z-1)+}) = -\Delta_R G^\circ \quad (2.3)$$

The gas-phase proton affinity of $\text{MH}_{z-1}^{(z-1)+}$ is defined as the negative change in enthalpy (2.2), while gas-phase basicity of $\text{MH}_{z-1}^{(z-1)+}$ is defined as the negative change in Gibbs free energy (2.3) of reaction (R 2.7) [120]. The GB of the $\text{MH}_{z-1}^{(z-1)+}$ ion reflects

²⁴The different solvation behavior between the gas and solution phase can be attributed to the different basicities of water and methanol. Relative basicities among molecules usually differ in the gas phase and in solution. Water is more basic than methanol in solution, but in the gas phase it is less basic [12, 119]. For the term gas-phase basicity see section 2.2.2.

2 Introduction

the proton transfer reactivity of the MH_z^{z+} ion [121]. According to the laws of thermodynamics, proton transfer to a solvent S occurs when $\text{MH}_{z-1}^{(z-1)+}$ exhibits a lower GB than S (R 2.6). PA and GB values are often derived from kinetic measurements of proton transfer equilibria [81, 120]:



Since ΔG° of the equilibrium reaction (R 2.8) corresponds to the difference between $\text{GB}(\text{X})$ and $\text{GB}(\text{MH}_{z-1}^{(z-1)+})$, $\text{GB}(\text{MH}_{z-1}^{(z-1)+})$ can be determined if $\text{GB}(\text{X})$ is known; thus, X is called a reference base.

For $z = 1$, GB and PA values are experimentally readily determined and thus well-documented [120, 122]. Reaction a) in Figure 2.6 shows a qualitative interaction potential representing proton transfer from MH^+ to a base X, which has a PA identical to that of M ($\text{PA}(\text{M}) = \text{PA}(\text{X})$) so that proton transfer from MH^+ to X becomes thermoneutral.²⁵ In contrast, determinations of the GB and PA of charged species ($z > 1$) is rendered more difficult by the presence of a reverse activation barrier, which arises from the separation of the two charged products (Coulomb repulsion). GB and PA values for $z > 1$ are therefore assessed by the technique of *bracketing*. Proton transfer from MH_2^{2+} to a base Y, which has a PA identical to that of MH^+ ($\text{PA}(\text{MH}^+) = \text{PA}(\text{Y})$, reaction b) in Figure 2.6) will be slow under typical experimental conditions due to the high activation barrier. Proton transfer reactions become kinetically favorable when the barrier is reduced; this occurs for reactions with bases that have higher PAs. This is illustrated for a base Z, which has a sufficiently high PA to lower the activation barrier for proton transfer (E_A) to a negligible value (reaction c) in Figure 2.6). Reactions with bases that have PAs between those of Y and Z will be slow, and these bases will appear to be less basic than MH^+ . The base Z is the first base that appears to be more basic than MH^+ , hence the term *apparent proton affinity* PA^{app} (or *apparent gas-phase basicity* GB^{app}) is used to describe the value obtained from these bracketing measurements. $\text{PA}^{\text{app}}(\text{MH}^+)$ is greater than $\text{PA}(\text{MH}^+)$ by a value close to the reverse activation barrier [86, 87, 123].

In multiply protonated molecules the gas-phase basicity²⁶ of various sites of protonation has to be considered. As a result, the GB of an amino-acid residue within a multiply protonated protein/peptide differs from the corresponding individual amino-acid residue.²⁷ This was demonstrated, for example, for several peptides containing one basic amino acid by Williams and co-workers [87]. The energetics and reaction dynamics of proton transfer reactions are changed due to intramolecular interactions (internal solvation) and, on the other hand, due to the presence of nearby charges (Coulomb repulsion). Therefore, GB^{app} values for various sites on a protein depend

²⁵It is assumed that entropy effects are negligible, so that $\text{PA} = \text{GB}$ [86, 87].

²⁶For reasons of simplicity, in the following only the term gas-phase basicity (GB) instead of PA and GB is used. Unless otherwise stated, statements presented here apply for PA and GB.

²⁷Although PA/GB values of individual amino-acids are not suitable to estimate the PA/GB of a multiply protonated protein, this approach is applied in the literature [85, 93].

2.2 Transferring Ions to the Mass Analyzer and Detector

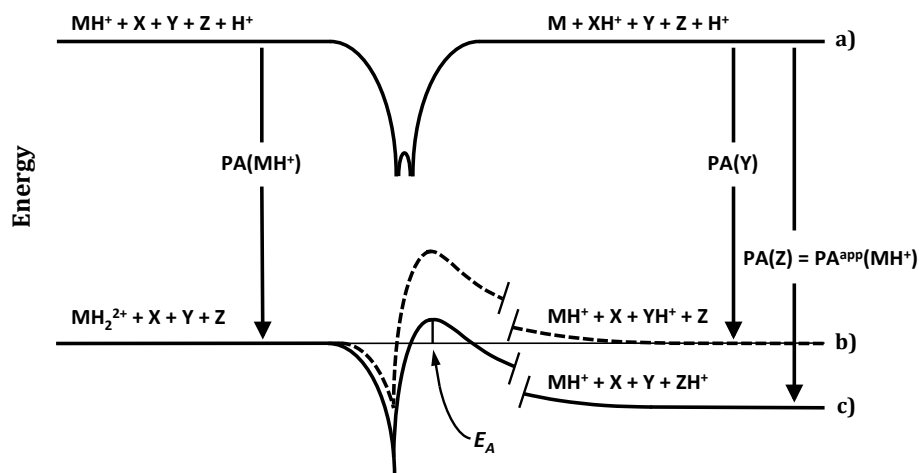


Figure 2.6: Schematic of interaction potentials for proton transfer reactions of singly and doubly protonated M and reference bases (X, Y, Z). a) Reaction of MH^+ with X, $\text{PA}(\text{M}) = \text{PA}(\text{X})$; b) reaction of MH_2^{2+} with Y, $\text{PA}(\text{MH}^+) = \text{PA}(\text{Y})$; c) reaction of MH_2^{2+} with Z, $\text{PA}^{\text{app}}(\text{MH}^+) = \text{PA}(\text{Z})$. Based on ref. [87].

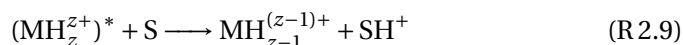
upon the degree of solvation and upon the combined Coulomb energy which all other charge sites exert on a given charge site [21]. Investigations on the reactivity including determinations of reaction rates of various proteins transferring protons to reference bases were performed [19, 124, 125]. In several studies the GB^{app} of multiply protonated molecules, mostly proteins, was estimated in dependence of the charge state and the conformation [86, 87, 123, 126, 127]. Within a given charge state, the relative ordering of the GB^{app} for different conformations is: compact < partially folded < elongated [128]. The GB^{app} values decrease and the reactivities increase with increasing charge state. The magnitude of the decrease of GB^{app} is consistent with an increase in Coulomb repulsion in the highly protonated species, which can be calculated with electrostatic models [87, 127, 129]. These results are in accord with determinations of Coulomb energy of doubly protonated diamines having different chain lengths and GB^{app} values [129, 130] and representing less complex molecular systems than proteins. Therefore, it is assumed that Coulomb repulsion plays a critical role in the maximum number of charges that an ion can retain in the electrospray ionization process.

However, in several experimental studies [52, 85, 93, 131, 132], proton transfer reactions between ions and solvents are assumed to occur even though the GB of the solvent is much smaller than that of the ion; following the laws of thermodynamics, these reactions are endergonic. Due to extensive use of solvents as modifiers in IMS and DMS instruments, unexpected proton transfer leading to charge reduc-

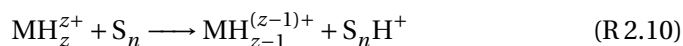
2 Introduction

tion is often observed in mobility measurements. For example, alkyl benzyl ketones, e.g. octanophenone (PA \approx 840 kJ/mol), are deprotonated by methanol (PA = 754.3 kJ/mol, GB = 724.5 kJ/mol) [131]. Furthermore, proton transfer from doubly protonated bradykinin to hexanol occurs although the GB of bradykinin+H⁺ (GB^{app} = 941 kJ/mol [133]) is significantly higher than that of hexanol (PA = 799 kJ/mol [134], GB < PA). The authors suggest that the required energy may be provided via collisional heating in the DMS. In addition, intramolecular proton transfer to a solvent cluster, perhaps driven by collisional heating as well, is considered since the proton affinity of a solvent increases with solvation, i.e., the cluster size [132]. Both propositions resemble Williams' considerations [86]: "However, in the interface region, energetic collisions with solvent molecules can occur. These collisions can provide sufficient energy to drive a reaction over an activation barrier resulting in proton transfer reactions that would not otherwise occur under thermal conditions. In addition, solvent clusters that are more basic than an individual solvent molecule can be present in the interface region. Both of these factors would result in the production of lower charge state ions." Therefore, three processes are taken into consideration to rationalize the unexpected proton transfer reactions to solvents:

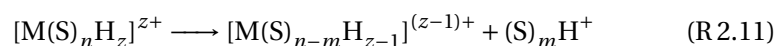
- a) Energetic collisions leading to a collisionally activated ion (marked with an asterisk) facilitate the proton transfer to a solvent, which is not observed under thermal conditions due to an activation barrier:



- b) Proton transfer occurs to a solvent cluster S_n having a higher relative GB instead of proton transfer to a single solvent molecule:



- c) Dissociation of a solvated ion occurs, leading to *intramolecular* or *intracluster* proton transfer to a solvent cluster including activation by energetic collisions:



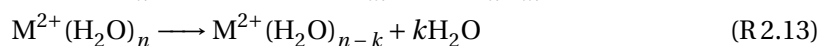
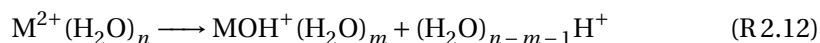
It is noted that the first process (R 2.9) does not occur, when the proton transfer from MH_z^{z+} to S is endergonic, i.e., $\text{GB}(\text{S}) < \text{GB}(\text{MH}_{z-1}^{(z-1)+})$. Considering a thermal equilibrium, only collisional heating/activation supplies the required activation energy. This does not change the equilibrium position (cf. Figure 2.6).²⁸ In other words, energetic collisions can drive reactions over a barrier, which are otherwise kinetically hindered [121]. The processes (R 2.10) and (R 2.11) both describe the proton transfer

²⁸Collisional activation can induce significant ion heating, which in turn may change the thermodynamic equilibrium position due to the temperature dependence of ΔG [135]. In addition, proton transfer dynamics at non-equilibrium conditions, e.g. at high reduced field strengths, might lead to a non-equilibrium ion distribution [136].

2.2 Transferring Ions to the Mass Analyzer and Detector

to a solvent cluster instead of a single solvent molecule. This proceeds either by gas-phase collisions (R 2.10) or by solvent loss (evaporation) from an ion-solvent cluster (R 2.11) in which the charge is partitioned between the analyte ion and the departing solvent [67]. Both reactions can occur even when $GB(S) < GB(MH_{z-1}^{(z-1)+})$. The PA and GB of solvent clusters S_n increase with cluster size n . Particularly protic solvents can assemble to form large clusters because the extended hydrogen bonding network favorably stabilizes the additional positive charge with cluster size [137]. For example, the GB of isopropyl alcohol (IPA) increases from $GB \approx 760 \text{ kJ/mol}$ ($n = 1$) to $GB \approx 960 \text{ kJ/mol}$ ($n = 5$) [52].²⁹ Experimentally, proton transfer to solvent clusters (R 2.10) as well as intracuster proton transfer reactions (R 2.11) are hard to study, because the protonated solvent clusters do not appear in the recorded mass spectra due to fragmentation/declustering upon transfer and/or analysis and due to limited m/z low-mass ranges [67, 85, 87].

Intracuster proton and charge transfer has been studied for alkaline earth and transition metal ions, M^{2+} , comparing different solvents/ligands (H_2O , DMSO, NH_3) regarding their properties to accelerate or to retard the onset of CID induced charge transfer [138, 139]. In general, CID may lead to declustering, i.e., neutral solvent/ligand loss, proton/charge transfer and/or fragmentation of a solvated ion depending on the collision energy, the relative basicity between solvent (cluster) and ion, the solvation energy and the stability of the ion (e.g. Coulomb repulsion vs. internal solvation). The competition between charge/proton transfer leading to charge reduction (R 2.12) and neutral solvent loss (R 2.13) has been investigated for hydrated metal ions M^{2+} :



In the case of H_2O , charge reduction represents an intracuster proton transfer reaction which is driven by Coulomb repulsion as well as by the formation of the strong bond between the metal M^+ and OH. Replacing H_2O with NH_3 increases the tendency for charge reduction while DMSO decreases it. Since charge reduction by DMSO represents a simple charge transfer (as compared to proton transfer) no strong covalent bond, as in MOH^+ , is produced and the charge transfer reaction is more endothermic. Therefore, DMSO protects the doubly charged metal ion [139].

2.2.3 Collisional Activation and Collision Induced Dissociation

In the preceding sections the terms collisional activation and collision induced dissociation (CID) are mentioned several times without further explanation. In the following, these terms are elucidated focusing on selected technical implementations in MS experiments.³⁰ Collisional activation of an ion requires that relative energy of

²⁹See also Table 4.2 for PA values of solvent clusters in dependence of their cluster size.

³⁰The terms collision induced dissociation (CID) and collisionally activated dissociation (CAD) are both recommended by the IUPAC and can be used interchangeably, i.e., as synonyms [140]. Sometimes

2 Introduction

motion, namely translational energy, is converted into internal energy of the ion. The translational energy of the ion is defined by the electric potentials, e.g., applied to lens elements, in the mass spectrometer. This translational energy can be converted into internal energy when the ion collides with thermal neutral matrix species. It is noted that this energy conversion only occurs in inelastic collisions. Obviously, collisions can lead to reactions between the collision partners, such as solvation (cf. section 2.2.1) or proton transfer (cf. section 2.2.2), but these processes fall under the scope of ion-molecule chemistry [143, 144]. For a detailed description of collisional activation of ions in MS see [144, 145]; for the fundamentals of ion-molecule chemistry the reader is referred to [7].

The term CID defines the dissociation of an ion after collisional activation [140] occurring when the internal energy of the ion is increased to a level that causes rupture of a noncovalent interaction, e.g. hydrogen bridges,³¹ or a covalent bond. A distinction is made between different collisional activation methods (low-energy activation, high-energy activation, and surface-induced activation) as well as between locations where activation is performed, e.g., during ion transfer from the ion source to vacuum, in an ion trap or a collision cell. Therefore, a variety of terms exists characterizing CID, e.g. low-energy CID, up-front CID, surface-induced dissociation (SID) [12]. Within the scope of this work, up-front CID,³² i.e., dissociation of an ion as a result of collisional activation during ion transfer [140], and low-energy CID performed in a quadrupole ion trap is investigated.

As mentioned before, the collision rate between ions and neutrals decreases and the collision energy increases during the ion transfer from the atmospheric pressure ion source to the high vacuum of the mass analyzer. CID is most efficient when the pressure is sufficiently low to allow a significant mean free path of movement before a collision occurs, but sufficiently high to result in multiple collision events [12]. CID processes hardly occur inside the ion source because the ions do not gain sufficient kinetic energy between two collisions. In the high vacuum region of the mass spectrometer, ion dissociation processes become essentially negligible due to extremely low collision frequencies [143, 149]. Up-front CID occurs in the intermediate pressure transmission region caused by increased potential differences.³³ Up-front CID ions are formed by dissociation in an uncontrolled manner without prior isolation

also the term collisionally activated decomposition (CAD) is used in recent literature to describe the dissociation of a loosely bound complex, e.g., an ion-solvent cluster [141, 142].

³¹Rupture of a noncovalent bond can lead to dissociation of, e.g. a protein complex or a cluster ion, ejecting a subunit/ligand of the complex/cluster ion. In addition to dissociation, rupture of noncovalent bonds can lead to unfolding of an intramolecularly solvated ion. Unfolding may occur prior to or instead of dissociation [146–148].

³²The IUPAC suggests using the term in-source CID. Since the term in-source may be misleading because dissociation does not occur *in* the ion source but during transfer, here the term up-front CID is used.

³³In Figure 3.3 the transfer system of two mass spectrometers is shown. Here, up-front CID is performed by increasing the potential difference between e.g. the capillary exit and skimmer or between the skimmer and first multipole.

2.2 Transferring Ions to the Mass Analyzer and Detector

or ion selection. Additionally, the fragment ion patterns depend on the instrument because the fragmentation process is pressure and collision energy dependent, as discussed [150]. The major advantage of this method is its simplicity and the efficient transport of the fragment ions into the mass analyzer [12]. Although up-front CID is also a low-energy collision process [151], low-energy CID is usually referred to CID performed in tandem MS (MS/MS, MS²), i.e., two stages of mass analysis exist to isolate precursor ions in the first stage and to detect their fragment/product ions in the second stage. The fragmentation step between these two stages involves low-energy CID in a collision cell or an ion trap [12]. In ion trapping instruments, the precursor ion kinetic energy can only be increased to a level where stable ion motion still occurs. The kinetic energy is increased by applying a radio-frequency (RF) waveform in resonance with the axial frequency of selected precursor ions [12]. Because of the relatively high pressure of the bath/collision gas in the trap, such as helium, the trapped ions collide many times in the course of the experiment [144].

CID of multiply protonated/charged ions has been investigated in dependence of the charge/protonation state. As the charge of an ion increases it should become easier to dissociate via CID, because the collision energy is proportional to the number of charges and therefore the dissociation barrier is passed easier. In addition, the Coulomb repulsion energy increases with ion charge, thus the dissociation is thermodynamically more favored. Experimental [10, 147, 148, 152] as well as theoretical support [153] is reported for the increased CID efficiency of higher charged ions. Furthermore, ions with high charge states lead to fragmentation patterns different from ions with lower charge states as the dissociation of internal rather than terminal bonds is favored for highly charged ions [153].

3 Methods

3.1 Experimental Methods

3.1.1 Chemicals

Nitrogen (5.0 purity, Messer Industriegase GmbH, Germany) or boil-off nitrogen (Linde Gases Division, Pullach, Germany), and helium (5.0 purity, Messer Industriegase GmbH, Germany) were used for the operation of the different instruments. Solvents, formic acid and supercharging agents used for ESI solutions as well as solvents for gas phase modification all have analytical or chromatographic (HPLC grade) purity and were purchased from Sigma Aldrich GmbH (Munich, Germany). Chemicals applied as analytes, Substance P and various alkyl(di)amines, were also purchased from Sigma Aldrich GmbH and used without further purification.

3.1.2 Mass Spectrometry

Nanoelectrospray Ionization Source

A custom nanoelectrospray ionization (nanoESI) source was used in positive mode for the standalone MS experiments. The technical drawing of the ion source is shown in Figure 3.1 depicted as half-section. The ion source is mounted directly onto the inlet capillary (20 cm length, 0.5 mm inner diameter) of the mass spectrometer. The sprayer is coaxially aligned with the capillary inlet. The sprayer consists of a nano spray tip (8 μm /15 μm PicoTip™, New Objective, Inc., Woburn, MA, USA) connected to a non-coated fused silica capillary (75 μm) via a stainless steel union. The union is held at a potential in the range of 1.4 kV to 2 kV supplied by a 3 kV power supply (Ortec 456, Ametek Inc., Berwyn, PA, USA). The gastight aluminum housing, which includes the inlet capillary entrance cone, is grounded and acts as counter electrode for the electrospray tip (cf. section 2.1.2, in particular Figure 2.3). The ESI current is measured with a multimeter (VC870, Voltcraft, Conrad Electronic, Hirschau, Germany). The ES solution is supplied using a 100 μL syringe (1710, Hamilton Bonaduz AG, Bonaduz, GR, Switzerland), and the liquid flow is controlled by a single-syringe infusion pump (model 781100K, kd scientific, Holliston, MA, USA).¹ The flow rate is typically 300 nL/min. The source chamber is constantly flushed with nitrogen. The matrix gas in the ion source is nearly completely transferred into the MS transfer

¹The term nanoelectrospray originally refers to a self-flow that is not forced by a driven syringe but runs due to the pull of the applied electric field on the solution at the capillary tip [12]. Meanwhile, the term nanoESI is used when the flow rate is in the nanoliter-per-minute region.

stage; to maintain atmospheric pressure conditions only a small excess flow is vented through a bubbler filled with silicon oil acting as a seal.

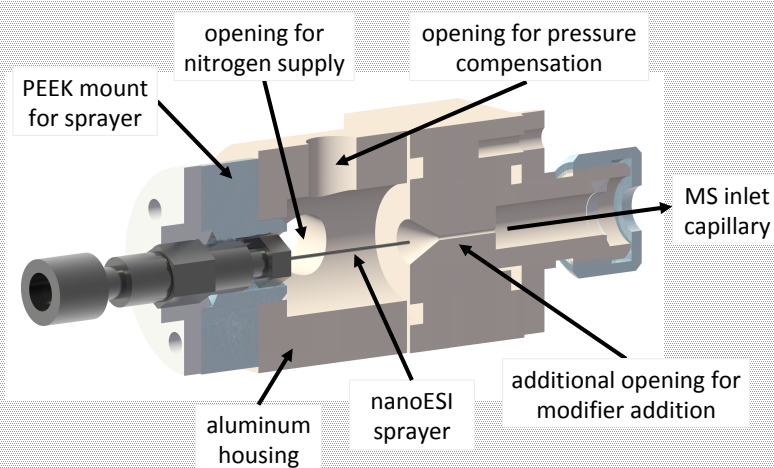


Figure 3.1: Half section of the custom nanoelectrospray ionization (nanoESI) source. Adapted with permission from [68]. ©2020 American Chemical Society.

Gas and solution phase modification Figure 3.2 shows a flow diagram, which illustrates the gas and solution flows and, in particular, the gas phase and solution phase modification. For gas phase modification a flow of nitrogen is bubbled through a gas washing bottle, which is filled with a solvent, called modifier. Acetonitrile (ACN), acetone, dimethyl ether, methanol (MeOH), ethanol (EtOH) and water were used as modifiers. Two different modifiers were added simultaneously in some experiments by means of an second gas washing bottle and further flow controller (not depicted in Figure 3.2). Both modifier-enriched nitrogen gas flows can be merged outside the ion source and then added to the ion source. Furthermore, there is an option to use two different entrance ports for the supply of two modifier-enriched gas flows so that one modifier is added to the spray region (via the nitrogen supply entrance cf. Figure 3.1) and the other modifier is added to the capillary in front of the MS inlet capillary (via the additional port for modifier addition, cf. Figure 3.1). It is also possible to use only the additional port at the capillary.² In addition to the liquid modifiers, ammonia gas was used as modifier, which was mixed with the nitrogen flow without using the modifier reservoir. The resulting mixing ratio of the modifier in the ion source is determined by its saturation vapor pressure and subsequent dilution fac-

²Since the nanoESI source is depicted as half section, the additional opening is not visible in Figure 3.1. The arrow tip points to the location, where the opening, which is drilled through the aluminum housing perpendicularly to the capillary, is connected to the capillary.

3 Methods

tors of the saturated gas. Depending on the applied modifier and its vapor pressure, mixing ratios up to 15 %V can be achieved. The total source gas flow is always kept constant and is determined by the gas intake at the MS inlet capillary, i.e., the first pumping stage of the mass spectrometer. All gas flows are controlled by mass flow controllers via a power supply and read-out module (Multi Gas Controller 647B, MKS Instruments, Munich, Germany).

For solution phase modification a supercharging agent (SCA) is added (1 %V) to the analyte solution, which consists of a 1-1000 mmol/l solution of the analyte in ACN/H₂O or MeOH/H₂O with 0.1 % formic acid added. DMSO and sulfolane were used as SCA.

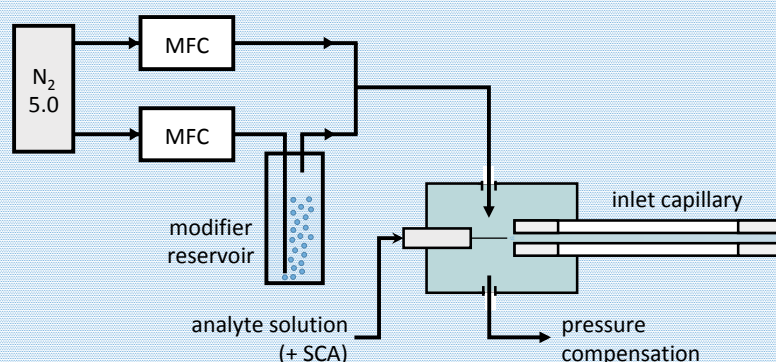


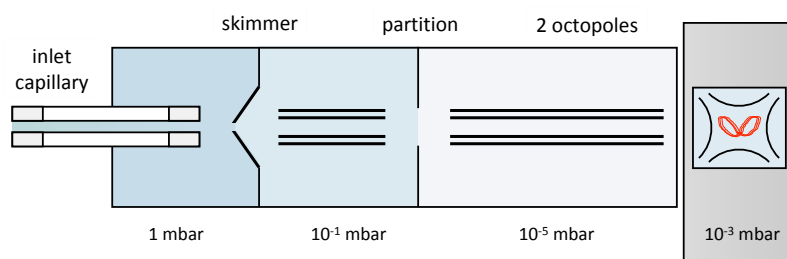
Figure 3.2: Setup of the nanoESI source indicating the gas and solution flow. Gas flows are controlled by mass flow controllers (MFC). For gas phase modification nitrogen is bubbled through a liquid reservoir of the respective modifier. Supercharging agents (SCA) are added to the sprayed solution for solution phase modification. Adapted with permission from [68]. ©2020 American Chemical Society.

Ion Trap Mass Spectrometer

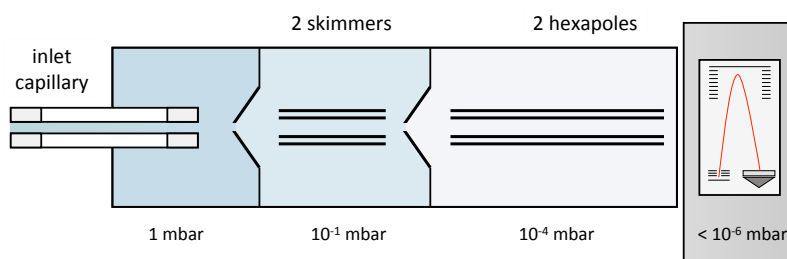
Two quadrupole ion trap (QIT) mass spectrometers were used for most mass spectrometric experiments: an esquire3000, which was modified with a high capacity trap cell (HCT), and an esquire6000 instrument (Bruker Daltonics, Bremen, Germany). Since a custom nanoESI source is directly mounted onto the transfer capillary (see section 3.1.2), the operating mode of the ion source interface is modified. The spray shield and the capillary cap are removed and nebulizer and drying gas flows are turned off. With the exception to the installed ion trap cell, both instruments are identical. Figure 3.3a schematically depicts the transfer system and the ion trap analyzer. A skimmer is placed about 1 cm behind the capillary exit to separate the first

3.1 Experimental Methods

and the second vacuum stages. Due to the capillary the pressure drops from atmospheric pressure to about 1 mbar to 5 mbar in the first vacuum stage. The pressure decreases between the skimmer and the entrance to the ion trap. Since helium gas is introduced into the ion trap for efficient trapping and cooling of the ions, an elevated pressure of approximately 10^{-3} mbar is present in the analyzer. In the chamber surrounding the ion trap and the detector the pressure is about 10^{-6} mbar [154]. Detailed information on the operating principle of the ion trap analyzer is not given here and can be found in [154, 155]. Voltages are applied to the capillary exit, the skimmer, the two octapoles (radio frequency (RF) voltage and a direct current (DC) offset voltage), and the lenses at the end of the ion transfer optics, which are not depicted in Figure 3.3a. Additionally, the trap drive, which refers to the low-mass cut-off of the quadrupolar field [154], is set. In addition to these voltages, the accumulation time, the loading capacity, the scan rate and the m/z range can be adjusted.



(a) Schematic of the Bruker esquire3000 and esquire6000 QIT mass spectrometers.



(b) Schematic of the Bruker micrOTOF mass spectrometer.

Figure 3.3: Schematic of the transfer and analyzer system of the quadrupole ion trap (QIT) instrument (top) and the time-of-flight (TOF) instrument (bottom).

The ion transfer stage voltages as well as the trap drive are generally optimized for minimum CID, i.e., the reduced field strengths are kept low. The small voltage differences result in less efficient ion focusing and transport. Ion transfer stage voltages of two different methods applied in the experiments are listed in Table 3.1. CID experiments were performed by increasing the potential difference between the capillary

3 Methods

exit and the skimmer, between the skimmer and the octopole DC, and between the two octopoles as well as by increasing the trap drive.

Table 3.1: Settings of ion transfer stage voltages in ion trap experiments

	Method DA	Method [MH ₂] ²⁺
Capillary Exit	50 V	50 V
Skimmer	35 V	35 V
Octopole 1 DC	22 V	13 V
Octopole 2 DC	15 V	3.5 V
Octopole RF	40 Vpp	50 Vpp
Lens 1	-20 V	-20 V
Lens 2	-100 V	-100 V
Trap Drive	40	16.5

As already mentioned, two different ion trap analyzers are installed in the QIT mass spectrometers. The main difference between the ion trap of the esquire6000 instrument and the HCT, installed in the esquire3000 instrument, is the optimized geometry of the HCT, which minimizes ion-ion interactions, i.e., space charge, leading to an elevated ion capacity. This geometry optimization is accompanied with an optimized ion ejection process. The HCT is able to analyze roughly four to five times more ions than the previous generation ion trap. Furthermore, higher scan rates are enabled by the HCT. In this work, the implications of these differences were not studied, a comparison between the HCT and a previous generation ion trap is found in [155]. Instrument operation was performed with the esquireControl version 5.3 software (esquire3000) and with the esquireControl version 6.1 (esquire6000). Processing of the raw data was performed with Data Analysis version 4.4 from Bruker Daltonics and subsequent data treatment was performed with custom analysis and visualization scripts implemented in the Python programming language (version 3.6.3) [156] with the Matplotlib [157] and NumPy [158] libraries.

MS/MS and Collision Gas Modification The ion trap allows MS/MS experiments: ions can be isolated, excited, and trapped without excitation. Excitation is used to induce CID processes; the excitation in an ion trap is mass-dependent. Only the selected m/z value or range is activated, therefore the fragment spectra are generally the result of a single stage of excitation because the fragment ions are not further activated [154]. Isolation, excitation, and/or trapping can be iterated several times (MS(n), $n \leq 10$) and the time period for isolation as well as for trapping (with and without excitation) can be set from 1 ms to 1000 ms. Thus, ions can be stored in the trap (with or without prior isolation) for up to 20 seconds to essentially use the ion trap as a gas-phase reactor. To study ion-solvent reactions, in particular the reaction

pathways between alkyldiamine ions and acetonitrile (ACN), a helium/ACN mixture is introduced via the helium collision gas line into the ion trap (collision gas modification). The formation of reaction products is investigated in dependence of the trapping/reaction time, the ACN mixing ratio, and the excitation energy.

Time-of-Flight Mass Spectrometer

A time-of-flight (TOF) mass spectrometer (microTOF, Bruker Daltonics, Bremen, Germany) was used for comparison studies regarding the influence of the employed analyzer type on the observed cluster distributions, and for the Substance P (SP) experiments. Figure 3.3b schematically depicts the ion transfer system and the analyzer of the microTOF instrument. The reader is referred to [159] for a detailed description of the microTOF instrument. The comparison of Figures 3.3a and 3.3b shows that the transfer systems of the QIT and the TOF instruments are similar but not identical. Both transfer systems are divided into three different vacuum stages; a second skimmer is placed between the two hexapoles of the TOF instrument. Due to this skimmer the pressure drops from approximately 10^{-1} mbar to approximately 10^{-4} mbar before the ions are transferred by lenses, which are not depicted in Figure 3.3b, to the analyzer and detector region operating at a pressure of 5×10^{-7} mbar [159]. In contrast to the QIT analyzer, the determination of the m/z ratio takes place in a collision-free region, the flight tube of the TOF. Therefore, ions generally do not undergo any ion transformation processes after they have entered the mass analyzer, except for unimolecular decay due to previous excitation. Consequently, CID processes occur only during ion transfer. The ion transfer stage voltages are generally optimized for minimum CID, as with the QIT instruments. In CID experiments the potential difference between the capillary exit and the first skimmer, between the first skimmer and the first hexapole DC, and between the second skimmer and the second hexapole DC were increased. Ion transfer stage voltages of two different methods minimizing CID are listed in Table 3.2.

3.1.3 Ion Mobility Spectrometry

Atmospheric Pressure Drift Tube Ion Mobility Spectrometer

A high-resolution atmospheric pressure drift tube IMS (AP-IMS) was used for ion mobility measurements. The IMS system is coupled via a gated transmission stage to a microTOF mass spectrometer (cf. section 3.1.2). The experimental setup is schematically depicted in Figure 3.4. Dry, purified N_2 is used as drift gas entering the drift tube at the detector. The drift gas can be modified by, e.g. H_2O or ACN. Terminal alkyldiamines were used as analytes. ESI and a Corona discharge, referred to as chemical ionization (CI) in Figure 3.4, are available as ionization methods. It can be swiftly switched between these two ionization methods and sources, respectively, because the different regions of the IMS (ionization, drift, and detector region) are stacked. For CI, the analyte containing gas flow is introduced into the ionization region; the

3 Methods

Table 3.2: Settings of ion transfer stage voltages in TOF experiments

	Method SP	Method DA
Capillary Exit	50 V	50 V
Skimmer 1	35 V	35 V
Hexapole 1 DC	28.5 V	22 V
Skimmer 2	23.9 V	23 V
Hexapole 2 DC	18.5 V	20.6 V
Hexapole RF	200 Vpp	80 Vpp
Lens 1 Storage	30 V	30 V
Lens 1 Extraction	21.3 V	21.5 V
Lens 2	9 V	9 V
Lens 3	-20 V	-20 V
Lens 4	0 V	0 V
Lens 5	-27.5 V	-27.5 V

analyte mixing ratio is controlled via a permeation oven. For ESI, 0.1-1 mM solutions of terminal alkyldiamines in ACN/H₂O or MeOH/H₂O with 0.0001 % formic acid were used. A homogeneous electrical field of approximately 650 V/cm is maintained in the drift region resulting in a reduced field strength of 2.7 Td. With a three-grid ion gate, measurements can be performed in the IMS mode or the IMS-MS mode. In the selective IMS-MS mode, single ion peaks of the ion mobility spectrum are transferred to the mass spectrometer. Further information about the IMS is found in [160] and a detailed description of the IMS-MS coupling is given in [161].

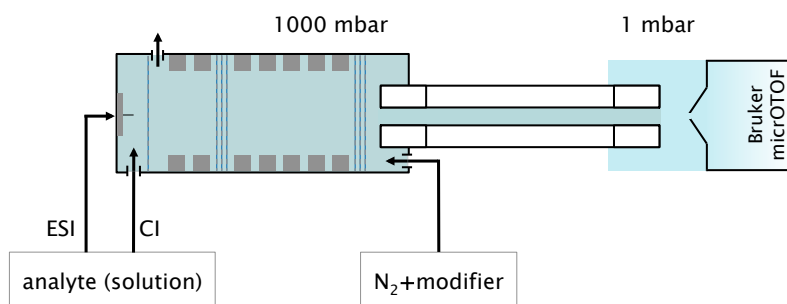


Figure 3.4: Schematic of the atmospheric pressure drift tube ion mobility spectrometer coupled to a Bruker micrOTOF mass spectrometer (cf. Figure 3.3b).

3.2 Computational Methods

3.2.1 Ab Initio Calculations

Calculations were carried out with the Gaussian09 [162] program package on a compute server with openSUSE 42.3 on AMD Opteron 6282SE processors. Density functional theory (DFT) is used with the B3LYP functional including dispersion correction and def2-TZVPP basis set for every geometry optimization. For thermochemical data the B3LYP-D/def2-TZVPP optimized geometries are used to conduct frequency calculations for obtaining zero-point energy and thermodynamic functions at the same level of theory [163]. The graphical user interface GaussView 6.0.16 [164] was used on a personal computer running with Windows 7 Professional as operating system. GaussView was utilized to generate start geometries (initial guess structures), to visualize optimized geometries and to examine the calculated thermochemical data. With increasing complexity of the modeled ion, i.e., the number of clustered molecules, the number of isomeric start geometries increases. Modelling of the start geometries was performed considering previously published structures [165, 166]. With the Gibbs free energy corrected total energy, $\mathcal{E}_0 + G_{\text{corr}}$, the local and global minimum structures for each cluster molecule are determined. Additionally, the Gibbs free energy corrected total energy of the optimized geometries is used to examine (thermodynamically) allowed reaction pathways by calculating the Gibbs free energy of a reaction $\Delta_R G^\circ$ by analogy with Hess' law.

$$\Delta_R G^\circ = \sum_{\text{products}} \Delta_f G^\circ - \sum_{\text{reactants}} \Delta_f G^\circ \quad (3.1)$$

Since Gaussian provides the sum of electronic and thermal free energies, also referred to $\mathcal{E}_0 + G_{\text{corr}}$, the difference of the sums of these values is taken for the reactants and the products leading to equation (3.2) [167].

$$\Delta_R G^\circ = \sum_{\text{products}} (\mathcal{E}_0 + G_{\text{corr}}) - \sum_{\text{reactants}} (\mathcal{E}_0 + G_{\text{corr}}) \quad (3.2)$$

$\Delta_R G^\circ$ was determined for solvation/clustering reactions and ligand/solvent switch reactions. Reactions with the solvents H_2O and ACN were investigated applying $\mathcal{E}_0 + G_{\text{corr}}(\text{H}_2\text{O}) = -76.463572 E_h$ and $\mathcal{E}_0 + G_{\text{corr}}(\text{ACN}) = -132.793846 E_h$. Energy values for the ionic species are given in section 5.3.1.

3.2.2 Collision Cross Section Calculations

Collision cross section (CCS) calculations are accomplished using the MobCal software, in particular the MobCal-MPI code [168], which is a refined implementation of the commonly used MobCal code [169]. Mobcal-MPI calculates the orientationally averaged CCS, Ω_{avg} , for collisions with N_2 at 298.15 K. Since the MobCal-MPI implementation models Ω_{avg} more accurately, such calculations require more computing time as compared to applying the native MobCal code. A comparison of the two

3 Methods

methods was conducted. Regardless of the code that is used, the molecule data, in particular the coordinates, resulting from the geometry optimization with Gaussian, are converted to a Mobcal input file without user and computational effort. CCS calculations are then performed on the compute server. The output file provides the modeled CCS value including its uncertainty.

To minimize the computing time, CCS calculations were only performed for the global minimum structure of each cluster species, i.e., the most stable isomer. The determined value was then adapted for all isomers. When energetically comparable isomers (in relation to the global minimum) were identified, CCS calculations are carried out for these local minima.

3.2.3 Determination of Cluster Distributions and Ion Mobilities

The modeling of ion mobility requires the calculation of the collision rate between an ion and the neutral buffer gas under specific conditions, i.e., electric field, pressure, and temperature. The individual rate of collision is highly dependent on the ionic CCS, more specifically the orientally averaged CCS Ω_{avg} . Under low-field conditions, i.e., reduced electric field strengths below 2-10 Td, the ion mobility K is satisfactorily described by the Mason–Schamp relation [170]:

$$K = \frac{3}{16} \sqrt{\frac{2\pi}{\mu k_b T}} \frac{ze}{\Omega_{\text{avg}} N} \quad (3.3)$$

where μ is the reduced mass of the ion-neutral pair, k_b is the Boltzmann constant, T is the temperature, z is the charge, e is the elementary charge, and N is the number density of the gas. Therefore, the ion mobility of each molecule geometry can be obtained with the calculated CCS (Ω_{avg}) values.

To model an ion mobility peak or a mean ion mobility of a specific cluster reaction system, the distribution of the isomeric cluster species as well as the entire cluster distribution need to be known. The cluster species population of an individual reaction system is calculated for standard reaction conditions ($T = 296.15\text{ K}$, $p = 1\text{ bar}$) in dependence of the solvent concentration [S]. To obtain the population distribution, a thermalized (equilibrated) system is assumed. The relative population P_i of a cluster species i is calculated from the harmonic superposition partition function \mathcal{Z}_i using the Boltzmann distribution [95, 171]:

$$P_i = \frac{\mathcal{Z}_i}{\sum_j \mathcal{Z}_j} \quad (3.4)$$

where the sum in the denominator runs over all species considered (local and global minima). The partition function is calculated from the Gibbs free energy corrected total energies $\mathcal{E}_0 + G_{\text{corr}}$, readily available from ab initio calculations. However, the energies of the individual cluster species need be normalized to the same number of

3.2 Computational Methods

atoms to achieve that all energies are on the same potential energy surface. The normalized energy $\mathcal{E}_i^{\text{norm}}$ of species i with n_i solvent molecules is determined as follows:

$$\mathcal{E}_i^{\text{norm}} = (\mathcal{E}_0 + G_{\text{corr}})_i + (\bar{n} - n_i)(\mathcal{E}_0 + G_{\text{corr}})_S \quad (3.5)$$

with \bar{n} being the largest cluster size considered. In addition to the Boltzmann factor, the solvent concentration [S] has to be considered to describe \mathcal{Z}_i , leading to

$$\mathcal{Z}_i = \left(\frac{[\text{S}]}{N}\right)^{n_i} \exp\left(-\frac{\mathcal{E}_i^{\text{norm}} - \mathcal{E}_{\text{ref}}^{\text{norm}}}{k_b T}\right) \quad (3.6)$$

where N is the total particle density and $\mathcal{E}_{\text{ref}}^{\text{norm}}$ is the normalized energy of the most stable species, i.e., those with the lowest normalized energy. This method has been successfully applied for other cluster reaction systems [95]; a detailed description of the method is given in [172].

Using P_i as weighting factor for the individual ion mobilities K_i the mean ion mobility of an ensemble of ions, e.g. a cluster distribution, can be determined.

$$K^{\text{mean}} = \sum_i P_i K_i. \quad (3.7)$$

The reduced ion mobility K_0 is defined by [170]

$$K_0 = K \frac{p}{1 \text{ atm}} \frac{273.15 \text{ K}}{T}. \quad (3.8)$$

Thus, the average ion mobility for an analyte-solvent cluster ensemble can be modeled from ab initio calculation results.

4 Results and Discussion: Substance P

Mass spectra of Substance P (SP, an undecapeptide, sequence: RPKPQQFFGLM-NH₂) were recorded with the TOF-MS using method SP (corresponding transfer stage settings are listed in Table 3.2). A 1 μmol/l solution of SP in ACN/H₂O with 0.1 % formic acid added was used as spray solution. In comparison experiments, a solution of SP in MeOH/H₂O was used leading to the same ion population and intensity ratio in the mass spectrum. The mass spectrum of SP, depicted in Figure 4.1 (top), shows the signals of the doubly ([M+2H]²⁺, SP²⁺) and the triply protonated molecule ([M+3H]³⁺, SP³⁺) at *m/z* 674.3 and 449.9, respectively, which is in agreement with literature spectra [173]. SP³⁺ is the maximum observed charge state *z*_{max} in the experiments, which corresponds to the number of charge sites in the SP molecule (the N-terminus, the arginine (R¹) side chain guanidinium ion and the ε-ammonium ion of the lysine (K³) side chain) [174]. Experimental studies on the desolvation process of SP ions generated by ESI have demonstrated that compact conformers are favored for SP³⁺ ions in the gas phase, which are stabilized via intramolecular interactions. Significant interactions were found between the ammonium ion of the N-terminus and the amide C-terminus as well as between the ammonium ion of K³ and the Q⁵/Q⁶ [174, 175]. Two charge sites of SP³⁺ and SP²⁺ are therefore stabilized by intramolecular hydrogen bonding. Upon collisional activation, these bonds can be disrupted resulting in thermodynamically stable elongated conformations [175]. However, the singly protonated species is never observed in the experiments, the average charge state *z*_{avg} thus varies between 2 and 3, calculated as follows

$$z_{\text{avg}} = \frac{\sum_i^N z_i \cdot I_i}{\sum_i^N I_i} \quad (4.1)$$

where *N* is the total number of detected charge states, *z*_{*i*} the charge number, and *I*_{*i*} the intensity of the *i*th charge state. When there are multiple ion signals which exhibit the same charge state, the intensity *I*_{*i*} is considered as the sum of those signals. The signal intensity as well as the intensity ratio between the two SP charge states (and thus *z*_{avg}) are dependent on the experimental conditions, e.g. the spray current, liquid flow, solution composition and analyte concentration. Unfortunately, mass spectra are not always reproducible even when the same experimental conditions and settings are applied. Especially, the total and the analyte signal intensity varies significantly, sometimes even during one acquisition run, indicating that the spraying/ionization process fluctuates. The relative signal intensities however are more

stable. Based on the determination of the standard deviation of the signal intensities in each measurement comprised of at least 90 individual mass spectra, the uncertainty of z_{avg} amounts to ± 0.01 . The depicted mass spectrum of SP (top spectrum in Figure 4.1) corresponds to $z_{\text{avg}} = 2.55$. The variation of z_{avg} under similar experimental conditions is easily noticed by the variation of z_{avg} at 0%V modifier mixing ratio visible in Figure 4.2.

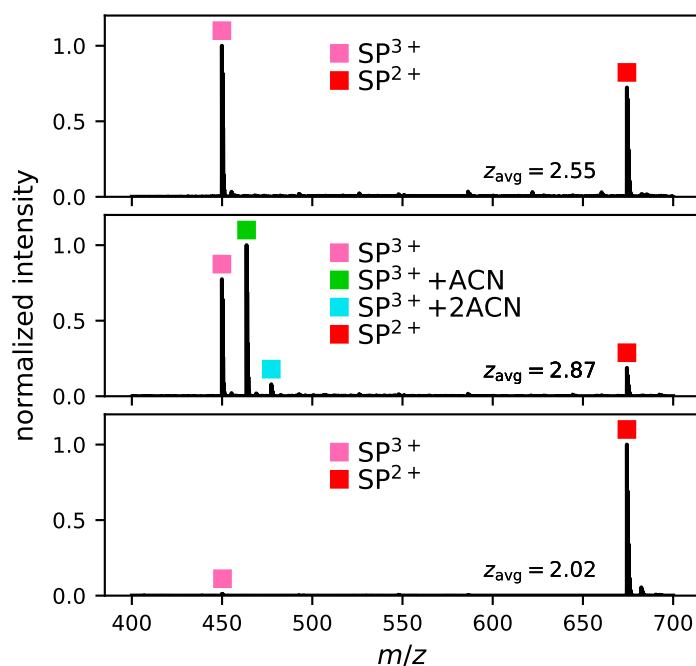


Figure 4.1: Mass spectra of Substance P (SP) without modifier addition (*top*), with 9.5%V acetonitrile (ACN) present (*center*) and with 1.9%V methanol (MeOH) present (*bottom*). The signal intensities are normalized to the maximum value in each spectrum.

4.1 Gas Phase Modification

The observed ion population and average charge state significantly change when solvent vapors are added as gas phase modifiers to the ion source. Different organic solvents were used as gas phase modifiers as well as ammonia gas.¹ The modifiers

¹In the following, for reasons of simplicity the term “solvent” and the symbol S is used for all applied gas phase modifiers, although ammonia is a gas.

4 Results and Discussion: Substance P

and their physicochemical properties are listed in Table 4.1. Taking their effects on the ion population and charge state distribution into consideration, the modifiers can be divided in two groups:

- 1) Modifier addition leads to promotion of the SP^{2+} signal and reduction of the SP^{3+} signal resulting in a reduced z_{avg} .
- 2) Modifier addition leads to promotion of the SP^{3+} signal accompanied by observation of SP^{3+} -modifier clusters resulting in an increased (or at least unaltered) z_{avg} .

Water (H_2O), methanol ($MeOH$), ethanol ($EtOH$), and ammonia (NH_3) are assigned to the first group and acetonitrile (ACN), acetone ($MeAc$), and diethylether (Et_2O) to the second. Figure 4.1 depicts the intensities of SP^{2+} , SP^{3+} and SP^{3+} -modifier clusters and the resulting average charge state, when $MeOH$ (bottom) and ACN (center) are applied as modifiers representing examples for the first and the second group, respectively.

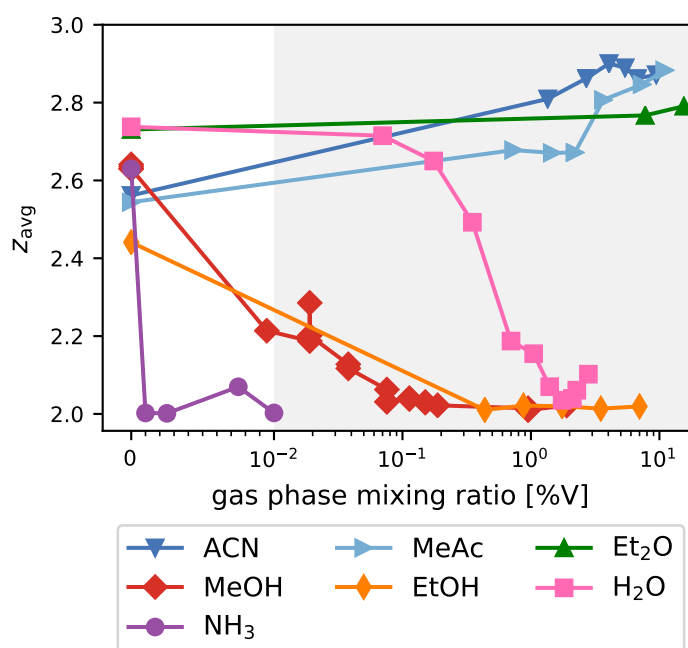


Figure 4.2: Average charge state z_{avg} of SP ions in dependence of the gas phase modifier mixing ratio for selected polar aprotic solvents (group 1, decrease of z_{avg}) and polar protic solvents (group 2, increase of z_{avg}). Note that the abscissa is linear between 0 and 10^{-2} %V (white background) and logarithmic above 10^{-2} %V (grey background).

Table 4.1: Relevant physicochemical properties of the applied gas phase modifiers and supercharging agents (SCAs)

Modifier/ SCA	neutral mass [Da]	vapor pressure ^a [kPa]	surface ten- sion ^b [mN/m]	PA ^c [kJ/mol]	GB ^c [kJ/mol]	dipole moment ^d [D]	dielectric constant ^e	polarity
Ammonia	17.03	994	-	853.6	819.0	1.47	16.9	polar protic
Ethanol	46.07	7.87	22.39	776.4	746	1.44	24	polar protic
Methanol	32.04	16.9	22.5	754.3	724.5	1.7	33	polar protic
Water	18.02	3.17	72.88	691.0	660.0	1.85	80.1	polar protic
Acetone	58.08	30.6	29.26	812	782.1	3.68 [176]	21	polar aprotic
Acetonitrile	41.05	11.8	29.29	779.2	748	3.92	37.5	polar aprotic
Diethylether	74.12	66.9	16.65	828.4	801	1.15	4.3	(polar) aprotic
DMSO	78.13	0.080	43.54	884.4	853.7	3.96	46.7	polar aprotic
Sulfolane	120.17	0.0091 [57]	48 [76]	830	801	4.70 [177]	43.3 [178]	polar aprotic

^a Vapor pressures are calculated at 298 K via the Antoine equation with parameters from NIST [179] unless stated otherwise.

^b Surface tensions at 293 K are taken from [180] unless stated otherwise.

^c Proton affinities (PA) and gas-phase basicities (GB) at 298 K are taken from [122].

^d Dipole moments are taken from [181] unless stated otherwise.

^e Dielectric constants at 298 K are taken from [182] unless stated otherwise.

4 Results and Discussion: Substance P

When a solvent S of the second group is added as gas phase modifier, the observed ion population changes significantly. Additional signals are observed, which are assigned to clusters of the composition $[\text{SP}+n(\text{S})+3\text{H}]^{3+}$ with $n = 1, 2$. They are termed SP^{3+} -solvent clusters in the following and are labeled as $\text{SP}^{3+}+n\text{S}$ in the figures. The $n = 1$ cluster is always the most abundant cluster signal and the ratio between clustered and bare SP^{3+} signals depends on the mixing ratio of the respective solvent, as seen in Figure 4.3. Above 2 %V ACN (and 6 %V MeAc, respectively) mixing ratio in the AP ion source, the cluster signal intensity becomes larger than the bare SP^{3+} signal. In contrast, addition of Et_2O results in minor cluster signal intensity; the observed spectrum and z_{avg} , show only minimal changes (see green curve in Figure 4.2). This is most likely due to the relatively low polarity of Et_2O (cf. Table 4.1). In general, no clusters are observed for the SP^{2+} ion, not even when the ion source matrix gas is saturated with the respective modifier. Instead, the relative signal intensity of the SP^{2+} ion decreases when ACN or MeAc is added. Therefore, z_{avg} increases with rising ACN/MeAc mixing ratio up to a maximum of 2.9, when the source gas is saturated (cf. Figure 4.2).

When a solvent of the first group is used as gas phase modifier, completely different results are obtained. SP^{3+} -solvent clusters are not observed with H_2O , EtOH , MeOH or NH_3 . Instead, the SP^{3+} signal is depleted and the SP^{2+} signal gains in intensity (cf. Figure 4.1 (bottom));² as a result, z_{avg} is lowered to 2, as depicted in Figure 4.2. Again, the intensity ratio and thus z_{avg} highly depend on the mixing ratio of the respective modifier; in Figure 4.4 the MeOH , H_2O , and NH_3 mixing ratio dependent intensities of SP ions are shown. There is a large difference between the required amount of modifier to reach near quantitative suppression of the SP^{3+} signal and thus a constant intensity ratio between the two SP species (saturation limit). At the lowest (experimentally possible) NH_3 mixing ratio of 10 ppmV, the SP^{3+} signal is already below the detection limit; a mixing ratio of 1000 ppmV MeOH is required to completely suppress SP^{3+} signals. Addition of H_2O results in an efficient depletion of the SP^{3+} signal above 1 %V mixing ratio (cf. Figure 4.4). The order of charge depleting modifiers is thus: $\text{NH}_3 \gg \text{MeOH} > \text{H}_2\text{O}$.³

The depletion of the SP^{3+} signal is coupled to a corresponding elevation of the SP^{2+} signal intensity. This observation suggests that SP^{3+} is deprotonated by $\text{NH}_3/\text{MeOH}/\text{EtOH}/\text{H}_2\text{O}$ via a proton transfer reaction (cf. section 2.2.2) to yield SP^{2+} .⁴ Comparing only the gas-phase basicities of the different modifiers (cf. Table 4.1) one cannot rationalize why addition of $\text{NH}_3/\text{MeOH}/\text{EtOH}/\text{H}_2\text{O}$ (modifiers of group 1) leads to

² SP^{2+} -solvent clusters, e.g. $[\text{SP}+(\text{MeOH})+2\text{H}]^{2+}$ and $[\text{SP}+(\text{MeOH})+(\text{H}_2\text{O})+2\text{H}]^{2+}$, are observed very rarely and with very low intensity, see [183].

³Unfortunately, insufficient data points are available to rank EtOH (cf. Figure 4.2).

⁴Further deprotonation of SP^{2+} does not seem to occur since the SP^{1+} ion was never detected. This can be rationalized by an intramolecular stabilization of the remaining charged sites of SP^{2+} and by a lower Coulomb repulsion, both leading to a higher proton affinity and a decreased proton transfer reactivity, respectively (cf. section 2.2.2).

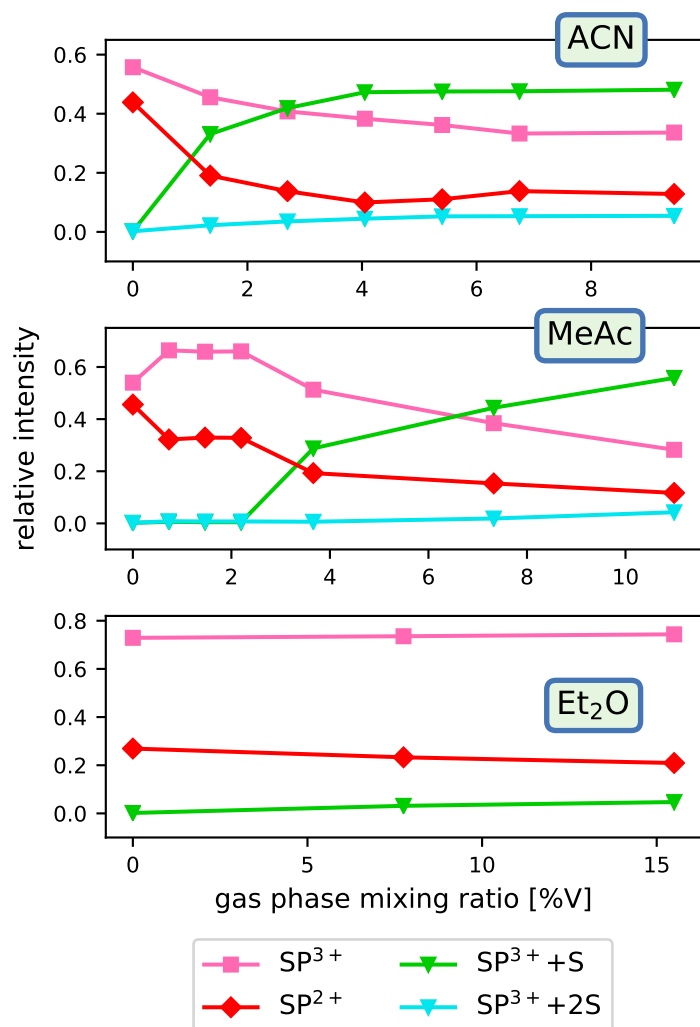


Figure 4.3: Intensities of SP²⁺, SP³⁺, and SP³⁺-solvent cluster signals, SP³⁺+S and SP³⁺+2S, in dependence of the acetonitrile (S = ACN) mixing ratio (*top*), acetone (S = MeAc) mixing ratio (*center*), and diethyl ether (S = Et₂O) mixing ratio (*bottom*). Each intensity is plotted relative to the corresponding summed intensity of all SP signals.

4 Results and Discussion: Substance P

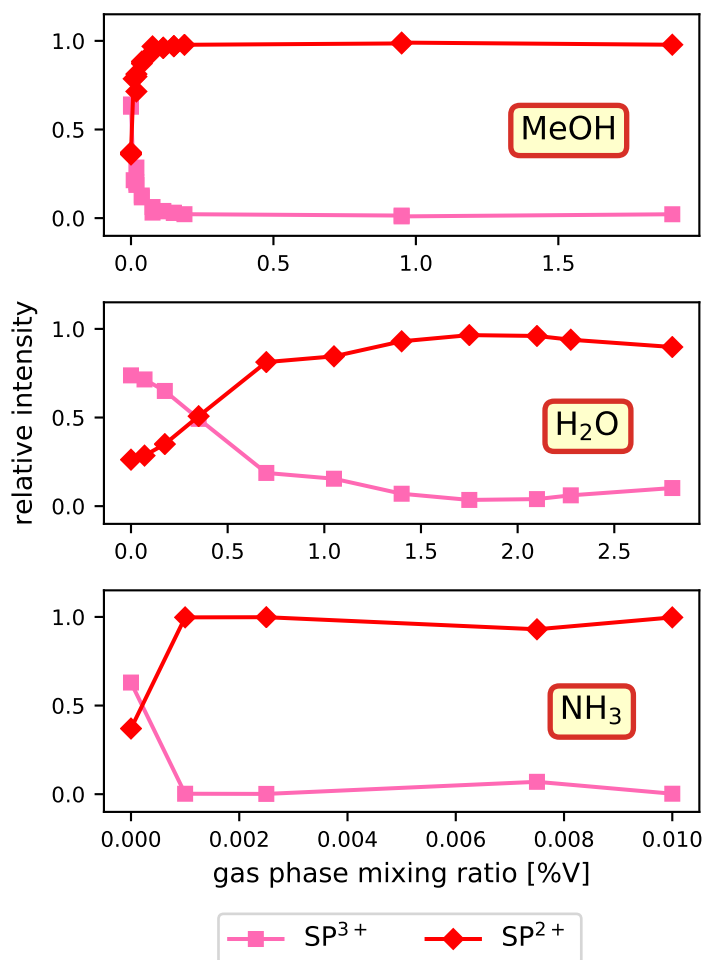


Figure 4.4: Intensities of SP²⁺ and SP³⁺ signals in dependence of the methanol (MeOH) mixing ratio (*top*), water (H₂O) mixing ratio (*center*), and ammonia (NH₃) mixing ratio (*bottom*). Each intensity is plotted relative to the corresponding summed intensity of both SP signals.

deprotonation and addition of ACN/MeAc/Et₂O (modifiers of group 2) does not. Irrespective of the GB of SP²⁺, if H₂O (GB = 660.0 kJ/mol) and MeOH (GB = 724.5 kJ/mol) were able to deprotonate a protonated site of SP³⁺, ACN (GB = 748 kJ/mol) is expected to induce a thermodynamically even more favored proton transfer reaction. However, depletion of the higher charge state is not observed at all with ACN. In section 2.2.2 the difficulty of determining the PA/GB of multiply protonated macromolecules was discussed, and furthermore, the observation of unexpected proton transfer reactions leading to charge reduction was noted. Two processes ((R2.10) and (R2.11)) were presented, which explain unexpected or apparently “forbidden” proton transfer reactions to solvent clusters S_n instead of transfer to single solvent molecules. In general, the PA/GB of solvent clusters S_n increases with the cluster size *n*. However, polar protic solvents, such as NH₃, MeOH, and H₂O, can form large stable cluster structures S_nH⁺ through hydrogen bond networks. For polar aprotic solvents, such as ACN, MeAc, and Et₂O, proton bound dimers, in which two molecules are symmetrically positioned around the central proton, represent stable closed shell clusters (cf. section 2.2.1). These dimers do not possess hydrogens that can form stable hydrogen bonding networks beyond the dimer. Therefore, no further closed shell is formed beyond the first shell for *n* = 2. Hydrogen bond networks cannot be formed with aprotic solvents because the proton can be further stabilized only by weaker interactions such as dipole-dipole interactions. Protonated trimers or even higher clusters of aprotic solvents are thus rarely observed [113, 184]. The cluster size-dependent PA values of the protic solvents NH₃, MeOH, and H₂O are listed and compared to the PA values of the monomers and dimers of the aprotic solvents ACN and MeAc in Table 4.2.

Table 4.2: Gas-phase proton affinities of (NH₃)_{*n*}, (MeOH)_{*n*}, (H₂O)_{*n*} (*n* = 1–5) [137] and of (ACN)_{*n*}, (MeAc)_{*n*} (*n* = 1, 2) [184] in kJ/mol

<i>n</i>	NH ₃	MeOH	H ₂ O	ACN	MeAc
1 ^a	853.6	754.3	691.0	779.2	812
2	950	883	816	912.9	948.9
3	996	937	862		
4	1029	967	900		
5	1054	979	904		

^a PA for *n* = 1 are taken from [122].

The PA of all solvents increases with cluster size *n*, the largest increase in PA is observed for the cluster reaction 1 → 2. Comparing the PA values of the protic solvents NH₃, MeOH, and H₂O for a given *n* PA(NH₃) > PA(MeOH) > PA(H₂O) applies, which is in accordance with the observed charge depletion efficiency (see above). A much higher content of H₂O than NH₃ in the ion source is needed to observe equivalent

4 Results and Discussion: Substance P

decrease in z_{avg} . This could be due to the fact that a higher cluster size n is needed for $(\text{H}_2\text{O})_n$ than for $(\text{NH}_3)_n$ to reach a certain threshold PA value resulting in efficient proton transfer from SP^{3+} to $(\text{H}_2\text{O})_n$ and $(\text{NH}_3)_n$, respectively. As mentioned before, proton transfer to solvent clusters S_n can be rationalized in terms of two processes: a direct proton transfer to S_n (R2.10) or an intracuster proton transfer (R2.11). The PA values listed in Table 4.2 only hold true for the direct proton transfer to S_n . In the $[\text{SP}+n(\text{S})+3\text{H}]^{3+}$ clusters, the PA of a solvent residue as well as of a basic site of SP highly depends on the chemical environment and therefore on the structure of the SP^{3+} -solvent cluster. The structure of SP^{3+} is complex and characterized by intramolecular charge stabilizing interactions [174, 175]. Additionally, with increasing cluster size n , i.e., the number of attached solvent molecules, the number of possible isomeric structures increases strongly. Therefore, a quantitative comparison between the PAs of S_n and basic sites of SP is not reliable. Only a good qualitative agreement between the n -dependent PA of the modifiers including the classification of protic vs. aprotic properties as crucial factor, and their effect on z_{avg} of SP ions is found. This is aggravated by the fact that the protonated solvent clusters S_nH^+ , that should be formed in both considered proton transfer processes, are not discernible in the recorded mass spectra. As mentioned before, protonated solvent clusters remain undetected due to fragmentation processes and limited low m/z mass ranges (cf. section 2.2.2). Therefore, providing experimental evidence for the assumed proton transfer reactions is rendered difficult. Servage and co-workers [185] studied the charge reduction of SP^{3+} mutant ions⁵ via proton transfer reactions to H_2O . They observed the proton transfer step forming $(\text{H}_2\text{O})_n\text{H}^+$ ions and charge-reduced SP^{2+} mutant ions during IMS, along with mass spectrometric detection of the protonated water clusters [185]. In a work from Smith and Ogorzalek Loo [93] the proton transfer reactions between electrosprayed cytochrome c and water as well as ammonia are discussed. Regarding the proton transfer to water, the authors note that shifts in the charge state distribution towards smaller charge states “were only observed for occasional scans and appeared to correlate with transmission of water droplets through the reagent line.” [93] Reactions with NH_3 leading to much smaller charge states were observed, although the PA of NH_3 is lower than that of the isolated amino acids in cytochrome c. The authors assessed the reactivity of NH_3 as “surprising”. In the same study, a negative temperature dependence of proton transfer reactions between protonated proteins and ammonia was found. This result is rationalized by a cluster-mediated proton transfer [93]. These findings reinforce the concept of proton transfer reactions to solvent clusters in the present nanoESI experiments.

However, in contrast to aprotic solvents, protic solvents can form large stable gas-phase clusters of the type S_nH^+ with $n > 2$, which exhibit significantly larger PAs than

⁵Replacement of individual amino acids in the sequence with other amino acids, e.g. changing the glutamine residues in the sequence of SP with alanine, is called amino acid mutation and the resulting ions are called mutant ions. Amino acid mutation leads to modification or even elimination of intramolecular interactions [185].

the bare solvent molecules, increasing with n . Therefore, it is feasible for protic solvents to form aggregates at protonated sites of SP^{3+} , which eventually abstract the proton forming a stable protonated solvent cluster. Aprotic solvents tend to conserve the maximum possible charge state of SP, thus they do not facilitate proton transfer reactions leading to charge reduction. This approach was further investigated experimentally and theoretically by using doubly protonated alkyldiamines as less complex target ions as compared to SP^{3+} . The results concerning the charge state manipulation of alkyldiamines due to ion-solvent interactions are described in section 5.

Aprotic solvents, such as ACN, conserve the maximum charge state, which the SP ions exhibit in the solution phase or droplet. This charge retention is accompanied by the formation of stable SP^{3+} -solvent clusters, the extent of cluster formation appears to depend on the solvent's dipole moment. SCAs, which are added to the sprayed analyte solutions in ESI-MS to achieve higher charge states (supercharging), are characterized by their high dipole moment and their low vapor pressure. As described for various analytes and SCAs in the literature, SCAs form clusters with analyte ions and with increasing analyte charge state a concomitantly increase of clustering is discovered. Furthermore, supercharging is promoted with increasing dipole moment of the SCA (cf. section 2.1.4). Therefore, there is obviously a relation between the formation of highly charged analyte-solvent/SCA clusters and the prevention of charge reduction processes. One charge reduction process, the proton transfer to solvent clusters appears to play a significant role, when protic solvents, e.g. MeOH, are present at elevated mixing ratios in the nanoESI source. To further examine the role of ion-bound solvent clusters in the observed charge retention and depletion processes of SP, the addition of the gas phase modifiers MeOH and ACN were combined with the use of DMSO and sulfolane as SCAs. The results are presented and discussed in section 4.2.

4.1.1 Comparison Investigations with the Bruker CaptiveSpray nanoBooster

ACN clusters strongly with SP ions and has therefore a strong effect on z_{avg} . Actually, adding ACN vapor into the ion source to increase z_{avg} is an approach, which is commercially available as an add-on - called nanoBooster [187] - for the Bruker CaptiveSpray ion source [186]. Bruker advertises the nanoBooster as follows: "The nanoBooster device enhances signal intensity and charge states [...]. Charge-state control can be achieved by choosing the appropriate dopant." [187] Preliminary SP comparison measurements with the commercially available CaptiveSpray nanoBooster [186, 187] using ACN as modifier showed similar results than obtained with the nanoESI source (cf. section 3.1.2) with even improved performance regarding the charge state shift and intensity gain. This improved performance is caused by the optimized geometry of the ion source [68]. Additionally, Alagesan and co-workers [188] investigated the effect of different solvent vapors using the CaptiveSpray source with attached nanoBooster regarding the ionization of (glyco)peptides. In accordance with the SP results presented in this work, addition of aprotic solvents (ACN and

MeAc) leads to higher z_{avg} values and in some cases even to a higher z_{max} whereas addition of protic solvents (MeOH, EtOH, and IPA) results in decrease of z_{avg} . In addition, with the protic solvents a higher level and with the aprotic solvents a lower level of background noise - compared with no modifier addition - is reported [188]. Similar results regarding the signal-to-noise ratio were obtained applying ACN and MeOH as modifiers and the nanoESI setup, which is used for this work [189]. It is therefore concluded that findings which are obtained with the captiveSpray nanoBooster [20, 190] are generally comparable with results obtained with the nanoESI setting applied in this work.

4.2 Combined Solution Phase and Gas Phase Modification

There are two different approaches to change charge state distributions in ESI-MS. In section 4.1, the effect of solvent vapors added into the ion source (gas phase modification) regarding the ionization of SP was discussed; a distinction between aprotic and protic polar solvents was identified. Addition of protic solvents leads to charge depletion whereas addition of aprotic solvents results in charge retention accompanied by intense formation of SP^{3+} -solvent clusters. The more conventional way to achieve higher charge states (supercharging) is adding SCAs to the sprayed analyte solution (cf. section 2.1.4). This is considered as solution phase modification. DMSO and sulfolane, which are both described as SCAs in the literature [57, 77, 173], were added to the sprayed SP solution (1 %V DMSO or sulfolane in ACN/ H_2O or MeOH/ H_2O with 0.1 %V formic acid⁶) leading to the observation of clusters with SP^{3+} of the composition $[\text{SP}+n(\text{S})+3\text{H}]^{3+}$ with $\text{S} = \text{DMSO}$ or sulfolane and $n = 1, 2$, but generally not with SP^{2+} .⁷ Again, no significant change in the recorded mass spectra was observed when spraying a solution of SP with SCA in MeOH/ H_2O instead of ACN/ H_2O .⁸ When sulfolane is used as SCA, the mass spectrum is dominated by the clustered and unclustered SP^{3+} species and the cluster with $n = 1$ represents the most intense ion signal (cf. the relative ion intensities at 0 %V modifier mixing ratio in Figure 4.6 c). Clustering with DMSO is observed to a smaller extent, which may be caused by the lower dipole moment as compared to sulfolane (cf. Table 4.1). In addition to the higher dipole moment, sulfolane exhibits a lower vapor pressure compared to DMSO. The very low sulfolane vapor pressure may also promote the occurrence of cluster signals. Consequently, an increased z_{avg} of almost 3 is observed with sulfolane while z_{avg} re-

⁶The spray solution always contains 0.1 %V formic acid, regardless of the composition (ACN/ H_2O or MeOH/ H_2O). For clarity of presentation, the formic acid content is not explicitly mentioned in the following.

⁷Very rarely SP^{2+} clustered with one DMSO molecule or with one DMSO and one H_2O molecule is observed, but with very low signal intensity. A detailed overview of the observed ion population is given in [183].

⁸A detailed comparison of the observed ion population between DMSO containing ACN/ H_2O and MeOH/ H_2O solution is given in [183].

4.2 Combined Solution Phase and Gas Phase Modification

mains unaltered with DMSO. This becomes apparent upon comparing the z_{avg} values in Figure 4.5 between DMSO (orange and green trace) and sulfolane (light blue and purple trace) at 0 %V modifier mixing ratio. The PAs of DMSO and sulfolane are relatively high as compared to the other modifiers (cf. Table 4.1), underlining again that deprotonation by single solvent molecules cannot be responsible for charge loss with protic gas phase modifiers, e.g. MeOH. The same effect on z_{avg} of SP was found for DMSO and sulfolane by Miladinovic and co-workers using in-spray supercharging, whereby the formation of SP^{3+} adducts was only observed with DMSO [173]. However, based on the results presented in this work, both SCAs, DMSO and sulfolane, show a similar behavior as the aprotic modifiers ACN and MeAc, although the SCAs are added to the solution and the modifiers to the gas phase. This suggests a “connection” between gas phase and liquid phase based charge retention/supercharging mechanisms. Furthermore, this analogy raises the question, if and to what extent liquid phase based charge retention processes are affected by gas phase based charge depletion processes (e.g., the addition of MeOH vapor) as well as by gas phase based charge retention processes (e.g., the addition of ACN vapor).

A combination of gas phase and solution phase modification was performed to examine these questions. DMSO and sulfolane were used as SCAs, MeOH and ACN as gas phase modifiers. Both SCAs were added to ACN/ H_2O and MeOH/ H_2O solutions of SP, i.e., SP was sprayed from each of these four different solutions and exposed to ACN and MeOH vapor resulting in a total of eight combinations. When examining the effects of a simultaneous gas and solution phase modification, no significant difference could be found between the use of ACN/ H_2O and MeOH/ H_2O as analyte dilution. Therefore, only four different combinations are discussed in the following (cf. Figure 4.6): a) DMSO + ACN vapor, b) DMSO + MeOH vapor, c) sulfolane + ACN vapor, and d) sulfolane + MeOH vapor. The results of the combined solution phase and gas phase modification are compared to classical gas phase modification, as shown in Figure 4.5. The amount of SCA in the sprayed solution was always 1 %V but the mixing ratio of the added vapor was varied between 0 and 2-4 %V.

The results⁹ obtained for DMSO and sulfolane, respectively, are very different. Both the average charge state z_{avg} (Fig. 4.5) and the ion population (Fig. 4.6) are affected differently. DMSO present in the solution prevents the depletion of SP^{3+} when adding MeOH vapor and z_{avg} is not notably changed (cf. orange curve in Figure 4.5). In contrast, sulfolane only retards the charge depletion by MeOH, compared to the experiment without sulfolane present. At low MeOH mixing ratios SP^{3+} species are still present in the spectrum but at MeOH mixing ratios above 2 %V z_{avg} is efficiently shifted toward SP^{2+} (cf. red and purple curve in Figure 4.5). As mentioned above, using DMSO as SCA, z_{avg} is not changed significantly; using in addition ACN as gas phase modifier increases z_{avg} only slightly (cf. green curve in Figure 4.5). With sul-

⁹The results of the combined solution and gas phase modification were published in a previous journal article [68]. The following paragraph therefore resembles section 3.3 in [68].

4 Results and Discussion: Substance P

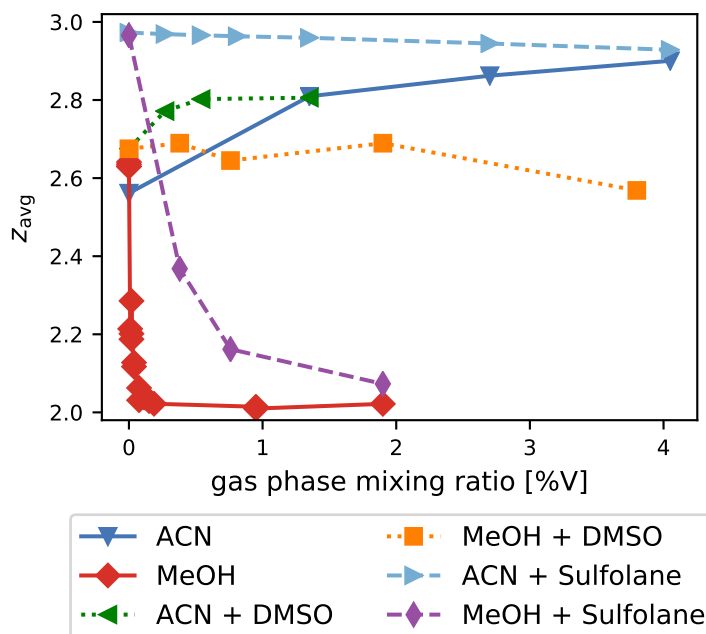


Figure 4.5: Average charge state z_{avg} of SP ions in dependence of the gas phase modifier (ACN and MeOH) mixing ratio in combination with the addition of the supercharging agents (DMSO and sulfolane) to the ESI solution.

folane as SCA, z_{avg} is almost completely shifted to 3; additional application of ACN vapor reduces the charge state slightly and at high ACN mixing ratios the same z_{avg} is obtained without sulfolane present (cf. blue curves in Figure 4.5). In summary, sulfolane does not change the general effect of the gas phase modifier, while DMSO inhibits the effect of the gas phase modifier almost entirely. These results suggest a significant exchange of ACN and MeOH with SP^{3+} -sulfolane clusters but not with SP^{3+} -DMSO clusters.

In Figure 4.6 the relative intensities of the SP ion signals are depicted in dependence of the gas phase modifier mixing ratio. In the case of DMSO, SP^{3+} -DMSO clusters are detected with high abundance, while the abundance of SP^{3+} -ACN clusters remain low with added ACN. In contrast, SP^{3+} -DMSO cluster intensities increase with ACN addition whereas the bare ions SP^{3+} and SP^{2+} decrease in intensity (cf. Figure 4.6 a). It follows that ACN reacts primarily with the bare SP^{3+} and does not exchange DMSO. The same holds true for MeOH. When MeOH vapor is applied, the ion population remains unchanged up to a mixing ratio of 1 %V. At higher mixing ratios, the bare SP^{3+} signal intensity decreases whereas the SP^{3+} -DMSO clusters and SP^{2+} increase in intensity (cf. Figure 4.6 b). In contrast, with sulfolane pronounced exchange with both gas phase modifiers is observed. When ACN is added, SP^{3+} -sulfolane cluster

4.2 Combined Solution Phase and Gas Phase Modification

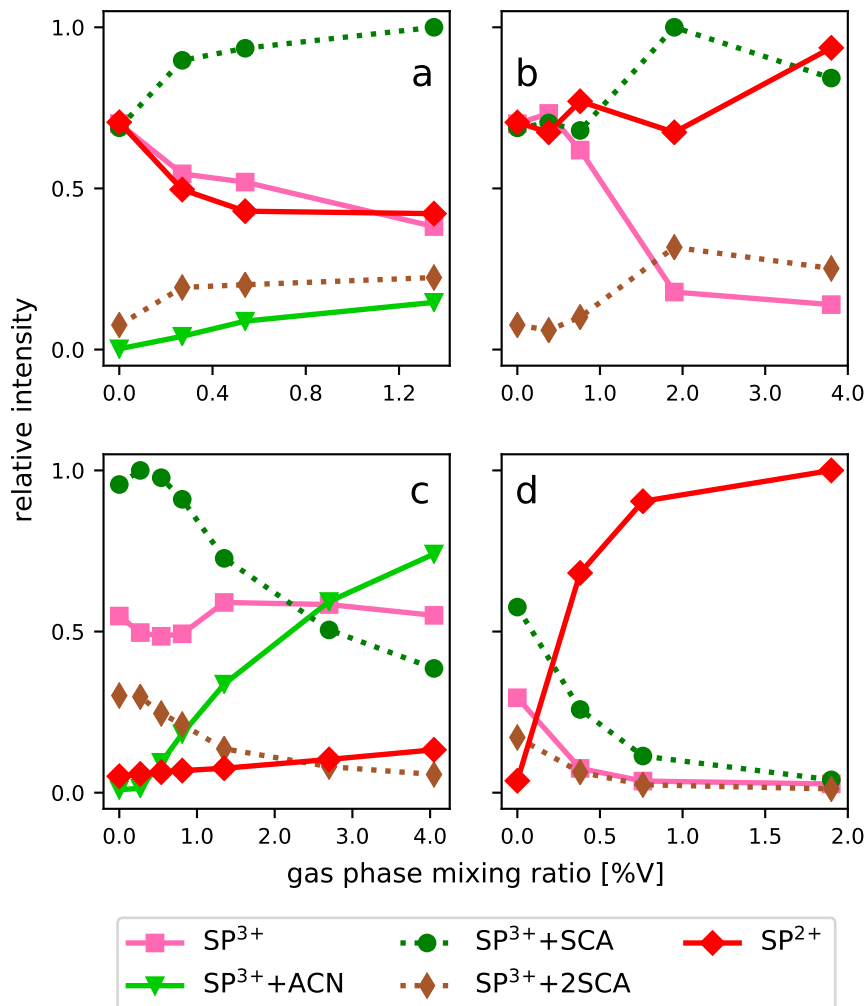


Figure 4.6: Intensities of observed SP ion species in dependence of the gas phase modifier mixing ratio, obtained with combined solution (DMSO and sulfolane) and gas phase modification (ACN and MeOH). **a:** 1 %V DMSO + ACN vapor; **b:** 1 %V DMSO + MeOH vapor; **c:** 1 %V sulfolane + ACN vapor; **d:** 1 %V sulfolane + MeOH vapor. In the legend SCA stands for DMSO or sulfolane, respectively. The intensities of each data set (a,b,c,d) are plotted relative to the corresponding maximum value.

4 Results and Discussion: Substance P

signals decrease in favor of SP^{3+} -ACN cluster signals (cf. Figure 4.6 c). When MeOH is added, all SP^{3+} signals are depleted and the bare SP^{2+} signal is promoted until SP^{2+} is the only SP ion signal observed in the mass spectrum (cf. Figure 4.6 d). The strong contrast to the DMSO experiments is rationalized in terms of different solvation energies of SP^{3+} -DMSO and SP^{3+} -sulfolane clusters. As mentioned before, sulfolane exhibits a higher dipole moment and lower vapor pressure than DMSO. Both properties may promote the observation of SP^{3+} -sulfolane clusters. In addition, preferential solvation by sulfolane in the liquid phase could lead to high abundance of SP^{3+} -sulfolane clusters, as supported by the experiments using sulfolane as SCA without modifier addition. In the presence of gas phase modifiers, the SCAs have to compete with the modifier molecules for solvation. The experimental results indicate that DMSO is competing with ACN and MeOH but sulfolane is not (except in the case of low ACN mixing ratios). It can be assumed that the thermodynamic stability of the SP^{3+} -sulfolane clusters is lower than the stability of the SP^{3+} -ACN and SP^{3+} -MeOH clusters, i.e., sulfolane exhibits a lower solvation energy than ACN and MeOH regarding the solvation of SP^{3+} in the gas phase. Consequently, DMSO should have a higher solvation energy both in solution and gas phase than ACN and MeOH, and accordingly than sulfolane¹⁰. However, ligand exchange of DMSO with ACN/MeOH could also be kinetically hindered. Therefore, different affinities of MeOH and ACN toward sulfolane and DMSO attached to SP^{3+} may also lead to different reactions, e.g. ligand exchange, deprotonation, dissociation.

Mixed-solvent clusters attached to SP^{3+} of the form, $[\text{SP}+n(\text{S}_1)+m(\text{S}_2)+3\text{H}]^{3+}$, e.g. $[\text{SP}+(\text{MeOH})+(\text{DMSO})+3\text{H}]^{3+}$ or $[\text{SP}+2(\text{ACN})+(\text{H}_2\text{O})+3\text{H}]^{3+}$, were rarely observed. Due to the lack of experimental data, mixed-solvent clusters are therefore not considered in the charge retention/charge depletion model (cf. section 4.4). However, mixed-solvent clusters are most probably also of importance for the cluster chemistry determining the ion population observed in nanoESI-MS. The stability and structure of various protonated mixed-solvent clusters including the solvents H_2O , MeOH, EtOH, ACN, and NH_3 have been studied experimentally and theoretically [91, 94, 113]. Depending on the cluster structure, the proton can be stabilized by hydrogen bonds resulting in high PA values. For example, a stable solvation structure of the proton formed by strong H-O-H hydrogen bonds was found for $[(\text{ACN})_n+(\text{H}_2\text{O})_{n-2}+\text{H}]^+$ with $n \leq 7$ [113]. Proton transfer to solvent clusters which contain aprotic as well as protic solvents is conceivable since their cluster size and thus their PA can reach high values.

¹⁰There are studies which report that sulfolane shows weaker interactions with inorganic ions, e.g. alkali or transition metal cations, than DMSO [191, 192].

4.3 Collision Induced Dissociation

CID experiments were performed to study the influence of the gas and solution phase modification on the fragmentation pattern of SP and particularly on the stability of the different SP^{3+} clusters.¹¹ The potential difference between the capillary exit and the first skimmer in the TOF-MS, i.e., in the first vacuum stage (see Figure 3.3b), was increased to induce CID. As expected, CID results in fragmentation of SP ions. The typical fragmentation pattern of SP is observed, yielding mainly a and b fragments [193, 194]. Fragmentation is accompanied by intensity loss. The SP signal intensity (excluding fragments) in dependence of the acceleration voltage is given in Figure 4.7. In the absence of a modifier or an SCA, the SP signal intensity drops steeply with increasing acceleration voltage (cf. black trace in Figure 4.7). The fragmentation of SP^{3+} sets in at lower acceleration voltages as compared to SP^{2+} , which is due to the difference in m/z and the charge state, respectively (cf. section 2.2.3). The same holds true when DMSO is added to the solution. Additionally, declustering of SP^{3+} -DMSO clusters is observed at low activation voltages leading to an increase of SP^{3+} signal intensity, whereas at higher activation voltages a prominent increase of the SP^{2+} signal intensity is observed. At the same time, the SP^{3+} -DMSO signal intensities vanish, which is attributed to proton transfer from SP^{3+} to DMSO upon forced dissociation. Therefore, loss of SP signal intensity is also observed when DMSO is used as SCA, but the decrease sets in at higher acceleration voltages (cf. Figure 4.7, green and black traces). In contrast, adding a gas phase modifier decreases the extent of fragmentation of SP in dependence of the modifier mixing ratio. At low modifier mixing ratios, e.g. < 1%V MeOH, fragmentation is strongly reduced (cf. red curve in Figure 4.7). At high modifier mixing ratios, e.g. > 5%V ACN, no fragmentation is observed at all (cf. blue curve in Figure 4.7). Furthermore, higher acceleration voltages lead to even a small ion signal intensity gain, likely due to improved transmission; the intensity ratio of clustered (SP^{3+} -ACN cluster) and unclustered SP^{3+} is barely changing.

In summary, declustering and dissociation of SP^{3+} -DMSO clusters is observed, while the relative intensity of SP^{3+} -ACN clusters remains constant in the CID experiments. This is explained by the different mixing ratios of DMSO and ACN. When an SP^{3+} -DMSO cluster loses a DMSO molecule, the probability of the back-reaction is low, due to the low gas phase mixing ratio (≈ 1 ppmV). In contrast, ACN is abundantly present (in the percentage by volume range) in the collision region between the capillary and the first skimmer of the instrument since the modifier-enriched gas is quantitatively transferred from the ion source into the vacuum system (cf. section 3.1.2). Therefore, the SP^{3+} -ACN cluster equilibrium is nearly maintained in the first vacuum region. Experimental work from Morsa and co-workers [195] revealed that ACN adducts are formed with electrophilic benzylium “thermometer” cations both

¹¹The results of these experiments are described in detail in [68]. In this work, only a short overview is given because further CID experiments were performed using alkyldiames instead of SP (see section 5.1.3).

4 Results and Discussion: Substance P

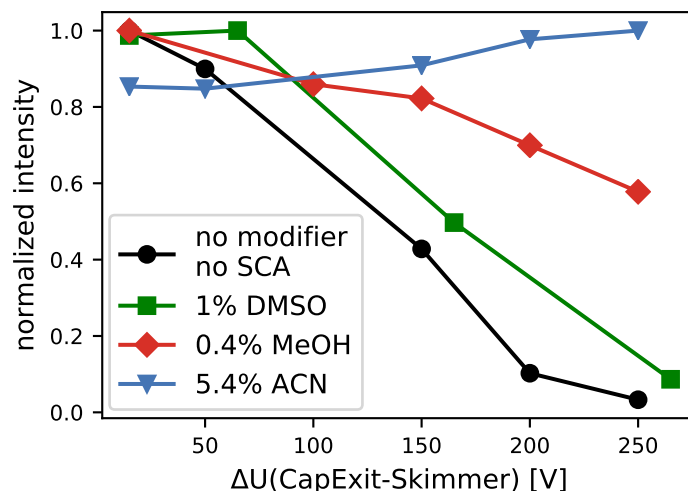


Figure 4.7: Intensities of the sum of all SP signals (fragments are not included) in dependence of the acceleration voltage (potential difference between the capillary exit and the first skimmer of the TOF instrument (cf. Figure 3.3b)). Intensities are normalized to the TIC and to the maximum value.

in the ESI source and inside the IMS tunnel. The authors stated that the adduct formation occurs probably because of residual solvent vapor carried by the buffer gas flow along the pressure gradient, supporting the presented experimental results and underlining that interactions between ions and solvent vapors play a crucial role in ESI-MS. Furthermore, it is reasonable to assume that the droplet evaporation and ion desolvation processes significantly change in the presence of modifiers. Most probably, droplet evolution has not progressed to the extent that only gaseous compounds and bare ions enter the second stage ion guides. This assumption is supported by the absence of any fragmentation with a gas phase modifier present, since fragmentation occurs only when ion release from charged droplets and desolvation/declustering is completed either due to or even without additional activation [68]. Similar observations were also previously reported regarding stabilization of non-covalent protein complexes by addition of polar solvent vapors [17, 196].

It is important to keep in mind that SP ions can undergo structural changes due to collisional activation. As mentioned before, the SP^{3+} ion, in particular the charge sites, are stabilized by intramolecular interactions. Upon collisional heating, these interactions can be disrupted. Elimination of these interactions reduces, even eliminates, the ability to stabilize the present charges due to an increase of Coulomb repulsion resulting in a reduction in the GB of the charge sites [174, 185]. Therefore, charge depletion processes, e.g., proton transfer or fragmentation, are favored by gas-phase

rearrangement of conformation induced by collisional activation. In general, in absence of external solvation, intramolecular solvation plays a critical role in stabilizing ion conformations as well as ESI charge state distributions (cf. section 2.1.1). Consequently, maintaining external solvation, e.g. due to addition of gas phase modifiers, aids in preventing structural changes. Therefore, the use of gas phase modifiers might support the preservation of the native conformations of proteins, as the evaporating solvent can be replaced by the modifier during the ESI droplet evolution [54]. This reasoning also explains the observed decrease in or even absence of fragmentation when gas phase modifiers are applied in CID experiments, as described above.

To reduce the intramolecular effects, the influence of gas phase modification on the fragmentation/dissociation of ion-solvent clusters was further studied with alkyldiamines, which represent less complex molecular systems than the peptide Substance P. Therefore, the formation and stability of protonated alkyldiamine-solvent clusters is more favorably described on the molecular level, minimizing effects based on crucial structural or chemical dynamics. Since aminic charge sites are also present in peptide or protein ions, alkyldiamines with varying chain length are suitable to simulate spatially close charge sites in macromolecules, e.g. proteins. The results of these further CID experiments are described in section 5.1.3.

4.4 Charge Retention/Charge Depletion Model

The experimental results presented in the previous sections receive distinct ion-chemical pathways for the interpretation of mass spectra of multiply charged SP ions when using nanoESI in combination with solution and/or gas phase modification. The different processes derived from experimental observations are mainly rationalized in terms of cluster chemistry. A distinction is made between charge depletion and charge retention processes. Figure 4.8 summarizes charge depletion and retention processes at different stages of the ion release and transfer process.

As discussed in section 2.1.1, the formation of gas-phase clusters prior to the formation of desolvated gas-phase ions is in accord with the models IEM, CRM, and CEM, explaining ion formation in ESI. When an SP (cluster) ion is released from a charged droplet it may carry up to three protons, as this is the highest charge state observed in the experiments. Such an ion undergoes clustering and declustering reactions, which mainly take place in the intermediate pressure region (green region in Figure 4.8). In the nanoESI setup used all gases present in the ion source, i.e., nitrogen, sprayed solvents, and when applied additionally modifiers and/or SCA, enter the first vacuum stage. SP^{3+} -solvent clusters are only observed when a modifier and/or SCA are applied. Therefore, the SP^{3+} -solvent clusters originating from sprayed solvents dissociate within the ion transfer stage by ion activation (red region in Figure 4.8). During this process the charge state of some SP^{3+} ions may be reduced via proton transfer to the solvent. Proton transfer to solvent clusters is possible, the crucial cluster number m depends on the solvent and on the kinetic energy of the ions. The

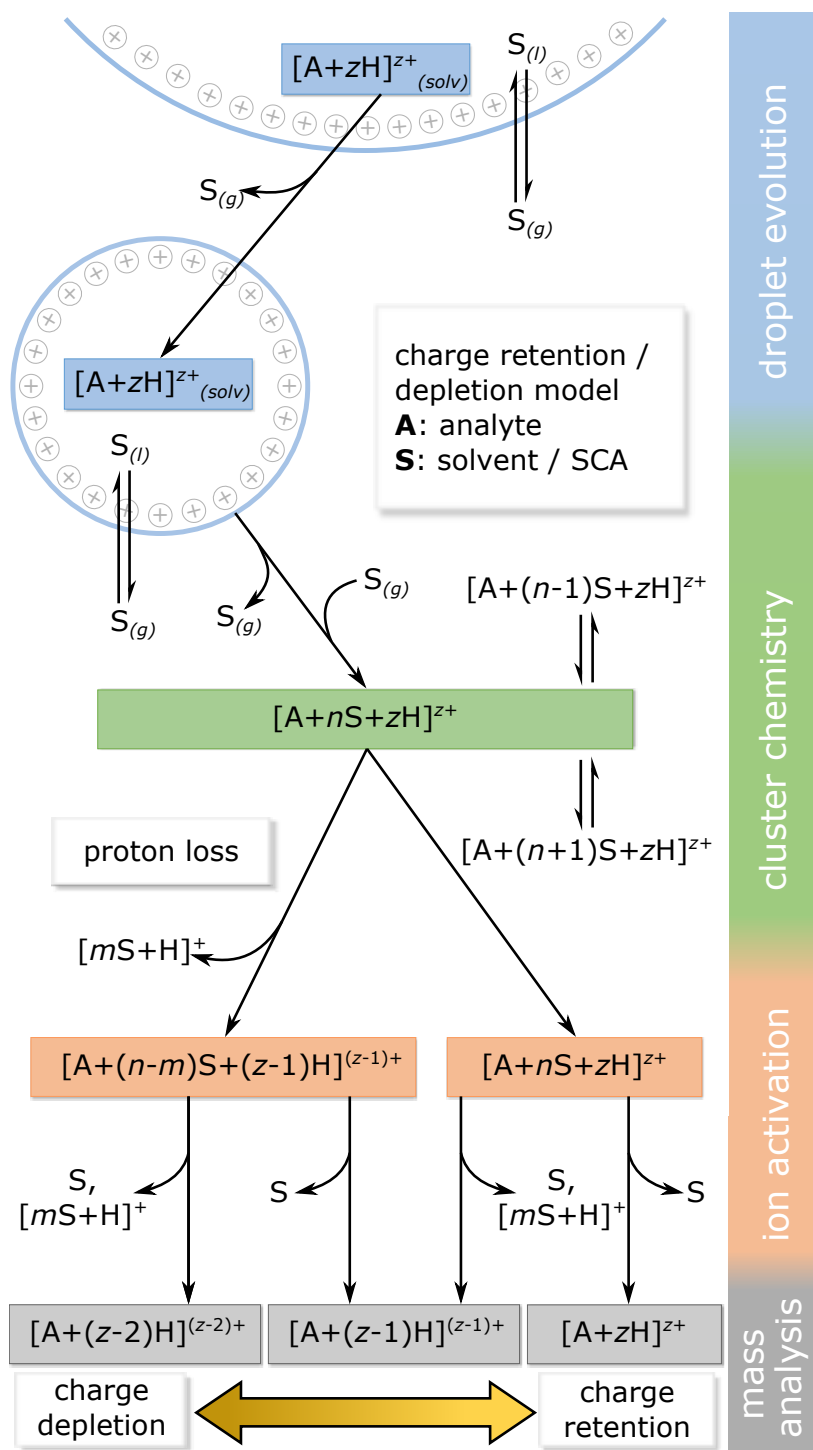


Figure 4.8: Sketch of a charge retention/charge depletion model showing the processes at different stages of the ion release and transfer process which lead to ionic species observed in nanoESI-MS. Adapted with permission from [68]. ©2020 American Chemical Society.

mixing ratio of ACN and MeOH, respectively, originating only from the evaporating droplets is in the range of 100 ppmV at typical nanoliter-per-minute flow rates and has no impact on the observed z_{avg} . In comparison studies with SP solutions consisting of equal quantities of H₂O/ACN and H₂O/MeOH the same ratios of SP²⁺ and SP³⁺ are observed. Therefore, neither sufficient amount of MeOH for charge depletion nor sufficient amount of ACN for charge retention is present. According to the CRM, the composition of a droplet consisting primarily of water and another, more volatile organic solvent will change in favor of water. Thus, in its final stage, an SP ion is mostly solvated by water in either case. During the declustering process protons may either be retained at SP or be lost to water, which determines the observed ratio of SP²⁺ and SP³⁺ ions.

Adding a modifier to the matrix gas leads to an enrichment of the modifier in the droplet (blue region in Figure 4.8). Furthermore, the cluster equilibria are shifted to larger cluster sizes (green region in Figure 4.8). This in turn drives proton loss to modifiers, i.e., polar protic solvents, which are able to form large cluster structures. The PA/GB of the solvent cluster exceeds that of the SP protonation site and charge depletion is observed. In contrast, the PA/GB of polar aprotic solvent clusters is limited due to their inability to form large hydrogen bond networks eliminating the deprotonation step and charge retention is observed. Adding an SCA to the solution results in enrichment of the SCA in the droplet and yields SP³⁺-SCA clusters due to its low vapor pressure and high dipole moment, respectively. Solvation by an SCA prevents deprotonation due to the lack of multiple binding sites leading to charge retention. Since the SCA gas phase concentration is low, the cluster equilibrium is not maintained during ion transfer. SCAs are exchanged with other solvent molecules, which are abundantly present, e.g. modifiers, depending on the individual ion-molecule solvation energies and reaction dynamics (green region in Figure 4.8).

4.5 Summary and Conclusions

In the present work, the charge-retaining effect of both aprotic gas phase modifiers and SCAs are connected to their shared bonding properties (i.e., high dipole moment and only one hydrogen bonding site) and their elevated presence in droplets/clusters from which the detected SP ions are formed. SCAs exhibit low evaporation rates due to their low vapor pressure, leading to an enrichment of these reagents in charged droplets and thus in clusters that emerge from these droplets. Adding a modifier shifts the partition equilibrium between gaseous and liquid phase modifier toward the liquid state, which leads to an enrichment of the modifier in the droplet and an extended duration of complete solvent evaporation. Additionally, both aprotic gas phase modifiers and SCAs exhibit elevated dipole moments promoting the formation of stable ion-solvent gas-phase clusters. It is concluded that for the SP model system charge retention based on both solution and gas phase modification is driven by the change of the chemical environment of the ion, preventing deprotonation.

4 Results and Discussion: Substance P

Therefore, charge retention is considered as prevention of charge depletion, which occurs through proton transfer to solvent(cluster)s, often driven by collisional activation. Charge depletion observed with protic gas phase modifiers is attributed to the increased PA/GB of large solvent clusters, which are either formed in the gas phase or are residues from the final modifier-enriched droplet evaporation steps. These findings were summarized in a charge retention/charge depletion model.

The hypotheses I-IV, as listed in chapter 1, have been experimentally validated by the following findings:

- i Polar *aprotic* compounds (ACN, MeAc, Et₂O, DMSO, sulfolane) achieve charge retention due to formation of SP³⁺-solvent clusters resulting in an increased (or unaltered) z_{avg} .
- ii Polar *protic* compounds (H₂O, MeOH, EtOH, NH₃) induce depletion of the higher charge state (SP³⁺) resulting in reduction of z_{avg} . The charge depletion efficiency depends on the amount of modifier added and correlates with the PA/GB of the modifier.
- iii CID of SP³⁺ clustered with gas phase modifiers is inhibited by sufficient addition of a gas phase modifier. The dissociation of clusters with solution phase modifiers is observed with increasing acceleration voltage.
- iv Effects of gas phase and solution phase modification - including the phenomenon of *supercharging* by DMSO and sulfolane - are rationalized in a charge retention/charge depletion model based on ion-molecule cluster chemistry.

Based on these results, one additional hypothesis (v) is formulated:

- v Gas phase modification leads to the presence of the modifier in the transfer system of the mass spectrometer, thus enabling ion-molecule cluster reactions also during ion transfer and analysis.

Further experimental studies were conducted to validate the established charge retention/charge depletion model based on experimental observations with the peptide Substance P and to examine the postulated hypotheses i-v. Terminal alkyldiamines NH₂(CH₂)_kNH₂ with variable chain length k were used as analytes in the follow-up experiments. In the following chapter these investigations are presented and discussed.

5 Results and Discussion: Terminal Alkyldiamines

The exposure of electrospray droplets to polar organic solvent vapors (gas phase modifiers) revealed insights into ion-solvent clustering processes determining the observed ion population of Substance P (SP). A model was presented, which describes the ion-chemical pathways (cf. section 4.4). To validate this model, the influence of gas phase modifiers was further studied using terminal alkyldiamines, $\text{NH}_2(\text{CH}_2)_k\text{NH}_2$, as analytes representing suitable model systems for multiply protonated macromolecules. In addition to the terminal alkyldiamines, $\text{NH}_2(\text{CH}_2)_k\text{NH}_2$ with $k = 2, 3, 5, 8, 9$, i.e., the compounds 1,2-diaminoethane (DA-2), 1,3-diaminopropane (DA-3), 1,5-diaminopentane (DA-5), 1,8-diaminooctane (DA-8), and 1,9-diaminononane (DA-9), the aminic substances 1,4-diaminobenzene (DA-B) and diethylenetriamine (TA-4), $\text{NH}_2(\text{CH}_2)_2\text{NH}(\text{CH}_2)_2\text{NH}_2$, were used as analytes.

The terminal alkyldiamines, in the following termed diamines (DA), can be singly and doubly charged due to protonation of one or both aminic functions. Therefore, the average charge state z_{avg} of an observed ion population (cf. equation (4.1)) can vary between 1 and 2.¹ In general, diamines are strong bases with high GB; the (apparent) GB for the singly protonated diamine is always lower than that of the neutral diamine, caused by Coulomb repulsion. The Coulomb repulsion between the two charged $-\text{NH}_3^+$ substituents depends on their separation, i.e., on the chain length k as well as on the degree of solvation, as discussed in section 2.2.2. Ab initio calculations by Gronert and co-workers [129] yield a GB of ≈ 743 kJ/mol for the singly protonated diaminoheptane (DA-7, $k = 7$) and a GB of ≈ 894 kJ/mol for the neutral species (cf. GB values of the solvents used as modifiers and SCAs in Table 4.1). Furthermore, they predict an apparent GB for the singly protonated diaminoheptane of 818 kJ/mol when combining the calculated GB with an estimation of the reverse activation barrier (75 kJ/mol) [129], which is in good agreement with a value derived from experiments (820 kJ/mol) [104] (cf. section 2.2.2). The PA of the neutral (945.1 kJ/mol) and the singly protonated (412.0 kJ/mol) diaminoethane (DA-2) were also calculated by ab initio calculations [109]. These values demonstrate the strong influence of the chain length k on the basicity of the singly protonated species and thus on the reactivity of the doubly protonated diamine ions, which was also studied by Williams and co-workers [130]: with decreasing chain length the singly protonated ion exhibits a lower GB value promoting charge depletion of the doubly protonated ion by pro-

¹This is in analogy to Δz_{avg} determined for the SP experiments; the statistical uncertainty of z_{avg} amounts to a maximum of ± 0.01 .

ton transfer reactions. In addition, the difference between GB(M) and GB(MH⁺) increases with decreasing chain length of the diamines. Solvation energies of various protonated diamines are also reported for solvation by H₂O [81–84] and NH₃ [104], as well as intramolecular solvation energies leading to cyclization [107, 110] (cf. section 2.2.1). Therefore, the diamines are suitable compounds to investigate ion-solvent interactions in nanoESI-MS on a molecular level.

5.1 Gas Phase Modification: Charge Depletion vs. Charge Retention

The experimental nanoESI setup is described in section 3.1.2. Both, the TOF (cf. section 3.1.2) and the quadrupole ion trap (QIT) instrument, described in section 3.1.2, were used for the diamine experiments. The ion transfer stage voltages of both instruments were optimized for minimum CID and the lower m/z range (TOF: Method DA (see Table 3.2), QIT: Method DA (see Table 3.1)). 0.1 mmol/l and 1 mmol/l solutions of each diamine in ACN/H₂O and MeOH/H₂O, respectively, with 0.1 %V formic acid were used as spray solutions. ACN and MeOH were mainly used as modifiers. ACN represents a polar aprotic modifier and MeOH represents a polar protic modifier. The chain length k , modifier mixing ratio, solvent composition of the spray solution, diamine concentration, position of modifier addition (source vs. capillary), and the acceleration voltage in the first, second and third vacuum stage were systematically varied in the experiments to study their impact on charge depletion and retention processes occurring in ESI-MS. Most of the experiments were performed with the TOF-MS; the QIT instrument was used for comparison experiments (see Figure 5.11).

First, the observed ion population is described and explored regarding the influence of the solution composition, the modifier addition, and the chemical structure of the diaminic analytes. The occurrence and the ion distribution of the diamine-ACN clusters, $[M(\text{ACN})_n\text{H}_2]^{2+}$, in the mass spectra are investigated. Subsequently, effects on the observed average charge state are analyzed in detail in section 5.1.2. In particular, the dependence of the observed average charge state on the length of the alkyldiamines is investigated. Furthermore, the influence of the position of modifier injection location is elucidated. Section 5.1.3 addresses the impact of gas phase modifiers on collisional activation and dissociation of diaminic ions.

5.1.1 Observed Ion Population

Influence of the Solution Composition

In contrast to SP, the *composition of the spray solution*, in which the analyte is diluted, has a strong influence on the observed ion population and accordingly on z_{avg} . Spraying a diamine from ACN/H₂O - in absence of modifier - results in an ion population, which is dominated by diamine-ACN clusters of the composition $[M+n(\text{ACN})+2\text{H}]^{2+}$, with $1 < n < 6$ depending on the chain length k of the diamine.

5.1 Gas Phase Modification: Charge Depletion vs. Charge Retention

For simplicity these clusters are labeled as $[M(\text{ACN})_n\text{H}_2]^{2+}$ in the text and the figures. The first ACN cluster of the singly protonated ion, $[M+(\text{ACN})+\text{H}]^+$, was also observed for all diamines but this species exhibits low abundances in the recorded mass spectra. In Figure 5.1 the ion population of DA-3 (1 mmol/l) and in Figure 5.2 the ion population of DA-8 (0.1 mmol/l) is depicted using ACN/H₂O as spray solvent. The initial ion population is given at 0%V modifier mixing ratio in each plot. The diamine-ACN clusters $[M(\text{ACN})_3\text{H}_2]^{2+}$ and $[M(\text{ACN})_4\text{H}_2]^{2+}$ as well as the protonated dimer ion $[(M)_2\text{H}]^+$ mainly constitute the initial ion population of DA-3. This ion distribution corresponds to $z_{\text{avg}} \approx 1.42$ (cf. Figure 5.5 at 0%V mixing ratio). The initial ion population of DA-8 is dominated by the cluster ions, $[M(\text{ACN})\text{H}_2]^{2+}$ and $[M(\text{ACN})_2\text{H}_2]^{2+}$, and the protonated molecule $[\text{MH}]^+$. This ion distribution results in $z_{\text{avg}} \approx 1.65$ (cf. Figure 5.5 at 0%V mixing ratio). In contrast, only the bare ions, $[\text{MH}]^+$, $[(M)_2\text{H}]^+$ and $[\text{MH}_2]^{2+}$, are observed when the diamines are sprayed from MeOH/H₂O. However, the ion population is dominated by the singly protonated species, $[\text{MH}]^+$ and $[(M)_2\text{H}]^+$, resulting in z_{avg} values of about 1. For example $z_{\text{avg}} = 1.0$ applies to DA-3 and $z_{\text{avg}} = 1.1$ applies to DA-9 (both sprayed from MeOH/H₂O). As a consequence, charge depletion processes can hardly be explored spraying the diamines from MeOH/H₂O. The observation of low z_{avg} values when the diamines are electrosprayed from MeOH/H₂O is in accordance with experimental results of Williams and Iavarone [14]. Spraying diamines from solutions of MeOH results in lower z_{avg} than from H₂O solutions, e.g., for DA-7 $z_{\text{avg}} = 1.14$ (MeOH) compared to $z_{\text{avg}} = 1.56$ (H₂O), which is in accord with the determined trend in charge depletion efficiency $\text{NH}_3 > \text{MeOH} > \text{H}_2\text{O}$ (cf. section 4.1). For the shorter chain length diamines DA-4 and DA-5, z_{avg} becomes 1.0 when sprayed from MeOH. Interestingly, the authors do not consider that gas phase proton transfer from doubly protonated diamines to MeOH is responsible for the lower charge state, because the simple comparison between GBs of different solvents does not fit the observed z_{avg} values [14]. This underlines again the potential as well as the relevance of the charge retention/charge depletion model based on solvent clusters (cf. section 4.4).

In addition to the solvent composition, the diamine *concentration* in solution has a strong influence on the relative intensities of the observed ion species and therefore on z_{avg} . Thus, experiments with 0.1 mmol/l and 1 mmol/l solutions of the diamines were conducted. When comparing the observed ion species, no difference is noted. The same bare as well as clustered ions are present in the mass spectra. However, a significant difference in the relative intensities is observed: the relative intensities of the bare, singly protonated ions $[\text{MH}]^+$ and $[(M)_2\text{H}]^+$ are significantly larger, when the more concentrated solutions (1 mmol/l) are sprayed. This leads to smaller values for z_{avg} compared to the less concentrated solutions (0.1 mmol/l).²

To recapitulate, the observed ion population determining z_{avg} depends on the sol-

²This effect on z_{avg} is observed for the diamines DA-3, DA-5, DA-8 and DA-9 (experiments with 0.1 mmol/l solutions of DA-2 were never performed). The observed average charge state is plotted versus the chain length k for both diamine concentrations in Figure 5.7 illustrating the large difference between the obtained z_{avg} values (compare black and grey trace).

5 Results and Discussion: Terminal Alkyldiamines

vent composition of the spray solution as well as the diamine concentration of the solution. Therefore, to study the impact of the gas phase modifiers ACN and MeOH, these solution phase characteristics are taken into account. In the following, the findings of the gas phase modification experiments are described.

Impact of Gas Phase Modification by ACN and MeOH

The observed ion populations of the examined diamines change significantly when ACN or MeOH are added as gas phase modifiers to the ion source. In accordance with the SP experiments (cf. section 4.1), ACN addition results in an increase of z_{avg} (charge retention) and MeOH addition leads to a decrease of z_{avg} (charge depletion). Charge retention with ACN is based on an increase in intensity of the diamine-ACN cluster species $[\text{M}(\text{ACN})_n\text{H}_2]^{2+}$ accompanied by an increasing average cluster size n_{avg} , i.e., the number of ACN molecules attached to the doubly protonated diamine increases with the ACN mixing ratio. Charge depletion with MeOH as modifier occurs due to suppression of the diamine-ACN clusters and promotion of the singly protonated species, $[\text{MH}]^+$ and $[(\text{M})_2\text{H}]^+$.

In Figure 5.1 the observed ion population of DA-3 (1 mmol/l in ACN/H₂O) is plotted versus the ACN and MeOH mixing ratio. The initial ion population of DA-3 is dominated by the protonated dimer ion, $[(\text{M})_2\text{H}]^+$, and the ACN clusters with $n = 2, 3, 4$. ACN addition leads to promotion of these cluster species and simultaneous suppression of the dimer at first, eventually the smaller clusters decrease in intensity in favor of the larger clusters with $n = 5, 6$. With approximately 5 %V ACN present in the ion source, the singly protonated dimer signal is completely suppressed and the clusters with $n = 3-6$ characterize the observed ion population in the mass spectrum. The observed ion population tends to reach its saturation limit at 6.2 %V.³ At this ACN mixing ratio, the mass spectrum is dominated by doubly protonated ACN clusters with $n = 3-6$, which show a characteristic cluster distribution: the clusters with $n = 3$ and $n = 6$ exhibit a significantly lower intensity than the clusters with $n = 4$ and $n = 5$, which represent the intensity maximum of the distribution. In contrast, MeOH addition results in suppression of the cluster species in favor of the $[(\text{M})_2\text{H}]^+$; at a mixing ratio of 0.3 %V MeOH the ACN clusters are not detected anymore. Above this mixing ratio, the intensity of $[(\text{M})_2\text{H}]^+$ (normalized to the TIC) decreases to approximately 0.1, indicating that most of the detected ion signal is not related to DA-3. Therefore, MeOH addition results in a mass spectrum, which is dominated by ions not related to the analyte species and, in addition, the only analyte ion present is singly protonated. The initial mass spectrum (without modifier addition) is also characterized by various background signals. It is concluded that the low ionization yield of DA-3 is a result of the initial experimental conditions, and can be improved significantly by the use of ACN as gas phase modifier as well as become even worse upon MeOH gas phase addition.

³It is pointed out that 6.2 %V does not represent the saturation level of ACN in N₂. Saturation of ACN at room temperature is reached at a mixing ratio of 11.5 %V.

5.1 Gas Phase Modification: Charge Depletion vs. Charge Retention

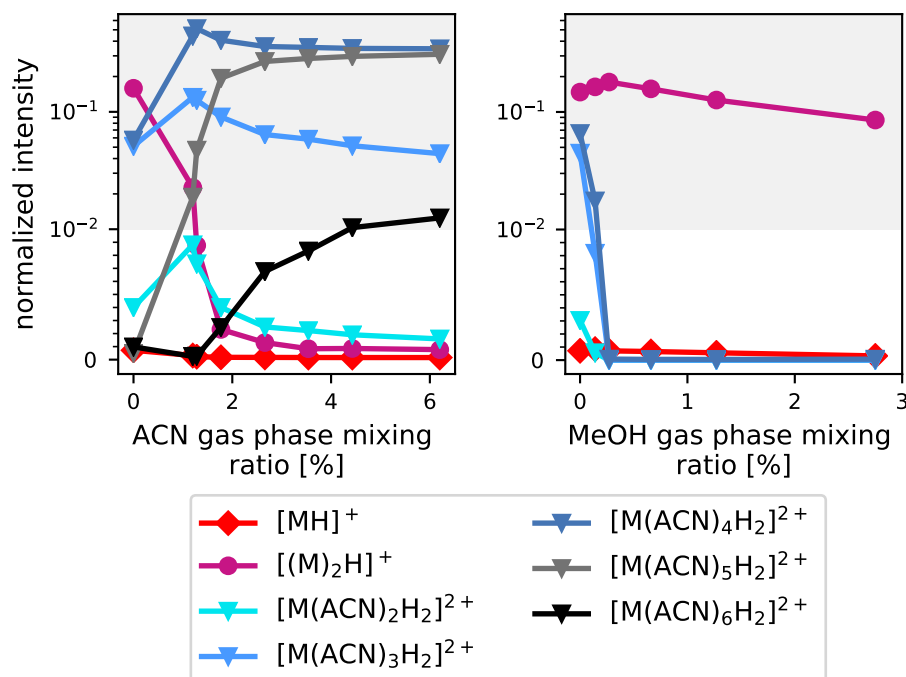


Figure 5.1: Intensities of observed 1,3-diaminopropane (DA-3) ion species in dependence of the ACN (*left*) and MeOH (*right*) gas phase mixing ratio. M represents DA-3 in the legend. Note that the ordinate is linear between 0 and 10^{-2} (white background) and logarithmic above (grey background). The intensities are normalized to the TIC. Mass spectra were recorded with the TOF-MS, method DA.

Figure 5.2 depicts the ion population of DA-8 (0.1 mmol/l in ACN/H₂O) in dependence of the mixing ratio of ACN and MeOH. Generally, the same effects as with DA-3 are observed. The cluster size increases from $n = 1,2$ to $n = 2,3,4$ with ACN addition, whereas the singly protonated species, $[MH]^+$ decreases in intensity. At approximately 5%V ACN mixing ratio, the clusters with $n = 3$ and $n = 4$ dominate. With increasing MeOH addition, the ACN clusters diminish accompanied by an promotion of $[MH]^+$. In contrast to the ion population of DA-3 depicted in Figure 5.1, $[MH]^+$ (instead of $[(M)_2H]^+$) represents the singly protonated species, which can be traced back to the different diamine concentration. Furthermore, a mixed solvent cluster, $[M(ACN)(MeOH)H_2]^{2+}$, is observed, when MeOH is added as modifier. ACN clusters, $[M(ACN)_nH_2]^{2+}$, are still observed, even when the MeOH mixing ratio exceeds 3%V. As a consequence, z_{avg} decreases less steeply with increasing MeOH mixing ratio as compared to DA-3 data. The z_{avg} values resulting from the ion populations depicted in Figures 5.1 and 5.2 are shown in Figure 5.5 and are further discussed below.

5 Results and Discussion: Terminal Alkyldiamines

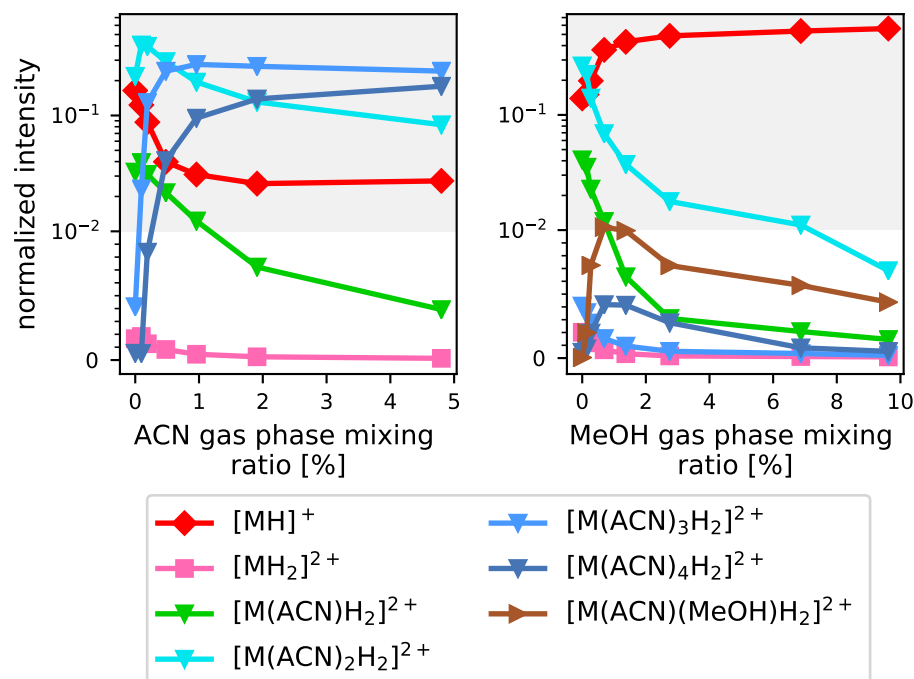


Figure 5.2: Intensities of observed 1,8-diaminooctane (DA-8) ion species in dependence of the ACN (*left*) and MeOH (*right*) gas phase mixing ratio. M represents DA-8 in the legend. Note that the ordinate is linear between 0 and 10^{-2} (white background) and logarithmic above (grey background). The intensities are normalized to the TIC. Mass spectra were recorded with the TOF-MS, method DA.

Influence of the Chemical Structure of the Diamines

The comparison between the modifier-dependent ion population of DA-3 and DA-8 indicates that the ionic species observed in the mass spectra depend on the structure of the diamine and its concentration. Independent of the concentration, some general trends in the observed ion population were discovered associated with the chemical structure of the diamines. Figure 5.3 shows the qualitative results for all observed ion species. The columns represent the analytes sorted by their chain length, i.e., the distance between the $-\text{NH}_2$ groups; the aromatic diamine (1,4-diaminobenzene, DA-B) is an exception. The matrix lines show the observed species for the individual analytes M. When an ion species was observed for a specific analyte, the associated matrix element is colored yellow; otherwise it is colored red. In case of DA-2, no experiments were conducted in which MeOH was used as solution component or added as modifier, therefore it was not possible to observe MeOH clusters. These ma-

5.1 Gas Phase Modification: Charge Depletion vs. Charge Retention

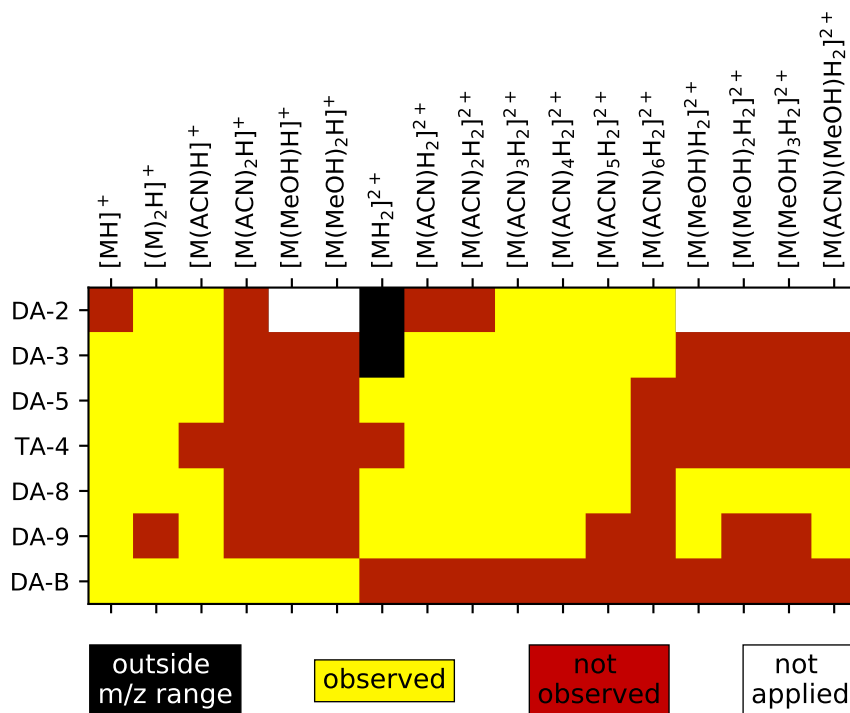


Figure 5.3: Overview of the observed ion species (TOF-MS) of the diaminic analytes depicted in a matrix representation. The species observed in the experiments are depicted in yellow, species not observed in red. When a species has an m/z ratio outside of the m/z range of the mass spectrometer, it is colored in black. Analysis of DA-2 was not combined using MeOH as solvent nor as modifier, DA-2-MeOH cluster species are thus colored in white.

matrix elements are colored white and labeled as not applied. Furthermore, some ions were not detected, because their m/z ratios were outside the m/z range of the TOF instrument. This applies for the doubly protonated ion, $[MH_2]^{2+}$, of DA-2 (m/z 31.0) and DA-3 (m/z 38.0). The lower limit of the mass range is m/z 30, as declared by the manufacturer.

However, ions exhibiting m/z ratios close to this limit are strongly mass discriminated and the detection probability is negligible even when the ion transfer parameters are optimized for small m/z ratios.⁴ The scan range was set to m/z 30–800 in

⁴IUPAC defines mass discrimination as follows [140]: “Differences in overall detection sensitivities for ions of different m/z values in a mass spectrum, caused by variations in ionization efficiency, transmission efficiency through the interface between the ion source and the analyzer vacuum system, analyzer, and detector response.” Here, mass discrimination caused by variations in transmission

5 Results and Discussion: Terminal Alkyldiamines

all diamine experiments and the ion transfer voltages were optimized for low mass ions (cf. method DA in Table 3.2) resulting in mass spectra showing most ion signal intensity between m/z 100 and m/z 300. The signal of the doubly protonated ion $[\text{MH}_2]^{2+}$ of DA-5 at m/z 52.1 represents the species with the lowest m/z associated with a detectable low mass analyte. Protonated ACN at m/z 42.0 was rarely observed. In contrast, the DA-2 ions $[\text{M}(\text{ACN})_n\text{H}_2]^{2+}$ with $n = 1, 2$ (m/z 51.5, 72.0) and MH^+ (m/z 61.0) as well as the TA-4 ion $[\text{MH}_2]^{2+}$ with m/z 52.5 were not discernible in the mass spectra. Consequently, ions were observed between m/z 42 and 75 but it is assumed that their intensity is severely mass discriminated. Therefore, if an ion species with an m/z ratio below 75 is not observed, e.g. the DA-2 ions $[\text{M}(\text{ACN})_n\text{H}_2]^{2+}$ with $n = 0, 1, 2$ (m/z 51.5, 72.0), it is unclear whether this species is not present or it is not visible due to mass discrimination. Furthermore, it is conceivable that the DA-2 ions $[\text{M}(\text{ACN})_n\text{H}_2]^{2+}$ with $n = 0, 1, 2$, and the DA-3 ion $[\text{M}(\text{ACN})_n\text{H}_2]^{2+}$ with $n = 0$ undergo efficient proton loss, leading to the formation of the singly protonated species, because $\text{GB}(\text{MH}^+)$ of DA-2 and DA-3 is too low. In accordance with the results presented in this work, also Kebarle and co-workers did not detect the doubly protonated species $[\text{MH}_2]^{2+}$ (or other doubly protonated species) of terminal alkyldiamines with $k < 4$ when electrospraying from MeOH and analyzing with a triple quadrupole mass spectrometer. The authors comment this finding as follows: "With electrospray, multiply protonated ions which are known to be present in the solution may not be observed in the gas phase when the sites of protonation are quite close to each other. The proton loss occurs in the transition from solution to gas phase as the ion is desolvated." [84] Williams and Iavarone noticed for diamines with $k = 4, 5, 7, 8, 10, 12$ electrosprayed from H_2O that "[...] a dramatic drop in dication abundance occurs for diamines with N–N distances below that of 1,7-diaminoalkane [...]" [14]. These findings suggests that the use of ACN/ H_2O as solvent for the ESI solution - instead of pure H_2O or MeOH - is crucial for the detection of doubly protonated diamine ions with adjacent charge sites, e.g. DA-2 and DA-3, due to the formation of stable clusters of the form $[\text{M}(\text{ACN})_n\text{H}_2]^{2+}$. The proton loss - reported by Kebarle - is inhibited by ACN; doubly protonated DA-2 and DA-3 ions present in solution are transferred to the gas phase and to the analyzer, while their charge state is retained in the cluster. Application of ACN as gas phase modifier even enhances the diamine-ACN cluster formation and therefore z_{avg} . In contrast, pronounced proton loss occurs when DA-2 and DA-3 are sprayed from pure H_2O or MeOH. Doubly protonated ions present in the solution are efficiently deprotonated in the transition from solution to the gas phase and/or in the gas phase, most probably via proton transfer reactions to polar solvent clusters S_n (according to reactions (R 2.9), (R 2.10) and (R 2.11)).

The doubly protonated diamine-ACN clusters, $[\text{M}(\text{ACN})_n\text{H}_2]^{2+}$, with the exception of the aromatic diamine DA-B, were observed for all diaminic analytes. The occurrence of these clusters in the mass spectra, focusing on the observed cluster number n , is described in detail in the paragraph "Average Cluster Number of $[\text{M}(\text{ACN})_n\text{H}_2]^{2+}$ "

and detection efficiency is meant.

5.1 Gas Phase Modification: Charge Depletion vs. Charge Retention

(below). Figure 5.3 highlights that MeOH clusters with the doubly protonated ions are only observed for the higher alkyldiamines (DA-8 and DA-9). These clusters were detected when MeOH was used as gas phase modifier, as shown for the first MeOH cluster of DA-8 in Figure 5.2, and showed low abundance in the mass spectra. However, observation of $[M(\text{MeOH})_n\text{H}_2]^{2+}$ indicates that these clusters exhibit a certain stability and do not quantitatively undergo proton transfer reactions to yield $[(\text{MeOH})_n\text{H}]^+$. The occurrence of MeOH clusters only for higher alkyldiamines is explained by lower Coulomb repulsions and thus higher $\text{GB}(\text{MH}^+)$, as compared to the diamines with shorter chain lengths. According to the charge retention/charge depletion model, larger MeOH clusters need to be present to facilitate proton transfer from the doubly protonated diamine to the MeOH cluster leading to formation of $[(\text{MeOH})_n\text{H}]^+$. The fact that $[M(\text{MeOH})_n\text{H}_2]^{2+}$ with $n = 1-3$ was observed for DA-8 and only the first cluster ($n = 1$) for DA-9 may be due to differences in the total signal intensity resulting in different sensitivities. Since the abundance of $[M(\text{MeOH})_n\text{H}_2]^{2+}$ ions are low in the mass spectra and decreases with the cluster size n , it is assumed that in the experiments the DA-9 ions $[M(\text{MeOH})_2\text{H}_2]^{2+}$ and $[M(\text{MeOH})_3\text{H}_2]^{2+}$ were below the detection limit.

Only singly protonated ions were observed for DA-B, as illustrated in Figure 5.3. The GB of neutral DA-B was determined experimentally (874.0 kJ/mol [122]) and computationally (884.5 kJ/mol [197]) and is assumed to be comparable to the other diaminic analytes. However, due to $\text{p}K_{\text{a}1} = 6.1$ and $\text{p}K_{\text{a}2} = 2.4$ [198], the chemical equilibrium is dominated by the neutral and the singly protonated species of DA-B in a neutral solution ($\text{pH} \approx 7$). In comparison to DA-5 exhibiting $\text{p}K_{\text{a}1} = 10.25$ and $\text{p}K_{\text{a}2} = 9.13$ [199], DA-B and particularly protonated DA-B are rather weak bases. As a consequence, no doubly protonated species were observed. It is noted that the clusters $[M(\text{S})_n\text{H}]^+$ with $n = 1, 2$ and $\text{S} = \text{ACN}$ as well as $\text{S} = \text{MeOH}$ are recorded with high abundance in the mass spectra when ACN or MeOH are applied as gas phase modifiers. At high modifier mixing ratios the signal intensity of the cluster species, even of the second cluster, exceeds the signal intensity of the bare ions $[\text{MH}]^+$ and $[(\text{M})_2\text{H}]^+$. In comparison to the other diaminic analytes, which only show the first cluster $[M(\text{ACN})\text{H}]^+$, intense clustering was observed for the singly protonated DA-B. Intense clustering with singly protonated species was also observed in experiments when spraying amines, e.g. *n*-hexylamine or *n*-butylamine [183]. Regarding the terminal alkyldiamines, the low abundance of the singly protonated cluster, $[M(\text{ACN})\text{H}]^+$, and the absence of higher singly protonated clusters is attributed to the missing substituent effect in singly protonated ions leading to lower solvation energies as compared to doubly protonated species. In addition, intramolecular interactions strongly influence the exergonicity of an external solvation reaction (see section 2.2.1 for the substituent effect as well as for internal solvation). In singly protonated terminal alkyldiamines the charge site ($-\text{NH}_3^+$) interacts with the non-protonated $-\text{NH}_2$ group, leading to formation of an H-bond and cyclization (proton-induced cyclization) [105, 106, 110]. Since the alkyl chain is flexible, internal solvation is possible for the terminal diamines. In contrast, in 1,4-diaminobenzene (DA-B)

5 Results and Discussion: Terminal Alkyldiamines

both amine groups are bound to opposite carbon atoms of the benzene ring, internal solvation is therefore impossible. Internal solvation does also not occur in the primary amines, e.g. *n*-hexylamine or *n*-butylamine, due to the lack of electronegative atoms or groups interacting with the protonation site. It is concluded that intense clustering is observed when external solvation is not hindered by internal solvation, in accordance with the SP experiments (cf. section 4). Since only singly protonated ions were detected, DA-B was not used in further charge retention/charge depletion studies.

Average Cluster Number of $[M(ACN)_nH_2]^{2+}$

Upon comparing the observed ion species of the different diaminic analytes a trend emerges for the doubly protonated diamine-ACN clusters: the observed cluster sizes n of $[M(ACN)_nH_2]^{2+}$ decrease with increasing chain length. Taking the intensity of each cluster species (of a specific cluster system, e.g. $[M(ACN)_nH_2]^{2+}$) into account, an average cluster number n_{avg} is determined for a cluster distribution observed in a mass spectrum. The average cluster number is calculated as follows

$$n_{avg} = \frac{\sum_i^N n_i \cdot I_i}{\sum_i^N I_i} \quad (5.1)$$

where N is the total number of observed cluster species, n_i the cluster number, and I_i the intensity of the i th cluster. The observed n_{avg} depends on the analyte and its chain length, and on the ACN mixing ratio present in the ion source.

Figure 5.4 shows the dependence of n_{avg} on the chain length (left plot) and on the ACN mixing ratio for each diamine (right plot). The influence of the chain length on the observed cluster number was studied with varying ACN gas phase mixing ratios. As expected, the average cluster number increases with an increase in the ACN mixing ratio for all diamines. With increasing chain length, n_{avg} decreases significantly from 4.5 (DA-2) to 1.7 (DA-9) when no modifier is added and from 4.9 (DA-2) to 2.8 (DA-8) when 1.9 %V ACN is present. The correlation between n_{avg} and the chain length is not described by a linear function but rather an inversely proportional function. As already mentioned, the dependence of n_{avg} on the chain length is caused by the substituent effect, which also leads to decreasing solvation energies with increasing chain length. Kebarle and co-workers measured the sequential solvation energy ($\Delta G_{n,n+1}^\circ$, $n = 2-5$) for the hydration of diaminic gas-phase ions, $NH_2(CH_2)_kNH_2$, with $k = 7, 8, 10, 12$ [82] and the change in energy for the monohydration of the diaminic ions with $k = 5-10, 12$ [84]. Plotting the solvation energy ($-\Delta G_{n,n+1}^\circ$ or $-\Delta H_{n,n+1}^\circ$) for a specific n against the chain length k results in similar curve shapes as plotting n_{avg} versus the chain length (compare the left plot of Figure 5.4 with Figure 2.5 in section 2.2.1). The decrease of the hydration exothermicity ($-\Delta H_{0,1}^\circ$) with increasing separation of the two charged centers is rationalized by Coulomb repulsion exerted from one charge site on the other (substituent effect) [84]. Coulomb repulsion increases the partial positive charge of the $-NH_3$ substituents

5.1 Gas Phase Modification: Charge Depletion vs. Charge Retention

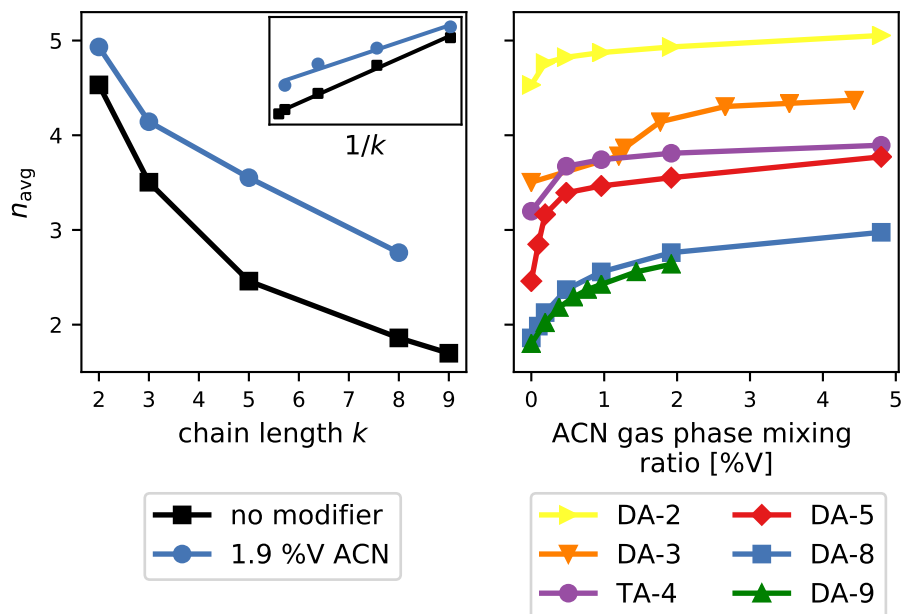


Figure 5.4: Average cluster number n_{avg} of $[\text{M}(\text{ACN})_n\text{H}_2]^{2+}$ in dependence of the chain length k (and the reciprocal chain length $1/k$) of the diamines (*left*) and of the ACN gas phase mixing ratio present in the nanoESI source (*right*). *Left:* n_{avg} is inversely proportional to k and linear to $1/k$, respectively. *Right:* n_{avg} increases with rising ACN mixing ratio. In all experiments ESI solutions of ACN/ H_2O contains 1 mmol/l of the respective diamine (except in the experiment using DA-9 (0.1 mmol/l) in combination with ACN addition, green trace in the right plot). Mass spectra were recorded with the TOF-MS, method DA.

leading to enhanced hydrogen bonding with water [84]. The change of the hydration enthalpy with the chain length k is therefore driven by changes of Coulomb repulsion or more precisely by changes of the Coulomb energy ((III) in eq. (5.4)). According to Coulomb's law, the force of repulsion between two point charges is directly proportional to the product of the magnitudes of charges and inversely proportional to the square of the distance between them.

$$|F| = k_e \frac{|q_1 q_2|}{r^2} \quad (5.2)$$

Here, k_e is the Coulomb's constant, q_1 and q_2 are the signed magnitudes of the charges, and the scalar r is the distance between the charges [200, 201]. The potential energy that results from Coulomb repulsion or Coulomb attraction, respectively, is termed the electric potential energy or Coulomb energy. The electric po-

5 Results and Discussion: Terminal Alkyldiamines

tential energy, U_E , of the point charge q_1 at position r in the presence of a second point charge q_2 , taking an infinite separation between the charges as the reference position, is [202]:

$$U_E = k_e \frac{|q_1 q_2|}{r} \quad (5.3)$$

Equation (5.3) represents a linear relationship between the Coulomb energy U_E and the reciprocal distance r between the point charges ((I) in eq. (5.4)). Since the doubly protonated diamines have a fully elongated structure, which was demonstrated by molecular modeling [109, 130], a linear relationship between the chain length k , i.e., the number of carbon atoms in the alkyl chain, and the distance r between the charge sites was found ((II) in eq. (5.4)) [130]. To summarize, the following relations are presumed:

$$(I) \ U_E \propto 1/r \quad (II) \ k \propto r \quad (III) \ -\Delta\Delta H_{n,n+1}^\circ(k) \propto \Delta U_E(r) \quad (5.4)$$

Therefore, a linear relationship between the solvation enthalpy and the reciprocal chain length k is expected:

$$(IV) \ \Delta H_{n,n+1}^\circ \propto 1/k \quad (5.5)$$

Relation (IV) was verified for the monohydration ($\Delta H_{0,1}^\circ$) of the diamines with $k = 5-10, 12$ [84]. The sequential solvation energies determine the observed average cluster number n_{avg} of the doubly protonated diamine-solvent clusters at a specific solvent mixing ratio. As a consequence, n_{avg} is assumed to show the same dependence on the chain length as the solvation energy. This assumption is supported by the experimentally determined n_{avg} regarding the external solvation of the diamines ($k = 2, 3, 5, 8, 9$) by ACN: n_{avg} is inversely proportional to the chain length (cf. left plot in Figure 5.4), in other words, a linear relationship is found between n_{avg} and the reciprocal chain length $1/k$ (cf. linear fit inset in the left plot of Figure 5.4). The correlation coefficients $R^2 = 0.996$ (no modifier), $R^2 = 0.968$ (1.9 %V ACN), and $R^2 = 0.957$ (4.8 %V ACN, not shown in Figure 5.4) suggest that the strength of the correlation is higher when no ACN is added as modifier. However, the presented data clearly show a correlation between n_{avg} and $1/k$. Due to the relatively low number of data points (five data points for the black trace (no modifier) and four for the blue trace (1.9 %V ACN)) as well as the experimental error in the n_{avg} values, the conclusion that a linear relationship exists between n_{avg} and $1/k$ may need further examination.

Clearly, n_{avg} decreases with increasing chain length, which is due to the substituent effect in accordance with the dependence of $\Delta G_{n,n+1}^\circ / \Delta H_{n,n+1}^\circ$ on the Coulomb energy. Furthermore, n_{avg} increases with increasing ACN gas phase mixing ratio, which is observed for all diamines (cf. right plot of Figure 5.4). The steep increase of n_{avg} is observed at low ACN mixing ratios ($\approx 0-1$ %V),⁵ saturating above 2 %V ACN.

⁵The DA-3 measurement (orange trace in Figure 5.4) represents an exception which can be traced back to experimental errors, e.g., a leakage in the gas line or a gas flow error leading to an erroneous determination of the ACN mixing ratio.

5.1 Gas Phase Modification: Charge Depletion vs. Charge Retention

This curve shape is rationalized as follows: With increasing ACN mixing ratio the rates of cluster formation (solvation) reactions increase, larger clusters are formed, and the final cluster distribution is shifted towards higher mean sizes. Since the gain in binding energy of the individual cluster steps decreases with n , further cluster growth resembles condensation at a specific cluster size depending on the analyte ion. This trend has been observed in most solvation sequences: $\Delta H_{n,n+1}^{\circ}$ decreases until it reaches the limiting value $\Delta H_{\text{condens}}^{\circ}$, which is often reached after four to six solvation steps (referring to a singly protonated ion) [94]. A representative example is the enthalpy sequence for $[(\text{H}_2\text{O})_n\text{H}]^+$, which was determined by several authors with equilibrium measurements [103, 203–205]. Since water forms hydrogen bond networks, extensively hydrated ions are produced by electrospray, which show solution-phase characteristics. Williams and co-workers [89] observed hydrated clusters of doubly protonated DA-7 with up to 24 H_2O molecules upon spraying from an aqueous solution. They reported that “for hydrated clusters with more than four water molecules per charge, hydrogen bonding [between the individual water molecules] play a dominant role.” [89] Due to the inability of ACN to form hydrogen bond networks, it is concluded that the maximum and consequently the mean cluster size of the doubly protonated diamine-ACN clusters rapidly approach a certain cluster size at high ACN mixing ratios, depending on the charge state and chemical structure of the core ion. Bollan and co-workers [206] reported that the maximum number of polar, aprotic ketone molecules binding to protonated hydrazine and ammonia ions, respectively, depends on the number of hydrogen atoms on the protonated nitrogen of the analyte, e.g., four in case of ammonia (NH_4^+). These results agree with the maximum observed number of six ACN molecules bound to a doubly protonated diamine, which has six protic hydrogen atoms (cf. Figure 5.3).

The detected ion distribution and therefore n_{avg} does not represent the equilibrated ion distribution in the ionization source, due to processes occurring during ion transfer, e.g., solvent loss, proton loss or fragmentation. It must be assumed that the detected n_{avg} of the cluster system $[\text{M}(\text{ACN})_n\text{H}_2]^{2+}$ is smaller than the average cluster size of the cluster distribution present in the ion source (at a defined ACN mixing ratio) because the probability for solvent loss (declustering) is appreciably higher as compared to solvation (clustering) in the low pressure region of the mass spectrometer. Furthermore, solvent loss is favored for higher clusters, because charge dispersion as well as repulsion among the solvent molecules increases with increasing cluster size, leading to weaker ion-solvent interactions. Therefore, the cluster distribution is shifted towards a lower mean size during ion transfer from the ion source to the analyzer. Although the ion acceleration in the transfer region was minimized in the present experiments, while maintaining sufficiently high ion focusing and transfer, declustering as consequence of energetic collisions can not be excluded. Suppression of larger clusters due to mass discrimination can be ruled out since ions with higher m/z values than the largest observed diamine clusters, $[\text{M}(\text{ACN})_{n_{\text{max}}}\text{H}_2]^{2+}$, were clearly detected.

5 Results and Discussion: Terminal Alkyldiamines

In summary and conclusion, the solvent composition of the ESI solution has a strong influence on the observed ion population and average charge state. Spraying from ACN/H₂O results in abundant formation of the doubly protonated diamine-ACN clusters, $[M(\text{ACN})_n\text{H}_2]^{2+}$, whereas mainly singly protonated ions are detected when the diamines are sprayed from MeOH/H₂O. These findings suggest that charge depletion processes are induced by protic solvents (MeOH and H₂O), which are initially present in the solution phase and droplets. In turn, the higher charge state (2+) is effectively retained when ACN is present in the solution phase. Assuming that all diamines ions are doubly protonated in solution - irrespective of the dilution in ACN/H₂O or MeOH/H₂O - deprotonation occurs upon transition from the solution to the gas phase and/or by proton transfer in the gas phase. According to the ion evaporation model (cf. section 2.1.3), ions are initially released as ion-solvent clusters into the gas phase. The solvent composition in solution thus determines the chemical structure of the ion-solvent cluster, which in turn defines if and under which circumstances proton transfer to the solvent cluster is feasible. In the case of SP, no dependence of the ion population on the ESI solution was observed. This was rationalized by the charged residue model (see section 2.1.3) assuming that the final droplets consist of water, regardless of spraying from ACN/H₂O or MeOH/H₂O solutions (see section 4.4). Since SP represents a high-molecular weight molecule as compared to the diamines used, it is conceivable that the release of SP ions from ESI droplets is described by the CRM, whereas ion formation of the diamines follows the IEM route.

The observed impact of the addition of the gas phase modifiers ACN and MeOH on the diaminic ion population is in accord with the charge retention/charge depletion mechanism, which was formulated on the basis of the SP experiments. Addition of MeOH vapor promotes the intensity of the singly protonated ions; the doubly protonated ions including the diamine-ACN clusters are depleted. In contrast, the presence of ACN vapor in the ion source results in retention of the higher charge state of the diamines in the course of ion release, transfer and analysis. The singly protonated species, $[\text{MH}]^+$ and $[(\text{M})_2\text{H}]^+$, are suppressed in favor of the clusters $[M(\text{ACN})_n\text{H}_2]^{2+}$, which show characteristic cluster distributions dominating the mass spectra at high ACN mixing ratios. An inverse correlation between the average cluster number n_{avg} and the chain length of the alkyldiamines was observed. With increasing distance between the charge sites, the Coulomb repulsion and thus the solvation energy decreases. As a consequence, n_{avg} decreases with the chain length of the diamines. Comparison with gas phase ion-solvent studies involving diaminic ions produced by electrospray showed that cluster formation with ACN facilitates detection of doubly protonated ions of short chain diamines, e.g. DA-2 and DA-3. Furthermore, poor solvation of the singly protonated alkyldiamines was traced back to cyclization leading to internal solvation, which is competing with external solvation. These results can be extrapolated to proteins, which show in general multiple potential charge sites and gas-phase structures. Therefore, the occurrence and characteristics of protein-solvent clusters allows conclusions to be drawn concerning the distance between

5.1 Gas Phase Modification: Charge Depletion vs. Charge Retention

charge sites, intramolecular interactions leading to internal solvation, and the gas-phase basicity of the individual charge sites.

The formation and stability of the clusters $[M(\text{ACN})_n\text{H}_2]^{2+}$ was further studied by implementing chemical modification of the collision gas present inside the ion trap - called collision gas modification - in combination with MS/MS experiments. The results are described and discussed in section 5.2. Furthermore, the solvation by ACN was explored for DA-2 using computational methods; the results are presented in section 5.3.

5.1.2 Average Charge State

Figure 5.5 depicts the dependence of the average charge state z_{avg} on the ACN and MeOH mixing ratio for DA-3 (1 mmol/l) and DA-8 (0.1 mmol/l).⁶ ACN addition results in a strong increase of the observed charge state: z_{avg} increases with rising ACN mixing ratio up to 1.99 for DA-3 and up to 1.94 for DA-8. When MeOH is used as gas phase modifier, z_{avg} is lowered to 1; complete suppression of the higher charge state is reached at 0.3 %V MeOH for DA-3 and at 9.6 %V MeOH for DA-8. In each of the four experiments, a sufficient amount of modifier was added to reach the saturation limit, i.e., z_{avg} becomes independent on the gas phase mixing ratio. To emphasize that Figure 5.5 does not show selected, non-representative cases but rather general trends, all results obtained with the TOF-MS for diamines (except DA-2) in combination with the gas phase modifiers ACN and MeOH are summarized in Figure 5.6. In each experiment, charge retention is observed with ACN and charge depletion with MeOH.⁷ In accordance with the SP experiments, MeOH addition results in decrease of z_{avg} approaching the minimum observed value (+1 in case of diamines and +2 in case of SP) at high MeOH mixing ratios. ACN addition results in the increase of z_{avg} approaching the maximum observed value (+2 in case of diamines and +3 in case of SP). Further analysis of the diamine experiments in Figure 5.6 - in particular the ACN experiments - clearly show that the absolute values and the relative changes of z_{avg} not only vary between the different diamines (comparing the different colors in each plot of Figure 5.6) but also with the experimental conditions (comparing the different measurement series of the same color). As mentioned above, the solvent composition and the diamine concentration affect z_{avg} at 0 %V modifier mixing ratio. How z_{avg} and its dependence on the modifier mixing ratio is affected by the diamine chain length k is discussed in the following.

⁶The corresponding ion populations in dependence on the ACN and MeOH mixing ratio are given in Figure 5.1 and Figure 5.2.

⁷The experiments performed with the QIT-MS also clearly demonstrate that ACN addition results in charge retention accompanied by the formation of clusters of the form $[M(\text{ACN})_n\text{H}_2]^{2+}$ and MeOH addition leads to charge depletion.

5 Results and Discussion: Terminal Alkyldiamines

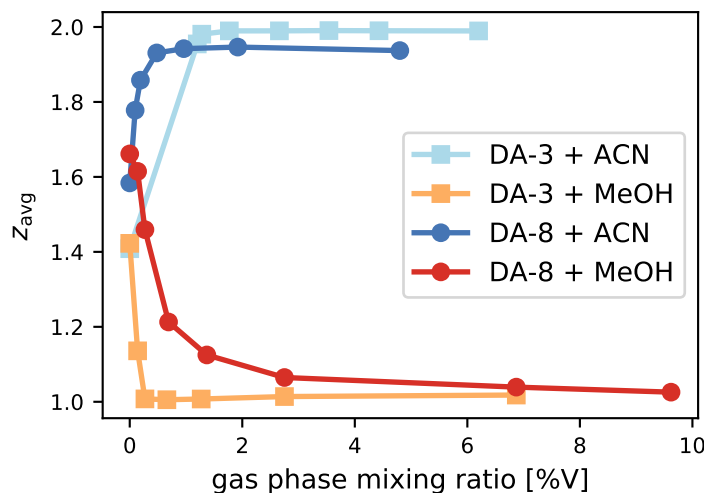


Figure 5.5: Average charge state z_{avg} of 1,3-diaminopropane (DA-3, 1 mmol/l) and 1,8-diaminooctane (DA-8, 0.1 mmol/l) ions in dependence of the acetonitrile (ACN) and methanol (MeOH) gas phase mixing ratio. The corresponding ion signal intensities in dependence of the gas phase modifier mixing ratio are given in Figure 5.1 for DA-3 and in Figure 5.2 for DA-8. Mass spectra were recorded with the TOF-MS, method DA.

Impact of the Alkyl Chain Length in Terminal Alkyldiamines

The dependence of z_{avg} on the chain length is depicted in Figure 5.7 for different experimental conditions. The influence of the diamine concentration on z_{avg} is discussed above and is quantifiable upon comparing the black and grey trace in Figure 5.7. Higher ion signal intensities were generated by spraying 1 mmol/l diamine solutions and, therefore, gas phase modification studies were performed spraying from 1 mmol/l dilutions. Comparing the black and the blue trace in Figure 5.7, the effect of applying ACN as gas phase modifier (1 %V) is noticed. The observed z_{avg} is increased almost to the maximum value for the smaller/shorter diamines (DA-2, DA-3 and DA-5: $z_{\text{avg}} \approx 1.95$), whereas for DA-8 an average charge state of 1.67 is observed. The contrary effect is discovered when MeOH (1.4 %V) is used as gas phase modifier: z_{avg} of the smaller diamines (DA-3 and DA-5) is lowered to the minimum value of 1 and the higher diamines (DA-8 and DA-9) show a z_{avg} of 1.06 and 1.34, respectively, approximating the z_{avg} values recorded without gas phase modification (black trace in Figure 5.7). Consequently, the observed z_{avg} of the higher diamines (applying 1 mmol/l dilutions) is less affected by gas phase modifiers, i.e., the longer the alkyl chain between the protonated sites, the less efficient charge depletion/charge retention processes become. In other words, the shorter the distance between the charge

5.1 Gas Phase Modification: Charge Depletion vs. Charge Retention

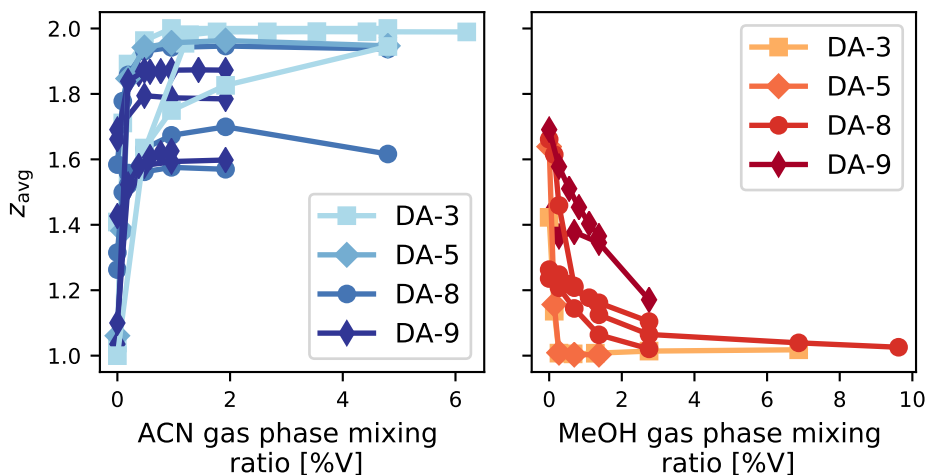


Figure 5.6: Average charge state z_{avg} of 1,3-diaminopropane (DA-3), 1,5-diaminopentane (DA-5), 1,8-diaminooctane (DA-8) and 1,9-diaminononane (DA-9) in dependence of the ACN gas phase mixing ratio (*left*) and of the MeOH gas phase mixing ratio (*right*). In each experiment *charge retention* is observed with ACN and *charge depletion* with MeOH. Mass spectra were recorded with the TOF-MS, method DA.

sites (assuming an elongated structure), the more the average charge state is affected by the presence of gas phase modifiers. Regarding charge depletion, this observation is in accord with determinations of $\text{GB}/\text{GB}^{\text{app}}(\text{MH}^+)$ of diamines with $k = 2, 7-10, 12$ and the derived dependence on the chain length [109, 129, 130]: with increasing chain length the singly protonated ions, $[\text{MH}]^+$, exhibit greater $\text{GB}/\text{GB}^{\text{app}}$ values impeding charge depletion via proton transfer from $[\text{MH}_2]^{2+}$ to bases. Consequently, in terms of the charge depletion/retention mechanism (cf. Figure 4.8), larger MeOH clusters (with higher GB values) are required to act as bases in a proton transfer reaction. Additionally, the stability of large MeOH clusters bound to doubly protonated diamines decreases as the chain length increases, since the solvation energy decreases with increasing chain length (due to reduction of Coulomb repulsion, see section 2.2.1). In addition to the results obtained by spraying 1 mmol/l diamine solutions, a few experiments were performed using 0.1 mmol/l dilutions. Experiments with 0.1 mmol/l solutions of DA-5, DA-8, and DA-9 in combination with MeOH modifier addition (1.4 %V) yield $z_{\text{avg}} = 1.0$ for DA-5, $z_{\text{avg}} = 1.12$ for DA-8, and $z_{\text{avg}} = 1.2$ for DA-9. Therefore, the statement “the longer the alkyl chain between the protonated sites, the less efficient charge depletion processes become” regarding the 1 mmol/l solutions also holds true for the less concentrated diamine solutions. In contrast, the observation of less efficient charge retention with increasing charge separation is not confirmed,

5 Results and Discussion: Terminal Alkyldiamines

due to the lack of data. Only for DA-8 ($z_{\text{avg}} = 1.94$) and DA-9 ($z_{\text{avg}} = 1.87$) data are available regarding 0.1 mmol/l dilutions, which do support the observed trend which is, however, determined by one data point (DA-8, 1 mmol/l, cf. blue trace in Figure 5.7). Nevertheless, the same argument is applied: using ACN as modifier, the extent of clustering/solvation declines with increasing chain length, therefore retention of the second charge becomes less effective.

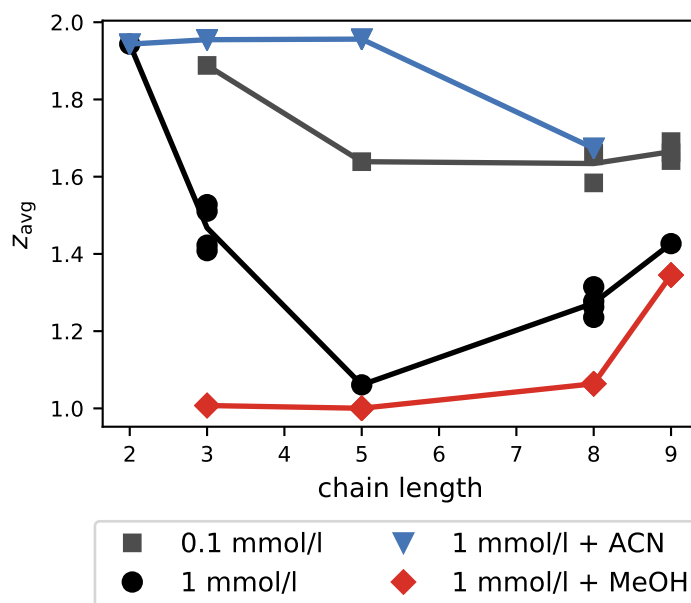


Figure 5.7: Average charge state z_{avg} of diamine ions in dependence of the chain length when no modifier (0.1 mmol/l and 1 mmol/l), ACN as modifier (1 mmol/l + 1 %V ACN), and MeOH as modifier (1 mmol/l + 1.4 %V MeOH) is applied. Mass spectra were recorded with the TOF-MS, method DA.

Without modifier present, a trend is noticeable, which is much more pronounced for 1 mmol/l than for 0.1 mmol/l diamine solutions (cf. black and grey traces in Figure 5.7): initially z_{avg} decreases with the chain length and then increases above a chain length of five C-atoms. This unexpected dependence can be associated with a varying abundance of the protonated dimer, $[(M)_2H]^+$, as illustrated in Figure 5.8 for 1 mmol/l solutions. The average charge state z_{avg} is determined as the ratio of the intensity of all singly protonated species M^+ (i.e. $[MH]^+$, $[(M)_2H]^+$ and $[M(\text{ACN})H]^+$) and the doubly protonated species M^{2+} (i.e. $[MH_2]^{2+}$ and $[M(\text{ACN})_nH_2]^{2+}$). Considering a relative intensity of the singly protonated species, $I_{\text{rel}}(M^+)$, of 0.2, z_{avg} thus amounts to 1.8. Consequently, $1 - I_{\text{rel}}(M^+) = 0.8$ corresponds to $z_{\text{avg}} = 1.8$. In Figure 5.8, $1 - I_{\text{rel}}([(M)_2H]^+)$ is plotted against the chain length demonstrating that the decrease of z_{avg} between 2 and 5 is solely determined by the increase in the abundance

5.1 Gas Phase Modification: Charge Depletion vs. Charge Retention

of the dimer ion $[(M)_2H]^+$ (cf. shape of black and pink trace), i.e. the abundance of the dimer ion determines the intensity of the singly protonated species, because almost no other singly protonated ions were observed for DA-2, DA-3 and DA-5. In contrast, the discrepancy between the pink and black trace for $k = 8, 9$ corresponds to the relative amount of other singly protonated species (mostly $[MH]^+$). The dimer ion of the higher diamines DA-8 and DA-9 was hardly detected but the bare singly protonated ion, $[MH]^+$, shows relatively high abundance (1 mmol/l, no modifier addition) leading to $z_{\text{avg}} = 1.28$ for DA-8 and $z_{\text{avg}} = 1.44$ for DA-9. Thus, an increase in z_{avg} is observed between $k = 8$ and $k = 9$.

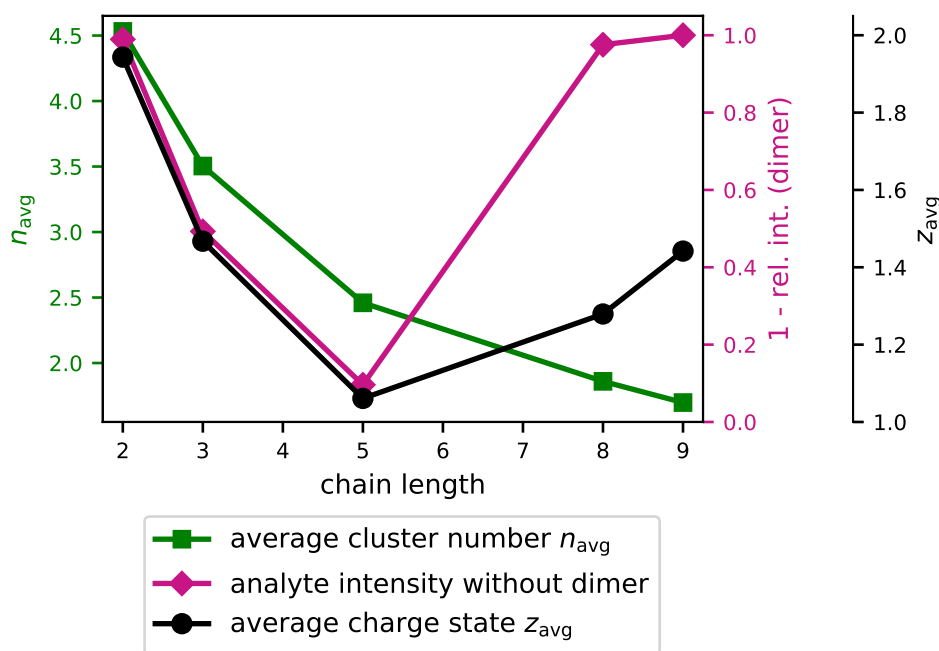


Figure 5.8: Average charge state z_{avg} (black trace and scale), average cluster number n_{avg} of $[M(\text{ACN})_n\text{H}_2]^{2+}$ (green trace and scale) and relative diamine ion intensity without the dimer $[(M)_2H]^+$ (pink trace and scale) in dependence of the chain length. Diamines were electrosprayed from solutions of ACN/ H_2O (1 mmol/l). Mass spectra were recorded with the TOF-MS, method DA.

Iavarone and Williams also studied the average charge state of the diamines with $k = 4, 5, 7, 8, 10, 12$ in dependence of the chain length k using a quadrupole mass spectrometer equipped with a home-built nanoESI source [14]. The diamines were electrosprayed from solutions of H_2O and MeOH (0.1 mmol/l) yielding both $[MH]^+$ and $[MH_2]^{2+}$; clusters with H_2O or MeOH were not observed. Consequently, the observed

5 Results and Discussion: Terminal Alkyldiamines

z_{avg} was determined as the ratio of the $[\text{MH}]^+$ and $[\text{MH}_2]^{2+}$ signal intensities. Plotting z_{avg} against k reveals a positive correlation: z_{avg} increases from 1.0 ($k = 4$) to ≈ 1.74 ($k = 12$) with H_2O and from 1.0 ($k = 4$) to ≈ 1.24 ($k = 12$) with MeOH [14]. Therefore, the dependence of z_{avg} on k (grey and black trace in Figure 5.7) does not agree with the experimental results obtained by Iavarone and Williams. However, when the diamines (1 mmol/l) were electrosprayed from MeOH/ H_2O instead of ACN/ H_2O , no clusters were detected resulting in low z_{avg} values: $z_{\text{avg}} = 1.0$ for DA-3, $z_{\text{avg}} = 1.0$ for DA-5, and $z_{\text{avg}} = 1.1$ for DA-9. These results do show qualitative agreement with the values obtained by Iavarone and Williams ($z_{\text{avg}} = 1.0$ for DA-5, $z_{\text{avg}} = 1.14$ for DA-8, and $z_{\text{avg}} = 1.19$ for DA-10, electrospraying from MeOH solutions [14]). In addition, a positive relationship between z_{avg} and k was found when MeOH was used as modifier (see red trace in Figure 5.7). Since the addition of MeOH vapor results in suppression of the cluster signals, z_{avg} is solely dependent on the ratio of the $[\text{MH}]^+$ and $[\text{MH}_2]^{2+}$ signal intensities, and increases with the chain length - as reported by Iavarone and Williams. This suggests that the anomalous dependence of z_{avg} on the chain length, which occurs when the diamines were electrosprayed from ACN/ H_2O without modifier addition, can be traced back to the strong impact of the abundance of cluster signals (and the dimer ion) on the observed charge state.

The dependence of n_{avg} on the chain length is also shown in Figure 5.8. As described in the previous section, the average cluster number of $[\text{M}(\text{ACN})_n\text{H}_2]^{2+}$ strongly decreases with increasing chain length as a result of the decrease in solvation energy which is based on diminishing Coulomb repulsion. The longer the chain length, the lower the number of ACN molecules interacting on average with the protons of $[\text{MH}_2]^{2+}$ ions. Simultaneously, a decrease in Coulomb repulsion results in an increased GB(MH^+) and, thus, in a lower proton transfer reactivity of $[\text{MH}_2]^{2+}$. These counteracting effects may explain the unexpected dependence of z_{avg} on the chain length (z_{avg} initially decreasing followed by an increase), which was observed for 0.1 mmol/l and 1 mmol/l diamine solutions. However, spraying from 1 mmol/l solutions the singly protonated species of DA-3 and DA-5 is represented by $[(\text{M})_2\text{H}]^+$ instead of $[\text{MH}]^+$ as for DA-8 and DA-9. The very pronounced formation of the proton-bound dimer for DA-3 and, in particular, for DA-5 (90 % of analyte signal intensity, cf. Figure 5.8) may be attributed to the inability to benefit from intramolecular solvation because cyclization leads to a large ring strain in small diamines. This large ring strain causes the enthalpy for internal hydrogen bonding between protonated and neutral amine function to become smaller than the dimerization energy [81]. Internal solvation by cyclization is thus thermodynamically more favored for longer chains [110]. Therefore, it is assumed that $[\text{MH}]^+$ of DA-8 and DA-9 undergo internal solvation leading to moderate amounts of $[\text{MH}]^+$ detected in the mass spectra. In contrast, $[\text{MH}]^+$ of DA-2, DA-3 and DA-5 are stabilized by dimerization, i.e., the formation of $[(\text{M})_2\text{H}]^+$.

Investigation of the average charge state in dependence of the chain length revealed that the abundance of cluster signals - resulting from the presence of ACN

5.1 Gas Phase Modification: Charge Depletion vs. Charge Retention

in the ESI solution and in case of gas phase modification from the high amounts in the gas phase - has a strong impact on the observed charge state. As a consequence, the dependence of z_{avg} on the chain length is altered. Experiments in which the diamines were sprayed from MeOH/H₂O or in which MeOH was used as modifier, clearly demonstrated the positive correlation of the charge state and the chain length, provided no cluster ions are observed (as it was also observed in experiments of Iavarone and Williams [14]). This correlation can be traced back to the increasing GB of [MH]⁺ with increasing chain length, i.e., increasing distance between the charge sites. The abundances of the cluster ions, in turn, depend on the substituent effect (Coulomb repulsion), which increases with decreasing chain length. Thus, the shorter the distance between the charge sites (and the stronger the Coulomb repulsion and therefore the larger the solvation energy), the more charge depletion and charge retention processes become effective. In other words, the average charge state of ions with adjacent charge sites is affected to a higher extent by both protic and aprotic solvents.

Impact of the Location of Modifier Addition: Source vs. Capillary

The impact of gas phase modifiers on the observed ion population and charge state of diamines and Substance P was studied by adding solvent vapor to a nanoESI source. The modifier-enriched nitrogen flow was introduced via a port located at one side of the spray chamber. The custom nanoESI source is also equipped with an additional port, leading to the capillary entrance of the aluminum housing. This capillary connects the spray chamber with the inlet capillary of the mass spectrometer and has the same inner diameter as the inlet capillary (cf. Figure 3.1). Modifier-enriched gas can thus be added in front of the entrance of the inlet capillary. Experiments were performed introducing MeOH and ACN vapor via this additional inlet port. The main nitrogen flow was still added to the spray chamber. The impact of the modifier addition to the capillary entrance on z_{avg} was studied and compared to the impact of the modifier addition to the source. The results - as depicted in Figure 5.9 - clearly demonstrate that an exposure to the modifiers ACN and MeOH has a stronger effect on z_{avg} when it occurs earlier in the electrospray process. Both, charge retention processes induced by ACN and charge depletion processes by MeOH, are more efficient when the respective modifier is added to the spray chamber. Between 15 and 50 % less enhancement and $\approx 45\%$ less reduction of z_{avg} is observed introducing ACN and MeOH, respectively, close to the capillary entrance. However, the amount of experiments and resulting data points do not suffice for a quantitative evaluation and only provide a qualitative assessment: addition of the modifier to the capillary instead of the spray chamber (source) significantly reduces the impact of gas phase modification on the observed charge state. These findings will be explained in terms of the charge retention/charge depletion model (cf. section 4.4). As discussed, charge depletion is based on the formation of large ion-solvent clusters, in which the GB of the protic solvent clusters exceed the GB of the protonated diamine. A reduced

5 Results and Discussion: Terminal Alkyldiamines

proton transfer rate - noticed by an elevated z_{avg} - is caused by insufficiently large cluster sizes. Adding MeOH vapor to the capillary entrance leads to a shorter reaction time in which the cluster equilibria are possibly shifted to lower average cluster sizes. In addition, the pressure and thus the collision rate gradually decreases within the capillary duct leading to a slower reaction rate and pressure dependent shift of the chemical equilibrium. Therefore, reduction of z_{avg} is less pronounced when MeOH is added to the capillary but z_{avg} declines continuously with increasing MeOH mixing ratio (compare solid and dashed red trace in Figure 5.9). Charge retention is understood as prevention of charge depletion. Aprotic solvents form ion-solvent clusters in which the GB of the solvent cluster does not exceed the GB of the protonated diamine, since the GB of aprotic solvent clusters is limited due to their inability to form H-bond networks. These ion-solvent clusters are stable and inhibit clustering with protic solvents when the aprotic solvent is present in high amounts in the gas phase. Adding an ACN-enriched gas flow to the capillary but not to the source significantly reduces the ACN gas phase mixing ratio in the spray chamber. Therefore, charge depletion processes can occur (e.g. by H_2O when sprayed from ACN/ H_2O) before ACN efficiently protects doubly protonated diamines against proton loss resulting in lower z_{avg} (compare solid and dashed blue colored traces in Figure 5.9).

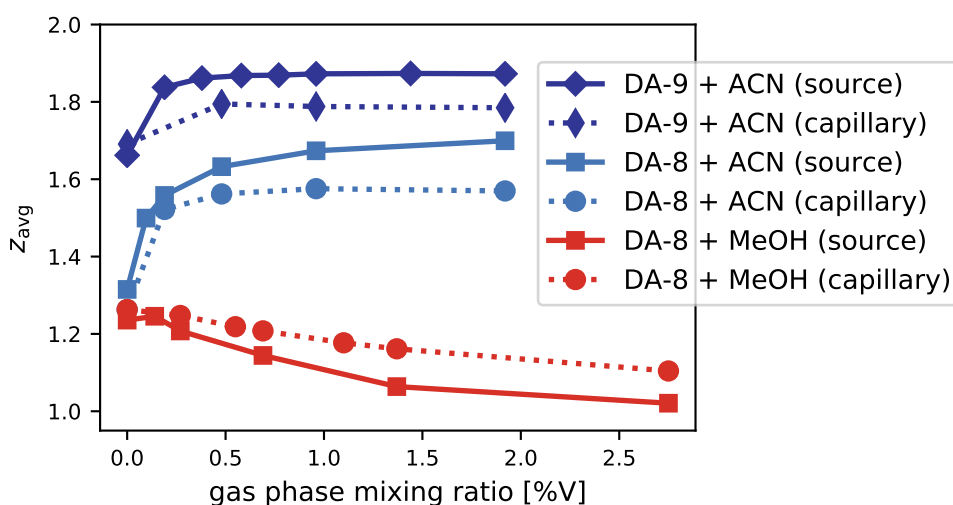


Figure 5.9: Average charge state z_{avg} of 1,8-diaminooctane (DA-8, 1 mmol/l) and 1,9-diaminononane (DA-9, 0.1 mmol/l) ions in dependence of the ACN and MeOH gas phase mixing ratio and the location of modifier addition (source vs. capillary). Modifier vapors were added to the spray chamber (source) or to the capillary entrance (capillary). Mass spectra were recorded with the TOF-MS, method DA.

5.1 Gas Phase Modification: Charge Depletion vs. Charge Retention

This assessment is supported by further experimental investigations: One modifier was added to the source and simultaneously the other to the capillary entrance. DA-8 (1 mmol/l in ACN/H₂O) and DA-9 (0.1 mmol/l in ACN/H₂O) were used in these experiments (as in the experiments depicted in Figure 5.9). For both analytes qualitatively the same effects were observed; the results of DA-9 are summarized in Table 5.1. The electrospray droplets containing DA-9 ions were exposed to ACN vapor first (source) and afterwards to MeOH (capillary, cf. Table 5.1a). Then, ACN was added to the capillary and MeOH to the source (cf. Table 5.1b). In both cases, the z_{avg} values resulting from simultaneous ACN and MeOH addition are compared to the average charge state, which was observed when only one or no gas phase modifier was applied. The resulting gas phase mixing ratio was calculated assuming a total gas flow of 1200 ml/min N₂, i.e., the given mixing ratios are valid only for an isotropic distribution of the vapor in the background gas. The main gas flow - containing optionally a certain amount of modifier vapor - was always introduced to the source and the minor gas flow, which was saturated by the other modifier, was added to the capillary entrance. It is noted that the addition of a small amount of modifier-saturated N₂ to the capillary entrance, e.g. 50 ml/min, does not result in an isotropic distribution of the modifier inside the ion source. As mentioned above, it is assumed that modifier addition to the capillary results in a locally enhanced concentration of this modifier in the capillary volume flow. Since the local gas phase mixing ratio of the modifier and its spatial distribution is not known, only the gas phase mixing ratio based on the assumption of an ideally mixed gas phase is given (cf. Table 5.1).

The experimentally determined z_{avg} of DA-9 listed in Table 5.1 demonstrate the impact of the location of the modifier addition. The application of 1 %V ACN (source) in combination with 1.4 %V and 2.7 %V MeOH (capillary) results in $z_{\text{avg}} = 1.83$ and $z_{\text{avg}} = 1.78$, respectively. When the same amount of ACN and MeOH was added the other way around, $z_{\text{avg}} = 1.72$ and $z_{\text{avg}} = 1.45$ is observed. This comparison shows that the modifier added to the source has the stronger effect on the observed charge state. Addition of ACN to the source leads to a higher z_{avg} due to charge retention. Simultaneous MeOH addition reduces the extent of the charge retention in dependence of the MeOH mixing ratio: with increasing MeOH mixing ratio z_{avg} decreases but ACN inhibits a sharp decrease of z_{avg} when MeOH (0.7 %V) is applied (1.87 → 1.83 instead of 1.69 → 1.40, cf. Table 5.1a). MeOH addition to the capillary entrance leads to an enrichment of MeOH in the present droplets/gas-phase clusters, and ACN has to compete with MeOH for solvation. The more MeOH is present in the gas phase, the higher the MeOH concentration in the droplet or the gas-phase cluster and therefore the more likely proton transfer occurs (charge depletion). To recapitulate, charge retention is understood as prevention of charge depletion; the results presented in Table 5.1a strongly supports this model. When MeOH is added to the source and ACN to the capillary entrance, an increase of z_{avg} as compared to 0 %V ACN but, on the contrary, no (significant) difference in z_{avg} between 0.5 %V and 1 %V ACN is observed (cf. Table 5.1b). This observation is explained by charge depletion processes, which are

5 Results and Discussion: Terminal Alkyldiamines

Table 5.1: Impact of the position of modifier addition on the observed z_{avg} of DA-9 (0.1 mmol/l): **(a)** ACN vapor added to the source and MeOH vapor to the capillary; **(b)** MeOH vapor added to the source and ACN vapor to the capillary. The given mixing ratios are valid for an isotropic distribution of the vapor in the background gas (1200 ml/min).

(a) MeOH addition to the capillary entrance reduces the extent of charge retention (ACN) in dependence of the MeOH mixing ratio (compare 0.7 %V, 1.4 %V and 2.7 %V in each line).

DA-9		capillary			
source	MeOH	0 %V	0.7 %V	1.4 %V	2.7 %V
	ACN				
	0 %V	1.69	1.40	1.37	-
	1 %V	1.87	1.83	1.83	1.78

(b) ACN addition to the capillary entrance reduces the extent of charge depletion (MeOH) without dependence on the ACN mixing ratio (compare 0.5 %V and 1 %V in each line).

DA-9		capillary		
source	ACN	0 %V	0.5 %V	1 %V
	MeOH			
	0 %V	1.69	1.79	1.79
	1.4 %V	-	1.72	1.72
	2.7 %V	1.20	1.46	1.45

initiated before ACN - added to the capillary entrance - can provide charge retention. Therefore, the observed z_{avg} depends on the MeOH and not on the ACN mixing ratio when the ACN mixing ratio is $\geq 0.5\%V$. Even when no MeOH is added to the source, z_{avg} does not change above 0.5 %V ACN (cf. DA-8/DA-9 + ACN (capillary) in Figure 5.9 and Table 5.1b). It is concluded that charge retention by ACN is more efficient when ACN is introduced to the spray chamber, i.e., when ESI droplets are exposed to ACN vapor at the earliest stage of their evolution. The impact of subsequent ACN addition (to the capillary) depends on the extent of charge depletion processes, which already took place in the spray chamber induced by solvent vapors, e.g. MeOH, and does not depend on the ACN mixing ratio (above a certain gas phase mixing ratio). Charge depletion induced by MeOH is also more efficient when MeOH is introduced to the spray chamber. However, charge depletion can occur at every stage of the droplet evolution, ion release, and transfer process. Depending on the gas phase mixing ratios and the location of the modifier addition, MeOH has to compete with other solvents, e.g. ACN, for solvation but with increasing MeOH mixing ratio proton transfer becomes more likely. Concerning doubly protonated diamine ions, as long as two

5.1 Gas Phase Modification: Charge Depletion vs. Charge Retention

protons reside on the ion the second proton can be retained. When the second proton is transferred to e.g. a solvent cluster, charge depletion has occurred and charge retention is no longer possible.

The discussion on the average charge state clearly shows that numerous parameters have an impact on z_{avg} of terminal alkyldiamines and thus many aspects (e.g. gas-phase clusters, internal and external solvation energies, Coulomb repulsion) have to be considered for the interpretation of the experimental data. The absolute charge state is influenced by the diamine and its chain length, the solution composition (diamine concentration, solvents), the presence of modifier(s) in the gas phase including the location of modifier addition, and probably other unknown experimental conditions. This leads to a restricted reproducibility of absolute z_{avg} values. In contrast, the relative change of z_{avg} due to gas phase modification shows a high reproducibility enabling validation of the charge retention/charge depletion model based on SP experiments.

5.1.3 Impact of Gas Phase Modification on CID

Section 4.3 discusses the influence of gas and solution phase modification on the fragmentation pattern of SP. It is observed that gas phase modification can diminish and even prevent fragmentation of SP ions, as well as declustering and dissociation of SP^{3+} -modifier cluster ions, which were electrically accelerated in the first vacuum stage. The extent of fragmentation and dissociation depends on the modifier gas phase mixing ratio (cf. Figure 4.7). Since SP ions can undergo structural changes due to disruption of intramolecular interactions induced by collisional activation, the influence of gas phase modification on ion fragmentation, and in particular on dissociation of ion-solvent clusters, was further studied with the diamines DA-3, DA-5, DA-8 and DA-9. In comparison to the peptide SP, the terminal alkyldiamines represent less complex systems allowing studies on the stability of ion-solvent clusters with less side effects.

As in the CID experiments regarding fragmentation/dissociation of SP ions, the gas phase modifiers ACN and MeOH were used in the diamine experiments. The acceleration voltages in the first, second, and third vacuum stage were varied. Furthermore, additional experiments with the ion trap instrument (cf. section 3.1.2) were performed. The intensities of DA-8 ions in dependence of the acceleration voltage in the first vacuum stage, i.e. in dependence of the potential difference between the capillary exit and the first skimmer, are depicted in Figure 5.10. The effect of ion acceleration on the observed ion population is compared between the cases of no, 4.8 %V ACN, and 0.7 %V MeOH modifier present in the ion source. The results from the measurements shown in Figure 5.10 (as well as results acquired from CID studies with DA-5 and DA-9) are in full accord with the findings from the SP experiments: The dissociation and fragmentation processes occurring upon ion acceleration when no modifier is applied, are significantly suppressed when a small amount of MeOH and

5 Results and Discussion: Terminal Alkyldiamines

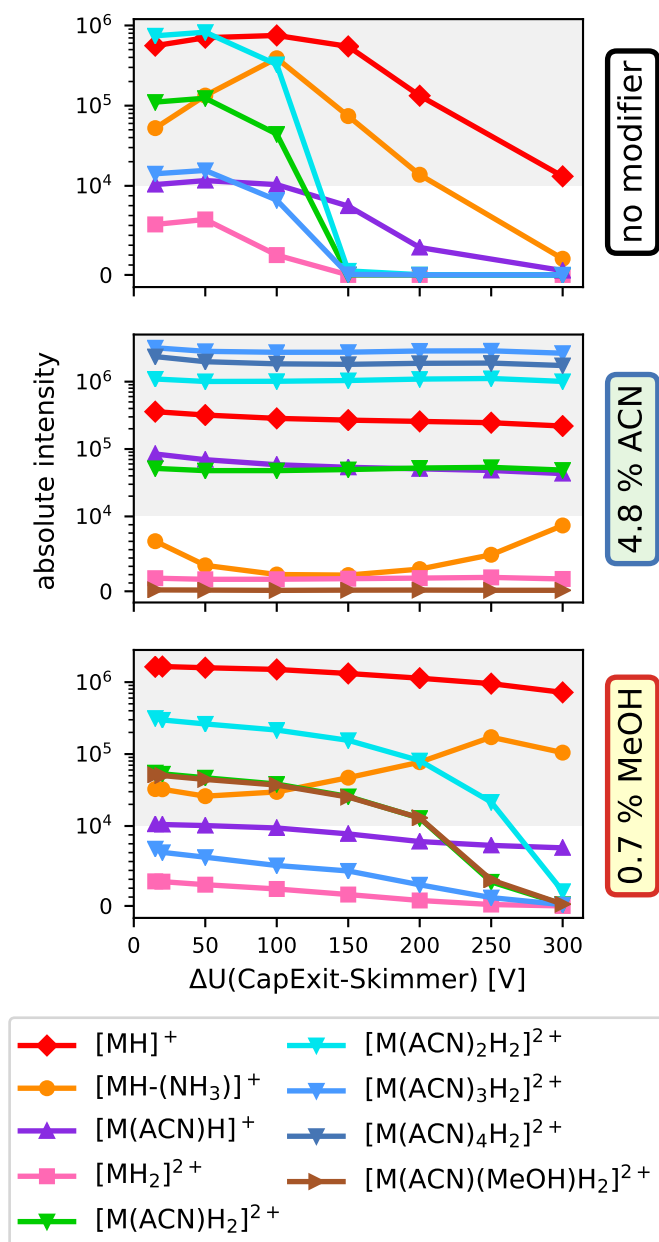


Figure 5.10: Intensities of observed 1,8-diaminooctane (DA-8) ion species in dependence of the acceleration voltage (potential difference between the capillary exit and the first skimmer of the TOF instrument (cf. Figure 3.3b)) when no (*top*), 4.8 %V ACN (*center*), and 0.7 %V MeOH (*bottom*) modifier is present in the ion source. M represents DA-8 in the legend. Note that the ordinate is linear between 0 and 10^4 (white background) and logarithmic above 10^4 (grey background). Mass spectra were recorded with the TOF-MS, method DA.

5.1 Gas Phase Modification: Charge Depletion vs. Charge Retention

completely prevented when a large amount of ACN was added. The top panel in Figure 5.10 shows the ion population in dependence of the potential difference between the capillary exit and the first skimmer, ΔU , with no modifier added. ΔU was normally set to 15 V. Increasing the potential difference (by increasing the potential at the capillary exit while the potential at the skimmer is held constant) results in dissociation of the doubly protonated ions $[M(\text{ACN})_n\text{H}_2]^{2+}$ with $n = 0-3$, which sets in above 50 V. Here, no dependence on the cluster size n is observed, i.e., successive declustering of the clusters beginning with the largest cluster is not observed. Even the bare doubly protonated ion, $[\text{MH}_2]^{2+}$, shows qualitatively the same change in intensity as the clusters. At 150 V potential difference, no doubly protonated species appears in the mass spectrum anymore; z_{avg} is lowered to 1. Dissociation of the doubly protonated ions leads to an increase in signal intensity of the singly protonated species $[\text{MH}]^+$ and $[\text{MH}-(\text{NH}_3)]^+$, the latter represents the protonated molecule, which has lost neutral NH_3 , i.e. a fragment ion. Simultaneous intensity increase of $[\text{MH}-(\text{NH}_3)]^+$ and decrease of $[M(\text{ACN})_n\text{H}_2]^{2+}$ ($n = 0-3$) was observed when no modifier and when 0.7 %V MeOH was added, as shown in the top and bottom plot of Figure 5.10, indicating that cluster dissociation results in the formation of $[\text{MH}-(\text{NH}_3)]^+$. In addition, the intensity of the sum of all DA-8 signals remains unchanged between 15 V and 100 V. It is assumed that the doubly protonated species clustered with ACN reacts quantitatively to $[\text{MH}]^+$ and $[\text{MH}-(\text{NH}_3)]^+$;⁸ CID is thus accompanied by proton loss/transfer. However, also the intensity of the singly protonated species decreases above 100 V potential difference, when no modifier is applied. The absolute signal intensities of $[\text{MH}]^+$, $[\text{M}(\text{ACN})\text{H}]^+$ and $[\text{MH}-(\text{NH}_3)]^+$ (as well as the TIC-normalized intensities) decrease significantly. To recapitulate, without the use of modifier z_{avg} drops steeply between 15 V and 100 V, followed by a strong decrease in intensity of the sum of all DA-8 ions between 100 V and 300 V.

As it was observed for SP^3+ and SP^2+ (cf. section 4.3 and Figure 4.7), addition of 4.8 %V ACN as gas phase modifier prevents dissociation/fragmentation of the doubly as well as of the singly protonated species; each signal intensity remains unchanged through the potential variation (cf. center panel of Figure 5.10).⁹ The observed cluster distribution of $[M(\text{ACN})_n\text{H}_2]^{2+}$ is maintained over the potential range due to the addition of 4.8 %V ACN leading to the abundant presence of ACN in the first vacuum stage. When only 1.9 %V ACN were added, a slight decrease in signal intensity of $[M(\text{ACN})_n\text{H}_2]^{2+}$ is noticed above 150 V; the signal intensities of each cluster drop by a factor of 2 at 300 V. Similar observations were made for the doubly protonated ions of DA-5 when comparing results with 4.8 %V and 1 %V ACN present. These findings support the notion that the amount of modifier present determines if and to what extent fragmentation and dissociation is suppressed. This notion is confirmed by the results depicted in Figure 5.11, which are discussed below.

⁸As a result of the low intensity of the bare doubly protonated ion, the dissociation product/channel of $[\text{MH}_2]^{2+}$ remains unclear.

⁹The variation of the $[\text{MH}-(\text{NH}_3)]^+$ signal intensity is not significant because $[\text{MH}-(\text{NH}_3)]^+$ represents a minor signal in the recorded mass spectra.

5 Results and Discussion: Terminal Alkyldiamines

The presence of 0.7 %V MeOH in the ion source leads to significant cluster dissociation above 150 V, which results in formation of $[\text{MH}-(\text{NH}_3)]^+$ as mentioned above (cf. bottom panel of Figure 5.10). Simultaneously, a decrease in intensity of the sum of all DA-8 ions as well as of the TIC is observed. The TIC-normalized intensity of $[\text{MH}]^+$ (as well as the TIC-normalized intensity of all DA-8 ions) slightly increase with ΔU . Loss of absolute intensity can be explained by charge depletion/proton transfer processes, which are kinetically hindered and thus promoted by collisional activation (cf. section 2.2.2). However, cluster dissociation occurs only at higher acceleration voltages as compared to the experiments without modifier addition indicating that even the presence of MeOH vapor stabilizes the ions clustered by ACN. When MeOH is present the $[\text{M}(\text{ACN})_n\text{H}_2]^{2+}$ ions are possibly also clustered by MeOH. Thus, moderate collisional activation may result in loss of the outer solvation shell consisting of MeOH molecules but not in complete elimination of external solvation, which does occur at $\Delta U = 300\text{V}$. The existence of mixed ion-solvent clusters, especially at low acceleration voltages, would support this notion, but only the mixed cluster $[\text{M}(\text{ACN})(\text{MeOH})\text{H}_2]^{2+}$ was observed (cf. bottom panel of Figure 5.10).

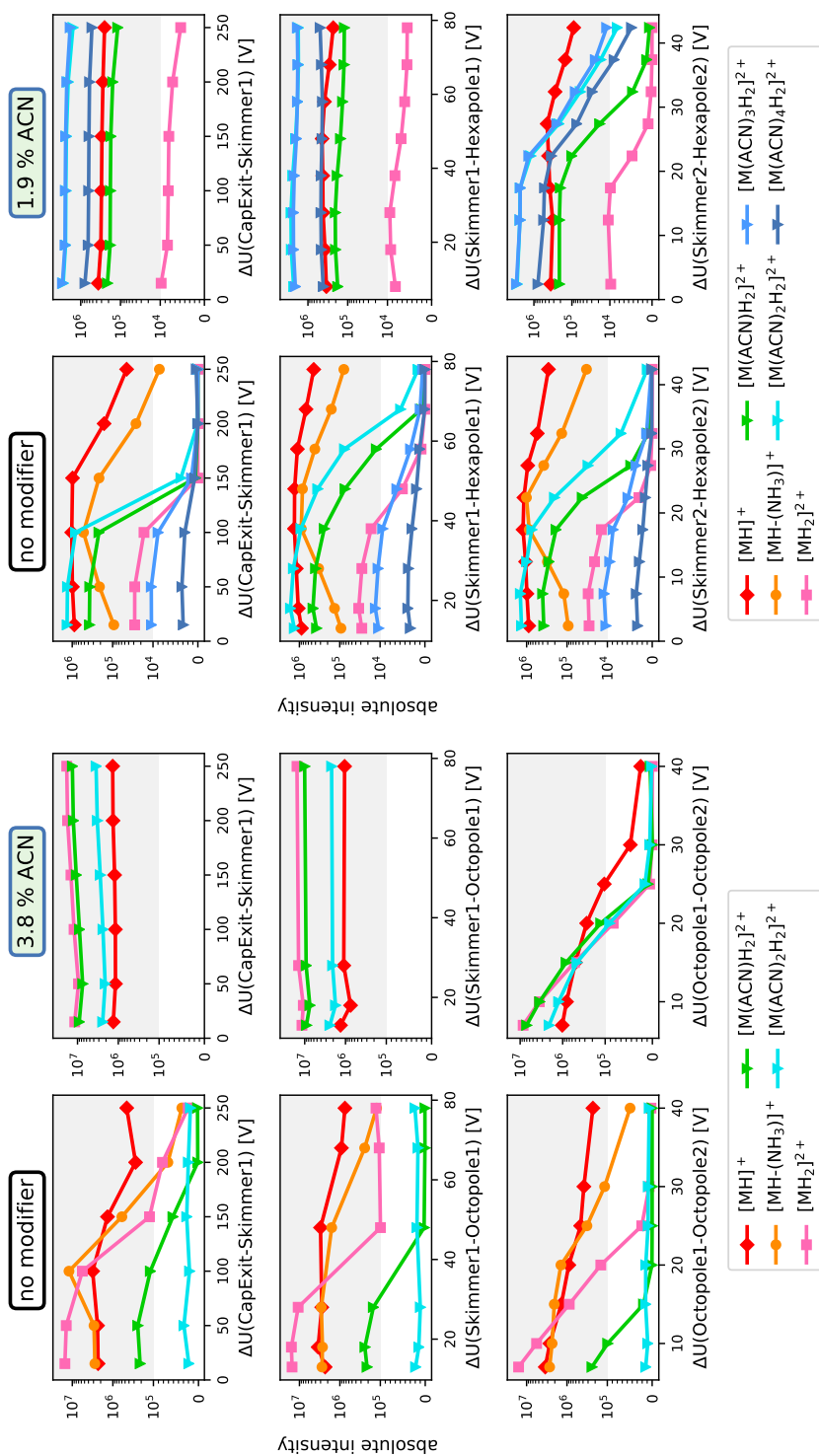
Without the use of modifier and increasing ΔU , the charge state of the DA-8 ions is effectively reduced to 1 (15 V to 100 V) followed by a significant loss of ion intensity (100 V to 300 V). Addition of 4.8 %V ACN to the ion source prevents reduction of both z_{avg} and the analyte ion intensity. When a small amount of MeOH is added as gas phase modifier, depletion of the higher charge state due to CID¹⁰ is retarded, i.e., z_{avg} is lowered to 1 only at 300 V. Additionally, upon MeOH addition, the loss of analyte ion intensity of the singly protonated species is significantly decreased. To summarize, qualitatively the same results are obtained with the diamines (data are only shown for DA-8 in Figure 5.10) and Substance P (cf. section 4.3), concerning the impact of gas phase modification on CID in the first vacuum stage, i.e. ion acceleration between the capillary exit and the first skimmer. Further investigations on CID in the second and third vacuum stage were performed using both, the TOF and the QIT instrument, to investigate the penetration depth of the ion source modifier addition affecting CID processes. The results of the TOF and QIT measurements are compared in Figure 5.11 and are discussed below.

The presentation of the experimental data in Figure 5.11 comprises three comparisons: impact on the detected ion population (1) with and without ACN as gas phase modifier present, (2) acquired with the TOF and the QIT¹¹ mass spectrometer, and (3) by voltage variations in the different transfer stage sections. Regarding the first vacuum stage, i.e., the potential difference between the capillary exit and the first skimmer, qualitatively the same results are obtained with DA-9 compared to DA-8 as well as with the QIT compared to the TOF instrument: ACN as modifier prevents ion dissociation and fragmentation, and thus the signal intensities and z_{avg} remain constant

¹⁰Of course, charge depletion due to the presence of MeOH is observed too. At 15 V, z_{avg} exhibits 1.21 when MeOH is present compared to $z_{\text{avg}} = 1.58$ without modifier addition.

¹¹As mentioned in section 3.1.2, two similar QIT instruments were available for experimental studies, the data shown in Figure 5.11a were measured with the esquire3000 instrument.

5.1 Gas Phase Modification: Charge Depletion vs. Charge Retention



(a) Ion population detected with the QIT-MS, method DA.

(b) Ion population detected with the TOF-MS, method DA.

Figure 5.1.1: Intensities of observed 1,9-diaminononane (DA-9) ion species in dependence of the acceleration voltage varied in the first (*top*), second (*center*) and third vacuum stage (*bottom*). Observed ion populations are compared between the use of no modifier and the use of ACN as well as between the QIT (**a**) and the TOF (**b**) instrument. Note that a white background indicates a linear ordinate and a grey background a logarithmic ordinate. M represents DA-9.

5 Results and Discussion: Terminal Alkyldiamines

(and both are enhanced due to the addition of ACN vapor). Without ACN as modifier present, the signal intensities of the doubly protonated species begin to decrease above 50 V potential difference accompanied by an increase of the $[\text{MH}(-\text{NH}_3)]^+$ signal abundance. The intensities of the singly protonated species decrease above 100 V, as a result the intensity of the sum of all DA-9 signals drastically decreases. In general, the same holds true for the second vacuum stage, i.e., the potential difference between the first skimmer and the first multipole. Minor modifications of ΔU lead to CID when ACN is not applied, which is caused by the lower background pressure in the second stage as compared to the first vacuum stage, so that ions gain higher kinetic energies between collisions with background gas particles. Hence, an even lower increase of the acceleration voltage induces CID in the third vacuum stage and - in contrast to the upstream regions - even when ACN is added as modifier. Upon ion source addition of ACN, ion dissociation/fragmentation as a result of collisional activation in front of the second multipole is only slightly diminished. With 1.9 %V ACN present in the ion source, an increase of the potential difference between the second skimmer and the second hexapole in the TOF instrument leads to a less steep decrease of the $[\text{M}(\text{ACN})_n\text{H}_2]^{2+}$ signal intensities. As a result, the TOF detects cluster ions with low abundance even at $\Delta U = 42\text{ V}$. CID in the third vacuum stage of the QIT was accomplished by variation of ΔU between the two octopoles. The potential at the partition, which is positioned between the two octopoles of the QIT, can not be modified in the user program but is automatically set. The increase of ΔU between the two octopoles immediately results in dissociation and a sharp decrease in analyte ion intensity, regardless whether ACN is added as gas phase modifier to the ion source or not.

To summarize, ACN addition to the ion source has a strong impact on the cluster equilibrium of $[\text{M}(\text{ACN})_n\text{H}_2]^{2+}$ throughout the first and second vacuum stage. It is concluded that ACN is abundantly present in these regions of the mass spectrometer and therefore the cluster equilibrium is mostly maintained. As a result, increase of ion acceleration does not lead to declustering, dissociation and fragmentation, as it is the case without ACN addition. Ion acceleration in the third vacuum stage results in significant ion loss due to dissociation/fragmentation - even when ACN is added - caused by the increased collision energy and a very low collision rate with ACN molecules in this region. These findings are in accord with studies on the stabilization of protonated ions in DMS-MS by modifier addition. Ieritano and co-workers [54] observed suppression of fragmentation occurring inside the DMS cell due to collisional activation by the separation field and Seale and co-workers [207] observed suppression of up-front CID (cf. section 2.2.3) when polar solvents are used as gas phase modifiers. The absence of fragment ions is accompanied by extensive ion clustering. Ieritano and co-workers suggested that ion solvation produces a *solvent air bag* sheltering the ionic species from activation by high-energy collisions. Calculations of the effective ion temperature in ion-solvent cluster populations illustrated the stabilizing effects. In addition, the largest degree of ion cooling occurs when ACN is used as solvating partner (in comparison to H_2O , MeOH, and IPA) [168]. In both studies, ion activation

5.1 Gas Phase Modification: Charge Depletion vs. Charge Retention

occurred at elevated pressure, supporting the assumption that ion activation leading to dissociation/fragmentation is mitigated only in solvating environments.

At a mixing ratio of 3.8 %V ACN, $[\text{M}(\text{ACN})_n\text{H}_2]^{2+}$ is the largest DA-9-ACN cluster discernible in the mass spectra recorded with the QIT (method DA without additional ion acceleration). The intensity of the $[\text{MH}_2]^{2+}$ ion is the most abundant signal. Compared to the ion population detected with the TOF, the average cluster number n_{avg} is much lower - although the present ACN mixing ratio was twice as high - but the average charge state z_{avg} is similar ($z_{\text{avg}} \approx 1.92$ at 3.8 %V ACN (QIT), $z_{\text{avg}} \approx 1.87$ at 1.9 %V ACN (TOF)). Therefore, declustering processes, i.e., loss of neutral ACN molecules, seem to occur more pronounced in the QIT than in the TOF instrument. It is striking that $[\text{MH}_2]^{2+}$ represents the most abundant ion signal in the mass spectra recorded with the QIT but is the lowest signal in the TOF spectra. This suggests that the ion transfer and/or analyzer system of the QIT strongly favors the generation/detection of the bare doubly protonated species; the assumed declustering process has to be very effective. Since the transfer systems between TOF and QIT are similar and the acceleration voltages were adjusted to be identical, declustering is most probably primarily occurring in the ion trap analyzer. Ions have to be injected into the ion trap for m/z analysis, where they collide with He molecules (collision gas) to lose their excess kinetic energy of several eV. The kinetic energy of the ions is reduced since impulse transfer occurs from the ions to the collision gas molecules due to the higher mass of the ions. This thermalization of the ions, defined as a reduction of molecular ion kinetic energy and its spatial distribution as well as the dissipation of internal energy of the ions, is called (*collisional*) *cooling* [155, 208]. Collisional cooling and collisional activation are, fundamentally, two results of the same energy transfer process: when the ions have low internal energy and undergo high relative kinetic energy collisions, the most probable result is a gain of internal energy; likewise, when ions have high internal energy and undergo low relative kinetic energy collisions, a loss of internal energy is favored [155]. Considering an ion-solvent cluster, loss of solvent molecules provides another avenue for ions to dissipate internal energy. Since the ACN molecules are only loosely bound in the cluster ions $[\text{M}(\text{ACN})_n\text{H}_2]^{2+}$ and therefore the dissociation thresholds are low, inelastic collisions with He followed by loss of m ($m \leq n$) ACN molecules are conceivable. In addition, declustering may occur due to inelastic collisions during the ejection process. Mass analysis in the applied ion trap is performed via resonance ejection. As an ion comes into resonance with the ejection frequency, it will gain kinetic energy and undergo energetic collisions with He present in the trap [155]. *Fragile ions* are known to undergo dissociation during this ejection process [209, 210]. Cluster ions $[\text{M}(\text{ACN})_n\text{H}_2]^{2+}$ are considered to fall into this category. This is further discussed in section 5.2.5. However, mass analysis with the QIT instrument yields smaller n_{avg} (compared to the TOF) whether declustering of $[\text{M}(\text{ACN})_n\text{H}_2]^{2+}$ occurs during the ion injection and/or ejection process. The comparative study clearly demonstrates consistency between both instruments regarding the impact of the transfer settings and the influence of the gas phase modifier ACN.

5.2 Chemical Modification of the Collision Gas

The results presented in section 5.1.3 clearly demonstrate that the addition of ACN vapor to the ion source in the percentage range (gas phase modification) results in a noticeable presence of neutral ACN molecules in all vacuum stages of both mass spectrometers. The presence of ACN in the background gas was noticed in CID experiments, in which the addition of ACN vapor led to inhibition or at least reduction of ion dissociation/fragmentation. Since a significant amount of ACN molecules, which do affect the cluster equilibrium of the ions, seems also be present in the third vacuum stage, it can be assumed that a smaller but not negligible amount of ACN vapor reaches the trap analyzer as well. Due to the addition of the helium collision gas, the pressure and thus the collision rate is elevated in the ion trap. Therefore, ion-molecule reactions occurring within the ion trap mass analyzer are plausible, which in turn would have a significant effect on the observed mass spectra. In other words, gas phase modification in the ion source is assumed to result in chemical modification of the collision gas in the ion trap.

5.2.1 Measurement Procedure

In order to verify this notion and to study the in-trap chemistry, ions were stored up to several seconds in the trap, using the ion trap mass analyzer as a chemical reactor (see also section 3.1.2). The general measurement procedure and the available experimental options are depicted in Figure 5.12: after ion accumulation, the ions are stored in the ion trap for a certain time period for collisional cooling, before they are ejected. The cooling and in this context reaction period can be increased up to 20 s.¹² Ions can also be isolated and/or excited within the trap. The isolation mode of the trap allows to select an isolation region defined by a target m/z and a window width around that m/z . The isolation width manipulates the additional waveform used to isolate the particular m/z range around the target mass for storage and subsequent collisional activation. The trajectories of ions with an m/z outside the isolation window become unstable and the respective ions are ejected from the trap. In experiments involving collisional activation the excitation amplitude is set to a value $> 0.0V$, which increases the energy of the ion of interest (target mass) by resonant excitation. Besides the excitation amplitude, the low-mass cutoff has to be set. All fragment or product ions with m/z values above the cutoff value are stored in the trap. Between several isolation and excitation cycles cooling periods can be inserted, as illustrated in Figure 5.12. Ion-molecule reactions between DA-9 and DA-5 ions and ACN were studied upon addition of ACN to the ion source - this method is defined as *gas phase modification* and the term *source-ACN* is used. Addition of ACN directly to the ion trap via the He gas line leads to *collision gas modification* and the term

¹²To enable a reaction period of 20 s, all 10 fragmentation boxes in the graphical user interface of the data acquisition software are checked and both the fragmentation delay and fragmentation time are set to 1 s. The excitation amplitude is set to 0.0 V.

trap-ACN is used.¹³ In these experiments the diamines were always sprayed from MeOH/H₂O solutions to exclude reactions between the ions and ACN molecules of the ESI solution. When MeOH was applied as modifier (source-MeOH), the diamines were sprayed from ACN/H₂O (see bottom plot of Figure 5.13).

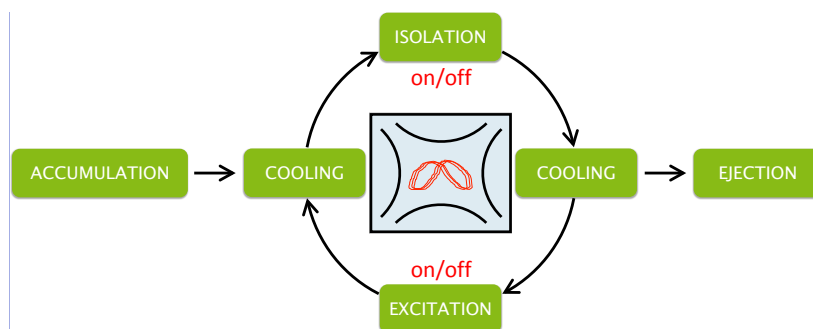


Figure 5.12: Schematic of the measurement procedure used for characterization and examination of ion-molecule reactions within the quadrupole ion trap mass analyzer.

5.2.2 Variation of the Cooling Time: Gas Phase Modification

For investigations regarding the extent of gas phase modification of the collision gas and the resulting ion-molecule reactions, the modifiers ACN and MeOH were added to the ion source and all ions in the mass range of m/z 15 to 250 were stored up to several seconds in the trap. No ion loss is observed during cooling, the total ion current (TIC) shows no dependence on the ions' residence time, only minor fluctuations. Therefore, each analyte ion intensity was normalized to the TIC or to the sum of all analyte ion intensities for data interpretation. Figure 5.13 depicts the observed normalized ion populations in dependence of the additional cooling time, called trapping time. Without the use of modifier, the analyte ions $[MH]^+$ and $[MH_2]^{2+}$ are present in the mass spectra; the doubly protonated ion shows a significantly higher intensity.¹⁴ Increasing the trapping time up to 1 s results in no significant change of the intensities of both ion species but the relative intensity of the $[MH]^+$ ion increases from 4 % to approximately 8 % after 3 s. As expected, the observed ion population changes when ACN vapor is added to the ion source: the cluster species $[M(ACN)_nH_2]^{2+}$ appear and n_{avg} increases with increasing ACN gas phase mixing ratio (compare 0.1 %V ACN and 1 %V ACN). Furthermore, z_{avg} is increased (no modi-

¹³Both methods lead to *chemical modification of the collision gas*, as will be shown in the following.

¹⁴The intensity ratio between $[MH]^+$ and $[MH_2]^{2+}$ and the relative intensities, respectively, depend on the transfer stage and analyzer settings, e.g. hexapole RF, trap drive. The settings of the applied method, which is optimized for the detection of $[MH_2]^{2+}$ and the cluster ions $[M(ACN)_nH_2]^{2+}$, are found in Table 3.1.

5 Results and Discussion: Terminal Alkyldiamines

fier: $z_{\text{avg}} = 1.96$, 0.1 %V ACN: $z_{\text{avg}} = 1.99$, 1 %V ACN: $z_{\text{avg}} = 1.99$ after 10 ms trapping time) emphasizing again the charge retention effect of ACN vapor. The increase of the trapping time reveals that even the presence of 0.1 %V ACN in the ion source leads to significant cluster growth in the ion trap, which is observed after 100 ms trapping time. The increase of n_{avg} is accompanied by decay of the $[\text{MH}_2]^{2+}$ and formation of the $[\text{MH}]^+$ ion. The relative signal abundance of the $[\text{MH}]^+$ ion reaches 9 % of the sum of all analyte ions after a reaction time of 6 s. Addition of 1 %V ACN results in a steeper decrease in intensity of the bare doubly protonated ion (note the logarithmic x-scale in Figure 5.13), whereby the enhancement of the singly protonated ion signal is comparable or rather less pronounced (6 % after 6 s trapping time). It is assumed that the reaction rate of $[\text{MH}_2]^{2+}$ is dependent on the ACN mixing ratio; the formation rate of $[\text{MH}]^+$ seems to be independent of the ACN mixing ratio in the ion source. Both assumptions were verified by examining the temporal decay of $[\text{MH}_2]^{2+}$ and the formation of $[\text{MH}]^+$; the results are presented in section 5.2.4, see Figure 5.15. Applying MeOH as gas phase modifier lowers the average charge state and the absolute ion intensity (the TIC is reduced to around one fifth of intensity) as compared to no modifier addition which is caused by charge depletion processes. Increase of the trapping time results in no significant change of the relative intensities of the observed ion species; only a minor increase in intensity of $[\text{MH}]^+$ and the clustered ion $[\text{M}(\text{MeOH})\text{H}_2]^{2+}$ is observed. Experiments in which the $[\text{MH}_2]^{2+}$ ion was isolated and subsequently trapped for 3 s for reaction with MeOH added to the ion source reveal the same reaction products, $[\text{M}(\text{MeOH})\text{H}_2]^{2+}$ and $[\text{MH}]^+$, and similar rates of formation.

Ion-molecule reactions between DA-9 ions, in particular $[\text{MH}_2]^{2+}$, and MeOH seems to proceed slower within the ion trap as compared to the observed reactions with ACN. Since both, ACN and MeOH, are present in the percentage range (1 %V and 1.4 %V, respectively, cf. Figure 5.13) in the ion source, comparable mixing ratios in the collision gas within the ion trap are assumed. To receive a significantly lower content of neutral MeOH molecules in the collision gas, MeOH should show a better pumpability, which seems unlikely though. Probably, the rate coefficients for the reactions with MeOH are much smaller and the reactions are not observed on the selected time scale. However, the rates of ion-molecule reactions are mostly determined by the collision frequency (collision control). Besides, the different stability of the ion-ACN and ion-MeOH clusters could account for the different results. Ion-MeOH clusters were only rarely observed with both instruments (TOF and QIT), indicating a low stability and/or high reactivity of the ion-MeOH clusters. A low binding/solvation energy will result in efficient declustering during the transfer and mass analysis process, especially during ion injection into the trap. Therefore, ion-MeOH clusters will not be present in the ion trap analyzer because the reaction rate of dissociation is higher than that of solvation. In fact, in the MeOH experiments the absolute abundance of $[\text{MH}_2]^{2+}$ was 5 to 10 times lower than in the ACN experiments, which is attributed to charge depletion processes. The intensity of $[\text{MH}_2]^{2+}$ is directly proportional to the reaction rate of $[\text{MH}_2]^{2+}$. To conclude, a lower mixing ratio of MeOH in the collision

5.2 Chemical Modification of the Collision Gas

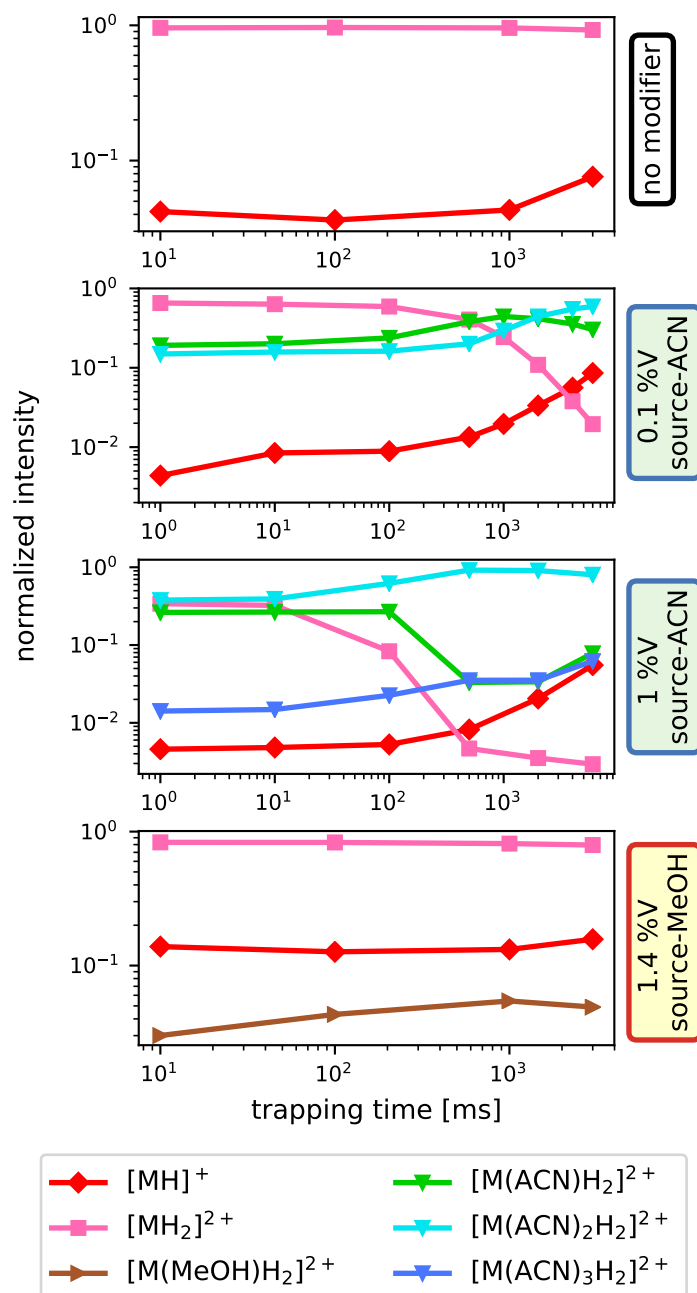


Figure 5.13: Intensities of observed 1,9-diaminononane (DA-9) ion species in dependence of the trapping time (without isolation and excitation) when no, 0.1 %V ACN, 1 %V ACN, and 1.4 %V MeOH modifier are present in the ion source. M represents DA-9 in the legend. Note that the ordinate and the abscissa are logarithmic. The intensities are plotted normalized to the sum of all analyte ion intensities. Mass spectra were recorded with the QIT-MS (esquire3000), method $[MH_2]^{2+}$.

5 Results and Discussion: Terminal Alkyldiamines

gas, a slower rate coefficient of the cluster build-up reaction, a lower stability of the ion-MeOH clusters, and a smaller $[\text{MH}_2]^{2+}$ ion intensity - as compared to the ACN experiments - may lead to the circumstance that with MeOH no significant formation of reaction products is observed on the selected time scale. The explanations do not contradict each other and it is likely that more than one mechanism causes the observed effect.

Recapitulating, the addition of high amounts (mixing ratio in the percentage range) of ACN to the ion source inevitable means that neutral ACN is not only present in all stages of the ion transfer but also in the ion trap promoting clustering reactions. Due to this fact the mean cluster size of $[\text{M}(\text{ACN})_n\text{H}_2]^{2+}$ increases with the trapping time. Successive cluster growth up to cluster $n = 3$ (1 %V ACN) and a strong decrease in intensity of the bare $[\text{MH}_2]^{2+}$ ion is observed. Besides, the singly protonated ion $[\text{MH}]^+$ gains in intensity. Therefore, the hypothesis V, see section 4.5, is validated by experiments.

5.2.3 Variation of the Cooling Time: Collision Gas Modification

Adding ACN directly to the ion trap analyzer via the He collision gas line (collision gas modification), the same modification of the detected ion population was observed as in the experiments applying source-ACN. He gas, saturated with ACN vapor, was mixed with pure He and added to the He collision gas line. Unfortunately, neither the mixing ratio of ACN in the He gas nor inside the trap is exactly known for these experiments (indicated as ? %V trap-ACN, cf. Figure 5.14). Comparison experiments with a gas mixture (50 ppmV ACN-d3 (CD_3CN) in He) revealed that a two orders of magnitude larger amount of ACN than 50 ppmV was present in the trap using the ACN-enriched He gas (compare ? %V trap-ACN with 50 ppmV trap-ACN in Figure 5.15a). The addition of ACN to the trap results in detection of the cluster ions $[\text{M}(\text{ACN})_n\text{H}_2]^{2+}$, in particular with $n = 1, 2$, even when the ions are analyzed immediately after injection, i.e., when a normal scan was performed without additional cooling via the MS/MS function. Since DA-9 was sprayed from MeOH/ H_2O only the bare ions are expected to enter the trap (see ion population resulting from no modifier addition in Figure 5.13). Therefore, clustering with ACN occurred also during the regular injection, accumulation and cooling process and/or even before the ions have entered the trap. As it is inevitable that the ACN-enriched trap collision gas leaks out of the trap into the transfer stage, the ACN mixing ratio around the trap entrance is elevated. Additional increase of the cooling duration from 1 ms to 2000 ms - enabled by activation of the MS/MS function - changes the ion population in favor of the cluster ions $[\text{M}(\text{ACN})_n\text{H}_2]^{2+}$. Figure 5.14 shows the DA-9 ion population resulting from application of the ACN-enriched He collision gas (? %V trap-ACN) when all ions were stored and analyzed in the trap (top) and when $[\text{MH}_2]^{2+}$ was isolated and subsequently trapped up to several seconds (bottom).¹⁵ Isolation of $[\text{MH}_2]^{2+}$

¹⁵Isolation of $[\text{MH}_2]^{2+}$ was performed with an isolation width of 3.0 (i.e. m/z 80.5 ± 1.5) and a low-mass cutoff of m/z 30.

5.2 Chemical Modification of the Collision Gas

and subsequent cooling of 2 ms results in a mass spectrum in which the first and second cluster ion show similar abundances as the previously isolated, bare $[\text{MH}_2]^{2+}$ ion. Therefore, about two third of the isolated $[\text{MH}_2]^{2+}$ ions already have reacted after 2 ms to form $[\text{M}(\text{ACN})\text{H}_2]^{2+}$ and $[\text{M}(\text{ACN})_2\text{H}_2]^{2+}$. After 100 ms of cooling, the cluster ions dominate the mass spectrum whereas the intensity of the bare $[\text{MH}_2]^{2+}$ ion is strongly decreased, regardless of whether all ions or only $[\text{MH}_2]^{2+}$ were initially stored in the ion trap. In contrast, the time-dependent abundances of the singly protonated DA-9 ion $[\text{MH}]^+$ and the proton bound acetonitrile dimer, $[(\text{ACN})_2\text{H}]^+$, differ significantly between these two experiments. Isolation of $[\text{MH}_2]^{2+}$ clearly demonstrates that the deprotonation reaction generating $[\text{MH}]^+$ is not accompanied by formation of $[(\text{ACN})_2\text{H}]^+$, as it could have been expected from the experiment without isolation (compare red and orange trace in both plots of Figure 5.14). Therefore, deprotonation of $[\text{M}(\text{ACN})_n\text{H}_2]^{2+}$ driven by formation of $[(\text{ACN})_m\text{H}]^+$, $m < n$, in a proton transfer reaction is ruled out. The deprotonation reaction rate and the formation rate of $[\text{MH}]^+$, respectively, should thus be independent of the ACN mixing ratio present in the ion trap. This was verified by determination of the reaction rate coefficients, see section 5.2.4. In contrast, the decay of $[\text{MH}_2]^{2+}$ strongly depends on the ACN mixing ratio: After about 1 s trapping time the intensity of the $[\text{MH}_2]^{2+}$ ion is below the detection limit when the ACN-enriched He collision gas is applied (compare Figures 5.13 and 5.14).

After a certain trapping/reaction time, which depends on the amount and method of ACN addition (source- or trap-ACN), the cluster with $n = 2$ shows the largest abundance in the mass spectra of DA-9 (see Figures 5.13 and 5.14) as well as of DA-5, indicating a relatively high solvation energy $-\Delta G_{1,2}^\circ$ compared to $-\Delta G_{2,3}^\circ$ for $[\text{MH}_2]^{2+}$ with $\text{M} = \text{DA-9}, \text{DA-5}$. Studies on the hydration of various doubly protonated alkyl-diamines [82–84] clearly demonstrated that there is no gradual decrease of $-\Delta G_{n,n+1}^\circ$ with n . Instead, the energy drops stepwise from the second to the third H_2O molecule (as well as from the fourth to the fifth, and the sixth to the seventh). In contrast to the second H_2O (or ACN) molecule, which interacts with the second protonated amino group, the third H_2O (or ACN) molecule will have to share one of the charged groups, and this interaction will be considerably weaker as the first two [83]. This pattern was reproduced in calculations of $-\Delta G_{n,n+1}^\circ$ for the solvation of doubly protonated diaminoethane (DA-2) by H_2O and ACN (see Table 5.2); results of the theoretical examinations are described and discussed in detail in chapter 5.3. A drop in solvation energy between the second and third ACN molecule solvating the larger doubly protonated diamines is expected and may explain the high abundance of the $[\text{M}(\text{ACN})_2\text{H}]^{2+}$ ion dominating the equilibrated cluster distributions and the resulting mass spectra of DA-9 and DA-5.

In conclusion, chemical modification of the ion source background gas results in chemical modification of the collision gas present inside the ion trap analyzer. Due to chemical modification by ACN, gas-phase ion molecule reactions are observed be-

5 Results and Discussion: Terminal Alkyldiamines

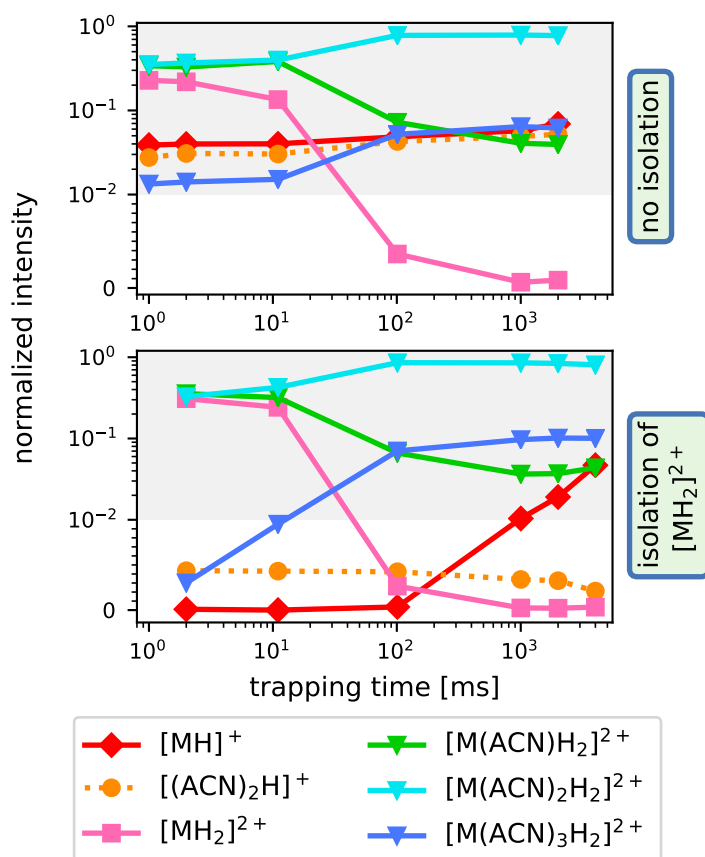
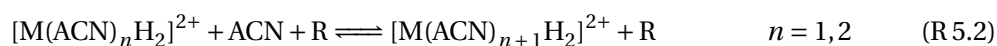
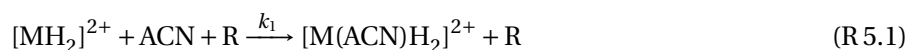


Figure 5.14: Intensities of observed 1,9-diaminononane (DA-9) ion species in dependence of the trapping time when ACN is present in the ion trap analyzer (? %V trap-ACN). *Top:* All ions in the range of m/z 15 to 250 were trapped and subjected to ion-molecule reactions. *Bottom:* Isolation of $[MH_2]^{2+}$ was performed prior to trapping. M represents DA-9 in the legend. Note that the ordinate and the abscissa have a logarithmic scale. The intensities are plotted normalized to the sum of all analyte ion intensities. Mass spectra were recorded with the QIT-MS (esquire3000), method $[MH_2]^{2+}$.

tween doubly protonated DA-9 ions and ACN leading to intense cluster formation. Clustering with ACN can be described as equilibrium reaction system, as stated in the charge retention/charge depletion model (see section 4.4 and in particular Figure 4.8). Cluster formation with ACN (an aprotic solvent), which is assumed to facilitate charge retention, can occur in the gas phase or more precisely between gas-phase ions and neutral vapors. In other words, doubly protonated diamine gas-phase ions, which were released from ESI droplets, will be solvated by ACN present in the gas phase. Therefore, chemical modification of the collision gas unequivocally proved that charge retention does occur in the gas phase. Solvation reactions occur most likely also in the liquid phase - due to enrichment of the modifier (e.g. ACN) in the ESI droplet - and/or at the gas-liquid interface.

5.2.4 Investigation of the Reaction Kinetics

Based on the time and concentration dependent ion populations observed in the experiments presented above, the reaction system within the chemically modified trap analyzer is described with the following reactions,



where R represents a neutral collision partner (e.g. He). The first cluster step (R 5.1) is expressed as a forward reaction in contrast to the subsequent cluster steps, which are described by equilibria (R 5.2). Since the experimental data clearly demonstrated that $[\text{MH}_2]^{2+}$ is highly reactive and not present in the equilibrated system under the given reaction conditions (e.g. total pressure and partial pressure of ACN), the reverse reaction of the first cluster step (declustering) is assumed to be negligible. Further clustering with ACN and declustering is described by reversible reactions, i.e., an equilibrium reaction system (R 5.2), which defines the relative abundances of the cluster species with $n = 1 - 3$ in the equilibrium state. In addition to the clustering/declustering reactions, formation of $[\text{MH}]^+$ was observed. $[\text{MH}]^+$ only can be generated by some kind of deprotonation reaction of a doubly protonated DA-9 species - possibly clustered by a solvent S - leading to the singly protonated ion and product(s) P (R 5.3), e.g. via proton transfer and/or dissociation. Potential singly protonated product ions, whose intensities shows a correlation with the increase in intensity of $[\text{MH}]^+$, were not found.

Decay of $[\text{MH}_2]^{2+}$

The intensity-time-profiles of the doubly protonated DA-9 ion, $[\text{MH}_2]^{2+}$, and of the singly protonated DA-9 ion, $[\text{MH}]^+$, were analyzed to determine the reaction order

5 Results and Discussion: Terminal Alkyldiamines

and thus to verify the postulated reaction equations (R 5.1) and (R 5.3). On the assumption that the $[\text{MH}_2]^{2+}$ ions only react with neutral molecules, which are present in large excess over the ion population, pseudo-first-order kinetics [136] is assumed for the decay of $[\text{MH}_2]^{2+}$. Assuming that the collision partner R is represented by a He molecule, it applies: $c(\text{R}) \gg c(\text{ACN}) \gg c([\text{MH}_2]^{2+})$ (cf. (R 5.1)). The reaction rate and the pseudo-first-order ion-molecule reaction rate coefficient k'_1 are estimated applying the rate equation (5.6).

$$-\frac{dc([\text{MH}_2]^{2+})}{dt} = k'_1 \cdot c([\text{MH}_2]^{2+}) \quad (5.6)$$

Since ACN was added in relatively high amounts to the ion source or trap and the clusters $[\text{M}(\text{ACN})_n\text{H}_2]^{2+}$ dominate the observed ion population, clustering with ACN is assumed to be mainly responsible for the decay of $[\text{MH}_2]^{2+}$ (R 5.1). Reactions with other solvents/reactants than ACN cannot not be entirely ruled out (see (R 5.3)). When the rate coefficient k'_1 primarily depends on the ACN concentration the following expression applies with good approximation.

$$k'_1 = k_1 \cdot c(\text{ACN}) \cdot c(\text{R}) \quad (5.7)$$

Integration ($t = 0 \rightarrow t = t$) of the differential rate equation (5.6) leads to the integrated rate law (5.8), which allows determination of the pseudo-first-order rate coefficient k'_1 by linear regression.

$$\ln\left(\frac{c_0([\text{MH}_2]^{2+})}{c_t([\text{MH}_2]^{2+})}\right) = k'_1 \cdot t \quad (5.8)$$

The measured signal intensity is used instead of the concentration c . The absolute intensity of $[\text{MH}_2]^{2+}$ was normalized to the TIC for each measurement to eliminate fluctuations in the total ion concentration. The reaction time t is equivalent to the ion storage time in the trap after injection (and isolation). As shown for different experiments in Figure 5.15a, plotting $\ln(I_0([\text{MH}_2]^{2+})/I_t([\text{MH}_2]^{2+}))$ against the storage time results in a linear relationship. The linearized plots with good correlation coefficients demonstrate that the experimental data support the assumption of pseudo-first-order kinetics regarding the reaction of $[\text{MH}_2]^{2+}$. In addition, increasing the amount of ACN inside the trap results in increasing values for the pseudo-first-order reaction rate coefficient k'_1 (represented by the slope of each regression line). Without modifier, i.e. without addition of source-ACN or trap-ACN, the intensity of $[\text{MH}_2]^{2+}$ is only slightly decreasing with increasing reaction time (see Figure 5.13); the corresponding rate coefficient is $k'_1 = 0.10 \pm 0.01$ s. As expected, each experiment in which ACN was present as modifier yields larger k'_1 values. Unfortunately, the absolute ACN mixing ratio in the collision gas is only known for the experiment introducing the premixed gas mixture - 50 ppmV ACN-d3 in He - into the ion trap. Comparing the slopes of the source-ACN measurements, the increase of one magnitude in concentration (0.1 %V to 1 %V ACN in source background gas) is reproduced in the values

5.2 Chemical Modification of the Collision Gas

for k'_1 ($k'_1(0.1\%V) = 0.78 \pm 0.05\text{ s}$ and $k'_1(1\%V) = 8.5 \pm 0.8\text{ s}$) supporting equation (5.7). Accordingly, addition of 0.1 %V ACN to the source gas results in a significantly higher ACN mixing ratio in the collision gas than 50 ppmV. The rate coefficient k'_1 obtained from the ? %V trap-ACN experiment is $41 \pm 1\text{ s}$ and thus the largest value, which is comparable to the value determined subsequent to isolation of $[\text{MH}_2]^{2+}$ at the same trap-ACN mixing ratio ($k'_1 = 49 \pm 2\text{ s}$). According to equation (5.7), the unknown trap-ACN mixing ratio (? %V) can thus be estimated to 0.5 %V using $k'_1(50\text{ ppmV})$ as reference. This result appears to be reasonable, since a small He volume, which was saturated with ACN (11.5 %V), was mixed with pure He to produce the ACN-enriched He flow. These results clearly demonstrate that the decay of $[\text{MH}_2]^{2+}$ follows pseudo-first-order kinetics. Thus the determined rate coefficients strongly depend on the ACN mixing ratio inside the ion trap analyzer: the rate coefficient k'_1 increases with increasing ACN mixing ratio present in the trap (see Figure 5.15a).

For an accurate determination of the rate coefficients and the actual ACN mixing ratios present in the trap, further experiments are required. In addition, simulations of ion trajectories considering collisions with background gas particles and chemical reactions are necessary to validate the experimental data.

Formation of $[\text{MH}]^+$

According to reaction (R 5.3), formation of $[\text{MH}]^+$ generally proceeds via deprotonation reactions of doubly protonated species $[\text{M}(\text{S})_n\text{H}_2]^{2+}$ with $n \geq 0$. Comparison of the time-dependent ion population of the different measurements, see Figures 5.13 and 5.14, suggests that the formation rate of $[\text{MH}]^+$ remains constant (note that the ordinate and the abscissa have a logarithmic scale). Although the relative (and absolute) intensity of the $[\text{MH}]^+$ ion varies between the individual experiments, the intensity of the sum of all doubly protonated species is at least one order of magnitude larger than $I([\text{MH}]^+)$. With $\text{R} = \text{He}$ it applies: $c(\text{R}) \gg c([\text{M}(\text{S})_n\text{H}_2]^{2+}) \gg c([\text{MH}]^+)$ (cf. (R 5.3)). The formation of $[\text{MH}]^+$ is assumed to follow zero-order kinetics [136]; the formation rate is thus described by the following rate equation (5.9):

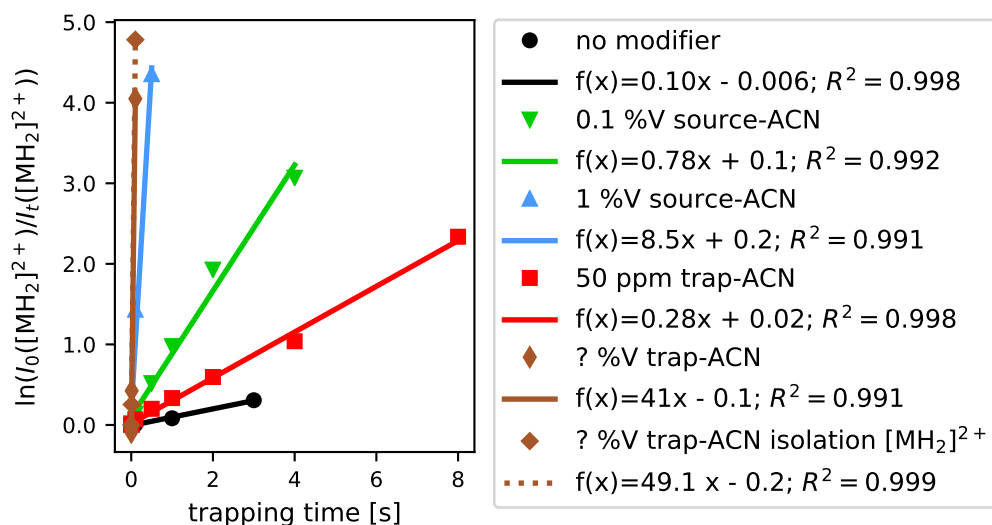
$$\frac{dc([\text{MH}]^+)}{dt} = k'_2. \quad (5.9)$$

Determination of the pseudo-zero-order rate coefficient k'_2 is enabled by integration ($t = 0 \rightarrow t = t$) of the differential rate equation (5.9) and linearization according to the obtained integrated rate law (5.10):

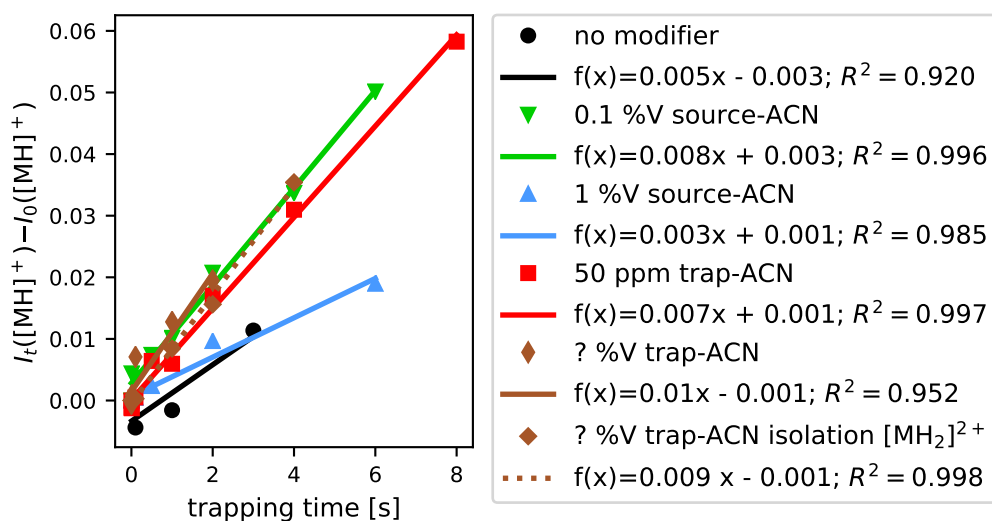
$$c_0([\text{MH}]^+) - c_t([\text{MH}]^+) = k'_2 \cdot t. \quad (5.10)$$

To verify the approach, $I_0([\text{MH}]^+) - I_t([\text{MH}]^+)$ is plotted against the trapping time t , as depicted in Figure 5.15b. Analogous to the kinetic analysis of the $[\text{MH}_2]^{2+}$ decay, the absolute intensities were normalized to the TIC. The linearized plots show

5 Results and Discussion: Terminal Alkyldiamines



(a) Logarithmic relative intensities of $[\text{MH}_2]^{2+}$ (normalized to TIC) in dependence of the trapping time. The slope of each regression line yields the pseudo-first-order rate coefficient k'_1 .



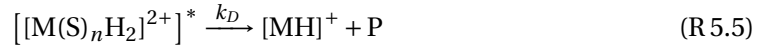
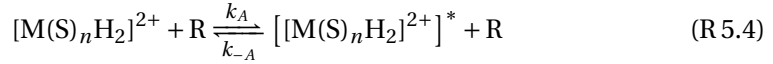
(b) Intensities of $[\text{MH}]^+$ (normalized to TIC) in dependence of the trapping time. The slope of each regression line yields the pseudo-zero-order rate coefficient k'_2 .

Figure 5.15: Determination of reaction rate coefficients of (a) the decay of $[\text{MH}_2]^{2+}$ and (b) the formation of $[\text{MH}]^+$. The corresponding intensity-time-profiles are depicted in Figures 5.13 and 5.14, respectively.

5.2 Chemical Modification of the Collision Gas

satisfactory correlation coefficients supporting the assumption of zero-order kinetics. The slopes of the linear regression lines do not vary significantly nor systematically for the different experiments, taking into consideration the uncertainties of the determined slopes and the partly restricted number of data points. The formation rate of the singly protonated ion is not affected by the ACN mixing ratio nor by the method of ACN addition (source- or trap-ACN). Furthermore, no difference in k'_2 (? %V trap-ACN) is determined between the experiment with ($k'_2 = 0.009 \pm 0.001$ s, see dotted brown slope in Fig. 5.15b) and without isolation ($k'_2 = 0.01 \pm 0.001$ s, see solid brown slope in Fig. 5.15b) of $[\text{MH}_2]^{2+}$, although a large difference in the relative intensity of $[\text{MH}]^+$ was noticed (compare the intensity-time-profiles in Figure 5.14).

The zero-order approach is rationalized by the large excess of $[\text{M}(\text{S})_n\text{H}_2]^{2+}$ ($n \geq 0$) over $[\text{MH}]^+$. Therefore, $c([\text{M}(\text{S})_n\text{H}_2]^{2+})$ is approximately constant - in addition to $c(\text{R})$ - leading to pseudo-zero-order kinetics and $k'_2 = k_2 \cdot c([\text{M}(\text{S})_n\text{H}_2]^{2+}) \cdot c(\text{R})$. It is also conceivable that the formation of $[\text{MH}]^+$ is described by the Lindemann mechanism [211]. The Lindemann mechanism is a reaction mechanism for unimolecular reactions, which is often used to model gas phase decomposition reactions. It is usually applied for reactions of neutral species, but an equivalent mechanism is established for ions [212]. Applying the Lindemann mechanism on reaction (R.5.3), decomposition of $[\text{M}(\text{S})_n\text{H}_2]^{2+}$ yielding $[\text{MH}]^+$ occurs via an activated reaction intermediate, labeled $[[\text{M}(\text{S})_n\text{H}_2]^{2+}]^*$. The activated ion is generated through collisions with a neutral molecule R, e.g. He or another neutral reactant, and can either be collisionally deactivated (rate coefficient k_{-A}) or dissociate (rate coefficient k_D) yielding $[\text{MH}]^+$ and product(s) P.



The steady-state assumption is applied for the activated ion as $c([[\text{M}(\text{S})_n\text{H}_2]^{2+}]^*) \ll c([\text{M}(\text{S})_n\text{H}_2]^{2+})$ [136]. According to the steady-state approximation, the rate of formation of $[[\text{M}(\text{S})_n\text{H}_2]^{2+}]^*$ equals the rate of consumption [136] leading to equation (5.11) for the apparent unimolecular rate coefficient k_2 [212].

$$k_2 = \frac{k_A k_D c(\text{R})}{k_{-A} c(\text{R}) + k_D} \quad (5.11)$$

Since the background gas pressure was not varied and also did not change during each experiment, $c(\text{R})$ is constant. With the assumption that $c([\text{M}(\text{S})_n\text{H}_2]^{2+})$ is also approximately constant over the reaction period considered, a pseudo-zero-order rate coefficient is obtained:

$$k'_2 = \frac{k_A k_D c(\text{R})}{k_{-A} c(\text{R}) + k_D} \cdot c([\text{M}(\text{S})_n\text{H}_2]^{2+}) \quad (5.12)$$

For further study of the formation of $[\text{MH}]^+$, a variation of the pressure inside the ion trap as well as chemical modification of the collision gas by other modifiers, e.g.

5 Results and Discussion: Terminal Alkyldiamines

MeOH or H₂O, should be performed. In addition, the effect of the RF voltage amplitude (trap drive) and thus the field strength inside the trap determining collision energies should be examined to characterize the reaction system and the stability of the cluster ions.

Furthermore, the time-intensity-profiles in Figures 5.13 and 5.14 show that the formation of [MH]⁺ occurs slowly; significant increase in intensity is only observed after 100 ms. As a consequence, the performed measurements only record the beginning of the reaction and, thus, the initial rate of [MH]⁺ production is determined. The initial rate of a reaction can often be modeled by a linear function, especially when the observed time period is short (in relation to the reaction rate) and/or a small number of data points are available. Both aspects apply to the present measurements. Further experiments with longer reaction times or higher ion concentrations are required in order to determine the reaction kinetics, in particular the order of the reaction, with a greater degree of certainty.

The present experimental data clearly demonstrate that the formation of the charge depleted [MH]⁺ ion of 1,9-diaminononane (DA-9) is not affected by the presence of ACN inside the trap; the rate of formation remains constant. Therefore, proton transfer to (ACN)_n (*n* = 0, 1, 2, ..) leading to protonated ACN (clusters) and [MH]⁺ is ruled out. It thus follows that another proton transfer reaction channel (or dissociation process) is responsible for the formation of [MH]⁺.

5.2.5 Implications of Chemical Modification of the Collision Gas for Mass Analysis

The DA-9 experiments presented in the previous section clearly demonstrate that addition of chemical modifiers to the ion source (gas phase modification) leads to chemical modification of the collision gas inside the trap. This was also achieved by addition of ACN directly to the ion trap via the collision gas line (collision gas modification). In both cases, chemical modification leads to intense cluster formation yielding the ionic species [M(ACN)_nH₂]²⁺ with *n* = 1, 2, 3 in the mass spectra; the observed cluster distribution depends on the residence time (trapping time) of the ions inside the trap analyzer (see Figures 5.13 and 5.14). In section 5.1.3 it was suggested that the diamine-ACN clusters are characterized as fragile. In the following, the fragility of [M(ACN)_nH₂]²⁺ is examined.

Effects of Fragile Ions on Mass Resolution and Isolation

For mass analysis, ions are ejected from the ion trap towards the detector. In the present ion traps, ions are excited resonantly using a dipole excitation field, while the amplitude of the RF drive potential is increased to eject ions from the ion trap at increasing *m/z* [155]. As an ion comes into resonance with the resonant ejection frequency, it will gain kinetic energy and undergo collisions with neutral atoms/-

5.2 Chemical Modification of the Collision Gas

molecules present in the trap, primarily He. Inelastic collisions can lead to dissociation. When dissociation occurs, the fragment ion with the lower m/z falls below the low-mass cutoff leading to an unstable trajectory and will thus be quickly ejected from the ion trap. Ion dissociation during ion ejection therefore results in the appearance of peak fronting and a mass shift, called *chemical mass shift*, caused by the premature ejection of the product ion. The mass shift $\Delta m/z$ is calculated by the difference of the measured mass-to-charge ratio m/z_{meas} , as determined by the peak maximum, and the true/theoretical mass-to-charge ratio of the ion m/z_{theo} :

$$\Delta m/z = m/z_{\text{meas}} - m/z_{\text{theo}} \quad (5.13)$$

Therefore, ion dissociation leading to premature ejection results in formal negative values for $\Delta m/z$. In modern commercial ion trap mass spectrometers, only fragile ions lead to the observation of chemical mass shifts caused by fragmentation.¹⁶ Fragile ions are ejected on average earlier than structurally stable ions [209, 210].

Plass and co-workers [210] studied the dependence of the chemical mass shift on the collision gas pressure and the scan rate experimentally and with quantitative simulations. Pressure effects on fragile ions were also examined by Baluya and Yost [213]. McClellan and co-workers [209] investigated the effects of fragile ion ejections on mass resolution and isolation, and developed criteria for the quantification of ion fragility. The investigations on the chemical mass shift of the molecular ion of *n*-butylbenzene, which is a common thermometer ion [208, 210, 214], revealed that the magnitude of the mass shifts depends on the collision gas pressure and is maximized for relatively large pressures, i.e., dissociation and premature ejection of product ions are enhanced as the collision frequency is increased [210, 213]. Decreasing the scan rate at a constant pressure also results in an increasing number of collisions due to the longer time that the ions are in resonance with the ejection field. The ions undergo more collisions and thus gain sufficient internal energy to dissociate. The difference in peak width of fragile ions and stable ions becomes larger as the scan rate decreases [209].¹⁷ Furthermore, McClellan and co-workers¹⁷ noted that in addition to resonant ejection, fragile ions are also fragmented by the application of the isolation waveform in MS/MS experiments. The width of the isolation waveform must be increased and/or the time period of isolation must be decreased to obtain adequate isolation of fragile ions [209].

¹⁶Mass shifts can also be a result of an ejection delay caused by field imperfections in ion traps with non-optimized geometry. These field imperfections result from holes in the end-cap electrodes and can be removed by increasing the end-cap spacing [155, 210]. Modern ion trap mass spectrometers are equipped with geometry-optimized trap analyzers, e.g. the Bruker high-capacity ion trap [154, 155]. Large chemical mass shifts arise as a result of dissociation, whereas field imperfections and elastic scattering cause only small mass shifts. Therefore, in the following the term “chemical mass shift” is related to peak broadening and mass shifts caused by premature ejection of the fragments of fragile ions.

¹⁷This finding of McClellan and co-workers was not reproduced in the DA-9 measurements with varying scan rate, see Figure 5.17a.

Influence of the Collision Gas Pressure on the Peak Shape

Figures 5.16 and 5.17 show mass spectra of DA-9 sprayed from MeOH/H₂O with exposure to ACN vapor in the ion source (source-ACN). Regular scans, i.e., without additional cooling in the trap analyzer, were recorded in the depicted experiments; therefore only the first and second ACN cluster are clearly discernible in the mass spectra (cf. Figure 5.13). The third cluster was hardly detected, thus only the m/z range 75 – 125 is shown in Figures 5.16 and 5.17. Comparison of the peak shapes of the bare doubly protonated species, [MH₂]²⁺, and the cluster species [M(ACN)H₂]²⁺ and [M(ACN)₂H₂]²⁺ reveals a significant peak broadening and fronting (chemical mass shift) of the cluster signals.

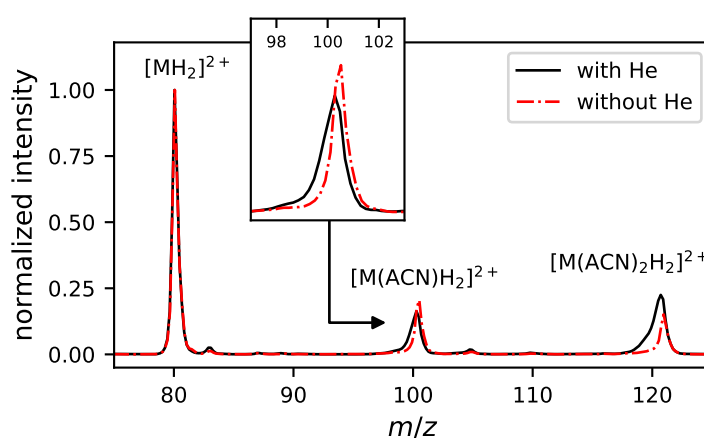


Figure 5.16: Mass spectrum of 1,9-diaminononane (DA-9) with (black, solid line) and without (red, dashdotted line) addition of the collision gas He to the ion trap analyzer. 0.1 %V ACN was added to the ion source (source-ACN). Mass spectra were recorded with the QIT-MS (esquire3000), method [MH₂]²⁺ (scan rate = 26000 m/zs^{-1}).

In accord with the work of Plass and co-workers [210] as well as of Yost and Baluya [213], the collision gas pressure has a strong impact on the extent of the chemical mass shift, as shown in Figure 5.16. The absolute pressure in the ion trap analyzer is unknown; only the background pressure present in the chamber surrounding the ion trap and the detector is recorded by the instrument. Switching off the He flow, a background pressure of 5.3×10^{-6} mbar was measured during the mass scan depicted in Figure 5.16 (without He). A background pressure of 9.6×10^{-6} mbar was recorded, when He was added as collision gas. Comparing the mass scans, a difference between the stable ion [MH₂]²⁺ and the presumably fragile ions [M(ACN)H₂]²⁺ and [M(ACN)₂H₂]²⁺ is clearly discernible. The peak width and shape as well as the position of the maximum intensity of the [MH₂]²⁺ signal do not change in the two

experiments. In contrast, both cluster signals become narrower and more symmetric and the peak maxima are shifted to higher m/z when the collision gas is switched off (see Figure 5.16, in particular, the enlarged section of the mass spectrum showing the $[\text{M}(\text{ACN})\text{H}_2]^{2+}$ signal). The positions of the peak maxima recorded without He (m/z 100.52 and 120.95) match much better with the monoisotopic molecular mass-to-charge ratios of $[\text{M}(\text{ACN})\text{H}_2]^{2+}$ (m/z 100.61) and $[\text{M}(\text{ACN})_2\text{H}_2]^{2+}$ (m/z 121.12).¹⁸ In other words, the mass shift $\Delta m/z$ (cf. eq. (5.13)) decreased from -0.33/-0.41 to -0.09/-0.17, respectively, upon pressure reduction.

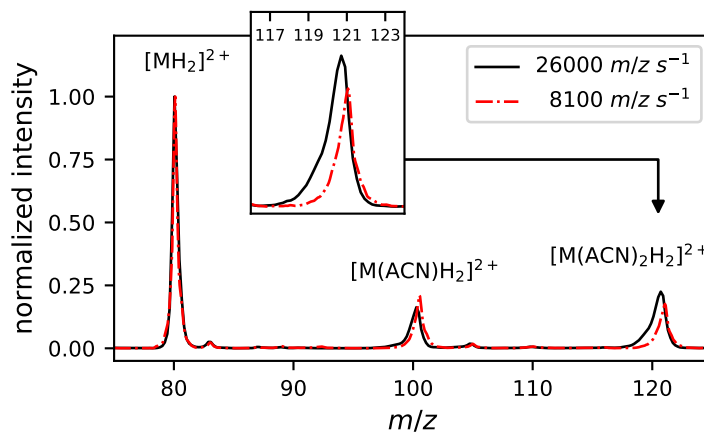
Switching off the collision gas leads to a decrease of the TIC and the signal intensity of $[\text{MH}_2]^{2+}$ by a factor of four. When the kinetic energy of the ions after injection is not reduced via buffer gas collisions, the kinetic energy may be sufficiently high for ions to escape immediately from the trap. Therefore, a lower number of ions are trapped when He was switched off. The observed increase in intensity (and the observed increase in peak width) induced by the pressure increase is in accord with the work of Yost and Baluya [213]. Their studies revealed a positive correlation between the signal intensity of the molecular ion of *n*-butylbenzene and the collision gas pressure (and a negative correlation between the mass assignment and the pressure, as mentioned above) [213]. They stated that “buffer gas is needed during ion injection in order to trap the ions efficiently, while the presence of buffer gas during ion detection can affect analysis of fragile ions and cause mass shifts.” They suggested a pulsed valve system to allow the pressure to be tailored for individual sections in the scan function (e.g. injection, excitation (CID), ejection) [213].

Influence of the Scan Rate on the Peak Shape

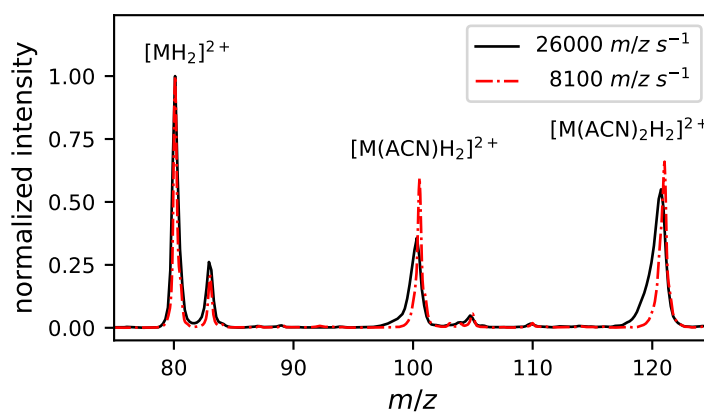
Similar effects regarding the peak shape of the cluster ions were observed upon variation of the scan rate (measured in $m/z s^{-1}$), i.e., the speed with which the amplitude of the RF drive potential is increased to progressively eject ions according to their m/z value. Mass spectra of DA-9 recorded with two different scan rates are compared to each other in Figure 5.17. The results of the experiment in the presence of 0.1 %V source-ACN, are shown in Figure 5.17a; addition of 1 %V source-ACN leads to the spectra depicted in Figure 5.17b. Both comparisons clearly demonstrate that a reduction of the scan speed (from 26000 $m/z s^{-1}$ to 8100 $m/z s^{-1}$) results in detection of significantly more symmetric and narrower peaks for the cluster signals $[\text{M}(\text{ACN})\text{H}_2]^{2+}$ and $[\text{M}(\text{ACN})_2\text{H}_2]^{2+}$. In addition, the peak maxima are shifted to higher m/z values, when the scan rate is decreased; the chemical mass shift is correspondingly lowered. For example, the position of the peak maximum of $[\text{M}(\text{ACN})\text{H}_2]^{2+}$, depicted in the enlarged section in Figure 5.17a, shifts from 120.71 ($\Delta m/z = 0.41$) to 121.06 ($\Delta m/z = 0.06$) and, simultaneously, the full width at half maximum (FWHM) decreases from 1.2 to 0.8. In contrast, the variation of the scan rate alters only slightly the peak shape of the bare $[\text{MH}_2]^{2+}$ ion; a small decrease of

¹⁸All mass spectra were recalibrated with theoretical m/z values of the signals of the stable ions $[\text{MH}_2]^{2+}$ and $[\text{MH}]^+$.

5 Results and Discussion: Terminal Alkyldiamines



(a) Mass signals of $[\text{MH}_2]^{2+}$, $[\text{M}(\text{ACN})\text{H}_2]^{2+}$ and $[\text{M}(\text{ACN})_2\text{H}_2]^{2+}$ recorded with a scan rate of 26000 m/z s^{-1} (black, solid line) and 8100 m/z s^{-1} (red, dashdotted line). 0.1 %V ACN were added as modifier to the ion source.



(b) Mass signals of $[\text{MH}_2]^{2+}$, $[\text{M}(\text{ACN})\text{H}_2]^{2+}$ and $[\text{M}(\text{ACN})_2\text{H}_2]^{2+}$ recorded with a scan rate of 26000 m/z s^{-1} (black, solid line) and 8100 m/z s^{-1} (red, dashdotted line). 1 %V ACN were added as modifier to the ion source.

Figure 5.17: Section of the mass spectrum of 1,9-diaminononane (DA-9) recorded with two different scan rates. ACN was added to the ion source: (a) 0.1 %V source-ACN, (b) 1 %V source-ACN. Mass spectra were recorded with the QIT-MS (esquire3000), method $[\text{MH}_2]^{2+}$.

the peak width with decreasing scan rate is visible for $[\text{MH}_2]^{2+}$ in Figure 5.17b. Generally, decreasing the scan rate results in a narrowing of the peak width and thus an increase of the mass resolution, mainly because the ions dwell longer in the excitation field, i.e., the ions experience a higher number of resonant oscillations before ejection [155,215]. Considering fragile ions, increasing the dwell time in which ions are in resonance with the ejection frequency may lead to a greater likelihood for dissociation and thus to peak fronting and broadening [209]. The mass spectra depicted in Figure 5.17 clearly show that decreasing the scan rate results in enhanced mass resolution for both bare and clustered doubly protonated ions of DA-9; the peak width of the cluster ions is improved even to a greater extent. The increasing peak width of fragile (clustered) ions as compared to stable ions at slower scan rate, as reported by McClellan and co-workers [209], was not reproduced in the DA-9 experiments. However, the peak width of the clustered ions is always greater than the peak width of the bare ions, which represents an important figure of merit for ion fragility.

Isolation and Excitation Processes

The minimum isolation width is a further figure of merit for ion fragility. McClellan and co-workers suggested that when the minimum isolation width - defined as the narrowest width providing an isolation intensity of 90 % of the maximum isolated ion intensity - equals 2.5 or larger, the ion is classified as fragile [209]. The influence of the isolation width on the isolation intensity was studied with the diamines DA-5 and DA-9. In both cases, isolation of $[\text{MH}_2]^{2+}$ led to isolation intensities > 90 %, even with an isolation width of 1. Varying the isolation width between 1 and 5 did not affect the isolation intensity of $[\text{MH}_2]^{2+}$, as expected for a stable ion [209]. In contrast, isolation of the cluster species was challenging. Despite a signal intensity of approximately 5×10^5 counts, isolation of $[\text{M}(\text{ACN})\text{H}_2]^{2+}$ did not generate a proper mass spectrum (i.e., contained less than 200 counts), even when the isolation width was increased to 9. In addition, mass selective excitation (with an amplitude of 0.2 V) resulted in complete loss of the $[\text{M}(\text{ACN})\text{H}_2]^{2+}$ signal when the selected target mass was in the range of $m/z([\text{M}(\text{ACN})\text{H}_2]^{2+}) \pm 2$ and in a significant reduction in intensity in the range of $m/z([\text{M}(\text{ACN})\text{H}_2]^{2+}) \pm 3$. When the isolation waveform is applied, energy is supplied at specific frequencies to eject all ions above and below the m/z range of the isolation width. The waveform will also impart some kinetic energy to ions that are to be isolated. This energy uptake may lead to collisional dissociation and can be reduced by increasing the isolation width [209]. In analogy, the mass selective excitation process occurs theoretically at a specified frequency, but space charge effects and nonlinear field components can lead to observation of broad resonances [216]. Therefore, isolation using a narrow isolation width as well as resonant excitation of close m/z values may lead to dissociation of fragile ions.

As mentioned above, isolation of cluster species was challenging in the experiments: $[\text{MH}_2]^{2+}$ of DA-5 was isolated and trapped for 2 s to react with ACN generating the first cluster, $[\text{M}(\text{ACN})\text{H}_2]^{2+}$. Subsequently, $[\text{M}(\text{ACN})\text{H}_2]^{2+}$ could be isolated

5 Results and Discussion: Terminal Alkyldiamines

with an isolation width of ≥ 2 leading to an isolation efficiency of only 3%. Due to the long trapping/reaction time, the cluster ions may gain lower kinetic as well as internal energies leading to delayed energy uptake for the dissociation to occur. In addition, isolation of $[\text{MH}_2]^{2+}$ decreases the amount of ions present inside the ion trap minimizing space charge effects.

Degree of Ion Fragility

In the conducted experiments, the second ACN cluster, $[\text{M}(\text{ACN})_2\text{H}_2]^{2+}$, shows a larger mass shift as well as a more pronounced peak fronting and broadening. These results suggest that $[\text{M}(\text{ACN})_2\text{H}]^{2+}$ has a higher degree of ion fragility. The degree of ion fragility - in other words the likelihood for ion dissociation occurring during ejection - depends on several structure-dependent properties. The clusters $[\text{M}(\text{ACN})\text{H}_2]^{2+}$ and $[\text{M}(\text{ACN})_2\text{H}_2]^{2+}$ differ with regard to: (1) the solvation energy, as $-\Delta G_{n,n+1}^\circ$ decreases with n and, therefore, the second ACN molecule is more loosely bound to the doubly protonated diamine facilitating dissociation; (2) the collision cross section, as it increases with n and, thus, the number of potentially energetic collisions during ejection, and (3) the number of internal degrees of freedom increases, among which the internal energy is statistically distributed. The first and the second point supports the notion that the second cluster, $[\text{M}(\text{ACN})\text{H}_2]^{2+}$, exhibits a higher degree of ion fragility, whereas the third point does not: The second cluster showed a higher degree of fragility under the given experimental conditions, which is explained by a smaller solvation energy and a larger collision cross section. Further experiments - including variation of the background pressure, excitation amplitude, ion loading, and trapping time - are required for an in-depth analysis of the deactivation (cooling) and activation (excitation) effects, including ion fragility, of the diamine-ACN clusters. These competitive effects control the average internal energy deposition into the ions in the ion trap [214].

In summary, the experimental results clearly show that the cluster ions $[\text{M}(\text{ACN})\text{H}_2]^{2+}$ and $[\text{M}(\text{ACN})_2\text{H}_2]^{2+}$ of DA-5 and DA-9 are characterized as fragile ions, whereas the bare $[\text{MH}_2]^{2+}$ ion shows no sign of ion fragility.

5.3 Theoretical Investigations of Ion-Solvent Clusters

The theoretical studies are conducted for 1,2-diaminoethane (DA-2), in the following termed ethylenediamine (EDA),¹⁹ to save computational time. In the mass spectrometric experiments, ethylenediamine was rarely used as analyte because of the low molecular mass. However, the set of observed analyte (cluster) species in the mass spectrometric experiments provides a basis for the geometry optimization. In the nanoESI-MS experiments, the analytes were generally sprayed from ACN/H₂O and analyte-ACN clusters were observed, at least when ACN vapor was added to the gas phase. The ion mobility measurements were conducted using ethylenediamine as target molecule with acetonitrile and water as solvents. Therefore, clusters consisting of one or two EDA molecules, various ACN or H₂O molecules, and one or two protons are considered. Since the IMS (see section 3.1.3) operates at low-field conditions (reduced field strength of ≈ 2.7 Td) and the residence time of the ions is in the millisecond range, a fully equilibrated reaction system is assumed; therefore, thermochemical data are calculated. The aims of the theoretical investigations are to (1) determine potential cluster structures, (2) assess the thermodynamic stability of the individual clusters and the thermochemistry of cluster and ligand switch reactions, (3) calculate equilibrated cluster distributions, and (4) calculate the corresponding ion mobilities at different solvent gas phase concentrations by means of modeled collision cross sections. This procedure allows a comparison between theoretically and experimentally determined cluster distributions and ion mobilities to be made. Furthermore, using the thermochemical data, the Gibbs free energy of a reaction ($\Delta_R G$) is calculated and thermodynamically favored reaction pathways are identified. The theoretical investigations aid in getting a better understanding of the highly dynamic ion-solvent cluster equilibria in atmospheric pressure ionization sources; these equilibria are crucial elements of the charge retention/charge depletion mechanism (cf. section 4.4).

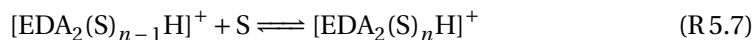
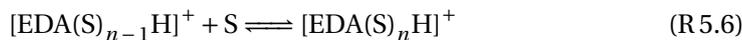
5.3.1 Cluster Structures and Thermochemistry

Based on the observed ionic species of ethylenediamine (EDA) and the other alkyldiamines, cf. Figure 5.3, geometry optimizations (cf. section 3.2.1) of various EDA-ACN and EDA-H₂O clusters were performed. The singly and doubly protonated EDA species, [EDA_H]⁺ and [EDA_H₂]²⁺, as well as the proton bound dimer, [EDA₂H]⁺, clustered with numerous ACN or H₂O were considered. Mixed solvent-EDA clusters, [EDA(ACN)_n(H₂O)_mH_z]^{z+}, were not taken into account. Each cluster reaction system is described by an equilibrium reaction (analogous to reaction (R 2.5)), where S

¹⁹Usually, ethylenediamine is shortened to EDA. In the previous sections, DA-2 was used as acronym for 1,2-diaminoethane and ethylenediamine, respectively, to accentuate the length of alkyl chain with the label, which was suitable for the systematic comparison of the different diamines. Regarding the cluster structures and their molecular formulae, EDA is a more useful abbreviation.

5 Results and Discussion: Terminal Alkyldiamines

(solvent) is H₂O or ACN:



Multiple configurations were modeled for most cluster species. Besides the structure, the Gibbs free energy corrected total electronic energy $\mathcal{E}_0 + G_{\text{corr}}$ is obtained for every configuration. Only the minimum energy structures and the corresponding energies are used for the determination of $\Delta_R G^\circ$ (according to Hess' law, cf. equations (3.1) and (3.2)), the collision cross sections, and the mean ion mobilities (via equation (3.7)), respectively.

Sequential Solvation by H₂O and ACN

To evaluate the thermodynamic stability of the individual EDA-solvent clusters, $\Delta_R G^\circ$ of each cluster growth step (R5.6), (R5.7) and (R5.8) is calculated. In Table 5.2 the $\Delta_R G^\circ$ values of the sequential solvation reactions are compiled. In Figure 5.18, the calculated $-\Delta_R G^\circ$ values, in the following termed $-\Delta G_{n-1,n}$, are plotted against the cluster number n for each cluster species, illustrating the different behavior of the solvents H₂O and ACN with regard to the three diaminic core ions. The experimentally determined values from Meot-Ner and co-workers [81] for the hydration of $[\text{EDA}(\text{S})_n\text{H}]^+$ are also shown.

Generally, the largest amount of energy is released when the first solvent molecule binds to an EDA ion; in this case, $-\Delta G_{0,1}$ is about two times higher for ACN than for H₂O. As the cluster number n increases, $-\Delta G_{n-1,n}$ decreases, as it is expected for sequential/stepwise solvation (cf. section 2.2.1); for the solvation by ACN this decline is less sharp. As a consequence, formation of $[\text{EDA}(\text{ACN})_5\text{H}]^+$ and $[\text{EDA}_2(\text{ACN})_4\text{H}]^+$ becomes endergonic ($\Delta_R G^\circ > 0$, cf. Table 5.2). A less steep and more uniformly decrease in $-\Delta G_{n-1,n}$ is observed for the hydration of each species. This trend is in qualitative agreement with the experimentally determined $-\Delta G_{n-1,n}$ of $[\text{EDA}(\text{S})_n\text{H}]^+$. The difference of the theoretically and experimentally determined $-\Delta G_{n-1,n}$ values is caused by taking only individual minimum energy structures and their corresponding energies into account. In contrast, an ensemble of all conformers and isomers is present in the experiment leading to lower $-\Delta G_{n-1,n}$ values. Intramolecular hydrogen bonds within $[\text{EDAH}]^+$ leading to a cyclic structure is adding to this effect. Figure 5.19 shows the cyclic and the open structure of $[\text{EDAH}]^+$. Computational studies found that in the gas phase the cyclic conformer of $[\text{EDAH}]^+$ is lower in energy than the open conformer [107–109]. Since the EDA ions were generated by chemical ionization in the gas phase [81], the experimentally determined solvation energies mainly derive from $[\text{EDAH}]^+$ ions, which are solvated by internal hydrogen bonds. As internal solvation generally lessens external solvation, the positive deviation of the calculated from the experimental $-\Delta G_{n-1,n}$ values is comprehensible.

5.3 Theoretical Investigations of Ion-Solvent Clusters

Table 5.2: Change of Gibbs free energy $\Delta_R G^\circ$ at standard conditions in kJ/mol for the reactions $[\text{EDA}(\text{S})_{n-1}\text{H}]^+ + \text{S} \rightarrow [\text{EDA}(\text{S})_n\text{H}]^+$, $[\text{EDA}(\text{S})_{n-1}\text{H}_2]^{2+} + \text{S} \rightarrow [\text{EDA}(\text{S})_n\text{H}_2]^{2+}$, and $[\text{EDA}_2(\text{S})_{n-1}\text{H}]^+ + \text{S} \rightarrow [\text{EDA}_2(\text{S})_n\text{H}]^+$, where S is H_2O or ACN

Species	n	$\Delta_R G^\circ$		Species	n	$\Delta_R G^\circ$	
		S= H_2O	S=ACN			S= H_2O	S=ACN
$[\text{EDA}(\text{S})_n\text{H}]^+$	1	-36.0(31.7 ^a)	-73.3	$[\text{EDA}(\text{S})_n\text{H}_2]^{2+}$	1	-80.6	-141.7
	2	-34.1(20.4 ^a)	-47.3		2	-76.0	-122.4
	3	-24.9(11.9 ^a)	-37.0		3	-56.6	-88.0
	4	-19.0	-9.5		4	-52.0	-87.1
	5	-11.7	+1.5		5	-46.1	-58.7
$[\text{EDA}_2(\text{S})_n\text{H}]^+$	1	-24.2	-49.9	6	-40.8	-55.1	
	2	-20.9	-41.1	7	-24.2	-16.0	
	3	-12.2	-10.6	8	-22.6	-5.1	
	4	-6.2	+1.9	9	-18.1	-10.7	

^a Experimentally determined values from Meot-Ner and co-workers [81].

Regarding the solvation of ACN one or more sharp steps of the $-\Delta G_{n-1,n}$ values are found for all species at certain cluster steps $n \rightarrow n+1$: $[\text{EDA}(\text{ACN})_n\text{H}]^+$ $n=3 \rightarrow 4$, $[\text{EDA}_2(\text{ACN})_n\text{H}]^+$ $n=2 \rightarrow 3$, and $[\text{EDA}(\text{ACN})_n\text{H}_2]^{2+}$ $n=2 \rightarrow 3$, $n=4 \rightarrow 5$, $n=6 \rightarrow 7$. Each cluster number n refers to a closed solvent shell cluster [103, 113, 217] and is termed $n_S(\text{ACN})$ (cf. section 2.2.1). The effect of closed solvent shell clusters is visible, in particular, for the doubly protonated ion $[\text{EDA}(\text{S})_n\text{H}_2]^{2+}$. Here, also small steps in the solvation energy are observed for the solvation by H_2O at $n=2 \rightarrow 3$ and $n=6 \rightarrow 7$. For diaminic ions the occurrence of closed solvent shell clusters, accompanied by steep decreases in $-\Delta G_{n-1,n}$ is rationalized as follows. For singly protonated diaminic ions, e.g. $[\text{EDA}(\text{ACN})_n\text{H}]^+$, a gradual decrease of $-\Delta G_{n-1,n}$ is expected when the first (inner) shell with three solvent molecules is built up. The fourth solvent molecule has to begin a second shell, since all protic hydrogens are occupied [82, 83]. H_2O can hydrogen-bond to an inner shell H_2O molecule, whereas the fourth ACN molecule interacts only weakly with the inner-shell ACN molecules, leading to a large drop in energy at $n=3 \rightarrow 4$ (cf. left panel in Figure 5.18). For doubly protonated diaminic ions, e.g. $[\text{EDA}(\text{ACN})_n\text{H}_2]^{2+}$, one expects a different situation, since solvation of two separate protonated amino groups occurs and the solvent molecules are distributed between them [82]. The first two solvent molecules go each to the protonated amino groups. Since the third and fourth solvent molecule occupy similar positions, the solvation energies $-\Delta G_{2,3}$ and $-\Delta G_{3,4}$ exhibit similar values; the same will apply to the fifth and sixth molecule ($-\Delta G_{4,5}$ and $-\Delta G_{5,6}$). Large energy drops arise between the

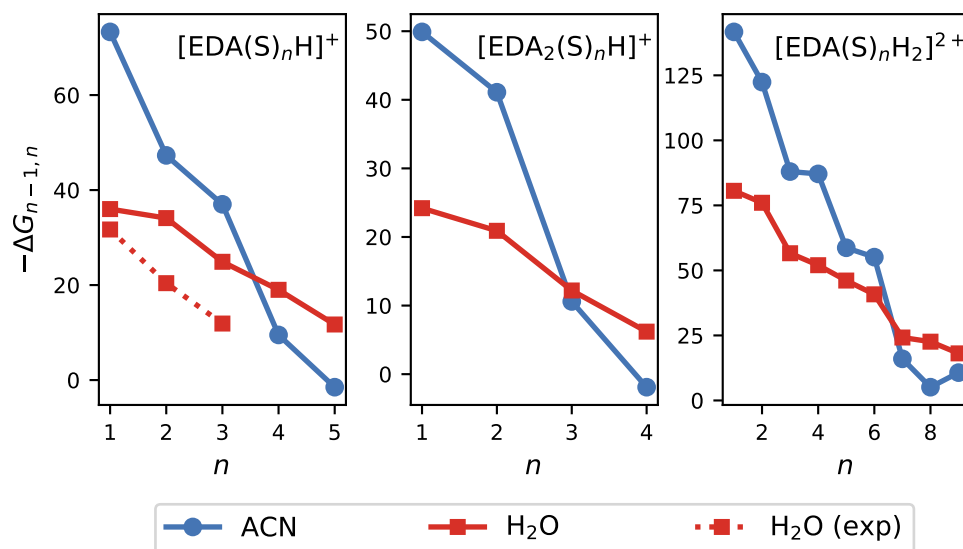


Figure 5.18: Calculated solvation energy $-\Delta G_{n-1,n}$ of the sequential solvation of the protonated ethylenediamine (EDA) species, $[\text{EDA}(\text{S})_n\text{H}]^+$ (*left*), $[\text{EDA}_2(\text{S})_n\text{H}]^+$ (*center*), and $[\text{EDA}(\text{S})_n\text{H}_2]^{2+}$ (*right*) for ACN and H_2O versus the cluster number n . For determination of $-\Delta G_{n-1,n}$ only the optimized global minimum energy structures and their corresponding energies are used. The experimentally determined values for H_2O (exp) were taken from ref. [81].

second and the third, the fourth and the fifth, and the sixth and the seventh solvent molecule. The resulting pattern are clearly discernibly - particularly for ACN - in the right panel of Figure 5.18. Considering a dimeric ion, e.g. $[\text{EDA}_2(\text{ACN})_n\text{H}]^+$, one proton is shared between the two EDA molecules. Therefore, only two protic hydrogens are available for hydrogen bonding leading to $n_S(\text{ACN}) = 2$. In the following, the term closed solvent shell cluster and the cluster number $n_S(\text{ACN})$ refers to these clusters: $[\text{EDA}(\text{ACN})_3\text{H}]^+$, $[\text{EDA}(\text{ACN})_2\text{H}_2]^{2+}$, and $[\text{EDA}(\text{ACN})_6\text{H}_2]^{2+}$.

Since $-\Delta G_{n-1,n}$ of the stepwise hydration declines less steeply and more uniformly, $-\Delta G_{n-1,n}$ of H_2O exceeds the values of ACN at $n > n_S(\text{ACN})$ (cf. Figure 5.18). The structural differences of H_2O (protic solvent) and ACN (aprotic solvent) and their EDA clusters, respectively, are discussed in the following in reference to the modeled cluster structures with $n = n_S(\text{ACN}) + 1$.

$[\text{EDA}(\text{S})_n\text{H}]^+$ In Figure 5.20 selected $[\text{EDA}(\text{S})_4\text{H}]^+$ clusters are shown. For simplicity reasons, EDAH^+ is considered in the open structure, i.e., without intramolecular proton binding between the protonated and unprotonated amine group (cf. Figure

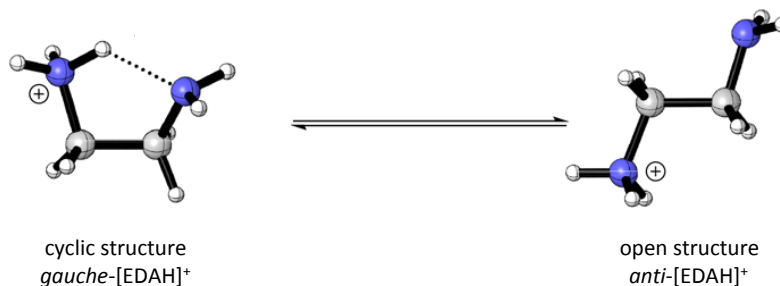


Figure 5.19: Structure of the cyclic (*gauche*) and the open (*anti*) conformer of protonated ethylenediamine, $[\text{EDA}(\text{H})_2]^+$. The intramolecular H-bond in the cyclic structure is indicated by the dotted line. Reprinted with permission from [108]. ©2018 American Chemical Society.

5.19).²⁰ As mentioned above, the fourth solvent molecule can not directly hydrogen-bond to one of the three protic hydrogens of the protonated amine (which represents the charge site) because these positions are already occupied. In the minimum energy structure of $[\text{EDA}(\text{H}_2\text{O})_4\text{H}]^+$ the fourth H_2O molecule interacts via H-bridges with one H_2O molecule binding to the charge site and with the nitrogen atom of the neutral amino group. In the optimized structure the H-N distance between the H-atom of the fourth H_2O and the nitrogen atom of the neutral amine is 1.88 Å and the H-O distance between the two water molecules amounts to 1.75 Å. When comparing the hydrogen bond lengths and angles with Jeffrey's classification of hydrogen bonds [218] all five H-bonds in $[\text{EDA}(\text{S})_4\text{H}]^+$ are characterized as *moderate (medium)* and thus the type of interaction as *dominant electrostatic*.²¹ Therefore, the bond characteristics of the four H_2O molecules in the cluster are comparable; this is reflected in the less pronounced and rather monotone decrease of $-\Delta G_{n-1,n}$ for hydration of $[\text{EDA}(\text{S})_n\text{H}]^+$ (cf. left panel in Figure 5.18). Due to the ability of H_2O to interact with other H_2O molecules via hydrogen bonding, the stability of the clusters declines slightly with increasing number of bound H_2O molecules. Therefore, $[\text{EDA}(\text{H}_2\text{O})_n\text{H}]^+$ clusters with even $n > 5$ may be stable and formed at sufficiently high H_2O mixing ratios.

Two minimum energy structures, $[\text{EDA}(\text{ACN})_4\text{H}]^+\text{a}$ and $[\text{EDA}(\text{ACN})_4\text{H}]^+\text{b}$, which are energetically equivalent, are calculated for $[\text{EDA}(\text{ACN})_4\text{H}]^+$ (cf. Figure 5.20). In the conformation $[\text{EDA}(\text{ACN})_4\text{H}]^+\text{a}$ the fourth ACN molecule coordinates with the CN lone pair to the $\text{C}_2\text{H}_4\text{NH}_2$ -chain; the shortest N-H distance (2.37 Å) is found for the hydrogen of the amine. Considering the different N-H distances and bond angles,

²⁰Conformers for $\text{EDA}(\text{H})^+$ and EDA_2H^+ considering inter- and intramolecular hydrogen bonds are discussed in detail in [108].

²¹Strong (proton-shared) H-bonds are classified as strongly covalent and ionic, respectively, and weak (conventional) H-bonds result from electrostatic and dispersion interactions. For the detailed description of the classification criteria see [218].

5 Results and Discussion: Terminal Alkyldiamines

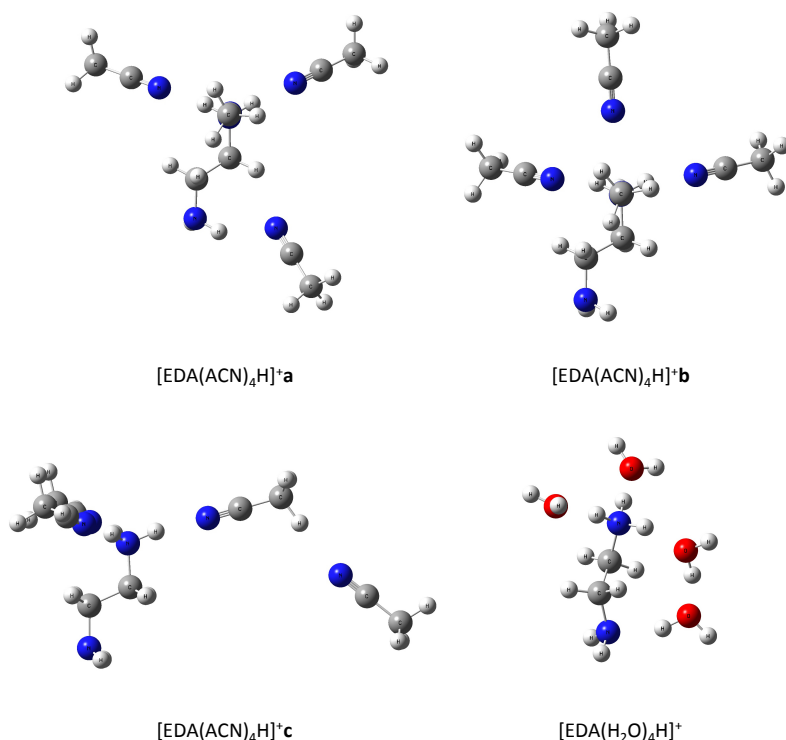


Figure 5.20: Optimized geometries of the $[\text{EDA}(\text{ACN})_4\text{H}]^+$ and $[\text{EDA}(\text{H}_2\text{O})_4\text{H}]^+$ clusters. $[\text{EDA}(\text{ACN})_4\text{H}]^+$ a and $[\text{EDA}(\text{ACN})_4\text{H}]^+$ b (linear NH_3 attack) represent the minimum energy structures, $[\text{EDA}(\text{ACN})_4\text{H}]^+$ c (linear CH attack) is 4.08 kJ/mol less stable. For $[\text{EDA}(\text{H}_2\text{O})_4\text{H}]^+$ only the global minimum structure is shown.

it seems that the binding situation does not represent a classical H-bond but rather a weak interaction between the CN lone pair and the $\text{C}_2\text{H}_4\text{NH}_2$ -group, which may be described as three weak H-bonds. In the conformation, $[\text{EDA}(\text{ACN})_4\text{H}]^+$ b, the fourth ACN binds to the NH_3 -group, which represents the charge site. This geometry results from a linear NH_3 attack.²² In addition, the structures resulting from the linear CH attack and the π attack were studied.²³ The geometry resulting from the linear CH attack, $[\text{EDA}(\text{ACN})_4\text{H}]^+$ c, is energetically comparable (4.1 kJ/mol relative to the global minimum structure) and is formed in an exergonic reaction ($\Delta_R G^\circ = -5.4$ kJ/mol);

²²Linear NH_3 attack refers to a coaxial alignment of the ACN main bond axis (N-C-C) with the N-C bond axis of the amino group.

²³The linear CH as well as the linear CH_3 attack are known from the optimized geometries of $(\text{ACN})_n\text{H}^+$ and $(\text{ACN})_n\text{Li}^+$ [91,219]. For the proton-bound ACN trimer, $(\text{ACN})_3\text{H}^+$, Haack and co-workers found a minimum structure where the third ACN binds through an interaction of the CN lone pair with the π -system of another ACN molecule (π attack) [165].

5.3 Theoretical Investigations of Ion-Solvent Clusters

hence the presence of this isomer in a thermodynamic equilibrium is possible. The π attack approach for $[\text{EDA}(\text{ACN})_4\text{H}]^+$ results in a thermodynamically less stable geometry (19.1 kJ/mol relative to the global minimum structure) formed in an endergonic reaction ($\Delta_R G^\circ = 9.6$ kJ/mol). Interestingly, a π interaction is observed for the global minimum structure of $[\text{EDA}(\text{ACN})_5\text{H}]^+$, which is, however, formed in an endergonic reaction (cf. Table 5.2).

Therefore, the comparison of the optimized geometries of $[\text{EDA}(\text{S})_n\text{H}]^+$ supports the assumption that the formation of moderate hydrogen bonds between the individual solvent molecules is crucial for the stabilization of large ion-solvent clusters. Since each H_2O molecule can form two H-bonds, the number of H_2O molecules binding to an $[\text{EDA}(\text{H})]^+$ ion is not limited by the number of protic hydrogen atoms provided by the ion, as in the case of ACN. The key role of inter- and intramolecular hydrogen bonding is described comprehensively for $[\text{EDA}(\text{H}_2\text{O})_3\text{H}]^+$ by Boo and co-workers [166].

$[\text{EDA}_2(\text{S})_n\text{H}]^+$ ACN and H_2O clusters of the proton bound dimer were studied assuming a simple configuration for the $[\text{EDA}_2\text{H}]^+$ molecule: both EDA molecules (having the open structure, cf. Figure 5.19) interact with their amine function via an H-bond with the proton. These two H-bonds binding the proton are not equally long (1.12 Å and 1.60 Å) so that one amine group is preferably solvated due to the increased charge density. Duncan and co-workers discussed isomers of the protonated EDA dimer, where the proton is stabilized by more than two proton bridges due to intramolecular interactions resulting from cyclisation [108]. In these conformers the proton is more shielded and diluted (due to the further hydrogen bonding), thus less pronounced clustering with solvent molecules is expected. Therefore and for simplicity reasons, only the conformation with two H-bonds binding the proton (termed open structure analogous to $[\text{EDA}(\text{H})]^+$) is considered (cf. Figure 5.21).

As already mentioned, one amino group is preferably solvated; after the addition of two solvent molecules the two available protic hydrogen atoms are occupied and the third solvent has to bind to the less preferred amino group of the other EDA molecule (in the case of ACN) or to one of the solvent molecules (in the case of H_2O), according to the global minimum structures depicted Figure 5.21. The addition of the third ACN weakens the existing H-bonds due to electrostatic repulsion of the ACN molecules and charge dilution: the N-H-N bond angles decrease and the bond lengths increase; whereas binding the third H_2O to the existing H_2O shortens the H-bond of the latter. Here again, the structural differences between H_2O and ACN and their different ability to establish moderate H-bonds between them may explain the different decrease of the cluster stability for $n > 2$ (cf. Figure 5.18).

$[\text{EDA}(\text{S})_n\text{H}_2]^{2+}$ The doubly protonated EDA has six equivalent protic hydrogen atoms, which all can bind one solvent molecule via linear hydrogen bonding. Closed solvent shell clusters were found for $n_S(\text{ACN}) = 2, 4, 6$. The largest drop in solvation

5 Results and Discussion: Terminal Alkyldiamines

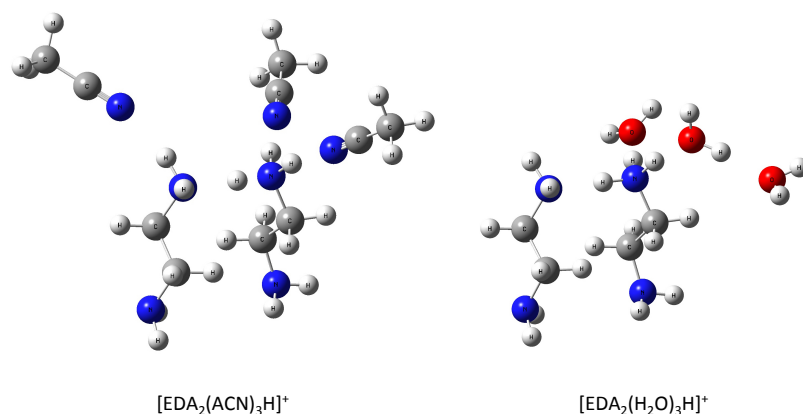


Figure 5.21: Optimized geometries of the $[\text{EDA}_2(\text{ACN})_3\text{H}]^+$ and $[\text{EDA}_2(\text{H}_2\text{O})_3\text{H}]^+$ clusters. Only the minimum energy structures are shown.

energy was observed for the cluster step $n = 6 \rightarrow 7$. Therefore, the optimized structures of $[\text{EDA}(\text{S})_7\text{H}_2]^{2+}$ are discussed in the following.

In the minimum structure of $[\text{EDA}(\text{H}_2\text{O})_7\text{H}_2]^{2+}$ the seventh H_2O molecule binds via an H-bond (1.72 Å) to another H_2O molecule (cf. Figure 5.22). As observed for $[\text{EDA}_2(\text{H}_2\text{O})_3\text{H}]^+$, the already existing hydrogen bond between the sixth H_2O molecule and the hydrogen of the NH_3 group is shortened upon binding the seventh H_2O . The bond characteristics of the seven H_2O molecules in the cluster are comparable regarding the bond lengths and angles and are characterized as moderate. For $[\text{EDA}(\text{ACN})_7\text{H}_2]^{2+}$ three energetically similar structures are calculated (cf. Figure 5.22), which are all formed in exergonic reactions. Analogous to the structures of $[\text{EDA}(\text{ACN})_4\text{H}]^+$, the interaction between the CN lone pair and the $\text{C}_2\text{H}_4\text{NH}_2$ -group, $[\text{EDA}(\text{ACN})_7\text{H}_2]^{2+}\text{a}$, the linear NH_3 attack, $[\text{EDA}(\text{ACN})_7\text{H}_2]^{2+}\text{b}$, and the linear CH attack, $[\text{EDA}(\text{ACN})_7\text{H}_2]^{2+}\text{c}$, is studied (cf. Figure 5.22). In contrast to $[\text{EDA}(\text{ACN})_4\text{H}]^+$, the linear CH attack results in the global minimum structure $[\text{EDA}(\text{ACN})_7\text{H}_2]^{2+}\text{c}$. The geometry $[\text{EDA}(\text{ACN})_7\text{H}_2]^{2+}\text{a}$ is 5.0 kJ/mol and the geometry $[\text{EDA}(\text{ACN})_7\text{H}_2]^{2+}\text{b}$ is 3.3 kJ/mol less stable. In each isomer, the seventh ACN molecule is coordinated via a weak interaction or a weak, non-linear H-bond, respectively.

A comparison of the geometry optimized structures of $[\text{EDA}(\text{S})_n\text{H}]^+$, $[\text{EDA}_2(\text{S})_n\text{H}]^+$, and $[\text{EDA}(\text{S})_n\text{H}_2]^{2+}$ with $\text{S} = \text{H}_2\text{O}$, ACN revealed that the number of protic hydrogen atoms limits the number of ACN molecules binding via moderate H-bonds to the EDA ion and defines $n_{\text{S}}(\text{ACN})$. In contrast, since each H_2O molecule can form two H-bonds, the binding characteristics do not significantly change when all protic hydrogen atoms are occupied and, therefore, the stability of the H_2O -EDA clusters declines more uniformly. It follows that the formation of moderate H-bonds between the individual solvent molecules is crucial for the stabilization of large ion-solvent clusters.

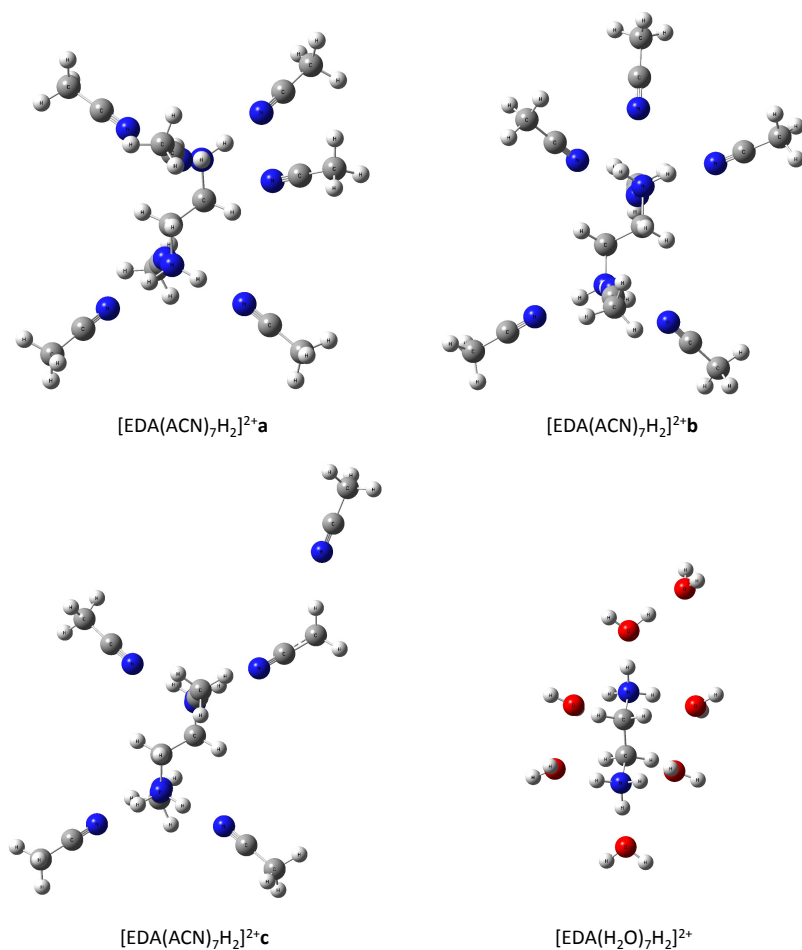


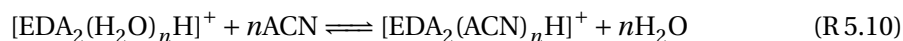
Figure 5.22: Optimized geometries of the $[\text{EDA}(\text{ACN})_7\text{H}_2]^{2+}$ and $[\text{EDA}(\text{H}_2\text{O})_7\text{H}_2]^{2+}$ clusters. $[\text{EDA}(\text{ACN})_7\text{H}_2]^{2+}$ a, $[\text{EDA}(\text{ACN})_7\text{H}_2]^{2+}$ b (linear NH_3 attack) and $[\text{EDA}(\text{ACN})_7\text{H}_2]^{2+}$ c (linear CH attack) represent the minimum energy structures. For $[\text{EDA}(\text{H}_2\text{O})_7\text{H}_2]^{2+}$ only the global minimum structure is shown.

5 Results and Discussion: Terminal Alkyldiamines

The weak binding character of the seventh ACN molecule and the resulting closed solvent shell number, $n_S(\text{ACN}) = 6$, may explain the experimentally determined maximum cluster number $n = 6$ for $[\text{EDA}(\text{ACN})_n\text{H}_2]^{2+}$ (cf. Figure 5.3 in section 5.1.1 and Figure 5.23 in section 5.3.2). Since ACN clusters of $[\text{EDA}_2\text{H}]^+$ were not observed and only the first ACN cluster, $[\text{EDA}(\text{ACN})\text{H}]^+$, was detected, the calculated $\Delta_R G^\circ$, listed in Table 5.2, values may be overestimated. Haack and co-workers compared the calculated stability of homologous ACN clusters, $(\text{ACN})_n\text{H}^+$, with experimental data and found an overestimated stability of the larger clusters probably caused by anharmonic effects of the NH-N bridges [165, 220]. Such overestimations cannot be ruled out for EDA-ACN clusters. Furthermore, as mentioned before, only the global minimum geometries of the open structures (without internal solvation) were used to determine $\Delta_R G$ and the stability of the clusters, respectively, whereas in experiments an ensemble of all conformers and isomers is observed. Interestingly, all ACN cluster species with an absolute stability $> 50 \text{ kJ/mol}$ (cf. Table 5.2) were detected in the MS experiments: $[\text{EDA}(\text{ACN})\text{H}]^+$ and $[\text{EDA}(\text{ACN})_n\text{H}_2]^{2+}$, with $n = 3-6$ (cf. Figure 5.3). In section 5.3.2 calculated and experimentally observed cluster distributions, where the former were determined considering all local minimum geometries of the open cluster conformations and not only the global minimum structures. Further limitations and difficulties arising from comparison of calculated and measured data are discussed in the course of this section. Ligand switch reactions may have caused that EDA- H_2O clusters were not detected, see next section.

Ligand Switch Reactions

The thermochemistry of the following ligand (solvent) switch reactions were studied to evaluate the stability of the EDA-solvent clusters.



Since mixed solvent-EDA clusters were experimentally not observed and therefore not treated in the theoretical investigations, only the ligand switch reactions, in which $n \text{ H}_2\text{O}$ molecules are exchanged by $n \text{ ACN}$ molecules, are considered. $\Delta_R G^\circ$ values for the studied (forward) ligand switch reactions are summarized in Table 5.3. To calculate $\Delta_R G^\circ$ the energies of the global minimum structures were used. All (forward) ligand switch reactions are exergonic; maximum gain in energy is noted upon reaching the closed shell cluster number $n_S(\text{ACN})$. Therefore, exchange of H_2O by ACN is thermodynamically favored; according to the calculation results, the forward ligand switch reactions should proceed spontaneously.

The thermodynamic data in Table 5.2 and 5.3 may explain why EDA- H_2O clusters were experimentally not observed, even when H_2O was present in higher gas phase

5.3 Theoretical Investigations of Ion-Solvent Clusters

Table 5.3: Change of Gibbs free energy $\Delta_R G^\circ$ at standard conditions in kJ/mol for the reactions $[\text{EDA}(\text{H}_2\text{O})_n\text{H}]^+ + n\text{ACN} \rightarrow [\text{EDA}(\text{ACN})_n\text{H}]^+ + n\text{H}_2\text{O}$, $[\text{EDA}(\text{H}_2\text{O})_n\text{H}_2]^{2+} + n\text{ACN} \rightarrow [\text{EDA}(\text{ACN})_n\text{H}_2]^{2+} + n\text{H}_2\text{O}$ and $[\text{EDA}_2(\text{H}_2\text{O})_n\text{H}]^+ + n\text{ACN} \rightarrow [\text{EDA}_2(\text{ACN})_n\text{H}]^+ + n\text{H}_2\text{O}$

Species	n	$\Delta_R G^\circ$	Species	n	$\Delta_R G^\circ$
[EDA(S) $_n$ H] $^+$	1	-37.3	[EDA(S) $_n$ H $_2$] $^{2+}$	1	-61.1
	2	-50.5		2	-107.6
	3	-62.6		3	-138.9
	4	-53.1		4	-174.0
	5	-40.0		5	-186.5
[EDA $_2$ (S) $_n$ H] $^+$	1	-25.7		6	-200.8
	2	-45.9		7	-192.5
	3	-44.3		8	-175.0
	4	-36.3		9	-167.7

mixing ratios than ACN. When both solvents are present, e.g. upon spraying EDA from an ACN/H₂O solution, the EDA ions are preferentially solvated by ACN because the calculated solvation energy $\Delta G_{n-1,n}$ exhibit higher values for solvation by ACN as compared to H₂O (cf. Table 5.2). If, however, EDA-H₂O clusters are formed, e.g. due to formation of EDA gas-phase ions from water enriched droplets according to the IEM model, which are then exposed to ACN vapor, ligand switch reactions ((R 5.9), (R 5.10), and (R 5.11)) occur resulting in formation of EDA-ACN clusters. The theoretical results are thus in good agreement with experimental observations.

The theoretical and experimental results are also in accordance with investigations of Hopkins and co-workers [53]. They studied the preferential solvation of protonated quinoline derivatives in mixed-modifier environments using DMS and computational methods. Upon varying the composition of mixtures of H₂O, ACN, and IPA vapors, the DMS experiments revealed that modifier mixtures of H₂O and ACN (or IPA) results in dispersion plots, which are nearly identical to those recorded when only ACN (or IPA) is used as modifier. They concluded that the ions are solvated by ACN, whether ACN or a mixture of ACN and H₂O is present in the buffer gas. In addition, the experiments demonstrated that the ions of the quinolinium derivatives have the strongest interaction/binding with ACN, followed by IPA and then H₂O, as observed by characteristics of the dispersion plot data. The experimentally determined trend in relative binding affinity (ACN > IPA > H₂O) was supported by calculations of standard Gibbs binding energies ($\Delta G_{0,1}^\circ$) for all quinolinium derivatives. All solvation reactions were found to be exergonic; the calculated energies are up to twice as high for ACN as compared to H₂O. They concluded that the quinolinium ions

bind exclusively to the solvent of strongest interaction, regardless of the presence of other modifier gases. Furthermore, the global minimum structure of the most ion-solvent clusters shows an ionic hydrogen bond between the protonated site and the respective solvent molecule [53]. Therefore, the results of Hopkins and co-workers support a) the detection of EDA-ACN clusters only in the presence of H₂O vapor in the nanoESI-MS experiments and b) the calculated structures of the EDA-ACN and -H₂O clusters along with the corresponding thermochemical data.

5.3.2 Cluster Distributions

By means of the Gibbs free energy corrected total energies ($\mathcal{E}_0 + G_{\text{corr}}$), which are obtained from geometry optimization for each considered structure, the relative population of each cluster conformation i and, in addition, the relative population of each cluster number n in an equilibrated cluster system is calculated²⁴ in dependence of the solvent mixing ratio. Reactions between the different cluster systems, [EDA(S)_{*n*}H]⁺, [EDA₂(S)_{*n*}H]⁺, and [EDA(S)_{*n*}H₂]²⁺, as well as ligand switch reactions (cf. reactions (R 5.9), (R 5.10), (R 5.11)) are not taken into consideration. The cluster distribution at a specific solvent concentration of H₂O or ACN is determined for each cluster system individually. Calculated cluster distributions at different H₂O and ACN mixing ratios and their corresponding mean ion mobilities are presented in Figure 5.24 in the next section. A comparison between calculated and experimentally determined (MS) cluster distributions of [EDA(ACN)_{*n*}H]⁺ and [EDA(ACN)_{*n*}H₂]²⁺ is given in Figure 5.23.

Only the clusters [EDA(ACN)H]⁺ and [EDA(ACN)_{*n*}H₂]²⁺, with $n = 3-6$, were observed in the mass spectrometric experiments; the protonated dimer, [EDA₂H]⁺, was detected only as bare ion. In Figure 5.23, the cluster distributions of [EDA(ACN)_{*n*}H]⁺ and [EDA(ACN)_{*n*}H₂]²⁺ measured with 70 ppmV ACN mixing ratio present in the ion source are compared to the modeled, equilibrated cluster distributions (298.15 K, 70 ppmV ACN). The experimental distributions show significantly smaller cluster sizes than the modeled distributions, resulting in a large deviation between the measured and theoretically determined averaged cluster number: [EDA(ACN)_{*n*}H]⁺: $n_{\text{avg}}(\text{exp}) = 1$, $n_{\text{avg}}(\text{theo}) = 3$; [EDA(ACN)_{*n*}H₂]²⁺: $n_{\text{avg}}(\text{exp}) = 4.5$, $n_{\text{avg}}(\text{theo}) = 6.1$. The deviation between the cluster distributions and n_{avg} , respectively, increases with increasing ACN mixing ratio regarding [EDA(ACN)_{*n*}H]⁺. In the experiments only [EDA(ACN)H]⁺ was observed leading to $n_{\text{avg}}(\text{exp}) = 1$, whereas the modeled distribution shifts to higher clusters as the ACN mixing ratio is increased. This also applies to [EDA₂H]⁺, since only the bare ion ($n = 0$) was detected in the mass spectra. The calculations result in a cluster distribution showing mainly the second and also the third cluster depending on the ACN mixing ratio (cf. Figure 5.24). The cluster distributions of [EDA(ACN)_{*n*}H]²⁺ differ also more strongly when the ACN mixing ratio is enhanced. At

²⁴The relative population of a cluster species is calculated from the harmonic superposition partition function using the Boltzmann distribution. See section 3.2.3 and, in particular, ref. [172] for a detailed description of this method.

5.3 Theoretical Investigations of Ion-Solvent Clusters

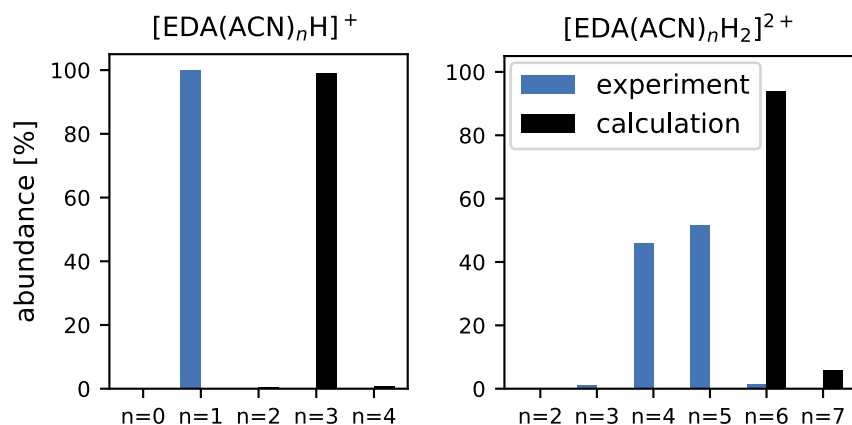


Figure 5.23: Comparison between the modeled and measured cluster distribution of $[\text{EDA}(\text{ACN})_n\text{H}]^+$ (left) and $[\text{EDA}(\text{ACN})_n\text{H}_2]^{2+}$ (right). Calculations were performed for an ACN mixing ratio of 70 ppmV and 298.15 K considering all geometry optimized conformers and their corresponding energies. In the experiment 70 ppmV ACN was present in the ion source and the ion population was detected with the TOF-MS, method DA.

1 % ACN mixing ratio, the calculated ion population shows mainly $[\text{EDA}(\text{ACN})_7\text{H}_2]^{2+}$ (cf. Figure 5.24) leading to $n_{\text{avg}}(\text{theo}) = 7$; in contrast, $n_{\text{avg}}(\text{exp}) = 4.9$ was determined experimentally when 1 %V ACN was added to the source gas. In summary, the modeled cluster distributions of all considered ACN cluster systems, $[\text{EDA}(\text{ACN})_n\text{H}]^+$, $[\text{EDA}_2(\text{ACN})_n\text{H}]^+$, and $[\text{EDA}(\text{ACN})_n\text{H}_2]^{2+}$, are shifted to higher cluster sizes compared to the experimentally determined ion distributions.

The differences between the experimental and the calculated, equilibrated cluster distributions can be explained by several effects. First, the calculated stabilities of the individual clusters, presented in Table 5.2, are most probably overestimated caused by anharmonic effects of the NH-N bridges, as mentioned before. Furthermore, overestimation of the stability of the singly protonated EDA-solvent clusters may occur through the limitation to the open structure of $[\text{EDA}\text{H}]^+$ and $[\text{EDA}_2\text{H}]^+$. Since ab initio calculations revealed that the closed cyclic structures resulting from intra- (monomer) and intermolecular (dimer) proton bridges are in both cases lower in energy than the open structures [107, 108], and the fact that internal solvation hinders external solvation by solvents [81], the modeled stabilities of the solvent clusters of $[\text{EDA}\text{H}]^+$ and $[\text{EDA}_2\text{H}]^+$ may be overestimated. Regarding the doubly protonated EDA, the considered open structure is the most stable conformer due to steric and electrostatic repulsion between the two protonated amine groups, which was shown by density functional calculations [109]. Therefore, the differences between the de-

5 Results and Discussion: Terminal Alkyldiamines

tected and modeled cluster distributions of $[\text{EDA}\text{H}]^+$ and $[\text{EDA}_2\text{H}]^+$, but not the observed deviations regarding the cluster system $[\text{EDA}(\text{ACN})_n\text{H}_2]^{2+}$, can be explained by these restrictions.

In addition, the calculated cluster distributions are based on geometry optimized local minimum structures and their energies, respectively, which are modeled for room temperature (298.15 K). Experimentally, always an ensemble of various conformers and isomers is observed. Also the ions have higher temperatures, caused by ion acceleration and collision in the transfer and analysis stages in the instruments. As a consequence, cluster formation, which occurs in the ion source at atmospheric pressure, at a specific solvent mixing ratio and temperature, results in an equilibrated cluster distribution, which is shifted to smaller clusters by declustering during ion transfer and mass analysis. Due to the decreasing background pressure and solvent mixing ratio as well as the increasing collision energies, the initial cluster equilibrium is not maintained. Only cluster species with a calculated stability above 50 kJ/mol, cf. Table 5.2, were observed with the TOF instrument when applying method DA. 50 kJ/mol corresponds to about 0.5 eV energy per molecule. This value represents an amount of energy which is potentially accumulating in the ions upon transfer even when the transfer settings are optimized for “soft” conditions, as in method DA. The investigations regarding the influence of the acceleration voltage on the observed ion population revealed that the doubly protonated diamine-ACN clusters are efficiently dissociated/fragmented by increasing potential differences in the first, second, and third vacuum stage (cf. section 5.1.3). Furthermore, it was found that ACN as gas phase modifier suppresses declustering and fragmentation. However, no stepwise declustering beginning with the largest cluster, which exhibits the lowest stability, was observed when increasing ion acceleration (cf. Figures 5.10 and 5.11). It follows that relative stabilities of the individual clusters cannot be derived from the CID measurements. The fact that no dependence of the cluster stability on the cluster size n was determined may be caused by the large steps in which the electric potential difference was varied. As a result, the stepwise change in the average energy uptake of the ions may exceed the differences in stability of the individual cluster species and the intensity decrease of the individual clusters occurs simultaneously.

Upon comparing the theoretically and experimentally determined cluster distributions of $[\text{EDA}(\text{ACN})_n\text{H}]^+$, $[\text{EDA}_2(\text{ACN})_n\text{H}]^+$, and $[\text{EDA}(\text{ACN})_n\text{H}]^{2+}$, large deviations regarding the abundance of the individual cluster numbers n and n_{avg} are noticed, which are explained by overestimating the calculated cluster stabilities and by non-equilibrium conditions prevailing in the vacuum region of the mass spectrometer. As a result, the experimentally determined distributions show smaller cluster sizes than the calculated distributions.

5.3.3 Collision Cross Sections and Ion Mobilities

Based on the geometry optimization, collision cross section (CCS) calculations were performed using the MobCal code [169] as well as the MobCal-MPI implementation [168]. Comparison of the calculated CCS of several $[\text{EDA}(\text{S})_n\text{H}]^+$ and $[\text{EDA}(\text{S})_n\text{H}_2]^{2+}$ clusters revealed that the MobCal code determines significantly smaller CCS values than the MobCal-MPI code, however with comparable relative changes with n . The MobCal-MPI implementation models the CCS in N_2 instead of He as bath gas. Generally, more accurate results are obtained because van der Waals potentials that are better suited for accurate CCS calculations and parameterization for nearly all atom types are included [168]. Therefore, the remaining CCC calculations were performed with the MobCal-MPI method and only these results were used for the determination of the ion mobilities. Only the global minimum structures were used to determine the CCS of each cluster species, to save computing time. In Table 5.4 the calculated collision cross sections Ω_{avg} in N_2 at 298.15 K and the reduced mobility values K_0 are summarized. The ion mobility is determined with the Mason-Schamp equation (3.3). Using the K_0 values of the individual cluster species, a mean ion mobility, K_0^{mean} , for each equilibrated cluster distribution as well as mobility peaks in the ion mobility spectrum can be calculated in dependence on the solvent gas phase mixing ratio. The equilibrated ion distribution is calculated for each cluster reaction system (cf. sections 3.2.3 and 5.3.2). Figure 5.24 shows calculated distributions and corresponding K_0^{mean} values, exemplary for three different solvent (H_2O and ACN) gas phase mixing ratios (1 ppmV, 100 ppmV, 1 %) for the cluster systems, $[\text{EDA}(\text{S})_n\text{H}]^+$, $[\text{EDA}_2(\text{S})_n\text{H}]^+$ and $[\text{EDA}(\text{S})_n\text{H}_2]^{2+}$.

As expected, the calculated CCS' of the singly protonated clusters, $[\text{EDA}(\text{S})_n\text{H}]^+$ and $[\text{EDA}_2(\text{S})_n\text{H}_2]^+$ ($\text{S} = \text{H}_2\text{O}, \text{ACN}$), increase with increasing cluster number n , and, consequently, the corresponding reduced mobilities K_0 decrease. In addition, for $n > 0$ the respective ACN-cluster exhibits a larger CCS than the respective H_2O -cluster caused by the larger CCS of ACN as compared to H_2O . In contrast, the calculated CCS' of the doubly protonated clusters do not steadily increase with the cluster size n (cf. Table 5.4).²⁵ Regarding both solvents, H_2O and ACN, the calculated CCS' of the smaller clusters of $[\text{EDA}(\text{S})_n\text{H}_2]^{2+}$ show an unexpected trend: a) Within uncertainty limits the CCS' of $[\text{EDA}(\text{H}_2\text{O})_n\text{H}_2]^{2+}$ with $n = 1 - 6$ do not vary significantly and b) the CCS values of $[\text{EDA}(\text{ACN})_n\text{H}_2]^{2+}$ initially increases significantly for $n > 2$. This trend was reproduced by the CCS calculations, which were performed with the MobCal code applying the same geometry optimized cluster structures, although these calculations yielded much smaller absolute CCS values. Although the spatial volume increases with the number n of bound solvent molecules, the calculated Ω_{avg}

²⁵Unfortunately, CCS calculation of the geometry optimized structure of $[\text{EDA}(\text{H}_2\text{O})_2]^{2+}$ failed and $\Omega_{\text{avg}}([\text{EDA}(\text{H}_2\text{O})_2]^{2+})$ was not determined (cf. Table 5.4). To calculate K_0^{mean} of a specific cluster distribution, $\Omega_{\text{avg}}([\text{EDA}(\text{H}_2\text{O})_2]^{2+})$ was estimated to be 210 \AA^2 (i.e. $K_0([\text{EDA}(\text{H}_2\text{O})_2]^{2+}) = 2.33 \text{ cm}^2 \text{ V}^{-1} \text{ s}^{-1}$) because CCS calculations using the MobCal code yielded similar values for $[\text{EDA}(\text{H}_2\text{O})_2]^{2+}$ and $[\text{EDA}(\text{ACN})_2\text{H}_2]^{2+}$ and $[\text{EDA}(\text{H}_2\text{O})_2]^{2+}$, respectively.

5 Results and Discussion: Terminal Alkyldiamines

values of the doubly protonated solvent-EDA clusters do not initially increase with n (or even slightly decrease). This behavior is rationalized as follows: since both amino groups are protonated and repel each other, $[\text{EDA}(\text{H}_2\text{O})_n]^{2+}$ shows a highly localized, anisotropic charge density. External solvation by polar solvent molecules will dilute and delocalize the charges and result in a more isotropic charge density, which in turn significantly lessens the interaction potential between the ion and the buffer gas (N_2). The charge distributions of the geometry optimized structures are provided in Gaussian. The charge distributions of the $[\text{EDA}(\text{H}_2\text{O})_n]^{2+}$ clusters show that the charge density at the EDA-ion core becomes more isotropic when n is increased; the excess charge at the ion core is shielded by the surrounding H_2O molecules. It is assumed that the increase in spatial volume with n is compensated by charge dilution and shielding; the effective CCS essentially remains unchanged. In comparison, ACN is significantly larger than H_2O and thus the increase in spatial volume is not counterbalanced by charge delocalization. Thus, solvation by the third ACN molecule results in a significantly larger CCS. However, the calculated reduced mobilities K_0 of $[\text{EDA}(\text{ACN})_n]^{2+}$ and $[\text{EDA}(\text{H}_2\text{O})_n]^{2+}$ decrease continuously with increasing n although the CCS values do not increase continuously. With increasing n the mass of the cluster ion and the reduced mass of the ion- N_2 pair, respectively, increases. According to the Mason-Schamp equation (3.3), K_0 is proportional to $(\Omega_{\text{avg}}\sqrt{\mu})^{-1}$. Therefore, a continuous decrease of K_0 with n is determined for $[\text{EDA}(\text{S})_n]^{2+}$ (cf. Table 5.4).

As a result, the increase of n_{avg} of each cluster system leads to the decrease of the corresponding reduced mean ion mobility K_0^{mean} , as depicted for three different solvent mixing ratios (1 ppmV, 100 ppmV, and 1 %V) and cluster distributions, respectively, in Figure 5.24. Comparison of the cluster distributions of H_2O (red color) and ACN (blue color) shows that n_{avg} of the H_2O -cluster systems grows faster with the solvent concentration and, in addition, the cluster distributions of H_2O are generally broader.²⁶ Both issues are caused by the smaller differences of the subsequent solvation energies $\Delta G_{n-1,n}^\circ$ of H_2O as compared to ACN (cf. Table 5.2 and Figure 5.18). Since the stabilities of individual EDA-ACN clusters differ more strongly, the cluster distributions of ACN are generally dominated by one cluster species. As a consequence, K_0^{mean} of the EDA- H_2O cluster systems alters more strongly with the solvent mixing ratio than that of the EDA-ACN clusters. Comparing K_0^{mean} of the different cluster systems at a specific H_2O or ACN mixing ratio, the following trend is noted: $K_0^{\text{mean}}([\text{EDA}(\text{S})_n]^{2+}) > K_0^{\text{mean}}([\text{EDA}(\text{S})_n]^{1+}) > K_0^{\text{mean}}([\text{EDA}_2(\text{S})_n]^{1+})$.

Armenta and Blanco [221] experimentally determined the reduced ion mobility of EDA in N_2 to $2.28 \text{ cm}^2 \text{ V}^{-1} \text{ s}^{-1}$. Since EDA was ionized through atmospheric pressure chemical ionization (APCI) and only one mobility signal (in addition to the internal calibrant nicotinamide) was observed in the ion mobility spectra, it is con-

²⁶The cluster distribution of $[\text{EDA}(\text{H}_2\text{O})_n]^{2+}$ at 1 %V H_2O has an exceptional character. Here, $n = 9$ represents the highest cluster number, which was considered in the calculations. Therefore, it is very likely that higher cluster numbers ($n > 9$) are populated at 1 %V H_2O , based on the trend of the calculated cluster stabilities resulting in a broader distribution.

5.3 Theoretical Investigations of Ion-Solvent Clusters

Table 5.4: Calculated collision cross section Ω_{avg} in N_2 at 298.15 K in \AA^2 and the reduced ion mobility K_0 in $\text{cm}^2 \text{V}^{-1} \text{s}^{-1}$ of $[\text{EDA}(\text{S})_n\text{H}]^+$, $[\text{EDA}(\text{S})_n\text{H}_2]^{2+}$, and $[\text{EDA}_2(\text{S})_n\text{H}]^+$. S = H_2O or ACN

Species	n	Ω_{avg}	K_0	Species	n	Ω_{avg}	K_0
$[\text{EDA}(\text{H}_2\text{O})_n\text{H}]^+$	0	115 ± 1	2.14 ± 0.02	$[\text{EDA}(\text{H}_2\text{O})_n\text{H}_2]^{2+}$	0	-	-
	1	116 ± 1	2.05 ± 0.02		1	214 ± 3	2.21 ± 0.02
	2	119 ± 2	1.94 ± 0.02		2	210 ± 2	2.19 ± 0.02
	3	125 ± 1	1.81 ± 0.01		3	209 ± 2	2.16 ± 0.02
	4	127 ± 2	1.77 ± 0.02		4	210 ± 2	2.13 ± 0.02
	5	134 ± 2	1.67 ± 0.02		5	211 ± 3	2.10 ± 0.03
$[\text{EDA}_2(\text{H}_2\text{O})_n\text{H}]^+$	0	127 ± 1	1.78 ± 0.01	6	213 ± 3	2.06 ± 0.03	
	1	132 ± 1	1.68 ± 0.02	7	216 ± 2	2.02 ± 0.02	
	2	139 ± 1	1.58 ± 0.02	8	220 ± 3	1.97 ± 0.02	
	3	147 ± 2	1.49 ± 0.02	9	221 ± 2	1.95 ± 0.02	
	4	154 ± 2	1.42 ± 0.02				
$[\text{EDA}(\text{ACN})_n\text{H}]^+$	0	115 ± 1	2.14 ± 0.02	$[\text{EDA}(\text{ACN})_n\text{H}_2]^{2+}$	0	-	-
	1	121 ± 2	1.89 ± 0.03		1	212 ± 3	2.16 ± 0.03
	2	138 ± 2	1.60 ± 0.02		2	210 ± 3	2.12 ± 0.03
	3	162 ± 2	1.35 ± 0.02		3	216 ± 4	2.02 ± 0.03
	4	178 ± 6	1.21 ± 0.04		4	223 ± 2	1.94 ± 0.02
	5	198 ± 2	1.08 ± 0.01		5	243 ± 3	1.76 ± 0.02
$[\text{EDA}_2(\text{ACN})_n\text{H}]^+$	0	127 ± 1	1.78 ± 0.01	6	259 ± 3	1.64 ± 0.02	
	1	142 ± 1	1.55 ± 0.01	7	283 ± 3	1.49 ± 0.02	
	2	163 ± 2	1.33 ± 0.01	8	287 ± 3	1.47 ± 0.02	
	3	188 ± 2	1.14 ± 0.01	9	296 ± 3	1.41 ± 0.02	
	4	198 ± 2	1.08 ± 0.01				

5 Results and Discussion: Terminal Alkyldiamines

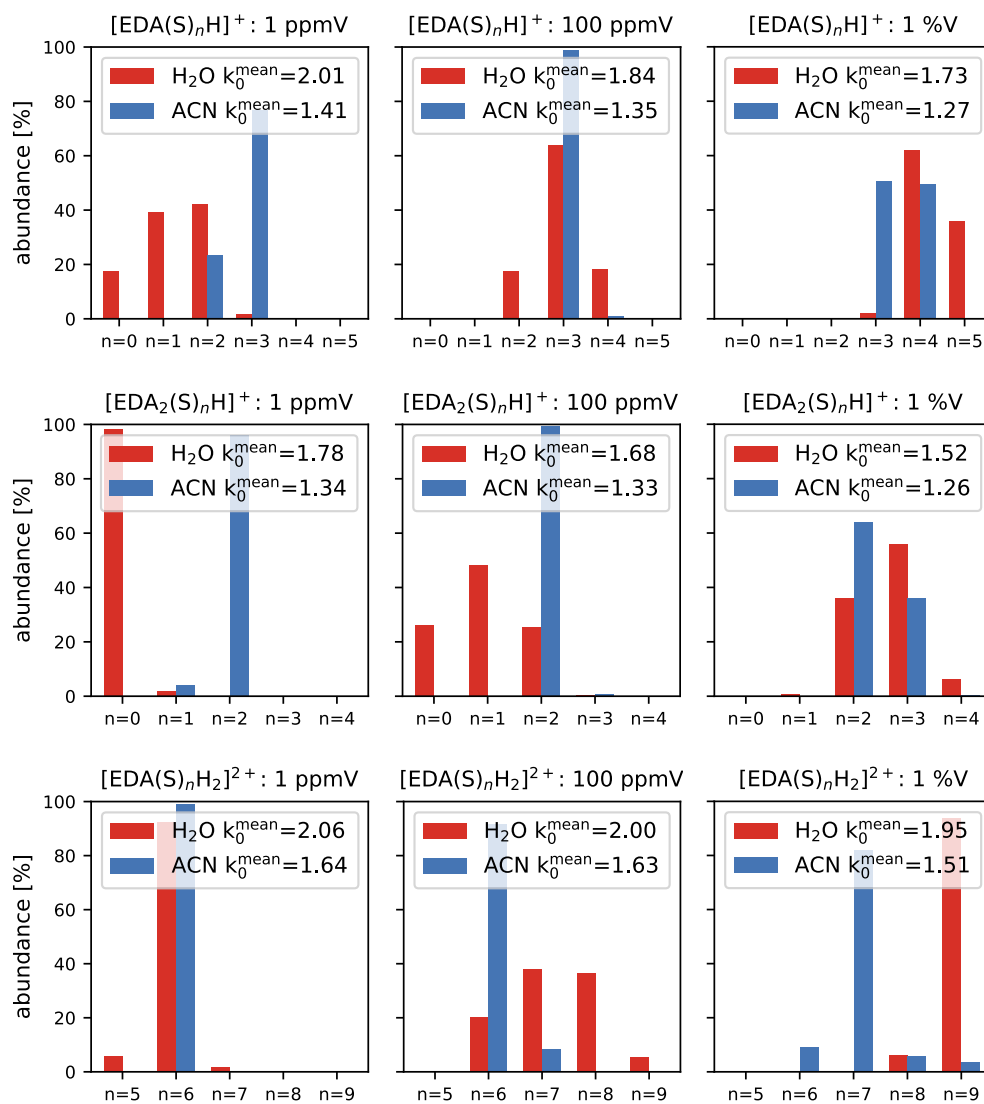


Figure 5.24: Modeled cluster distributions of $[\text{EDA}(\text{S})_n\text{H}]^+$ (top), $[\text{EDA}_2(\text{S})_n\text{H}]^+$ (center), and $[\text{EDA}(\text{S})_n\text{H}_2]^{2+}$ (bottom) with $\text{S} = \text{H}_2\text{O}$, ACN at 296.15 K and solvent mixing ratios of 1 ppmV, 100 ppmV, and 1 %V. The reduced mean ion mobility K_0^{mean} is given for each cluster distribution.

5.3 Theoretical Investigations of Ion-Solvent Clusters

cluded that the detected peak corresponds to the protonated molecule, $[\text{EDAH}]^+$, or to a protonated solvent-EDA cluster, $[\text{EDA}(\text{S})_n\text{H}]^+$, most probably with $\text{S} = \text{H}_2\text{O}$. The CCS of $[\text{EDAH}]^+$ was calculated ($K_0 = 2.14 \text{ cm}^2 \text{ V}^{-1} \text{ s}^{-1}$) based on the open structure, i.e., without intramolecular hydrogen bonding between the two basic amino groups sharing the proton. The open structure represents the *anti*-conformer of $[\text{EDAH}]^+$, whereas the cyclic structure is termed *gauche*- $[\text{EDAH}]^+$, cf. Figure 5.19. Computational analysis revealed that formation of the *gauche*- $[\text{EDAH}]^+$ is favored in the gas phase by 39 kJ/mol [108] / 65 kJ/mol [109]. Solvent interactions lower the rotational barrier of 65 kJ/mol (gas phase) to 36 kJ/mol (aqueous solution) [109]. The preference for the cyclic structure in the gas phase was verified experimentally by infrared spectroscopy [108]. Since EDA was first evaporated and then ionized in the gas phase in the ion mobility measurements, it is reasonable to assume that K_0 determined by Armenta and Blanco refers to a distribution of isomers, in which *gauche*- $[\text{EDAH}]^+$ is the most abundant species. Based on the geometry optimized structures of the *gauche*- and *anti*- $[\text{EDAH}]^+$ ion given in [108], a lower CCS and therefore a higher ion mobility is predicted for the *gauche*- $[\text{EDAH}]^+$, since a) the spatial structure is more compact and b) internal solvation causes charge dilution and delocalization. Charge dilution should weaken the ion-neutral potential, which is in turn related to the effective CCS.

As repeatedly noted, intramolecular/internal solvation weakens the bonding to external solvent molecules and vice versa. External solvation by solvents delocalizes the charge from the protonated function and thus weakens its ability to engage in internal solvation. In the solution phase, e.g. in an ESI droplet, external solvation may be favored over internal solvation. In electrospray ionization, prior to the formation of a naked gas-phase ion, a gas-phase ion-solvent cluster is formed. The nanoESI-MS experiments with EDA and the other alkyldiamines revealed that both, the singly and the doubly protonated monomer ion, are detected as ACN clusters, even when ACN is initially only present in the ESI solution; cluster formation is enhanced when ACN is added to the gas phase as modifier. The hypothesis that ions are highly solvated by ACN in solution and external solvation is maintained during ion release and transfer is most likely. Naturally, the number of solvent molecules solvating the diaminic ion changes in dependence of the ACN gas phase mixing ratio and the extent of ion activation. In contrast, when EDA is ionized in the gas phase to solely yield singly protonated ions (e.g. by APCI), internal solvation may play a more dominant role.

Each calculated ion cluster distribution represents a thermalized equilibrium state at a specific solvent concentration and room temperature. Ion distributions obtained in mass spectrometric experiments hardly represent a thermalized reaction system because reaction dynamics under non-equilibrium conditions determines the detected ion population distribution, as discussed in section 5.3.2. In contrast, atmospheric pressure ion mobility instruments can be used to investigate cluster reactions systems at equilibrium conditions. Therefore, the calculated cluster distributions and ion mobilities can be verified with results of ion mobility measurements upon varying the solvent (modifier) concentration.

Comparison with Ion Mobility Measurements

A high-resolution atmospheric pressure drift tube ion mobility spectrometer coupled via a gated transmission stage to a TOF-MS was used for the ion mobility measurements. ESI and APCI are available as ionization methods. Ethylenediamine (EDA), propylenediamine (PDA), and octanediamine (ODA) were employed as analytes. Solutions of EDA and PDA in ACN/H₂O or MeOH/H₂O with 0.0001 % formic acid are sprayed for ESI. A permeation oven is used to generate a constant analyte vapor concentration for APCI. Nitrogen is used as drift gas, which enters the drift tube at the detector site and establishes a counter flow for the drifting ions. The humidity as well as the ACN mixing ratio in the drift gas are controlled. With the three-grid ion gate, measurements can be performed in the IMS mode or the selective IMS-MS mode. In the selective IMS-MS mode single mobility peaks of the drift spectrum - or more precisely, defined time domains of the ion mobility spectrum - are transferred to the mass spectrometer, called *peak snipping*. The experimental setup is described in section 3.2.3 and depicted in Figure 3.4; further information about the IMS and the IMS-MS coupling is found in [160, 161].

The selective IMS-MS mode allows investigations of the ion-solvent cluster reaction systems, which create the observed mobility peaks in the IMS spectra. Comparison of the data recorded with two different ion sources (APCI and ESI) facilitates peak identification, since only singly protonated ions are generated with APCI and also doubly protonated diamines are formed in ESI. Unfortunately, only singly protonated diamine ions, MH⁺, and ACN dimer ions, (ACN)₂H⁺, were detected in the IMS-MS experiments. In one experiment, the doubly protonated ion of octanediamine (ODA) clustered with one ACN molecule, [M(ACN)H₂]²⁺, was observed in the MS spectrum at *m/z* 93.68; this observation was not reproducible in other experiments. The characterization of the individual mobility peaks was thus not possible. The absence of doubly protonated ions or even cluster species in the mass spectra may be explained by fragmentation and declustering processes during ion transmission from the drift tube to the inlet system of the mass spectrometer. Efficient ion transmission in the IMS-MS setup requires much stronger ion focusing and acceleration than in the nanoESI-MS setup. The investigations concerning CID, presented in section 5.1.3, demonstrated that an increase of the acceleration voltage (without sufficient addition of a modifier) results in declustering and fragmentation and even complete loss of the doubly protonated diamines, whereas the intensity of the singly protonated ion is only lowered. MH⁺ ions are transferred and detected even at elevated reduced field strengths with the nanoESI-MS setup (cf. Figure 5.11).

Ion mobility spectra of EDA and ACN are shown in Figure 5.25. Chemical ionization (APCI) of EDA leads to the IM spectra depicted in green in Figure 5.25. Two main mobility peaks are observed, which correspond to reduced mobilities of 1.726 and 1.566 cm²V⁻¹s⁻¹; additionally, a small peak is discernible at 6.448 ms corresponding to 1.683 cm²V⁻¹s⁻¹. The mass spectrum of each peak, recorded via peak snipping, shows protonated EDA (MH⁺) and in some cases unknown signals. Addition of

5.3 Theoretical Investigations of Ion-Solvent Clusters

ACN as modifier changes the IM spectrum drastically. In addition to MH^+ , $(\text{ACN})_2\text{H}^+$ signals appear in the mass spectra. ACN is protonated when added as modifier. Whether protonation of ACN occurs by proton transfer from protonated water clusters (or other reactant ions present) and/or intracuster proton transfer and fragmentation processes during ion transfer lead to formation of $(\text{ACN})_2\text{H}^+$, remains unclear. The spectrum generated by APCI of ACN (black color) shows one major signal ($K_0 = 1.628 \text{ cm}^2 \text{ V}^{-1} \text{ s}^{-1}$) and several minor peaks with higher ion mobilities, which are most probably reactant ion peaks.

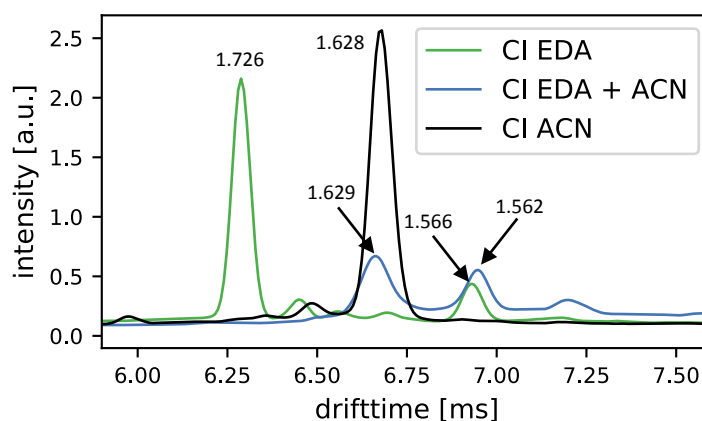


Figure 5.25: Chemical ionization ion mobility spectra (APCI-IMS) of ethylenediamine (EDA) without (green) and with addition of ACN as modifier (blue), in comparison to the APCI-IMS of ACN (black). Numbers indicate the reduced ion mobility K_0 in $\text{cm}^2 \text{ V}^{-1} \text{ s}^{-1}$ of the corresponding mobility peak. N_2 containing 3 ppmV H_2O was used as drift gas.

IM spectra of PDA are shown in Figure 5.26. ESI was used to generate ions. Spectra with and without addition of ACN as modifier are depicted and, in addition, compared to the APCI-IMS of ACN. Analogous to the data for EDA, employing ACN as modifier leads a) to small shifts of mobility peaks towards higher drift times (cf. peaks between 8 and 9 ms in Figure 5.26 and the peak around 6.95 ms in Figure 5.25) and b) to large peak shifts or formation of “new” peaks. When ACN is added as modifier or only ACN is present in the drift tube, a peak corresponding to a reduced ion mobility of $\approx 1.63 \text{ cm}^2 \text{ V}^{-1} \text{ s}^{-1}$ is recorded. This peak is probably generated by a cluster reaction system, which represents the thermodynamic sink for protonated ACN for the given reaction conditions (pressure, temperature, humidity, field strength). Generally, this reaction system is characterized by the clusters of the structure $[(\text{ACN})_m(\text{H}_2\text{O})_n\text{H}]^+$ and the corresponding cluster reactions.

Introduction of modifiers (e.g. 2-butanol) caused only small changes in IMS data of molecules with two amine groups (e.g. arginine, histidine, lysine), as described

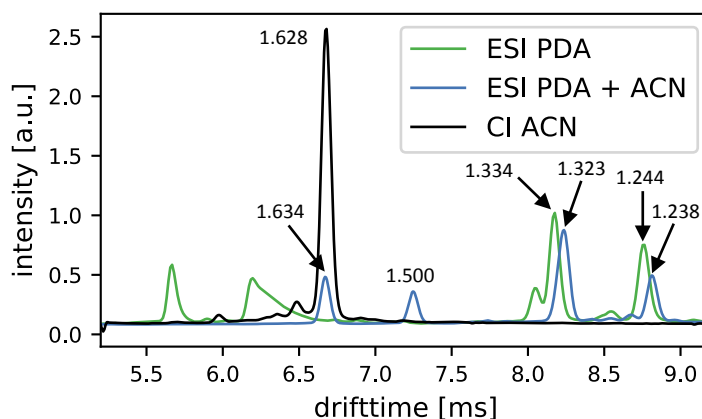


Figure 5.26: Electrospray ionization ion mobility spectra of ethylenediamine (EDA) without (green) and with addition of ACN as modifier (blue), in comparison with the chemical ionization ion mobility spectrum (APCI-IMS) of ACN (black). Numbers indicate the reduced ion mobility K_0 in $\text{cm}^2 \text{V}^{-1} \text{s}^{-1}$ of the corresponding mobility peak. N_2 containing 3 ppmV H_2O was used as drift gas and PDA was sprayed from ACN/ H_2O containing 0.0001 % formic acid.

by Fernandez-Maestre and co-workers [101, 106, 222]. The small response of the singly protonated ions to the addition of modifiers, as compared to the case of analyte ions having no basic amine groups, was explained by formation of an intramolecular proton bridge between the two amine functions, hindering attachment of modifier molecules caused by steric hindrance and charge delocalization. This effect has been discussed several times within the scope of this work. It is also known that reactant ion peaks can disappear when modifier is added in sufficient amounts to the drift gas because the reactant ion population changes [101]. Considering the peak with $K_0 = 1.566 \text{ cm}^2 \text{V}^{-1} \text{s}^{-1}$ in the APCI-IMS spectrum of EDA (cf. green trace in Fig. 5.25), a small shift to $K_0 = 1.562 \text{ cm}^2 \text{V}^{-1} \text{s}^{-1}$ (cf. blue trace) is observed, which correspond to a difference of 0.004 units in K_0 and of 0.017 ms in t . In the ESI-IMS spectrum of PDA the peaks with $K_0 = 1.334$ and $K_0 = 1.244 \text{ cm}^2 \text{V}^{-1} \text{s}^{-1}$ are shifted to $K_0 = 1.323 \text{ cm}^2 \text{V}^{-1} \text{s}^{-1}$ and $K_0 = 1.238 \text{ cm}^2 \text{V}^{-1} \text{s}^{-1}$, respectively, leading to $\Delta K_0 = 0.011 \text{ cm}^2 \text{V}^{-1} \text{s}^{-1}$ and $\Delta K_0 = 0.006 \text{ cm}^2 \text{V}^{-1} \text{s}^{-1}$. In comparison to mobility shifts observed for several combinations of protonated analytes and modifiers [101, 106, 223], the present mobility shifts are small. Such small differences may arise from: (1) formation of ion-modifier clusters or, in case of ESI, from small changes in the ion-cluster equilibrium, i.e., the average cluster size, which are determining the ion mobility, (2) modified properties of the buffer gas (e.g. viscosity, polarity) and/or the ESI spray, and (3) the standard deviation of the drift time measurements. In con-

trast, large mobility shifts and/or the appearance of new peaks (both effects are not necessarily distinguishable) may be traced back to significant changes of the chemical reaction system caused by intense ion-modifier clustering and formation of modifier related reactant peaks, e.g. $[(\text{ACN})_m(\text{H}_2\text{O})_n\text{H}]^+$, as discussed above. According to the work of Fernandez-Maestre and co-workers (modifier effects on ion mobility of diaminic compounds) [101, 106, 222] and Kebarle and co-workers (solvation of singly and doubly protonated alkyldiamines), it is reasonable to assume that the mobility peaks, which show minor mobility shifts upon ACN addition, are related to singly protonated EDA ions and the peaks, which show major mobility shifts, correspond to doubly protonated EDA ions or reactant ions, e.g. $[(\text{H}_2\text{O})_n\text{H}]^+$, $[(\text{ACN})_m(\text{H}_2\text{O})_n\text{H}]^+$.

The calculation of cluster distributions at different H_2O and ACN mixing ratios suggests that - not taking into account reactant ion peaks and mixed solvent EDA clusters - the mobility peak of the $[\text{EDA}(\text{S})_n\text{H}_2]^{2+}$ cluster system exhibits the shortest drift time, followed by the peaks of $[\text{EDA}(\text{S})_n\text{H}]^+$ and $[\text{EDA}_2(\text{S})_n\text{H}]^+$ (cf. Figure 5.24).

5.4 Proton Transfer Processes to Solvent Clusters

The results obtained for Substance P and the terminal alkyldiamines using nanoESI-MS strongly suggest the observed charge state distribution of ions formed by electrospray ionization is controlled by solvation/cluster reactions with solvent molecules. In ESI, solvated ions, i.e., ion-solvent clusters, are generated in (1) ion evaporation or (2) chain ejection processes (in both cases the ion is desorbed from a charged droplet with a significant number of solvent molecules attached) or (3) via the charged residue mechanism. Furthermore, in the ion source enclosure, ion bound clusters are build up via solvent condensation facilitated by the elevated solvent concentration and/or during sample gas expansion into the low pressure region of the mass spectrometer (cf. section 2.2.1). Charge/proton partitioning in a ion-solvent cluster is controlled by the relative GB of the solvent cluster and the analyte or its protonation site/residue, respectively. Solvent clusters have higher gas-phase basicities than individual solvent molecules and the cluster GB increases with size, i.e., the number of solvent molecules forming the cluster. Loss of a pure proton bound solvent cluster from an analyte ion-solvent cluster can result in lower charge state ions.

The feasibility of proton transfer reactions from ESI generated multiply charged ions to solvent clusters driven by ion solvation was already discussed in the early 1990s. Smith and co-workers [85] reported that addition of water vapor to the inlet capillary shifts the charge state distribution of cytochrome c to lower charge states, and that the extent of proton transfer gradually increases with the amount of water vapor added. They identified H_2O as the driver of the proton transfer processes, despite the fact that the individual charge sites of the analyte are more basic than H_2O . Furthermore, H_3O^+ was not observed in the mass spectra. The latter was rationalized in terms of (1) the high reactivity of H_3O^+ , (2) the discrimination of low molecular mass components (mass discrimination) and, remarkably, (3) by the for-

5 Results and Discussion: Terminal Alkyldiamines

mation or possible participation of larger water clusters. The authors concluded: "An interface that can efficiently diminish the amount of ion solvation, as well as limit the amount of solvent entering the mass spectrometer, will be capable of producing a mass spectrum of a multiply protonated species that more closely resembles the ion population initially formed." [85]. In 1995, Schnier, Gross and Williams proposed a mechanism for the maximum number of charges that can be retained by a protein ion formed by electrospray ionization [67]. In this mechanism the maximum charge state is formed through a process in which significant clustering of solvent molecules from the electrospray process with the protein ion prevails. The maximum charge state is thus determined by gas-phase reactions of the multiply protonated protein ion with solvents and particularly by the relative gas-phase proton transfer reactivity of the ion and the most basic solvent. It was evident to these authors that gas-phase reactions with bases added in solution or the gas phase changes the observed charge state distribution. This notion was strongly supported by several ESI-MS studies regarding (protein) ion charging [85, 87, 93, 124]. In contrast, the role of gas-phase chemistry in conventional ESI was rendered less clear. Schnier, Gross and Williams brought up that solvent clusters are more basic than individual solvent molecules; they also noted that protonated solvents are hardly observed in ESI mass spectra. They concluded that "gas-phase reactions are not likely to be the principal mechanism in the formation of the observed charge distribution, although instrumental factors, such as transmission efficiency, may contribute to the low abundance of these small ions." [67]

In 1995, Ogorzalek Loo and Smith proposed a cluster-mediated proton transfer mechanism to explain the negative temperature dependence of proton transfer reactions of multiply protonated ions reacting with weak bases [93]. Experiments in which the charge state of porphyrin ions was determined optically at various stages of the electrospray process indicated that charge reduction occurs relatively late in ESI process via loss of a charged solvent or solvent cluster [224]. This resulted in the following suggestion: it depends upon the degree of solvation, the relative locations of the charges, and the proton affinities of the solvent and its clusters, if loss of neutral solvent or loss of a protonated solvent molecule or cluster is favored. It was also noted that loss of a neutral solvent is reversible, whereas loss of differently sized protonated clusters is an irreversible reaction [224].

Interestingly, proton loss to solvents (or clusters) induced by ion solvation as well as proton/charge stabilization by ion solvation was discussed within the publications referenced above, but a systematical differentiation between charge depleting and charge retaining solvent molecules, based on their physical or chemical properties, was not made. Only the PA/GB values of solvents are considered and the fact that solvent clusters are more basic than individual solvent molecules.

In this work, the proposed charge retention/charge depletion mechanism (cf. section 4.4, addresses both effects of ion solvation. Depending on the degree of solvation and the relative GB of the respective solvent cluster, either loss of neutral solvent leading to charge retention or loss of a protonated solvent cluster leading to charge depletion is favored, as it was proposed by Chillier and co-workers [224]. The ability of a solvent to form a sufficiently large cluster around a proton and overcoming the GB of the protonation site was identified to be crucial for the likelihood of proton loss. Protic solvents are molecules, which form intermolecular (intracluster) H-bonds; thus, solvent chains and networks solvating a proton become feasible. Hydrogen bonds between individual H₂O or MeOH molecules, respectively, are identified in calculated structures of singly and doubly protonated EDA-H₂O clusters. These results are presented in section 5.3.1 as well as in optimized geometries of protonated methylamine and doubly protonated ethylene diamine (EDA) clustered by MeOH in [165]. The number of aprotic solvents binding via stable H-bonds to the ion is limited by the number of available protic H-atoms in the ion. Two ACN molecules always bind to different protons of the (di)amine, provided a second proton is available, see for example Figure 5.21. Hence, ACN molecules bound to the charge site of a (di)amine do structurally not resemble the most stable proton bound ACN clusters [(ACN)_nH]⁺. In contrast, protic solvents clustering at the charged site are reminiscent of the respective isolated protonated solvent clusters, i.e., [(H₂O)_nH]⁺ and [(MeOH)_nH]⁺, promoting proton transfer. This rationale is supported by potential energy surfaces calculated for proton transfer reactions from doubly protonated EDA to [(MeOH)_nH]⁺ ($n = 1 - 3$) and [(ACN)_mH]⁺ ($m = 1, 2$) [165]. All proton transfer processes considered, either to (MeOH)_n or (ACN)_m, are thermodynamically favored; proton transfer to (ACN)_m however is kinetically hindered by a high-energy transition state due to the required structural rearrangement. In contrast, the small energy barrier for proton transfer to (MeOH)_n is easily overcome and, in addition, becomes smaller with increasing cluster size n since the proton moves towards the MeOH ligands [165]. Thus, the calculations suggest that proton transfer to ACN clusters is unlikely to occur, while proton transfer to MeOH clusters is feasible. The notion that protic solvents remove a proton from multiply protonated analytes and aprotic solvents only bind to a proton without removing it, is therefore supported by the theoretical results. The latter are presented in detail in a recently published journal article [165].

The central result of the experimental and theoretical studies conducted in the course of this work is that the protic solvents H₂O and MeOH form hydrogen-bonded solvent networks around the site of protonation; this results in abstraction of a proton accompanied by formation of protonated solvent clusters, as they are thermodynamically favored. The aprotic solvent ACN builds stable diamine-ACN clusters, which stabilize the proton at the diamine. This leads to (1) kinetic hindrance of proton transfer to ACN clusters and (2) hindrance of clustering with present protic solvents (e.g. H₂O or MeOH). The latter occurs since the binding/solvation energy of ACN to aminic charge sites is exceeding that of H₂O and MeOH (see Table 5.2 and ref. [165]). This conclusion was supported by experiments using other protic (NH₃,

5 Results and Discussion: Terminal Alkyldiamines

EtOH) and aprotic (MeAc, Et₂O, DMSO) compounds. These findings are in accordance with recent experimental as well as theoretical investigations addressing ion (micro)solvation in DMS [52–54, 207]. The recent publication of the working group of Scott Hopkins [54] clearly demonstrates that the proposed charge retention/charge depletion model, which is based on nanoESI-MS experiments with Substance P and diamines, holds also true for protonated peptides and the dynamic clustering processes in ESI-DMS: addition of protic modifiers (H₂O, MeOH, EtOH, IPA) to the DMS cell causes nearly quantitative depletion of the higher charge state (3+) in favor of the lower charge state (2+), whereas addition of aprotic solvents leads to observation of ion-solvent clusters (3+ and 4+) but no charge reduction. Increase of the temperature in the DMS cell and/or increase of the separation voltage (SV) leads to reduction of the charge depletion efficiency of the protic modifiers. The authors concluded that with increasing effective ion temperature the number of solvent ligands in an ion-solvent cluster decreases, which in turn leads to a reduced proton affinity of the associated solvent cluster [54]. This supports the notion that proton transfer occurs intramolecularly through the solvent hydrogen-bond network established by protic solvents.

It remains unclear, whether proton transfer to solvents occurs during release of ion-solvent clusters at the liquid-gas interface, during solvent evaporation from a small droplet or within gas-phase ion-solvent clusters; most probably, all pathways are operative. The predominant pathway is governed by the structure, mass and charge state of the analyte, the chemical and physical properties of the liquid phase (e.g. surface tension, vapor pressure) and its components (e.g. PA/GB, intermolecular interactions, dipole moment, dielectric constant) as well as by instrumental parameters (e.g. use of dry and/or sheath gas, liquid flow rate). When spraying Substance P from ACN/H₂O or MeOH/H₂O solutions, no difference in the observed ion distribution as well as average charge state was observed (cf. section 4). In contrast, spraying the diamines from ACN/H₂O results in abundant formation of the doubly protonated diamine-ACN clusters, whereas mainly singly protonated ions are detected when the diamines are sprayed from MeOH/H₂O. As discussed in section 5.1.1 for diaminic analytes, this suggests that charge depletion processes are induced by protic solvents (MeOH and H₂O), which are initially present in the solution phase and droplets, and charge retention accompanied by cluster formation is achieved by aprotic solvents originating from the solution. It is reasonable to assume that the different results of the peptide Substance P and the rather small diaminic molecules are caused by different ion release mechanisms: release of SP ions from ESI droplets is described by CRM whereas diamine ion formation proceeds via the IEM mechanism (cf. section 2.1.3). As a consequence, without addition of gas phase modifiers or SCAs, SP ions are released as SP-H₂O clusters to the gas phase after the more volatile solvent (MeOH or ACN) has evaporated. Diamine ions are ejected as ion-solvent clusters from the charged droplets and the droplet composition as well as individual ion-solvent interactions determine the chemical structure of the ion-solvent clusters. Charge partition will happen between the escaping ion-solvent cluster and the droplet and subse-

quently, in the ion-solvent cluster between the ion and departing solvent molecules. Both processes are influenced by the composition of the liquid phase. Therefore, the observed charge state of diamines changes when using an protic solvent (MeOH) or an aprotic solvent (ACN) in addition to H₂O as spray solution. However, addition of a gas phase modifier shifts the observed charge states, no matter which ion release mechanism dominates, since enrichment of the modifier occurs in a droplet and/or in a gas-phase cluster.²⁷ The present charge retention/charge depletion model thus supports all proposed pathways of proton transfer to solvent clusters. Furthermore, the differentiation between charge retaining or charge depleting solvent molecules based on their aprotic or protic character is considered as an extension to the charge partition mechanisms, which were formulated in the early 1990s.

5.5 Summary and Conclusions

The observed effects on the ion population of terminal alkyldiamines resulting from gas phase modification with ACN (aprotic solvent) and MeOH (protic solvent) are described by the charge retention/charge depletion model: addition of MeOH to the ion source promotes the intensity of the singly protonated ions, whereas the addition of ACN vapor results in retention of the higher charge state (2+). The doubly protonated diamine-ACN clusters, $[M(\text{ACN})_n\text{H}_2]^{2+}$, show high abundance and characteristic cluster distributions in the mass spectrum, when ACN is present in the solution and/or the gas phase. Comparison with experimental results published by other researchers revealed that formation of $[M(\text{ACN})_n\text{H}_2]^{2+}$ clusters enables detection of ions with increased Coulomb repulsion, e.g. doubly protonated DA-2 and DA-3 ions, which are usually not observed in ESI mass spectra. Due to a decrease in Coulomb repulsion and thus solvation energy, the cluster number n decreases with increasing chain length and distance between the both charge sites, respectively. Furthermore, intramolecular interactions leading to internal solvation lessen external solvation by solvents.

As a consequence of the charge depletion and charge retention processes, the average charge state z_{avg} of the diamines is reduced to 1, when sufficient amounts of MeOH are present; in contrast, z_{avg} increases with the ACN mixing ratio up to 2. Systematic studies on the effect of the chain length demonstrates that z_{avg} of ions with adjacent charge sites is affected to a higher extent by both processes, charge depletion by protic solvents and charge retention by aprotic solvents. Experiments with simultaneous but spatially separated addition of ACN and MeOH to the background gas have underlined the notion that charge retention occurs due to prevention of charge depletion. In addition, charge depletion processes are also initiated by H₂O initially

²⁷Enrichment of ACN in a gas-phase cluster was demonstrated in experiments with collision gas modification; enrichment of gas phase modifiers in droplets is supported by other researchers as well [54], whereas enrichment of solution phase modifiers (SCAs) is suggested by molecular dynamics simulations [66, 225].

5 Results and Discussion: Terminal Alkyldiamines

mainly present in the solution phase. Therefore, the earlier aprotic solvents become abundant in the electrospray ionization process, the more efficient charge retention is.

Comprehensive studies on the impact of gas phase modification on CID (cf. section 5.1.3) illustrates that a solvating environment exists throughout the first and second vacuum stage of the mass spectrometer when a gas phase modifier is added in sufficient amounts to the ion source. In this case, the cluster equilibria are maintained, ions are shielded from activation due to solvation, and an increase of the acceleration voltage does not lead to dissociation or fragmentation. CID only occurs in the third vacuum stage. Furthermore, an efficient declustering process is observed in the QIT instrument, probably due to inelastic collisions with the helium buffer gas in the ion trap.

Chemical modification of the collision gas in the ion trap (cf. section 5.2) proved that cluster reactions between doubly protonated diamines and neutral ACN occur in the gas phase. Clustering with ACN is described with an equilibrium reaction system. The kinetics of the reactions between the diaminic gas-phase ions and ACN were investigated. In the presence of ACN, the intensity of the bare ion $[\text{MH}_2]^{2+}$ is depleted in favor of the cluster ions $[\text{M}(\text{ACN})_n\text{H}_2]^{2+}$. The decay of $[\text{MH}_2]^{2+}$ follows first-order-kinetics and the determined rate coefficients strongly depend on the ACN mixing ratio. In contrast, the observed formation of the charge depleted $[\text{MH}]^+$ ion does not correlate with the ACN mixing ratio; therefore, proton transfer processes to ACN clusters occurring in the gas-phase are ruled out. Furthermore, $[\text{M}(\text{ACN})_n\text{H}_2]^{2+}$ clusters are characterized as fragile ions (cf. section 5.2.5).

Theoretical methods were used to validate the experimental results, as described in section 5.3. They support the proposed charge retention/charge depletion model and underline crucial role of protic and aprotic compounds regarding cluster formation and proton transfer processes. Ethylenediamine (EDA) was selected as model system representing terminal alkyldiamines and molecules with adjacent charge sites. The structures of the clusters $[\text{EDA}(\text{S})_n\text{H}]^+$, $[\text{EDA}_2(\text{S})_n\text{H}]^+$, and $[\text{EDA}(\text{S})_n\text{H}_2]^{2+}$ with $\text{S} = \text{ACN}, \text{H}_2\text{O}$ were calculated using ab initio methods. The optimized geometries illustrate that the formation of stable hydrogen bonds between the solvent molecules is crucial for the stabilization of large ion-solvent clusters. Since ACN (aprotic solvent) can only act as a donor for one hydrogen bond without offering a new acceptor site, the number of available protic hydrogen atoms limits the number of ACN molecules binding to the charge site. This finding is in accord with the experimentally determined maximum cluster number $n = 6$ for $[\text{EDA}(\text{ACN})_n\text{H}_2]^{2+}$. Lack of detection of EDA- H_2O (or other DA- H_2O cluster species) is traced back to the high stability of the modeled smaller EDA-ACN clusters as compared to the EDA- H_2O clusters. The ligand switch reactions (R 5.9)-(R 5.11), in which $n \text{H}_2\text{O}$ are exchanged by $n \text{ACN}$, are thus exergonic. It is concluded that EDA ions are preferentially solvated by ACN; this finding is in accord with experimental and theoretical studies of other researchers addressing solvation of protonated ions by various polar solvents/modifiers.

5.5 Summary and Conclusions

Based on the optimized structures and their thermochemical data, equilibrated cluster distributions for different solvent mixing ratios were calculated. Large deviations exist between the calculated cluster distributions and the ion population observed in nanoESI-MS experiments. These deviations are explained by overestimations of the calculated cluster stabilities and, in particular, by the non-equilibrium conditions prevailing in the vacuum region of the mass spectrometer. Furthermore, the collision cross sections for the global minimum cluster structures were estimated, along with reduced mean ion mobility K_0^{mean} values. At a specific H₂O or ACN mixing ratio the following trend is observed: $K_0^{\text{mean}}([\text{EDA}(\text{S})_n\text{H}_2]^{2+}) > K_0^{\text{mean}}([\text{EDA}(\text{S})_n\text{H}]^+) > K_0^{\text{mean}}([\text{EDA}_2(\text{S})_n\text{H}]^+)$. Validation of the modeled distributions and K_0^{mean} values by IMS(-MS) experiments was restricted since unequivocal identification of the individual mobility peaks was not possible. Declustering and fragmentation processes occurring during ion transmission from the drift tube to the mass spectrometer lead to failure of detection of cluster species in the selective IMS-MS mode. The IMS experiments revealed that addition of ACN vapor to the drift tube leads to large mobility shifts caused by ion clustering, accompanied by the appearance of additional peaks, most probably ACN related reactant peaks, e.g. $[(\text{ACN})_m(\text{H}_2\text{O})_n\text{H}]^+$. Considering the experimental and theoretical results as well as works of other researchers addressing ion solvation, it is concluded that mobility peaks, which show minor mobility shifts, are related to singly protonated diamine ions, whereas peaks, which show major shifts, represent doubly protonated diamine ions or reactant ions.

Finally, proton transfer processes to solvent clusters are discussed on the basis of the experimental and theoretical results and in regard to the charge retention/charge depletion model (cf. section 5.4). In addition, earlier considerations regarding proton transfer reactions to solvents in ESI reported in the literature are taken into account. As a result, the proposed proton transfer processes are seamlessly integrating into the well-known ion release mechanisms and in the charge retention/charge depletion model. Furthermore, it is elucidated that the differentiation between charge depleting and charge retaining solvent molecules based on their protic and aprotic character, respectively, is considered as an extension to common charge partition mechanisms.

6 Conclusions and Outlook

In this work, ion-solvent interactions in ESI-MS leading either to charge retention or charge depletion of multiply protonated analytes were experimentally and theoretically investigated. Based on experiments with the peptide Substance P a charge retention/charge depletion model was developed and then comprehensively examined using terminal alkyldiamines with varying alkyl chain length acting as model systems for adjacent charge sites in multiply protonated (macro)molecules. The charge retention/charge depletion model describes ion transformation processes on the basis of ion-molecule cluster chemistry occurring in a multi-phase system.

The five hypotheses proposed in this work were validated:

- I Polar *aprotic* modifiers attach to multiply protonated ions and protect the charge(s) by formation of ion-modifier clusters.
- II Polar *protic* modifiers attach to multiply protonated ions and strip off protons to form proton-bound modifier clusters resulting in reduction of the ion charge state.
- III The occurrence of proton-bound clusters in the mass spectrum depends on the collision energies which the ions experience during the passage through the transfer stages of the mass spectrometer.
- IV The observed effects of both gas and solution phase modification are rationalized by enrichment of the modifiers/SCAs in the droplets/clusters leading to preferential ion solvation by the modifiers/SCAs.
- V Gas phase modification leads to the presence of the modifier in the transfer system of the mass spectrometer enabling ion-molecule cluster reactions to occur during ion transfer; when quadrupole ion traps are used also during mass analysis.

The investigations revealed that the presence of protic solvents leads to charge depletion, while the presence of aprotic solvents results in charge retention. It was hypothesized that formation of ion-solvent clusters facilitate intramolecular proton transfer to solvent clusters, when the gas-phase basicity of the solvent cluster solvating the charge site exceeds the GB of the charge site. Due to their ability to form hydrogen-bond networks, the number of protic solvent ligands of an ion-solvent

cluster and, therefore, the GB of the associated solvent cluster can increase until proton transfer becomes thermodynamically favorable. In contrast, the number of aprotic solvents solvating a charge site is limited because aprotic solvents can only act as a donor for one hydrogen bond without offering a new acceptor site. As a result, protic solvents form cluster structures at the charge site resembling pure stable solvent clusters, as illustrated by modeled ion-solvent structures, facilitating intracluster proton transfer. Furthermore, theoretical investigations on proton transfer reactions from doubly protonated ethylenediamine to MeOH and ACN clusters suggest that proton transfer to aprotic solvents is not thermodynamically but kinetically hindered due to a high-energy transition state. The notion that protic solvents can remove a proton from multiply protonated analytes, whereas aprotic solvents only bind to a proton without removing it, was validated by theoretical as well as experimental results. These considerations regarding formation of ion-solvent clusters and potential subsequent intramolecular proton transfer to solvent clusters are seamlessly integrated into common charge partition mechanisms as an extension.

In the presence of multiple solvents, as it is usually the case in electrospray ionization, external solvation of an ion is determined by the individual solvation energies and by the abundance of the solvents in the gas phase. Comparison of calculated solvation energies for different solvents and the occurrence of extensive clustering with ACN observed in experiments suggests that aminic charge sites are preferentially solvated by ACN. In a solvating environment, ion solvation is maintained throughout ion transfer and in special cases also during analysis. Therefore, addition of aprotic solvents, particularly when added as gas phase modifiers, can prevent charge depletion processes. CID experiments revealed that external solvation mitigates ion activation; ion activation usually leads to dissociation/fragmentation as well as to proton transfer processes, which are kinetically hindered under thermal conditions. Solvation by aprotic polar solvents can thus increase the observed average charge state and potentially maintain the solvation state and the conformation prevailing in the solution. In other words, ion transformation processes occurring during ion release and transfer are decreased or even inhibited by external solvation. Experiments show that the presence of ACN in the solution and/or gas phase enables the observation of charge states, which are otherwise not detected: doubly protonated ions of diamines with adjacent charge sites (ethylenediamine, propylenediamine), as observed by other researchers for non-covalent protein complexes or fragile peptides and polar modifier vapors. However, these higher charges states are usually detected as ion-solvent clusters and not as bare ions. Mass analysis of diamine-ACN clusters with a quadrupole ion trap revealed that these clusters can be characterized as fragile ions, which leads to large mass shifts, asymmetric and wide peak shapes, and a low isolation efficiency.

In (differential) ion mobility spectrometry, solvent vapor added to the drift gas leads to shifts of the mobility peaks when clustering between the ions and the solvent occurs. This results in an increased resolving power and allows separation of isomeric or even enantiomeric ions. The application of solvent vapor has become

6 Conclusions and Outlook

a common method in IMS and DMS and is extensively discussed in the literature. One goal of this work was to study ion-solvent interactions in ESI with AP-IMS experiments. It was intended to characterize the impact of addition of solvent vapor to the drift tube on the ion mobility peaks and the corresponding mass spectra. In contrast to the nanoESI-MS measurements, the ion-solvent dynamics are investigated under high pressure and low field and therefore nearly under equilibrium conditions, prevailing also in ESI ionization sources. It was hoped that the formation of protonated solvent clusters, potentially formed through proton transfer from doubly protonated diamine ions to solvent clusters, is observable with an AP-IMS-MS system. Unfortunately, the IMS experiments did not yield the expected results since identification of the mobility peaks was not possible. A systematic comparison between experimental and calculated cluster distributions and ion mobilities to elucidate the underlying ion-molecule reaction systems, was not possible. Further comprehensive IMS-MS experiments may lead to a better understanding of the characteristics of ion-solvent clusters present in ESI sources. Modeling of cluster structures and collision cross sections, in particular of mixed solvent-analyte clusters, will support in achieving this goal.

The proposed model of charge retention/charge depletion is supported by nanoESI experiments and theoretical investigations as well as by systematic experiments and calculations of other researchers. However, there are published results regarding the exposure of electrospray droplets to solvent vapor, which are neither in accord with each other nor with the model regarding the effect of protic and aprotic solvent vapor on the observed charge state distribution. A large number of parameters, e.g. the liquid flow rate, the application of dry/sheath gas, and the ion temperature highly influence the observed charge state and, in addition, the solvent vapor present in the gas phase impacts on the charge state. For this work, a nanoESI setup was employed to investigate gas phase modification in ESI-MS. The liquid flow rate was very low leading to minute amounts of the sprayed solvent in the gas phase. Therefore, it ought to be examined if the proposed model holds true for the examined analytes ionized in a commercial ESI source with substantially higher liquid flow rate. Furthermore, additional analytes could be investigated, in particular, analytes which do not have aminic charge sites.

The question whether enrichment of a gas phase modifier occurs mainly in charged droplets or in ion-solvent clusters due to ligand exchange reactions remains open. The question whether proton transfer to solvent clusters happens mainly during ion release at the liquid-gas interface, during solvent evaporation from a small droplet, or within a gas-phase cluster remains also unclear. Most probably, it depends on the analyte as well as on the physical, chemical, and fluid dynamical conditions in the ion source, which pathway is dominating. Application of deuterated solvents in experiments may reveal phase transfer processes and shed light on chemical dynamics of the solvation shell. In addition, molecular modeling will be beneficial to answer these questions, particularly, because preferential solvation in the solution phase does not necessarily correspond to the behavior in the gas phase. The preferential solvation

of diaminic ions in small droplets consisting of solvent mixtures is currently under investigation using molecular dynamics simulations.

The results of this work clearly demonstrate that for a deeper understanding of multiple charging phenomena in electrospray ionization mass spectrometry a distinction has to be drawn between protic and aprotic polar solvents and their impact on the recorded ion distribution. The crucial role of ion-solvent interactions in the ESI process, particularly the formation of proton-bound ion-solvent clusters, was elucidated. Charge depletion and charge retention processes are described on a molecular level in the proposed model based on external solvation of multiply charged ions. And finally, a connection was established between liquid and gas phase based charge retention (supercharging) mechanisms, which represents a major step forward regarding the comprehensive, multi-phase characterization of ESI processes.

List of Tables

2.1	Differences between nanoESI and conventional ESI	9
3.1	Settings of ion transfer stage voltages in ion trap experiments	36
3.2	Settings of ion transfer stage voltages in TOF experiments	38
4.1	Relevant physicochemical properties of the applied gas phase modifiers and supercharging agents (SCAs)	45
4.2	Gas-phase proton affinities of $(\text{NH}_3)_n$, $(\text{MeOH})_n$, $(\text{H}_2\text{O})_n$ ($n = 1-5$) and of $(\text{ACN})_n$, $(\text{MeAc})_n$ ($n = 1, 2$) in kJ/mol	49
5.1	Impact of the position of modifier addition on the observed z_{avg} of DA-9	86
5.2	Change of Gibbs free energy $\Delta_R G^\circ$ at standard conditions in kJ/mol for the reactions $[\text{EDA}(\text{S})_{n-1}\text{H}]^+ + \text{S} \rightarrow [\text{EDA}(\text{S})_n\text{H}]^+$, $[\text{EDA}(\text{S})_{n-1}\text{H}_2]^{2+} + \text{S} \rightarrow [\text{EDA}(\text{S})_n\text{H}_2]^{2+}$, and $[\text{EDA}_2(\text{S})_{n-1}\text{H}]^+ + \text{S} \rightarrow [\text{EDA}_2(\text{S})_n\text{H}]^+$, where S is H_2O or ACN	115
5.3	Change of Gibbs free energy $\Delta_R G^\circ$ at standard conditions in kJ/mol for the reactions $[\text{EDA}(\text{H}_2\text{O})_n\text{H}]^+ + n\text{ACN} \rightarrow [\text{EDA}(\text{ACN})_n\text{H}]^+ + n\text{H}_2\text{O}$, $[\text{EDA}(\text{H}_2\text{O})_n\text{H}_2]^{2+} + n\text{ACN} \rightarrow [\text{EDA}(\text{ACN})_n\text{H}_2]^{2+} + n\text{H}_2\text{O}$ and $[\text{EDA}_2(\text{H}_2\text{O})_n\text{H}]^+ + n\text{ACN} \rightarrow [\text{EDA}_2(\text{ACN})_n\text{H}]^+ + n\text{H}_2\text{O}$	123
5.4	Calculated collision cross section Ω_{avg} in N_2 at 298.15 K in \AA^2 and the reduced ion mobility K_0 in $\text{cm}^2\text{V}^{-1}\text{s}^{-1}$ of $[\text{EDA}(\text{S})_n\text{H}]^+$, $[\text{EDA}(\text{S})_n\text{H}_2]^{2+}$, and $[\text{EDA}_2(\text{S})_n\text{H}]^+$. S = H_2O or ACN	129

List of Figures

2.1	Model of a solvated ion in a polar solvent.	5
2.2	Model for the selective solvation of ions in a binary 1:1-mixture of the solvents S_1 and S_2	7
2.3	Schematic of the production of charged droplets by electrospray.	8
2.4	Comparison of well-established mechanisms for the formation of gas-phase ions from charged droplets.	13
2.5	Measured solvation energy for the hydration of singly and doubly protonated alkyldiamines in dependence of their chain length.	23
2.6	Schematic of interaction potentials for proton transfer reactions.	27
3.1	Half section of the custom nanoelectrospray ionization (nanoESI) source.	33
3.2	Setup of the nanoESI source indicating the gas and solution flow.	34
3.3	Schematic of the QIT and TOF instrument	35
3.4	Schematic of the AP-IMS instrument coupled to a microTOF mass spectrometer.	38
4.1	Mass spectra of SP without modifier addition, with ACN addition and with MeOH addition.	43
4.2	Average charge state of SP ions in dependence of the gas phase modifier mixing ratio.	44
4.3	Intensities of SP^{2+} , SP^{3+} , and SP^{3+} -solvent cluster signals in dependence of the ACN, MeAc, and Et_2O mixing ratio.	47
4.4	Intensities of SP^{2+} and SP^{3+} signals in dependence of the MeOH, H_2O , and NH_3 mixing ratio.	48
4.5	Average charge state of SP ions in dependence of the gas phase modifier mixing ratio in combination with the addition of SCAs.	54
4.6	Intensities of observed SP ion species in dependence of the gas phase modifier mixing ratio, obtained with combined solution (DMSO, sulfolane) and gas phase modification (ACN, MeOH).	55
4.7	SP signal intensity in dependence of the acceleration voltage.	58
4.8	Sketch of a charge retention/charge depletion model.	60
5.1	Intensities of observed DA-3 ion species in dependence of the ACN and MeOH phase modifier mixing ratio.	67
5.2	Intensities of observed DA-8 ion species in dependence of the ACN and MeOH phase modifier mixing ratio.	68

List of Figures

5.3	Overview of the observed ion species (TOF-MS) of the diaminic analytes depicted in a matrix representation.	69
5.4	Average cluster number of $[M(\text{ACN})_n\text{H}_2]^{2+}$ in dependence of the chain length and of the ACN gas phase mixing ratio present in the nanoESI source.	73
5.5	Average charge state of DA-3 and DA-8 ions in dependence of the ACN and MeOH gas phase mixing ratio.	78
5.6	Average charge state of DA-3, DA-5, DA-8 and DA-9 in dependence of the ACN and MeOH gas phase mixing ratio.	79
5.7	Average charge state of diamine ions in dependence of the chain length when no modifier, ACN as modifier, and MeOH as modifier is applied.	80
5.8	Average charge state, average cluster number of $[M(\text{ACN})_n\text{H}_2]^{2+}$ and relative diamine ion intensity without the dimer $[\text{M}_2\text{H}]^+$ in dependence of the chain length.	81
5.9	Average charge state of DA-8 and DA-9 ions in dependence of the ACN and MeOH gas phase mixing ratio and the location of modifier addition (source vs. capillary).	84
5.10	Intensities of observed DA-8 ion species in dependence of the acceleration voltage when no, ACN, and MeOH modifier is present in the ion source.	88
5.11	Intensities of observed DA-9 ion species in dependence of the acceleration voltage varied in the first, second and third vacuum stage. Observed ion populations are compared between the use of no modifier and the use of ACN as well as between the TOF and the QIT instrument.	91
5.12	Schematic of the measurement procedure used for characterization and examination of ion-molecule reactions within the QIT.	95
5.13	Intensities of observed DA-9 ion species in dependence of the trapping time when no modifier, ACN, and MeOH is present in the ion source.	97
5.14	Intensities of observed DA-9 ion species in dependence of the trapping time when ACN is present in the ion trap analyzer.	100
5.15	Determination of chemical reactions kinetics of the decay of $[\text{MH}_2]^{2+}$ and the formation of $[\text{MH}]^+$	104
5.16	Mass spectrum of DA-9 with and without addition of the collision gas He to the ion trap analyzer.	108
5.17	Section of the mass spectrum of DA-9 recorded with two different scan rates.	110
5.18	Calculated solvation energy of the sequential solvation of protonated EDA species by ACN and H_2O versus the cluster number.	116
5.19	Structure of the cyclic and the open conformer of $[\text{EDAH}]^+$	117
5.20	Optimized geometries of the $[\text{EDA}(\text{ACN})_4\text{H}]^+$ and $[\text{EDA}(\text{H}_2\text{O})_4\text{H}]^+$ clusters.	118
5.21	Optimized geometries of the $[\text{EDA}_2(\text{ACN})_3\text{H}]^+$ and $[\text{EDA}_2(\text{H}_2\text{O})_3\text{H}]^+$ clusters	120

5.22 Optimized geometries of the $[\text{EDA}(\text{ACN})_7\text{H}_2]^{2+}$ and $[\text{EDA}(\text{H}_2\text{O})_7\text{H}_2]^{2+}$ clusters. 121

5.23 Comparison between the modeled and measured cluster distribution of $[\text{EDA}(\text{ACN})_n\text{H}]^+$ and $[\text{EDA}(\text{ACN})_n\text{H}_2]^{2+}$ 125

5.24 Modeled cluster distributions of $[\text{EDA}(\text{S})_n\text{H}]^+$, $[\text{EDA}_2(\text{S})_n\text{H}]^+$, and $[\text{EDA}(\text{S})_n\text{H}_2]^{2+}$ with $\text{S} = \text{H}_2\text{O}$, ACN at different solvent mixing ratios 130

5.25 Chemical ionization ion mobility spectra (APCI-IMS) of EDA without and with addition of ACN as modifier in comparison to the APCI-IMS of ACN 133

5.26 Electrospray ionization ion mobility spectra of PDA without and with addition of ACN as modifier in comparison with the chemical ionization ion mobility spectrum of ACN 134

List of Abbreviations

<i>m/z</i>	mass to charge ratio
<i>z_{avg}</i>	Average charge state
Et ₂ O	Diethyl ether
ACN	Acetonitrile
APCI	Atmospheric Pressure Chemical Ionization
API	Atmospheric Pressure Ionization
APLI	Atmospheric Pressure Laser Ionization
APPI	Atmospheric Pressure Photoionization
CCS	Collision Cross Section
CEM	Charge Ejection Model
CID	Collision Induced Dissociation
CRM	Charged Residue Model
DA	Diamine
DA-2	1,2-diaminoethane
DA-3	1,3-diaminopropane
DA-5	1,5-diaminopentane
DA-8	1,8-diaminooctane
DA-9	1,9-diaminononane
DA-B	1,4-diaminobenzene
DMS	Differential Mobility Spectrometry
DMSO	Dimethyl sulfoxide
EDA	Ethylenediamine

List of Abbreviations

ES	Electrospray
ESI	Electrospray Ionization
EtOH	Ethanol
FWHM	Full Width at Half Maximum
GB	Gas-phase Basicity
IEM	Ion Evaporation Model
IMS	Ion Mobility Spectrometry
IPA	Isopropyl alcohol
MD	Molecular Dynamics
MeAc	Acetone
MeOH	Methanol
MS	Mass Spectrometry
nanoESI	Nanoelectrospray Ionization
NBA	Nitrobenzyl alcohol
ODA	Octanediamine
PA	Proton Affinity
PDA	Propylenediamine
QIT	Quadrupole Ion Trap
RF	Radio Frequency
SCA	Supercharging Agent
SP	Substance P
SP ²⁺	Doubly protonated Substance P ion
SP ³⁺	Triply protonated Substance P ion
TA-4	Diethylenetriamine
Td	Townsend, 1 Td=10 × 10 ⁻¹² Vm ²
TOF	Time-of-flight

Bibliography

- [1] E. Niyonsaba, J. M. Manheim, R. Yerabolu, and H. I. Kenttämäa. Recent Advances in Petroleum Analysis by Mass Spectrometry. *Analytical Chemistry*, 91(1):156–177, 2019.
- [2] G. Loos, A. Van Schepdael, and D. Cabooter. Quantitative mass spectrometry methods for pharmaceutical analysis. *Philosophical Transactions of the Royal Society A: Mathematical, Physical and Engineering Sciences*, 374(2079), 2016.
- [3] X. Wang, S. Wang, and Z. Cai. The latest developments and applications of mass spectrometry in food-safety and quality analysis. *Trends in Analytical chemistry*, 52:170–185, 2013.
- [4] J. J. Coon, J. E. Syka, J. Shabanowitz, and D. F. Hunt. Tandem mass spectrometry for peptide and protein sequence analysis. *BioTechniques*, 38(4):519–523, 2005.
- [5] J. R. Yates. Mass spectrometry and the age of the proteome. *Journal of Mass Spectrometry*, 33(1):1–19, 1998.
- [6] J. Aceña, S. Stampachiachiere, S. Pérez, and D. Barceló. Advances in liquid chromatography - High-resolution mass spectrometry for quantitative and qualitative environmental analysis. *Analytical and Bioanalytical Chemistry*, 407(21):6289–6299, 2015.
- [7] P. B. Armentrout. Fundamentals of ion-molecule chemistry. *Journal of Analytical Atomic Spectrometry*, 19:571–580, 2004.
- [8] S. Klee, V. Derpmann, W. Wißdorf, S. Klotowski, H. Kersten, K. J. Brockmann, T. Benter, S. Albrecht, A. P. Bruins, F. Dousty, T. J. Kauppila, R. Kostianen, R. O'Brien, D. B. Robb, and J. A. Syage. Are Clusters Important in Understanding the Mechanisms in Atmospheric Pressure Ionization? Part 1: Reagent Ion Generation and Chemical Control of Ion Populations. *Journal of The American Society for Mass Spectrometry*, 25(8):1310–1321, 2014.
- [9] S. Klee, A. Brockhaus, W. Wißdorf, M. Thinius, N. Hartmann, and T. Benter. Development of an ion activation stage for atmospheric pressure ionization sources. *Rapid Communications in Mass Spectrometry*, 29(2):143–154, 2015.
- [10] J. A. Loo, C. G. Edmonds, R. R. Ogorzalek Loo, H. R. Udseth, and R. D. Smith. Electrospray Ionization Mass Spectrometry and Tandem Mass Spectrometry of

- Large Biomolecules. In D. H. Russell, editor, *Experimental Mass Spectrometry*, chapter 7, pp. 243–286. Springer New York, New York, USA, 1st edition, 1994.
- [11] J. B. Fenn, M. Mann, C. K. M. Meng, S. F. Wong, and C. M. Whitehouse. Electrospray Ionization for Mass Spectrometry of Large Biomolecules. *Science*, 246(4926):64–71, 1989.
- [12] R. B. Cole. *Electrospray and MALDI Mass Spectrometry*. John Wiley & Sons, 2nd edition, 2010.
- [13] N. C. Polfer. Supercharging Proteins: How Many Charges Can a Protein Carry? *Angewandte Chemie - International Edition*, 56(29):8335–8337, 2017.
- [14] A. T. Iavarone and E. R. Williams. Mechanism of Charging and Supercharging Molecules in Electrospray Ionization. *Journal of the American Chemical Society*, 125(8):2319–2327, 2003.
- [15] R. R. Ogorzalek Loo, R. Lakshmanan, and J. A. Loo. What Protein Charging (and Supercharging) Reveal about the Mechanism of Electrospray Ionization. *Journal of The American Society for Mass Spectrometry*, 25(10):1675–1693, 2014.
- [16] A. T. Iavarone and E. R. Williams. Supercharging in electrospray ionisation: effects on signal and charge. *International Journal of Mass Spectrometry*, 219(1):63–72, 2002.
- [17] J. T. S. Hopper, K. Sokratous, and N. J. Oldham. Charge state and adduct reduction in electrospray ionization-mass spectrometry using solvent vapor exposure. *Analytical Biochemistry*, 421(2):788–790, 2012.
- [18] A. Kharlamova, B. M. Prentice, T.-Y. Huang, and S. A. McLuckey. Electrospray Droplet Exposure to Gaseous Acids for the Manipulation of Protein Charge State Distributions. *Analytical Chemistry*, 82(17):7422–7429, 2011.
- [19] A. T. Iavarone, J. C. Jurchen, and E. R. Williams. Effects of solvent on the maximum charge state and charge state distribution of protein ions produced by electrospray ionization. *Journal of the American Society for Mass Spectrometry*, 11(11):976–985, 2000.
- [20] S. Kaspar, T. Ledertheil, R. Hartmer, T. Hagedorn, C. Baessmann, and K. Nugent. Technical Note # TN-44: Increasing Peptide Identification Rates for Proteomics Samples by Controlling Peptide Charge States Using CaptiveSpray nanoBooster. Technical report, Bruker Daltonics, Bremen, Germany, 2013.
- [21] R. B. Cole. *Electrospray Ionization Mass Spectrometry*. John Wiley & Sons, New York, USA, 1997.
- [22] G. A. Krestov. *Thermodynamics of Solvation*. Ellis Horwood Limited, Chichester, England, 1991.

Bibliography

- [23] C. Reichardt. *Solvents and Solvent Effects in Organic Chemistry*. VCH, Weinheim, Germany, 2nd edition, 1988.
- [24] M. Soustelle. *Ionic and Electrochemical Equilibria*. John Wiley & Sons, Hoboken, New Jersey, USA, 2015.
- [25] R. R. Dogonadze, E. Kálmán, A. A. Kornyshev, and J. Ulstrup. *The Chemical Physics of Solvation*. Elsevier Inc., Amsterdam, The Netherlands, 1985.
- [26] A. Bagno. Probing the solvation shell of organic molecules by intermolecular ^1H NOESY. *Journal of Physical Organic Chemistry*, 15:790–795, 2002.
- [27] O. B. Nagy, M. W. Muanda, and J. B. Nagy. Competitive preferential solvation theory of weak molecular interactions. *Journal of the Chemical Society, Faraday Transactions 1: Physical Chemistry in Condensed Phases*, 74(3):2210–2228, 1978.
- [28] M. Szpakowska and O. B. Nagy. Application of the competitive preferential solvation theory to coordinative solute-solvent interactions. *Journal of the Chemical Society, Faraday Transactions 1: Physical Chemistry in Condensed Phases*, 85(9):2891–2899, 1989.
- [29] G. Taylor. Disintegration of water drops in an electric field. *Proceedings of the Royal Society of London. Series A. Mathematical and Physical Sciences*, 280(1382):383–397, 1964.
- [30] L. T. Cherney. Structure of Taylor cone-jets: limit of low flow rates. *Journal of Fluid Mechanics*, 378:167–196, 1999.
- [31] R. D. Smith, J. A. Loo, R. R. Ogorzalek Loo, M. Busman, and H. R. Udseth. Mass Spectrometry for Large Polypeptides and Proteins. *Mass Spectrometry Reviews*, 10:359–451, 1992.
- [32] P. Kebarle and M. Peschke. On the mechanisms by which the charged droplets produced by electrospray lead to gas phase ions. *Analytica Chimica Acta*, 406(1):11–35, 2000.
- [33] L. Konermann, E. Ahadi, A. D. Rodriguez, and S. Vahidi. Unraveling the Mechanism of Electrospray Ionization. *Analytical Chemistry*, 85(1):2–9, 2013.
- [34] L. Rayleigh. On the equilibrium of liquid conducting masses charged with electricity. *The London, Edinburgh, and Dublin Philosophical Magazine and Journal of Science*, 14(87):184–186, 1882.
- [35] Y. Kang, B. B. Schneider, and T. R. Covey. Improved Mass Spectrometer Robustness with DMS Pre-Filtering. In *Proceedings of 62nd ASMS Conference on Mass Spectrometry and Allied Topics*. 2014.

- [36] F. Stappert, C. Markert, M. Thinius, W. Wißdorf, H. Kersten, and T. Benter. Experimental Investigation of Charged Nanodroplets in MS Transfer Stages originating from ESI plumes. In *Proceedings of 68th ASMS Conference on Mass Spectrometry and Allied Topics*. 2020.
- [37] C. Markert, M. Rajkovic, W. Wißdorf, T. Benter, and H. Kersten. Simulations of Collision Induced Evaporation Processes of Nanodroplets in MS Inlet Stages. In *Proceedings of 68th ASMS Conference on Mass Spectrometry and Allied Topics*. 2020.
- [38] C. Markert, M. Thinius, L. Lehmann, C. Heintz, F. Stappert, W. Wissdorf, H. Kersten, T. Benter, B. B. Schneider, and T. R. Covey. Observation of charged droplets from electrospray ionization (ESI) plumes in API mass spectrometers. *Analytical and Bioanalytical Chemistry*, 2021.
- [39] Y. Kang, B. B. Schneider, and T. R. Covey. On the Nature of Mass Spectrometer Analyzer Contamination. *Journal of the American Society for Mass Spectrometry*, 28(11):2384–2392, 2017.
- [40] M. Smoluch, G. Grasso, P. Suder, and J. Silberring. *Mass Spectrometry: An Applied Approach*. John Wiley & Sons, Hoboken, New Jersey, USA, 2nd edition, 2019.
- [41] J. Fernandez De La Mora, G. J. Van Berkel, C. G. Enke, R. B. Cole, M. Martinez-Sanchez, and J. B. Fenn. Electrochemical processes in electrospray ionization mass spectrometry. *Journal of Mass Spectrometry*, 35(8):939–952, 2000.
- [42] B. P. Pozniak and R. B. Cole. Perspective on electrospray ionization and its relation to electrochemistry. *Journal of the American Society for Mass Spectrometry*, 26(3):369–385, 2015.
- [43] J. V. Iribarne and B. A. Thomson. On the evaporation of small ions from charged droplets. *The Journal of Chemical Physics*, 64(6):2287–2294, 1976.
- [44] M. Dole, L. L. Mack, R. L. Hines, R. C. Mobley, L. D. Ferguson, and M. B. Alice. Molecular beams of macroions. *The Journal of Chemical Physics*, 49(5):2240–2249, 1968.
- [45] L. L. Mack, P. Kralik, A. Rheude, and M. Dole. Molecular beams of macroions. II. *The Journal of Chemical Physics*, 52(10):4977–4986, 1970.
- [46] L. Konermann, A. D. Rodriguez, and J. Liu. On the formation of highly charged gaseous ions from unfolded proteins by electrospray ionization. *Analytical Chemistry*, 84(15):6798–6804, 2012.
- [47] E. Ahadi and L. Konermann. Modeling the behavior of coarse-grained polymer chains in charged water droplets: Implications for the mechanism of electrospray ionization. *Journal of Physical Chemistry B*, 116(1):104–112, 2012.

Bibliography

- [48] C. G. Enke. A Predictive Model for Matrix and Analyte Effects in Electrospray Ionization of Singly-Charged Ionic Analytes. *Analytical Chemistry*, 69(23):4885–4893, 1997.
- [49] R. Juraschek, T. Dülcks, and M. Karas. Nanoelectrospray - More than just a minimized-flow electrospray ionization source. *Journal of the American Society for Mass Spectrometry*, 10(4):300–308, 1999.
- [50] B. A. Thomson and J. V. Iribarne. Field induced ion evaporation from liquid surfaces at atmospheric pressure. *Journal of Chemical Physics*, 71(11):4451–4463, 1979.
- [51] T. Meyer, V. Gabelica, H. Grubmüller, and M. Orozco. Proteins in the gas phase. *Wiley Interdisciplinary Reviews: Computational Molecular Science*, 3(4):408–425, 2013.
- [52] W. S. Hopkins. Dynamic Clustering and Ion Microsolvation. In *Comprehensive Analytical Chemistry*, volume 83, chapter 4, pp. 83–122. Elsevier B.V., 1st edition, 2019.
- [53] N. J. Coughlan, C. Liu, M. J. Lecours, J. L. Campbell, and W. S. Hopkins. Preferential Ion Microsolvation in Mixed-Modifier Environments Observed Using Differential Mobility Spectrometry. *Journal of the American Society for Mass Spectrometry*, 30(11):2222–2227, 2019.
- [54] C. Ieritano, D. Rickert, J. Featherstone, J. F. Honek, J. L. Campbell, J. C. Y. L. Blanc, B. B. Schneider, and W. S. Hopkins. The Charge-State and Structural Stability of Peptides Conferred by Microsolvating Environments in Differential Mobility Spectrometry. *Journal of the American Society for Mass Spectrometry*, 2021.
- [55] J. Fernandez De La Mora. Electrospray ionization of large multiply charged species proceeds via Dole’s charged residue mechanism. *Analytica Chimica Acta*, 406(1):93–104, 2000.
- [56] E. Aliyari and L. Konermann. Formation of Gaseous Proteins via the Ion Evaporation Model (IEM) in Electrospray Mass Spectrometry. *Analytical Chemistry*, 92(15):10807–10814, 2020.
- [57] H. J. Sterling, J. S. Prell, C. A. Cassou, and E. R. Williams. Protein conformation and supercharging with DMSO from aqueous solution. *Journal of the American Society for Mass Spectrometry*, 22(7):1178–1186, 2011.
- [58] M. T. Donor, S. A. Ewing, M. A. Zenaidee, W. A. Donald, and J. S. Prell. Extended Protein Ions Are Formed by the Chain Ejection Model in Chemical Supercharging Electrospray Ionization. *Analytical Chemistry*, 89(9):5107–5114, 2017.

- [59] M. I. Oh and S. Consta. Charging and Release Mechanisms of Flexible Macromolecules in Droplets. *Journal of the American Society for Mass Spectrometry*, 28(11):2262–2279, 2017.
- [60] S. Consta and A. Malevanets. Manifestations of charge induced instability in droplets effected by charged macromolecules. *Physical Review Letters*, 109(14):1–5, 2012.
- [61] S. Consta, M. I. Oh, and A. Malevanets. New mechanisms of macroion-induced disintegration of charged droplets. *Chemical Physics Letters*, 663:1–12, 2016.
- [62] C. J. Hogan, J. A. Carroll, H. W. Rohrs, P. Biswas, and M. L. Gross. Charge carrier field emission determines the number of charges on native state proteins in electrospray ionization. *Journal of the American Chemical Society*, 130(22):6926–6927, 2008.
- [63] C. J. Hogan, J. A. Carroll, H. W. Rohrs, P. Biswas, and M. L. Gross. Combined charged residue-field emission model of macromolecular electrospray ionization. *Analytical Chemistry*, 81(1):369–377, 2009.
- [64] E. Ahadi and L. Konermann. Ejection of Solvated Ions from Electrosprayed Methanol/Water Nanodroplets Studied by Molecular Dynamics Simulations. *Journal of the American Chemical Society*, 133(24):9354–9363, 2011.
- [65] S. Consta, M. I. Oh, M. Sharawy, and A. Malevanets. Macroion-Solvent Interactions in Charged Droplets. *Journal of Physical Chemistry A*, 122(24):5239–5250, 2018.
- [66] H. Metwally, R. G. McAllister, V. Popa, and L. Konermann. Mechanism of Protein Supercharging by Sulfolane and *m*-Nitrobenzyl Alcohol: Molecular Dynamics Simulations of the Electrospray Process. *Analytical Chemistry*, 88(10):5345–5354, 2016.
- [67] P. D. Schnier, D. S. Gross, and E. R. Williams. On the maximum charge state and proton transfer reactivity of peptide and protein ions formed by electrospray ionization. *Journal of the American Society for Mass Spectrometry*, 6(11):1086–1097, 1995.
- [68] M. Thinius, C. Polaczek, M. Langner, S. Bräkling, A. Haack, H. Kersten, and T. Benter. Charge Retention/Charge Depletion in ESI-MS: Experimental Evidence. *Journal of the American Society for Mass Spectrometry*, 31(4):773–784, 2020.
- [69] A. T. Iavarone, J. C. Jurchen, and E. R. Williams. Supercharged protein and peptide ions formed by electrospray ionization. *Analytical Chemistry*, 73(7):1455–1460, 2001.

Bibliography

- [70] T. G. Flick and E. R. Williams. Supercharging with trivalent metal ions in native mass spectrometry. *Journal of the American Society for Mass Spectrometry*, 23(11):1885–1895, 2012.
- [71] H. J. Sterling, C. A. Cassou, A. C. Susa, and E. R. Williams. Electrothermal supercharging of proteins in native electrospray ionization. *Analytical Chemistry*, 84(8):3795–3801, 2012.
- [72] M. Šamalikova and R. Grandori. Protein Charge-State Distributions in Electrospray-Ionization Mass Spectrometry Do Not Appear to Be Limited by the Surface Tension of the Solvent. *Journal of the American Chemical Society*, 125(44):13352–13353, 2003.
- [73] M. Samalikova and R. Grandori. Testing the role of solvent surface tension in protein ionization by electrospray. *Journal of Mass Spectrometry*, 40(4):503–510, 2005.
- [74] H. J. Sterling, M. P. Daly, G. K. Feld, K. L. Thoren, A. F. Kintzer, B. A. Krantz, and E. R. Williams. Effects of Supercharging Reagents on Noncovalent Complex Structure in Electrospray Ionization from Aqueous Solutions. *Journal of the American Society for Mass Spectrometry*, 21(10):1762–1774, 2010.
- [75] H. J. Sterling and E. R. Williams. Origin of Supercharging in Electrospray Ionization of Noncovalent Complexes from Aqueous Solution. *Journal of the American Society for Mass Spectrometry*, 20(10):1933–1943, 2009.
- [76] C. A. Teo and W. A. Donald. Solution additives for supercharging proteins beyond the theoretical maximum proton-transfer limit in electrospray ionization mass spectrometry. *Analytical Chemistry*, 86(9):4455–4462, 2014.
- [77] S. H. Lomeli, I. X. Peng, S. Yin, R. R. Ogorzalek Loo, and J. A. Loo. New reagents for increasing ESI multiple charging of proteins and protein complexes. *Journal of the American Society for Mass Spectrometry*, 21(1):127–131, 2010.
- [78] K. A. Douglass and A. R. Venter. Investigating the role of adducts in protein supercharging with sulfolane. *Journal of the American Society for Mass Spectrometry*, 23(3):489–497, 2012.
- [79] K. Chingin, N. Xu, and H. Chen. Soft supercharging of biomolecular ions in electrospray ionization mass spectrometry. *Journal of the American Society for Mass Spectrometry*, 25(6):928–934, 2014.
- [80] I. Peters, H. Metwally, and L. Konermann. Mechanism of Electrospray Supercharging for Unfolded Proteins: Solvent-Mediated Stabilization of Protonated Sites during Chain Ejection. *Analytical Chemistry*, 91:6943–6952, 2019.

- [81] M. Meot-Ner, P. Hamlet, E. P. Hunter, and F. H. Field. Internal and External Solvation of Polyfunctional Ions. *Journal of the American Chemical Society*, 102(21):6393–6399, 1980.
- [82] J. S. Klassen, A. T. Blades, and P. Kebarle. Gas Phase Ion-Molecule Equilibria Involving Ions Produced by Electrospray. Hydration of Doubly Protonated Diamines. *Journal of the American Chemical Society*, 116(26):12075–12076, 1994.
- [83] J. S. Klassen, A. T. Blades, and P. Kebarle. Determinations of ion-molecule equilibria involving ions produced by electrospray. Hydration of protonated amines, diamines, and some small peptides. *Journal of Physical Chemistry*, 99(42):15509–15517, 1995.
- [84] A. T. Blades, J. S. Klassen, and P. Kebarle. Determination of Ion-Solvent Equilibria in the Gas Phase. Hydration of Diprotonated Diamines and Bis(trimethylammonium) Alkanes. *Journal of the American Chemical Society*, 118(49):12437–12442, 1996.
- [85] B. E. Winger, K. J. Light-Wahl, and R. D. Smith. Gas-phase proton transfer reactions involving multiply charged cytochrome c ions and water under thermal conditions. *Journal of the American Society for Mass Spectrometry*, 3(6):624–630, 1992.
- [86] E. R. Williams. Proton Transfer Reactivity of Large Multiply Charged Ions. *Journal of Mass Spectrometry*, 31(8):831–842, 1996.
- [87] P. D. Schnier, D. S. Gross, and E. R. Williams. Electrostatic Forces and Dielectric Polarizability of Multiply Protonated Gas-Phase Cytochrome c Ions Probed by Ion/Molecule Chemistry. *Journal of the American Chemical Society*, 117(25):6747–6757, 1995.
- [88] D. Zhan, J. Rosell, and J. B. Fenn. Solvation studies of electrospray ions - Method and early results. *Journal of the American Society for Mass Spectrometry*, 9(12):1241–1247, 1998.
- [89] S. E. Rodriguez-Cruz, J. S. Klassen, and E. R. Williams. Hydration of gas-phase ions formed by electrospray ionization. *Journal of the American Society for Mass Spectrometry*, 10(10):958–968, 1999.
- [90] M. Meot-Ner. Solvation of the Proton by HCN and CH₃CN . Condensation of HCN with Ions in the Gas Phase. *Journal of the American Chemical Society*, 100(15):4694–4699, 1978.
- [91] C. A. Deakyne, M. Meot-Ner, C. L. Campbell, M. G. Hughes, and S. P. Murphy. Multicomponent cluster ions. I. The proton solvated by CH₃CN/H₂O. *The Journal of Chemical Physics*, 84(9):4958–4969, 1986.

Bibliography

- [92] S. E. Rodriguez-Cruz, J. S. Klassen, and E. R. Williams. Hydration of Gas-Phase Gramicidin S $(M + 2H)^{2+}$ Ions Formed by Electrospray: The Transition From Solution to Gas-Phase Structure. *Journal of the American Society for Mass Spectrometry*, 8:565–568, 1997.
- [93] R. R. Ogorzalek Loo and R. D. Smith. Proton transfer reactions of multiply charged peptide and protein cations and anions. *Journal of Mass Spectrometry*, 30(2):339–347, 1995.
- [94] M. Meot-Ner. The ionic hydrogen bond. *Chemical Reviews*, 105(1):213–284, 2005.
- [95] A. Haack, J. Crouse, F. J. Schlüter, T. Benter, and W. S. Hopkins. A First Principle Model of Differential Ion Mobility: the Effect of Ion-Solvent Clustering. *Journal of the American Society for Mass Spectrometry*, 30(12):2711–2725, 2019.
- [96] R. Fernández-Maestre, C. Wu, and H. H. Hill. Using a Buffer Gas Modifier to Change Separation Selectivity in Ion Mobility Spectrometry. *International Journal of Mass Spectrometry*, 298:2–9, 2010.
- [97] B. B. Schneider, E. G. Nazarov, and T. R. Covey. Peak capacity in differential mobility spectrometry: Effects of transport gas and gas modifiers. *International Journal for Ion Mobility Spectrometry*, 15(3):141–150, 2012.
- [98] H. K. Holness, A. Jamal, A. Mebel, and J. R. Almirall. Separation mechanism of chiral impurities, ephedrine and pseudoephedrine, found in amphetamine-type substances using achiral modifiers in the gas phase. *Analytical and Bioanalytical Chemistry*, 404(8):2407–2416, 2012.
- [99] E. Waraksa, U. Perycz, J. Namiesnik, M. Sillanpää, T. Dymerski, M. Wójtowicz, and J. Puton. Dopants and gas modifiers in ion mobility spectrometry. *TrAC - Trends in Analytical Chemistry*, 82:237–249, 2016.
- [100] R. Fernández-Maestre, C. Wu, and H. H. Hill. Ammonia as a modifier in ion mobility spectrometry: Effects on ion mobilities and potential as a separation tool. *Journal of the Chilean Chemical Society*, 59(1):2398–2403, 2014.
- [101] R. Fernandez-Maestre. Buffer gas additives (modifiers/shift reagents) in ion mobility spectrometry: Applications, predictions of mobility shifts, and influence of interaction energy and structure. *Journal of Mass Spectrometry*, 53(7):598–613, 2018.
- [102] R. B. Cole and A. K. Harrata. Solvent effect on analyte charge state, signal intensity, and stability in negative ion electrospray mass spectrometry; implications for the mechanism of negative ion formation. *Journal of the American Society for Mass Spectrometry*, 4(7):546–556, 1993.

- [103] M. Meot-Ner and C. V. Speller. Filling of solvent shells about ions. 1. Thermochemical criteria and the effects of isomeric clusters. *The Journal of Physical Chemistry*, 90(25):6616–6624, 1986.
- [104] M. Peschke, A. Blades, and P. Kebarle. Charged states of proteins. Reactions of doubly protonated alkyldiamines with NH_3 : Solvation or deprotonation. Extension of two proton cases to multiply protonated globular proteins observed in the gas phase. *Journal of the American Chemical Society*, 124(38):11519–11530, 2002.
- [105] Z. Karpas. Evidence of Proton-Induced Cyclization of α,ω -Diamines from Ion Mobility Measurements. *International Journal of Mass Spectrometry and Ion Processes*, 93:237–242, 1989.
- [106] R. Fernández-Maestre, C. Wu, and H. H. Hill. Buffer gas modifiers effect resolution in ion mobility spectrometry through selective ion-molecule clustering reactions. *Rapid Communications in Mass Spectrometry*, 26(19):2211–2223, 2012.
- [107] S. Ikuta and O. Nomura. An ab initio study on the intramolecular hydrogen bond of protonated ethylene glycol and ethylenediamine. *Chemical Physics Letters*, 154(1):71–76, 1989.
- [108] J. P. Wagner, D. C. McDonald, and M. A. Duncan. Spectroscopy of Proton Coordination with Ethylenediamine. *Journal of Physical Chemistry A*, 122(23):5168–5176, 2018.
- [109] D. De Corte, C.-W. Schlöpfer, and C. Daul. A density functional theory study of the conformational properties of 1,2-ethanediamine: protonation and solvent effects. *Theoretical Chemistry Accounts*, 105:39–45, 2000.
- [110] R. Yamdagni and P. Kebarle. Gas-Phase Basicities of Amines. Hydrogen Bonding in Proton-Bound Amine Dimers and Proton-Induced Cyclization of α,ω -Diamines. *Journal of the American Chemical Society*, 95(11):3504–3510, 1973.
- [111] B. A. Thomson. Declustering and fragmentation of protein ions from an electrospray ion source. *Journal of the American Society for Mass Spectrometry*, 8(10):1053–1058, 1997.
- [112] R. R. Ogorzalek Loo and R. D. Smith. Investigation of the Gas-Phase Structure of Electrosprayed Proteins Using Ion-Molecule Reactions. *Journal of the American Society for Mass Spectrometry*, 5(4):207–220, 1994.
- [113] J. M. Mestdagh, A. Binet, and O. Sublemontier. Solvation Shells of the Proton Surrounded by Acetonitrile, Ethanol, and Water Molecules. *Journal of Physical Chemistry*, 93(26):8300–8303, 1989.

Bibliography

- [114] A. S. Lemoff, C. C. Wu, M. F. Bush, and E. R. Williams. Binding energies of water to doubly hydrated cationized glutamine and structural analogues in the gas phase. *Journal of Physical Chemistry A*, 110(10):3662–3669, 2006.
- [115] B. Gao, T. Wyttenbach, and M. T. Bowers. Hydration of Protonated Aromatic Amino Acids : Phenylalanine, Tryptophane, and Tyrosine. *Journal of the American Chemical Society*, 131(13):4695–4701, 2009.
- [116] V. Q. Nguyen, X. G. Chen, and A. L. Yergey. Observations of Magic Numbers in Gas Phase Hydrates of Alkylammonium Ions. *Journal of the American Society for Mass Spectrometry*, 8:1175–1179, 1997.
- [117] S. B. Nielsen, M. Masella, and P. Kebarle. Competitive Gas-Phase Solvation of Alkali Metal Ions by Water and Methanol. *Journal of Physical Chemistry A*, 103:9891–9898, 1999.
- [118] B. J. Duncombe, J. O. S. Rydén, L. Puškar, H. Cox, and A. J. Stace. A Gas-Phase Study of the Preferential Solvation of Mn^{2+} in Mixed Water/Methanol Clusters. *Journal of the American Society for Mass Spectrometry*, 19:520–530, 2008.
- [119] M. H. Amad, N. B. Cech, G. S. Jackson, and C. G. Enke. Importance of gas-phase proton affinities in determining the electrospray ionization response for analytes and solvents. *Journal of Mass Spectrometry*, 35(7):784–789, 2000.
- [120] S. G. Lias, J. F. Liebman, and R. D. Levin. Evaluated Gas Phase Basicities and Proton Affinities of Molecules; Heats of Formation of Protonated Molecules. *Journal of Physical and Chemical Reference Data*, 13(3):695–808, 1984.
- [121] P. D. Schnier, W. D. Price, and E. R. Williams. Modeling the maximum charge state of arginine-containing peptide ions formed by electrospray ionization. *Journal of the American Society for Mass Spectrometry*, 7(9):972–976, 1996.
- [122] E. P. L. Hunter and S. G. Lias. Evaluated Gas Phase Basicities and Proton Affinities of Molecules: An Update. *Journal of Physical and Chemical Reference Data*, 27(3):413–656, 1998.
- [123] S. Petrie, G. Javahery, and D. K. Bohme. First steps towards a gas-phase acidity ladder for derivatized fullerene dications. *International Journal of Mass Spectrometry and Ion Processes*, 124(2):145–156, 1993.
- [124] S. A. McLuckey, G. J. Van Berkel, and G. L. Glish. Reactions of dimethylamine with multiply charged ions of cytochrome c. *Journal of the American Chemical Society*, 112(14):5668–5670, 1990.
- [125] J. L. Stephenson and S. A. McLuckey. Ion/Ion Reactions in the Gas Phase: Proton Transfer Reactions Involving Multiply-Charged Proteins. *Journal of the American Chemical Society*, 118(31):7390–7397, 1996.

- [126] D. S. Gross and E. R. Williams. Structure of Gramicidin S $(M + H + X)^{2+}$ Ions ($X = \text{Li, Na, K}$) Probed by Proton Transfer Reactions. *Journal of the American Chemical Society*, 118(1):202–204, 1996.
- [127] J. L. Sterner, M. V. Johnston, G. R. Nicol, and D. P. Ridge. Apparent proton affinities of highly charged peptide ions. *Journal of the American Society for Mass Spectrometry*, 10(6):483–491, 1999.
- [128] S. J. Valentine, A. E. Counterman, and D. E. Clemmer. Conformer-Dependent Proton-Transfer Reactions of Ubiquitin Ions. *Journal of the American Society for Mass Spectrometry*, 0305(97):954–961, 1997.
- [129] S. Gronert. An ab initio study of proton transfers from gas-phase dications: Complications in kinetic methods for determining acidities. *Journal of the American Chemical Society*, 118(14):3525–3526, 1996.
- [130] D. S. Gross, S. E. Rodriguez-Cruz, S. Bock, and E. R. Williams. Measurement of Coulomb Energy and Dielectric Polarizability of Gas-Phase Diprotonated Diaminoalkanes. *Journal of Physical Chemistry*, 99(12):4034–4038, 1995.
- [131] D. Auerbach, J. Aspenleiter, and D. A. Volmer. Description of gas-phase ion/neutral interactions in differential ion mobility spectrometry: CV prediction using calibration runs. *Journal of the American Society for Mass Spectrometry*, 25(9):1610–1621, 2014.
- [132] V. Blagojevic, G. K. Koyanagi, and D. K. Bohme. Multi-component ion modifiers and arcing suppressants to enhance differential mobility spectrometry for separation of peptides and drug molecules. *Journal of the American Society for Mass Spectrometry*, 25(3):490–497, 2014.
- [133] N. P. Ewing, G. A. Pallante, X. Zhang, and C. J. Cassady. Gas-phase basicities for ions from bradykinin and its des-arginine analogues. *Journal of Mass Spectrometry*, 36(8):875–881, 2001.
- [134] J. L. Holmes, C. Aubry, and P. M. Mayer. Proton Affinities of Primary Alkanols: An Appraisal of the Kinetic Method. *Journal of Physical Chemistry A*, 103(6):705–709, 1999.
- [135] X. Cheng, Z. Wu, and C. Fenselau. Collision Energy Dependence of Proton-Bound Dimer Dissociation: Entropy Effects, Proton Affinities, and Intramolecular Hydrogen-Bonding in Protonated Peptides. *Journal of the American Chemical Society*, 115(11):4844–4848, 1993.
- [136] P. L. Houston. *Chemical Kinetics and Reaction Dynamics*. Dover Publications, Mineola, New York, USA, 2006.

Bibliography

- [137] R. Knochenmuss, O. Cheshnovsky, and S. Leutwyler. Proton transfer reactions in neutral gas-phase clusters: 1-Naphthol with H₂O, D₂O, CH₃OH, NH₃ and piperidine. *Chemical Physics Letters*, 144(4):317–323, 1988.
- [138] A. T. Blades, P. Jayaweera, M. G. Ikonou, and P. Kebarle. Studies of alkaline earth and transition metal M⁺⁺ gas phase ion chemistry. *The Journal of Chemical Physics*, 92(10):5900–5906, 1990.
- [139] A. T. Blades, P. Jayaweera, M. G. Ikonou, and P. Kebarle. Ion-molecule clusters involving doubly charged metal ions (M²⁺). *International Journal of Mass Spectrometry and Ion Processes*, 102(C):251–267, 1990.
- [140] K. Murray, R. Boyd, M. Eberlin, G. Langley, L. Li, Y. Naito, and J. Tabet. IUPAC standard definitions of terms relating to mass spectrometry. *Pure and Applied Chemistry*, 85(7):1515–1609, 2005.
- [141] M. J. Chalmers and S. J. Gaskell. Advances in mass spectrometry for proteome analysis. *Current opinion in biotechnology*, 11(4):384–90, 2000.
- [142] P. Kebarle. A brief overview of the present status of the mechanisms involved in electrospray mass spectrometry. *Journal of Mass Spectrometry*, 35:804–817, 2000.
- [143] H. Kambara and I. Kanomata. Collision-induced dissociation of water cluster ions at high pressure. *International Journal of Mass Spectrometry and Ion Physics*, 25(2):129–136, 1977.
- [144] P. M. Mayer and C. Poon. The mechanisms of collisional activation of ions in mass spectrometry. *Mass Spectrometry Reviews*, 28(4):608–639, 2009.
- [145] S. A. McLuckey and D. E. Goeringer. Slow heating methods in tandem mass spectrometry. *Journal of Mass Spectrometry*, 32(5):461–474, 1997.
- [146] V. Popa, D. A. Trecroce, R. G. McAllister, and L. Konermann. Collision-Induced Dissociation of Electrosprayed Protein Complexes: An All-Atom Molecular Dynamics Model with Mobile Protons. *Journal of Physical Chemistry B*, 120(23):5114–5124, 2016.
- [147] Z. Hall, A. Politis, M. F. Bush, L. J. Smith, and C. V. Robinson. Charge-state dependent compaction and dissociation of protein complexes: Insights from ion mobility and molecular dynamics. *Journal of the American Chemical Society*, 134(7):3429–3438, 2012.
- [148] M. Zhou, S. Dagan, and V. H. Wysocki. Impact of charge state on gas-phase behaviors of noncovalent protein complexes in collision induced dissociation and surface induced dissociation. *The Analyst*, 138(5):1353, 2013.

- [149] V. Derpmann. *Development and Characterization of capillary Atmospheric Pressure Electron Capture Ionization (cAPECI)*. Ph.D. thesis, Bergische Universität Wuppertal, Germany, 2014.
- [150] J. F. Parcher, M. Wang, A. G. Chittiboyina, and I. A. Khan. In-source collision-induced dissociation (IS-CID): Applications, issues and structure elucidation with single-stage mass analyzers. *Drug Testing and Analysis*, 10(1):28–36, 2018.
- [151] W. D. Van Dongen, J. I. Van Wijk, B. N. Green, W. Heerma, and J. Haverkamp. Comparison between collision induced dissociation of electrosprayed protonated peptides in the up-front source region and in a low-energy collision cell. *Rapid Communications in Mass Spectrometry*, 13(17):1712–1716, 1999.
- [152] C. J. Barinaga, C. G. Edmonds, H. R. Udseth, and R. D. Smith. Sequence determination of multiply charged peptide molecular ions by electrospray-ionization tandem mass spectrometry. *Rapid Communications in Mass Spectrometry*, 3(5):160–164, 1989.
- [153] A. L. Rockwood, M. Busman, and R. D. Smith. Coulombic effects in the dissociation of large highly charged ions. *International Journal of Mass Spectrometry and Ion Processes*, 111(C):103–129, 1991.
- [154] Bruker Daltonics. HCT ultra User Manual Version 1.2.1. Technical report, Bremen, Germany, 2006.
- [155] D. A. Kaplan, R. Hartmer, A. Brekenfeld, J. Franzen, and M. Schubert. 3D-Quadrupole Ion Trap Mass Spectrometry. In R. E. March and J. F. J. Todd, editors, *Practical Aspects of Trapped Ion Mass Spectrometry Vol. IV Theory and Instrumentation*, chapter 13. CRC Press, Boca Raton, FL, USA, 2010.
- [156] G. Van Rossum and F. Drake. *Python 3 Reference Manual*. CreateSpace, Scotts Valley, CA, USA, 2009.
- [157] J. D. Hunter. Matplotlib: A 2D Graphics Environment. *Computing in Science and Engineering*, 9(3):90–95, 2007.
- [158] C. R. Harris, K. J. Millman, S. J. van der Walt, R. Gommers, P. Virtanen, D. Cournapeau, E. Wieser, J. Taylor, S. Berg, N. J. Smith, R. Kern, M. Picus, S. Hoyer, M. H. van Kerkwijk, M. Brett, A. Haldane, J. F. del Río, M. Wiebe, P. Peterson, P. Gérard-Marchant, K. Sheppard, T. Reddy, W. Weckesser, H. Abbasi, C. Gohlke, and T. E. Oliphant. Array programming with NumPy. *Nature*, 585(7825):357–362, 2020.
- [159] Bruker Daltonics. micrOTOF User Manual Version 1.0. Technical report, Bremen, Germany, 2006.

Bibliography

- [160] A. T. Kirk, M. Allers, P. Cochems, J. Langejuergen, and S. Zimmermann. A compact high resolution ion mobility spectrometer for fast trace gas analysis. *The Analyst*, 138(18):5200–5207, 2013.
- [161] M. Allers, L. Timoumi, A. T. Kirk, F. Schlottmann, and S. Zimmermann. Coupling of a High-Resolution Ambient Pressure Drift Tube Ion Mobility Spectrometer to a Commercial Time-of-flight Mass Spectrometer. *Journal of the American Society for Mass Spectrometry*, 29(11):2208–2217, 2018.
- [162] M. J. Frisch, G. W. Trucks, H. B. Schlegel, G. E. Scuseria, M. A. Robb, J. R. Cheeseman, G. Scalmani, V. Barone, G. A. Petersson, H. Nakatsuji, X. Li, M. Caricato, A. V. Marenich, J. Bloino, B. G. Janesko, R. Gomperts, B. Mennucci, H. P. Hratchian, J. V. Ortiz, A. F. Izmaylov, J. L. Sonnenberg, D. Williams-Young, F. Ding, F. Lipparini, F. Egidi, J. Goings, B. Peng, A. Petrone, T. Henderson, D. Ranasinghe, V. G. Zakrzewski, J. Gao, N. Rega, G. Zheng, W. Liang, M. Hada, M. Ehara, K. Toyota, R. Fukuda, J. Hasegawa, M. Ishida, T. Nakajima, Y. Honda, O. Kitao, H. Nakai, T. Vreven, K. Throssell, J. A. J. Montgomery, J. E. Peralta, F. Ogliaro, M. J. Bearpark, J. J. Heyd, E. N. Brothers, K. N. Kudin, V. N. Staroverov, T. A. Keith, R. Kobayashi, J. Normand, K. Raghavachari, A. P. Rendell, J. C. Burant, S. S. Iyengar, J. Tomasi, M. Cossi, J. M. Millam, M. Klene, C. Adamo, R. Cammi, J. W. Ochterski, R. L. Martin, K. Morokuma, O. Farkas, J. B. Foresman, and D. J. Fox. Gaussian 16, Revision A.03, Gaussian Inc., Wallingford, CT, USA, 2016.
- [163] A. Haack. *Theoretical Investigations on Cluster Formation in Mass Spectrometry*. Ph.D. thesis, University of Wuppertal, 2020.
- [164] R. Dennington, T. A. Keith, and J. M. Millam. GaussView, Version 6.0.16, Semichem Inc., Shawnee Mission, KS, USA, 2016.
- [165] A. Haack, C. Polaczek, M. Tsolakis, M. Thinius, H. Kersten, and T. Benter. Charge Retention/Charge Depletion in ESI-MS: Theoretical Rationale. *Journal of the American Society for Mass Spectrometry*, 31(4):785–795, 2020.
- [166] D. W. Boo. Ab initio calculations of protonated ethylenediamine-(water)₃ complex: Roles of intramolecular hydrogen bonding and hydrogen bond cooperativity. *Bulletin of the Korean Chemical Society*, 22(7):693–698, 2001.
- [167] J. W. Ochterski. Thermochemistry in Gaussian. Technical report, Pittsburgh, PA, USA, 2000.
- [168] C. Ieritano, J. Crouse, J. L. Campbell, and W. S. Hopkins. A parallelized molecular collision cross section package with optimized accuracy and efficiency. *Analyst*, 144(5):1660–1670, 2019.

- [169] A. A. Shvartsburg and M. F. Jarrold. An exact hard-spheres scattering model for the mobilities of polyatomic ions. *Chemical Physics Letters*, 261(1-2):86–91, 1996.
- [170] E. Mason and E. W. McDaniel. *Transport Properties Of Ions In Gases*. John Wiley & Sons, New York, USA, 1988.
- [171] F. Calvo, J. P. K. Doye, and D. J. Wales. Equilibrium properties of clusters in the harmonic superposition approximation. *Chemical Physics Letters*, 366(1-2):176–183, 2002.
- [172] E. V. Krylov and E. G. Nazarov. Electric field dependence of the ion mobility. *International Journal of Mass Spectrometry*, 285(3):149–156, 2009.
- [173] S. M. Miladinović, L. Fornelli, Y. Lu, K. M. Piech, H. H. Girault, and Y. O. Tsybin. In-spray supercharging of peptides and proteins in electrospray ionization mass spectrometry. *Analytical Chemistry*, 84(11):4647–4651, 2012.
- [174] K. L. Fort, J. A. Silveira, N. A. Pierson, K. A. Servage, D. E. Clemmer, and D. H. Russell. From solution to the gas phase: Factors that influence kinetic trapping of substance P in the gas phase. *Journal of Physical Chemistry B*, 118(49):14336–14344, 2014.
- [175] J. A. Silveira, K. L. Fort, D. Kim, K. A. Servage, N. A. Pierson, D. E. Clemmer, and D. H. Russell. From solution to the gas phase: Stepwise dehydration and kinetic trapping of substance p reveals the origin of peptide conformations. *Journal of the American Chemical Society*, 135(51):19147–19153, 2013.
- [176] R. G. Pereyra, M. L. Asar, and M. A. Carignano. The role of acetone dipole moment in acetone-water mixture. *Chemical Physics Letters*, 507(4-6):240–243, 2011.
- [177] G. F. Longster and E. E. Walker. Effect of permanent dipoles on the cohesive energy and solvent action of some highly polar substances. *Transactions of the Faraday Society*, 49:228–233, 1953.
- [178] J. W. Vaughn and C. F. Hawkins. Physical Properties of Tetrahydrothiophene-1,1-Dioxide and 3-Methyltetrahydrothiophene-1,1-Dioxide. *Journal of Chemical and Engineering Data*, 9(1):140–142, 1964.
- [179] P. J. Linstrom and W. G. Mallard, editors. *NIST Chemistry WebBook, NIST Standard Reference Database Number 69*. National Institute of Standards and Technology, Gaithersburg MD, 20899, <http://webbook.nist.gov>.
- [180] J. J. Jasper. The Surface Tension of Pure Liquid Compounds. *Journal of Physical and Chemical Reference Data*, 1(4):841–1010, 1972.

Bibliography

- [181] R. D. Nelson, D. R. Lide, and A. A. Maryott. *Selected values of electric dipole moments for molecules in the gas phase*. National Bureau of Standards, Gaithersburg, MD, USA, 1967.
- [182] S. Murov. *Properties of Solvents Used in Organic Chemistry*. <http://murov.info/orgsolvents.htm>.
- [183] M. Thinius, C. Polaczek, C. Markert, D. Erdogdu, H. Kersten, and T. Benter. Systematic studies of the impact of chemical modifiers on the ion population observed with nESI MS. In *Proceedings of the 65th ASMS Conference on Mass Spectrometry and Allied Topics*. Indianapolis, IN, USA, 2017.
- [184] W. Y. Feng, M. Goldenberg, and C. Lifshitz. Reactions of proton-bound dimers. *Journal of the American Society for Mass Spectrometry*, 5(8):695–703, 1994.
- [185] K. A. Servage, J. A. Silveira, K. L. Fort, and D. H. Russell. From Solution to Gas Phase: The Implications of Intramolecular Interactions on the Evaporative Dynamics of Substance P During Electrospray Ionization. *The Journal of Physical Chemistry B*, 119(13):4693–4698, 2015.
- [186] Bruker Daltonics. Advance CaptiveSpray Source User Manual Revision 4. Technical report, Bremen, Germany, 2011.
- [187] Bruker Daltonics. CaptiveSpray nanoBooster, The Revolution in Proteomics Ionization. Technical report, Bremen, Germany, 2013.
- [188] K. Alagesan and D. Kolarich. To enrich or not to enrich: Enhancing (glyco)peptide ionization using the CaptiveSpray nanoBooster™. *bioRxiv*, 2019.
- [189] M. Thinius, M. Langner, H. Kersten, and T. Benter. Impact of chemical modifiers on the cluster chemistry during electrospray ionization. In *Proceedings of the 64th ASMS Conference on Mass Spectrometry and Allied Topics*. San Antonio, TX, USA, 2016.
- [190] K. Marx, A. Kiehne, and M. Meyer. Application Note # LCMS-93 amaZon speed ETD: Exploring glycopeptides in protein mixtures using Fragment Triggered ETD and CaptiveSpray nanoBooster. Technical report, Bruker Daltonics, Bremen, Germany, 2014.
- [191] R. Garnsey and J. E. Prue. Precise cryoscopic determination of osmotic coefficients for solutions of some alkali metal salts in dimethyl sulphoxide and in sulfolane. *Transactions of the Faraday Society*, 64:1206–1218, 1968.
- [192] T. L. Buxton and J. A. Caruso. Spectroscopic studies of solvation in sulfolane. *Journal of Physical Chemistry*, 77(15):1882–1884, 1973.

- [193] X.-Z. Qin and Y. Yuan. Electrospray ionization/collision-induced dissociation of protonated substance P ions - Effect of charge on the fragmentation patterns. *International Journal of Mass Spectrometry*, 237(2-3):123–133, 2004.
- [194] X.-T. Tang, P. Thibault, and R. K. Boyd. Fragmentation Reactions of Multiply-Protonated Peptides and Implications for Sequencing by Tandem Mass Spectrometry with Low-Energy Collision-Induced Dissociation. *Analytical Chemistry*, 65(20):2824–2834, 1993.
- [195] D. Morsa, E. Hanozin, G. Eppe, and E. D. Pauw. Solvent Adducts in Ion Mobility Spectrometry: Toward an Alternative Reaction Probe for Thermometer Ions. *Journal of the American Society for Mass Spectrometry*, 31(6):1167–1171, 2020.
- [196] J. C. Demuth and S. A. McLuckey. Electrospray droplet exposure to organic vapors: Metal ion removal from proteins and protein complexes. *Analytical Chemistry*, 87(2):1210–1218, 2015.
- [197] A. F. L. Santos and M. A. Ribeiro Da Silva. Diaminobenzenes: An experimental and computational study. *Journal of Physical Chemistry B*, 115(17):4939–4948, 2011.
- [198] R. Manoharan and S. K. Dogra. Spectral Characteristics of Phenylenediamines and Their Various Protonated Species. *Bulletin of the Chemical Society of Japan*, 60(12):4409–4415, 1987.
- [199] M. J. O’Neil. *The Merck index: an encyclopedia of chemicals, drugs, and biologicals*. Royal Society of Chemistry, Cambridge, UK, 15th edition, 2013.
- [200] C.-A. Coulomb. Premier mémoire sur l’électricité et le magnétisme. *Histoire de l’Académie Royale des Sciences*, 1785.
- [201] C.-A. Coulomb. Second mémoire sur l’électricité et le magnétisme. *Histoire de l’Académie Royale des Sciences*, 1785.
- [202] D. Halliday, R. Resnick, and J. Walker. Electric Potential. In *Fundamentals of Physics*. John Wiley & Sons, New York, USA, 5th edition, 1997.
- [203] P. Kebarle, S. Searles, A. Zolla, J. Scarborough, and M. Arshadi. Solvation of the hydrogen ion by water molecules in the gas phase. Heats and entropies of solvation of individual reactions: $\text{H}^+(\text{H}_2\text{O})_{n-1} + \text{H}_2\text{O} \rightarrow \text{H}^+(\text{H}_2\text{O})_n$. *Journal of the American Chemical Society*, 89(25):6393–6399, 1967.
- [204] Y. Lau, S. Ikuta, and P. Kebarle. Thermodynamics and kinetics of the gas-phase reactions: $\text{H}_3\text{O}^+(\text{H}_2\text{O})_{n-1} + \text{H}_2\text{O} = \text{H}_3\text{O}^+(\text{H}_2\text{O})_n$. *Journal of the American Chemical Society*, 104(6):1462–1469, 1982.

Bibliography

- [205] A. Cunningham, J. Payzant, and P. Kebarle. Kinetic study of the proton hydrate $H^+(H_2O)_n$ equilibriums in the gas phase. *Journal of the American Chemical Society*, 1870(5):7627–7632, 1972.
- [206] H. R. Bollan, J. A. Stone, J. L. Brokenshire, J. E. Rodriguez, and G. A. Eiceman. Mobility Resolution and Mass Analysis of Ions from Ammonia and Hydrazine Complexes with Ketones Formed in Air at Ambient Pressure. *Journal of the American Society for Mass Spectrometry*, 18(5):940–951, 2007.
- [207] B. Seale, B. B. Schneider, and J. C. Le Blanc. Enhancing signal and mitigating up-front peptide fragmentation using controlled clustering by gas-phase modifiers. *Analytical and Bioanalytical Chemistry*, 411(24):6365–6376, 2019.
- [208] P. Liere, S. Bouchonnet, R. E. March, and J. C. Tabet. Cooling time and pressure effects on competitive thermalization/activation processes by resonance excitation on ITMS. *Rapid Communications in Mass Spectrometry*, 9(15):1594–1598, 1995.
- [209] J. E. McClellan, J. P. Murphy, J. J. Mulholland, and R. A. Yost. Effects of fragile ions on mass resolution and on isolation for tandem mass spectrometry in the quadrupole ion trap mass spectrometer. *Analytical Chemistry*, 74(2):402–412, 2002.
- [210] W. R. Plass, H. Li, and R. G. Cooks. Theory, simulation and measurement of chemical mass shifts in RF quadrupole ion traps. *International Journal of Mass Spectrometry*, 228(2-3):237–267, 2003.
- [211] F. A. Lindemann, S. Arrhenius, I. Langmuir, N. R. Dhar, J. Perrin, and W. C. M. Lewis. Discussion on "the radiation theory of chemical action". *Transactions of the Faraday Society*, 17:598–606, 1922.
- [212] C. Lifshitz. Some recent aspects of unimolecular gas phase ion chemistry. *Chemical Society Reviews*, 30(3):186–192, 2001.
- [213] D. L. Baluya and R. A. Yost. 'Pressure Tailoring' for Improved Ion Trap Performance. In R. E. March and J. F. J. Todd, editors, *Practical Aspects of Trapped Ion Mass Spectrometry Vol. IV Theory and Instrumentation*, chapter 18. CRC Press, Boca Raton, FL, USA, 2010.
- [214] P. Liere, R. E. March, T. Blasco, and J.-C. Tabet. Resonance excitation in a quadrupole ion trap: modification of competing dissociative channel yields. *International Journal of Mass Spectrometry and Ion Processes*, 153(2-3):101–117, 2002.
- [215] J. C. Schwartz, J. E. Syka, and I. Jardine. High resolution on a quadrupole ion trap mass spectrometer. *Journal of the American Society for Mass Spectrometry*, 2(3):198–204, 1991.

- [216] R. E. March and J. F. J. Todd. *Quadrupole Ion Trap Mass Spectrometry*. John Wiley & Sons, Hoboken, New Jersey, USA, 2nd edition, 2005.
- [217] Y. Kawai, S. Yamaguchi, Y. Okada, and K. Takeuchi. Reactions of size-selected protonated water clusters $H^+(H_2O)_n$ ($n = 2-6$) with an acetone molecule in a guided ion beam apparatus. *International Journal of Mass Spectrometry*, 220:375-383, 2002.
- [218] S. J. Grabowski. *Hydrogen Bonding - New Insights*. Springer, Dordrecht, Netherlands, 2006.
- [219] K. Hirao, S. Yamabe, and M. Sano. Theoretical study on the stability and structure of $H^+(HCN)_n$ and $M^+(CH_3CN)_n$ ($M^+ = H^+, Li^+, \text{ and } Na^+$) clusters. *Journal of Physical Chemistry*, 86(14):2626-2632, 1982.
- [220] A. Haack, T. Benter, and H. Kersten. Computational analysis of the proton-bound acetonitrile dimer, $(ACN)_2H^+$. *Rapid Communications in Mass Spectrometry*, 34(11):1-9, 2020.
- [221] S. Armenta and M. Blanco. Ion mobility spectrometry for monitoring diamine oxidase activity. *Analyst*, 137(24):5891-5897, 2012.
- [222] R. Fernandez-Maestre, D. Meza-Morelos, and C. Wu. Mobility shifts when buffer gas temperature increases in ion mobility spectrometry are affected by intramolecular bonds. *International Journal of Mass Spectrometry*, 407:113-117, 2016.
- [223] R. Fernández-Maestre, D. Meza-Morelos, and C. Wu. Shift reagents in ion mobility spectrometry: The effect of the number of interaction sites, size and interaction energies on the mobilities of valinol and ethanolamine. *Journal of Mass Spectrometry*, 51(5):378-383, 2016.
- [224] X. F. D. Chillier, A. Monnier, H. Bill, F. O. Gülaçar, A. Buchs, S. A. McLuckey, and G. J. Van Berkel. A Mass Spectrometry and Optical Spectroscopy Investigation of Gas-phase Ion Formation in Electrospray. *Rapid Communications in Mass Spectrometry*, 10:299-304, 1996.
- [225] L. M. Martin and L. Konermann. Sulfolane-Induced Supercharging of Electro-sprayed Salt Clusters: An Experimental/Computational Perspective. *Journal of the American Society for Mass Spectrometry*, 2021.

Erklärung

„Ich versichere, die Arbeit selbstständig verfasst zu haben, nur die in der Dissertation angegebenen Hilfsmittel benutzt und alle wörtlich und inhaltlich übernommenen Stellen als solche gekennzeichnet zu haben, und dass die Dissertation in der gegenwärtigen oder einer anderen Fassung noch keiner anderen Fakultät, keiner Gesamthochschule und keiner anderen wissenschaftlichen Hochschule vorgelegen hat.“

Wuppertal, den 16.08.2021

Christine Polaczek

